



MINISTÉRIO DA CIÊNCIA, TECNOLOGIA, INOVAÇÕES E COMUNICAÇÕES
INSTITUTO NACIONAL DE PESQUISAS ESPACIAIS

sid.inpe.br/mtc-m21c/2018/05.02.13.07-TDI

TRAJECTORY AND ATTITUDE MODELING AND PROPAGATION FOR REENTRY DEBRIS WITH FRAGMENTATION IMPLEMENTING VOXELS MESHES

Jhonathan Orlando Murcia Piñeros

Doctorate Thesis of the Graduate Course in Space Engineering and Technology – Spatial Mechanics and Control, guided by Drs. Antonio Fernando Bertachini de Almeida Prado, and Ulisses Tadeu Vieira Guedes, approved in April 27, 2018.

URL of the original document:

<<http://urlib.net/8JMKD3MGP3W34R/3R34NKS>>

INPE

São José dos Campos

2018

PUBLISHED BY:

Instituto Nacional de Pesquisas Espaciais - INPE

Gabinete do Diretor (GBDIR)

Serviço de Informação e Documentação (SESID)

Caixa Postal 515 - CEP 12.245-970

São José dos Campos - SP - Brasil

Tel.:(012) 3208-6923/6921

E-mail: pubtc@inpe.br

**COMMISSION OF BOARD OF PUBLISHING AND PRESERVATION
OF INPE INTELLECTUAL PRODUCTION (DE/DIR-544):****Chairperson:**

Maria do Carmo de Andrade Nono - Conselho de Pós-Graduação (CPG)

Members:

Dr. Plínio Carlos Alvalá - Centro de Ciência do Sistema Terrestre (COCST)

Dr. André de Castro Milone - Coordenação-Geral de Ciências Espaciais e Atmosféricas (CGCEA)

Dra. Carina de Barros Melo - Coordenação de Laboratórios Associados (COCTE)

Dr. Evandro Marconi Rocco - Coordenação-Geral de Engenharia e Tecnologia Espacial (CGETE)

Dr. Hermann Johann Heinrich Kux - Coordenação-Geral de Observação da Terra (CGOBT)

Dr. Marley Cavalcante de Lima Moscati - Centro de Previsão de Tempo e Estudos Climáticos (CGCPT)

Silvia Castro Marcelino - Serviço de Informação e Documentação (SESID)

DIGITAL LIBRARY:

Dr. Gerald Jean Francis Banon

Clayton Martins Pereira - Serviço de Informação e Documentação (SESID)

DOCUMENT REVIEW:

Simone Angélica Del Duca Barbedo - Serviço de Informação e Documentação (SESID)

Yolanda Ribeiro da Silva Souza - Serviço de Informação e Documentação (SESID)

ELECTRONIC EDITING:

Marcelo de Castro Pazos - Serviço de Informação e Documentação (SESID)

André Luis Dias Fernandes - Serviço de Informação e Documentação (SESID)



MINISTÉRIO DA CIÊNCIA, TECNOLOGIA, INOVAÇÕES E COMUNICAÇÕES
INSTITUTO NACIONAL DE PESQUISAS ESPACIAIS

sid.inpe.br/mtc-m21c/2018/05.02.13.07-TDI

TRAJECTORY AND ATTITUDE MODELING AND PROPAGATION FOR REENTRY DEBRIS WITH FRAGMENTATION IMPLEMENTING VOXELS MESHES

Jhonathan Orlando Murcia Piñeros

Doctorate Thesis of the Graduate Course in Space Engineering and Technology – Spatial Mechanics and Control, guided by Drs. Antonio Fernando Bertachini de Almeida Prado, and Ulisses Tadeu Vieira Guedes, approved in April 27, 2018.

URL of the original document:

<http://urlib.net/8JMKD3MGP3W34R/3R34NKS>

INPE

São José dos Campos

2018

Cataloging in Publication Data

Murcia Piñeros, Jhonathan Orlando.

M939t Trajectory and attitude modeling and propagation for reentry debris with fragmentation implementing voxels meshes / Jhonathan Orlando Murcia Piñeros. – São José dos Campos : INPE, 2018.

xxx + 165 p. ; (sid.inpe.br/mtc-m21c/2018/05.02.13.07-TDI)

Thesis (Doctorate in Space Engineering and Technology – Spatial Mechanics and Control) – Instituto Nacional de Pesquisas Espaciais, São José dos Campos, 2018.

Guiding : Drs. Antonio Fernando Bertachini de Almeida Prado, and Ulisses Tadeu Vieira Guedes.

1. Fragmentation. 2. Reentry. 3. Six degrees of freedom. 4. Trajectory. 5. Orbital debris. I.Title.

CDU 629.7.05:692.7.076.8



Esta obra foi licenciada sob uma Licença [Creative Commons Atribuição-NãoComercial 3.0 Não Adaptada](https://creativecommons.org/licenses/by-nc/3.0/).

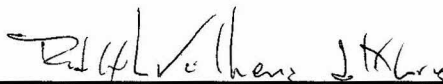
This work is licensed under a [Creative Commons Attribution-NonCommercial 3.0 Unported License](https://creativecommons.org/licenses/by-nc/3.0/).

Aluno (a): **Jhonathan Orlando Murcia Piñeros**

Título: "TRAJECTORY AND ATTITUDE MODELING AND PROPAGATION FOR REENTRY DEBRIS WITH FRAGMENTATION IMPLEMENTING VOXELS MESHES"

Aprovado (a) pela Banca Examinadora
em cumprimento ao requisito exigido para
obtenção do Título de **Doutor(a)** em
**Engenharia e Tecnologia Espaciais/Mecânica
Espacial e Controle**

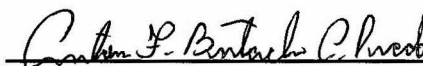
Dr. Rodolpho Vilhena de Moraes



Presidente / INPE / São José dos Campos - SP

() Participação por Video - Conferência

Dr. Antonio Fernando Bertachini de Almeida Prado



Orientador(a) / INPE / SJC Campos - SP

() Participação por Video - Conferência

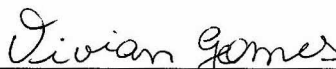
Dr. Ulisses Thadeu Vieira Guedes



Orientador(a) / INPE / SJC Campos - SP

() Participação por Video - Conferência

Dra. Vivian Martins Gomes



Convidado(a) / UNESP/FEG / Guaratinguetá - SP

() Participação por Video - Conferência

Dr. Francisco das Chagas Carvalho



Convidado(a) / ITA/DCTA / São José dos Campos - SP

() Participação por Video - Conferência

Este trabalho foi aprovado por:

() maioria simples

unanimidade

São José dos Campos, 27 de abril de 2018

“The dream of yesterday is the hope of today and the reality of tomorrow”.

Robert Goddard, 1904.

To Lina, with all my love.

ACKNOWLEDGMENTS

First of all, I want to thank the Architect of the Cosmos for giving me the opportunity to make this dream come true and for all the blessings received. This moment is the culmination of decades of study, discipline, dedication, love and dreams.

To Lina, thanks for the patience, for giving me strength, for motivating me every day and supporting me. To my parents Esperanza and Orlando, to my family Julian, Carmen, Angela, José, Daniela, who always supported and motivated me.

I especially want to thank my counselors Ulisses G. and Antonio F. B. A. P. for their patience, for the knowledge, advice and all the help provided, thank you very much.

To my teachers Gregorio P., Hernan Cerón, Andreas G., Francisco G., thank you for sharing your knowledge, for your advices and for motivating me to follow this path. To my work colleagues Aixa, Jairo M., Jairo R., Jesus B., John P., Andres J., Rosita, Juan Carlos C., Aurelio, Carlos C., for your advice. To my work team Saulo, Diego, Jenny, Johanna, Javier. To my friends Manuel C., Alejandro A., Aysses O., Lorena C., Luis M., Geraldo M., Alain G., Wilian C., Allan K. To my students Ceidy, Maria N., Andrea F., Jessica A., Daimer, Luis Carlos, Alejandro A., Eliana C., Nixón, Jaime Enrique O., Sergio P., Felipe B., Roy C., Andres, Arturo T.

To the Professors, Students and Secretaries of the postgraduate course in ETE-CMC. I wish to express my appreciation for the support to the National Institute for Space Research (INPE) and the scholarship provided by the National Council for the Improvement of Higher Education (CAPES) Code: #33010013009P6.

ABSTRACT

Actually, more than 17.000 objects are in orbit around the Earth, with an estimated total mass of 6.500.000 kg. All of them with dimensions superior to 10 cm and some orbiting without control. In other words, they are orbital debris. In orbit, the debris represents a hazard to operational satellites and aerospace operations due to the high probability of collisions. With the exponential increment of space activities and without regulations it is expected a proportional increment in the debris population and an increase the risk for the space activities. Because the interaction of the debris with the atmosphere of the Earth and the solar activity, the debris began to lose energy and decay. During the de-orbit process, the debris fall into the Earth's atmosphere at hypersonic speeds and these objects can be break-up and/or fragmented due to the aerodynamics, thermal and structural loads. It is important to obtain the trajectory and attitude of any fragment to determine the possible survival mass, impact area, hazard conditions and risk to the population, the air traffic control, and infrastructure. Different computational tools are used to determine the impact of the debris during reentry. These tools implement different models complemented with data from observations and laboratories. In this case, it is proposed a computational code to integrate the equations of motion and to propagate the dynamics and kinematics of the possible survival fragments. The new model implements the voxel method to determine the aerodynamic conditions and the fragmentation of the body. It is also analyzed the results of trajectories with six degrees of freedom, atmospheric winds, and Magnus effect. The mathematical model and computational code are validated in three degrees of freedom. Results are compared with data from other computational tools available in the scientific literature. The results show a good approximation with the report cases of study. New results are generated in the simulations of rotational bodies, due to the influence of aerodynamic forces in the trajectory and the changes in the stagnation regions. Because the implementation of wind and rotation of the debris, the fragments increased the survivability and the dispersion area. These information confirm the initial hypothesis and increases the applications of the actual tool in future reentry predictions.

Keywords: Fragmentation, Reentry, Six degrees of freedom, Trajectories, Orbital debris.

MODELAMENTO E PROPAGAÇÃO DA TRAJETÓRIA E ATITUDE DE DETRITOS ESPACIAIS COM FRAGMENTAÇÃO IMPLEMENTANDO UMA MALHA DE VOXELS

RESUMO

Atualmente, mais de 17.000 objetos orbitam em torno da Terra, com uma estimativa de massa superior a 6.500.000 kg. Todos eles com dimensões superiores a 10 cm e alguns orbitando sem controle, também conhecidos como detritos espaciais. Na órbita, os detritos representam risco para satélites operacionais e para as operações aeroespaciais porque aumentam as probabilidades de colisões. Com o incremento exponencial das atividades espaciais e a ausência de regulamentos, espera-se um incremento proporcional na população de detritos e o aumento do risco das atividades espaciais. A interação dos detritos com a atmosfera da Terra e a atividade solar fazem com que os detritos comecem a perder energia gerando o decaimento da órbita. Durante o processo de decaimento, os detritos caem na atmosfera da Terra a velocidades hipersônicas e podem ser quebrados e/ou fragmentados pelas cargas aerodinâmicas, térmicas e estruturais. É importante obter a trajetória e a atitude de qualquer fragmento para determinar a possível massa final, a área de impacto, condições de perigo e risco para a população, para o controle de tráfego aéreo e para a infraestrutura em terra. Diferentes ferramentas computacionais são implementadas para determinar o impacto dos detritos durante a reentrada. Qualquer uma dessas ferramentas implementa diferentes modelos matemáticos complementados com dados de observações e laboratórios. Neste caso, propõe-se um código computacional para integrar as equações de movimento e propagar a dinâmica e a cinemática dos possíveis fragmentos que conseguem sobreviver a reentrada. O modelo proposto implementa o método de voxels para determinar as condições aerodinâmicas e a fragmentação dentro do corpo, analisando os resultados de trajetórias com seis graus de liberdade, ventos atmosféricos e efeito Magnus. O modelo matemático e o código computacional são validados em três graus de liberdade. Os resultados foram comparados com dados de outras ferramentas computacionais disponíveis na literatura científica. Os resultados mostram uma boa aproximação com os casos estudados. Novos resultados foram gerados nas simulações de corpos rotativos e pode-se observar a influência das forças aerodinâmicas na trajetória e as mudanças nas regiões de estagnação dos fragmentos. Com a implementação do vento e a rotação dos detritos, os fragmentos aumentaram a capacidade de sobrevivência e a área de dispersão. Essas informações confirmam a hipótese inicial e aumentam as aplicações da ferramenta real em futuras previsões de reentrada.

Reentrada. Trajetórias. Fragmentação. Seis graus de liberdade. Detritos espaciais.

LIST OF FIGURES

	<u>Page.</u>
Figure 3.1 – Reference Earth´s system.....	24
Figure 3.2 – Forces acting in the body.	25
Figure 3.3 – Euler angles in the body system.....	26
Figure 3.4 – Aerodynamics angles.	31
Figure 3.5 – Earth inertial to geographic.	33
Figure 3.6 – LHRS and body system.....	34
Figure 6.1 – Voxel and panel methods.....	45
Figure 7.1 – Reentry fragmentation scheme.	50
Figure 8.1 – Sequential execution.	54
Figure 8.2 – Parallel execution.	55
Figure 8.3– Parallel execution.	55
Figure 9.1 – Flow diagram of the computational code.....	58
Figure 10.1 – Solid sphere mesh with 4145 nodes.....	63
Figure 10.2 – Solid sphere mesh with 73453 nodes.....	63
Figure 10.3 – Solid sphere mesh with 523185 nodes.....	64
Figure 10.4 – Voxel sphere mesh.....	65
Figure 10.5 – Spherical tank altitude vs time.....	68
Figure 10.6 – Spherical tank altitude vs time, zoom.	68
Figure 10.7 – Spherical tank altitude vs relative velocity.	69
Figure 10.8 – Spherical tank drag coefficient vs altitude.	70
Figure 10.9 – Reentries spherical coordinates.	71
Figure 10.10 – Reentries impact zone estimations.....	71
Figure 10.11 – Debris flight path angle vs time.	72
Figure 10.12 – Spherical tank relative energy vs time.....	73
Figure 10.13 – Spherical tank rotational energy vs time.....	73
Figure 10.14 – Spherical tanks altitude vs heat flux.	74
Figure 10.15 – Spherical tanks altitude vs load factor.....	75
Figure 10.16 – Spherical tanks altitude vs dynamic pressure.	75

Figure 10.17 – Surface temperature distribution tank in 3DOF.	76
Figure 10.18 – Surface CP distribution tank in 3DOF.....	77
Figure 10.19 – Surface temperature distribution tank in 6DOF.	77
Figure 10.20 – Surface CP distribution tank in 6DOF.....	78
Figure 10.21 – Surface temperature distribution tank at 1200RPM.....	78
Figure 10.22 – Surface CP distribution tank at 1200RPM.	79
Figure 10.23 – Surface temperature distribution tank at -1200RPM.....	79
Figure 10.24 – Surface CP distribution tank at -1200RPM.....	80
Figure 10.25 – Tank altitude vs time reentry with different materials.....	81
Figure 10.26 – Tank altitude vs velocity reentry with survival materials.	81
Figure 10.27 – Tank altitude vs mass, from left to right: Graphite, Aluminum, Titanium, Steel and Copper.....	82
Figure 11.1 – Graphite epoxy I spherical tanks reentry without initial angular velocity, altitude vs time.....	86
Figure 11.2 – Graphite epoxy I spherical tanks reentry $w_x=1200$ RPM, altitude vs time.....	86
Figure 11.3 – Graphite epoxy I spherical tanks reentry $w_y=1200$ RPM, altitude vs time.....	87
Figure 11.4– Graphite epoxy I spherical tanks reentry $w_z=1200$ RPM, altitude vs time.	87
Figure 11.5 – Graphite epoxy I spherical tanks reentry without initial angular velocity, altitude vs relative velocity.....	88
Figure 11.6 – Graphite epoxy I spherical tanks reentry $w_x=1200$ RPM, altitude vs relative velocity.	88
Figure 11.7 – Graphite epoxy I spherical tanks reentry $w_y=1200$ RPM, altitude vs relative velocity.	89
Figure 11.8 – Graphite epoxy I spherical tanks reentry $w_z=1200$ RPM, altitude vs relative velocity.	89
Figure 11.9 - Graphite epoxy I spherical tanks reentry without initial angular velocity, FPA vs Time.....	90

Figure 11.10 - Graphite epoxy I spherical tanks reentry $w_x=1200$ RPM, FPA vs Time.	91
Figure 11.11 - Graphite epoxy I spherical tanks reentry $w_y=1200$ RPM, FPA vs Time.	91
Figure 11.12 - Graphite epoxy I spherical tanks reentry $w_z=1200$ RPM, FPA vs Time.	92
Figure 11.13 - Graphite epoxy I spherical tanks reentry, Energy vs Time.	92
Figure 11.14 - Graphite epoxy I spherical tanks reentry trajectory.	93
Figure 11.15 – Survival Graphite epoxy I 2.5 cm tank, impact zone.	94
Figure 11.16 – Survival Graphite epoxy I 5 cm tank, impact zone.	95
Figure 11.17 – Survival Graphite epoxy I 10 cm tank, impact zone.	95
Figure 11.18 – Survival Graphite epoxy I 12.5 cm tank, impact zone.	96
Figure 11.19 – Survival Graphite epoxy I 25 cm tank, impact zone.	96
Figure 11.20 – Survival Graphite epoxy I 50 cm tank, impact zone.	97
Figure 11.21 – Titanium spherical tanks reentry without initial angular velocity, altitude vs time.	99
Figure 11.22 – Titanium spherical tanks reentry $w_x=1200$ RPM, altitude vs time.	99
Figure 11.23 – Titanium spherical tanks reentry $w_y=1200$ RPM, altitude vs time.	99
Figure 11.24 – Titanium spherical tanks reentry $w_z=1200$ RPM, altitude vs time.	100
Figure 11.25 – Titanium spherical tanks reentry without initial angular velocity, altitude vs relative velocity.	101
Figure 11.26 – Titanium spherical tanks reentry $w_x=1200$ RPM, altitude vs relative velocity.	101
Figure 11.27 – Titanium spherical tanks reentry $w_y=1200$ RPM, altitude vs relative velocity.	102
Figure 11.28 – Titanium spherical tanks reentry $w_z=1200$ RPM, altitude vs relative velocity.	102

Figure 11.29 - Titanium spherical tanks reentry without initial angular velocity, FPA vs Time.....	103
Figure 11.30 - Titanium spherical tanks reentry $w_x=1200$ RPM, FPA vs Time.	103
Figure 11.31 - Titanium spherical tanks reentry $w_y=1200$ RPM, FPA vs Time.	104
Figure 11.32- Titanium spherical tanks reentry $w_z=1200$ RPM, FPA vs Time.	105
Figure 11.33 – Survival Titanium 2.5 cm tank, impact zone.	105
Figure 11.34 – Survival Titanium 5 cm tank, impact zone.	106
Figure 11.35 – Survival Titanium 10 cm tank, impact zone.	106
Figure 11.36 – Survival Titanium 12.5 cm tank, impact zone.	106
Figure 11.37 – Survival Titanium 25 cm tank, impact zone.	107
Figure 11.38 – Survival Titanium 50 cm tank, impact zone.	107
Figure 11.39 – Survival percent of mass, tanks of Titanium without initial angular velocity.	110
Figure 11.40 – Survival percent of mass, tanks of Titanium $w_x=1200$ RPM. ..	110
Figure 11.41 – Survival percent of mass, tanks of Titanium $w_y=1200$ RPM. ..	111
Figure 11.42 – Survival percent of mass, tanks of Titanium $w_z=1200$ RPM. ..	111
Figure 11.43 – Aluminum spherical tanks reentry without initial angular velocity, altitude vs time.	112
Figure 11.44 – Aluminum spherical tanks reentry $w_x=1200$ RPM, altitude vs time.	113
Figure 11.45 – Aluminum spherical tanks reentry $w_y=1200$ RPM, altitude vs time.	113
Figure 11.46 – Aluminum spherical tanks reentry $w_z=1200$ RPM, altitude vs time.	114
Figure 11.47 – Aluminum spherical tanks reentry without initial angular velocity, altitude vs relative velocity.....	115
Figure 11.48 – Aluminum spherical tanks reentry $w_x=1200$ RPM, altitude vs relative velocity.....	115

Figure 11.49 – Aluminum spherical tanks reentry $w_y=1200$ RPM, altitude vs relative velocity.....	116
Figure 11.50 – Aluminum spherical tanks reentry $w_z=1200$ RPM, altitude vs relative velocity.....	116
Figure 11.51 - Aluminum spherical tanks reentry without initial angular velocity, FPA vs Time.....	117
Figure 11.52 - Aluminum spherical tanks reentry $w_x=1200$ RPM, FPA vs Time.	117
Figure 11.53 - Aluminum spherical tanks reentry $w_y=1200$ RPM, FPA vs Time.	118
Figure 11.54 - Aluminum spherical tanks reentry $w_z=1200$ RPM, FPA vs Time.	118
Figure 11.55 – Survival Aluminum 2.5 cm tank, impact zone.....	119
Figure 11.56 – Survival Aluminum 5 cm tank, impact zone.....	119
Figure 11.57 – Survival Aluminum 10 cm tank, impact zone.....	120
Figure 11.58 – Survival Aluminum 12.5 cm tank, impact zone.....	120
Figure 11.59– Survival Aluminum 25 cm tank, impact zone.....	121
Figure 11.60 – Survival Aluminum 50 cm tank, impact zone.....	121
Figure 11.61 – Survival percent of mass, tanks of Aluminum without initial angular velocity.	122
Figure 11.62 – Survival percent of mass, tanks of Aluminum $w_x=1200$ RPM.	123
Figure 11.63 – Survival percent of mass, tanks of Aluminum $w_y=1200$ RPM.	123
Figure 11.64 – Survival percent of mass, tanks of Aluminum $w_z=1200$ RPM.	124
Figure 11.65 – Standard Deviation in Position for a sphere of 2.5 cm.....	127
Figure 11.66 – Standard Deviation in Position for a sphere of 50 cm.....	128
Figure 11.67 – Standard Deviation in Position for a sphere of 2.5 cm with angular velocity in X_B	129
Figure 11.68 – Standard Deviation in Position for a sphere of 50 cm with angular velocity in X_B	130
Figure 11.69 – Standard Deviation in Position for a sphere of 2.5 cm with angular velocity in Y_B	130

Figure 11.70 – Standard Deviation in Position for a sphere of 50 cm with angular velocity in Y_B	131
Figure 11.71 – Standard Deviation in Position for a sphere of 2.5 cm with angular velocity in Z_B	131
Figure 11.72 – Standard Deviation in Position for a sphere of 50 cm with angular velocity in Z_B	132
Figure 11.73 – Standard deviation in position for a sphere of 2.5 cm with atmospheric and aerodynamic errors.	133
Figure 11.74 – Dispersion area for 2.5 cm tank.....	134
Figure 11.75 – Standard deviation in position for a sphere of 50 cm with atmospheric and aerodynamic errors.	135
Figure 11.76 - Dispersion area for 50 cm tank.	135
Figure 11.77 – Tiangong I orbit representation.....	136
Figure 11.78 – Tiangong I historical perigee altitude.....	137
Figure 11.79 - Tiangong-I diagram.	138
Figure 11.80 - Tiangong-I computational model approximation.....	138
Figure 11.81 - Tiangong-I decay propagations.....	139
Figure 11.82 – Tiangong-I cylinders approximation reentry.	140
Figure 11.83 - Tiangong-I cylinders velocity during reentry.....	141

LIST OF TABLES

	<u>Page.</u>
Table 2.1 – Comparison ORSAT vs. SCARAB.....	21
Table 2.2 – Debris impacted and recovered in Brazil	23
Table 10.1 – Materials data	62
Table 10.2 – Spherical tank Initial Conditions.....	66
Table 11.1 – Spherical tank dimensions.....	84
Table 11.2 – Final Energy in Jules for spherical tanks of Epoxy I.	98
Table 11.3 – Final Energy in Jules for spherical tanks of Titanium.....	108
Table 11.4 – Final Energy in Jules for spherical tanks of Aluminum.	122

LIST OF ABBREVIATIONS

AEB	Agência Espacial Brasileira
AOA	Angle Of Attack
DAS	Debris Assessment Software
DOF	Degrees Of Freedom
ESA	European Space Agency
FPA	Flight Path Angle
HAL	High Architecture Level method
IEAv	Instituto de Estudos Avançados
INPE	Instituto Nacional de Pesquisas Espaciais
ITA	Instituto Tecnológico de Aeronáutica
NASA	National Aeronautics and Space Administration
ORSAT	The Object Reentry Survival Analysis Tool
RKF	Runge Kutta Fehlberg
SCARAB	Spacecraft Atmospheric Re-entry and Aerothermal Break-Up
TLE	Two Line Elements

LIST OF SYMBOLS

A_F	Aerodynamic force, N
Alt	Altitude, m
C_D	Drag coefficient
C_{nm}	Spherical harmonics coefficients
C_L	Lift coefficient
D	Drag force, N
F	Function
G	Gravity, m/s^2
h	Step size, s
I	Inertia tensor, $kg.m^2$
I_{SP}	Specific impulse, s
K_{Bol}	Boltzmann constant
K_n	Knudsen number
K_{rad}	Radiation material constant
L	Lift force, N
l_B	Body length, m
M	Mach's number
M_E	Earth's mass, kg
m	Mass, kg
\mathcal{M}	Moments, N.m
n	Normal vector to surface
P_{atm}	Atmospheric pressure, Pa
P_{nm}	Legendre's Polynomial
Q	Heat flux, W/m^2
q	Dynamic pressure, Pa
r	Radius vector, m
r_B	Body radius, m
R	Gas constant, J/kg.K
R_E	Earth's mean radius, m
Re	Reynold's number
S	Surface, m^2

S_{nm}	Spherical harmonics coefficients
T	Thrust force, N
T_{atm}	Atmospheric temperature, K
T_s	Surface temperature, K
t	Time, s
U	Earth's geopotential
V_{atm}	Atmospheric velocity, m/s
V_I	Inertial velocity, m/s
V_R	Relative velocity, m/s
V_S	Speed of sound, m/s
V_W	Wind velocity, m/s
W	Weight, N
x_B, y_B, z_B	Body axis system
x_E, y_E, z_E	Earth's axis systems
x_I, y_I, z_I	Cartesian inertial axis system
x_W, y_W, z_W	Wind-body axis system
γ	Gas constant
\varnothing	Latitude angle, Deg°
υ	Flight path angle, Deg°
α	Angle Of Attack (AOA), Deg°
α_C	Thermal accommodation coefficient
α_k	Fehlberg's coefficients
β	Bank angle, Deg°
$\beta_{k\lambda}$	Fehlberg's coefficients
θ	Euler's angles, Deg°
Θ	Normal surface angle, Deg°
λ	Longitude angle, Deg°
μ	Fluid viscosity
ρ	Density, kg/m ³
σ	Standard Deviation.
ϕ	Panel incident angle, Deg°
Ω	Total Angular velocity, Deg°/s

ω	Local Angular velocity, Deg°/s
ω_B	Body angular velocity, Deg°/s
ω_E	Earth's angular velocity, Deg°/s

SUMMARY

		<u>Page.</u>
1	INTRODUCTION.....	1
2	REENTRY FRAGMENTATION REVIEW	7
2.1.	Software reentry tools and applications.....	9
2.2.	Reentries in Brazil	21
3	DYNAMICS AND KINEMATICS OF THE REENTRY	24
3.1.	Dynamics.....	24
3.2.	Attitude	26
3.3.	Forces	27
3.3.1.	Lift and Drag.....	28
3.3.2.	Thrust.....	29
3.4.	Angular momentum and auxiliary vector	29
3.4.1.	Lift vector.....	30
3.4.2.	Thrust vector	31
3.5.	Coordinate systems.....	32
3.5.1.	Spherical system	32
3.5.2.	Local horizontal system	33
4	ATMOSPHERE, WINDS AND GEOPOTENTIAL MODELS	35
4.1.	Atmospheric model.....	35
4.2.	Wind model	36
4.3.	Geopotential model	37
5	NUMERICAL ANALYSIS.....	38
5.1.	Runge-Kutta	38
5.2.	Covariance matrix	39
6	AERODYNAMICS AND AEROTHERMODYNAMICS	40
6.1.	Dimensionless numbers	40
6.2.	Aerodynamics.....	41
6.3.	Aerothermodynamics	46
7	FRAGMENTATION AND BREAK-UP	49
8	COMPUTATIONAL DISTRIBUTED METHOD	53

9	CODE STRUCTURE.....	56
10	STUDY CASES, ANALYSIS AND RESULTS.....	61
10.1.	Materials.....	61
10.2.	Mesh	61
10.3.	Validation.....	65
10.4.	Results of spherical tank in 6DOF	70
10.5.	Results of reentry tank with different materials.....	80
11	LEO (LOW EARTH ORBIT) DEBRIS REENTRY ANALYSIS.....	83
11.1.	Re-entry rotational spherical tanks analysis	83
11.1.1.	Reentry of spherical tanks of Graphite Epoxy – I	85
11.1.2.	Reentry of spherical tanks of Titanium	98
11.1.3.	Reentry of spherical tanks of Aluminum	111
11.2.	Error analysis	124
11.3.	Study case: Tiangong – I China Space Station, reentry estimation. 136	
12.	CONCLUSIONS	142
	REFERENCES.....	147

1 INTRODUCTION

In a single space mission around the Earth, three trajectory phases are described by the spacecraft in its lifetime. The first phase is to transport the spacecraft from the surface of the Earth to its orbit, called the launch phase. The second phase is when the spacecraft is in orbit, during its operational time, or after that, when it becomes a debris, as in the case of a rocket upper stage and/or another structure. Finally, the third phase is the disposal or de-orbit, is when the spacecraft begins to decay due to the atmospheric drag and gravitational forces. When the spacecraft or debris are at altitudes below 120 km from the Earth's surface, the air density is strong enough to generate significant drag and braking the spacecraft. Then the spacecraft velocity becomes lower than the orbital velocity and, at this point, the atmospheric re-entry begins.

In the descent trajectories, that last only seconds or minutes, the spacecraft decay rapidly into a higher density atmosphere, increasing the drag, the dynamic pressure and the temperature in its surface. Hypersonic, supersonic, transonic and/or subsonic flight can be obtained, according to the spacecraft geometry, materials, and atmospheric fluid properties. Few spacecraft or components are designed to survive the reentry phase, like human space capsules, nuclear warheads, inertial weapons, sounding rockets or microgravity experiments. Aeroshield technology is implemented to protect the payload dissipating the heat around the reentry probe. Additional recovery devices like aerodynamic decelerators and/or parachutes are implemented for the landing. All these methods are designed to recover the payload in optimal conditions. Experiences acquired from previous reentry missions are applied in planetary exploration missions in our solar system, like Spirit's, Opportunity or Curiosity on Mars. However, another object can reentry and survive in the atmosphere without being designed for this purpose, like orbital debris, superior rocket stages, tanks, batteries and natural bodies like the meteors. Many of these objects are disintegrate along the trajectory, due to the heat, dynamic pressure,

erosion, stress, mechanical conditions, ablations, explosions or another condition, but, sometimes, these objects or elements without control can survive the reentry and impact the Earth's surface at high speeds, becoming a risk for the population, transport, facilities, security, defense and environmental. Thanks to the higher kinetic energy at the impact, they can generate explosions like an atomic bomb (Ex. Tunguska incident).

The reentry trajectories can be classified in controlled and uncontrolled. Generally, the controlled trajectories are developed for manned spacecraft (Ex. Apollo, Mercury, Soyuz, and Space Shuttle) or larger bodies (Ex. Mir Space Station, Skylab, and Cosmos). Uncontrolled reentries are generated due to the orbit decay at the end of the lifetime and apply to bodies like satellites, rocket stages or debris. For the mission designer, uncontrolled reentry offers advantages like spacecraft mass reduction, reduction of systems, saving in propellant and costs reductions. Another methods, like insulator materials or intentional breakups, are implemented to reduce the survivability of reentry debris objects. During the reentry, the principal body can be disintegrated (breakup, fragmentation, explosion) into a cloud of small objects. These new objects create from the fragmentation, have new mass, geometry and different initial conditions with independent trajectories. The reentry problem is more complex when the fragmentation is present because the actual mathematical models are limited to predict the object mass, geometry, material properties and configuration. More experimental and observational data are necessary to test and to calibrate the fragmentation mathematical models during reentry.

Proportionally to the increment of space activities, it is the risk increment on-orbit collisions because the space debris, in the same way, the incremented of uncontrolled reentries (PATERA; AILOR, 1998). More than 17,000 tracked objects are in orbit actually, with an estimated total mass of 6,500,000 kg. All of these objects will be orbital debris, and some of them will survive the reentry, due to its material, mass, attitude, trajectory and/or geometry, that may generate a perfect combination that allows them to resist the highest reentry

temperatures and pressures (NASA; 2014, 2015, 2017). ESA is tracking 23,000 objects in orbit with 7,500 metric tons of total mass, where only 1,200 are operational. Results from simulations estimate an increment in 50% in the number of space debris for the next 200 years (LIOU; JOHNSON, 2006). Statistical models estimate around 290 break-ups, explosion or collision events, resulting in 29,000 objects higher than 10 cm of nominal diameter, 750,000 from 1 cm to 10 cm, and the alarming number of 166 million of objects from 1 mm to 1 cm (ESA, 2017). According to NASA, a survival debris is considered a risk when its final kinetic energy is higher than 15 J, which means that, for a survival reentry debris with 1 kg of mass, the impact velocity must be lower than 3.9 m/s, and human causality probability lower than 1:10,000 (NASA, 1998). Causality expectation and probability of causality varies according to the orbital inclination, population density, wind, epoch, controlled or uncontrolled reentry, material, radioactive elements, toxic elements and others (MROZINSKI et al., 2004).

It is estimated that around 100 uncontrolled debris reentry in aleatory conditions yearly (AILOR; WILDE, 2008). Only larger bodies are monitored and observed. The Aerospace corporation website presents a summary of more than 74 events of recovered reentry debris. Eleven objects were recovered from Brazil since 1962. The total reentry mass has not been estimated and the total survival reentry debris has not been found. Computational models to propagate reentry trajectories are simplified to reduce the simulation time and they generate alerts after the event.

The increment in space debris generates more probabilities to have reentry survival objects. Only a few of these objects are detected, monitored, tracked and predicted with high accuracy, generally the largest objects. Organizations like the Inter-Agency Space Debris Coordination Committee (IADC), with its 13 members agencies (ASI, CNES, CNSA, DLR, ESA, ISRO, JAXA, KARI, NASA, ROSCOSMOS, SSAU, UKSA) generate opportunities for cooperation in space research, exchange of information of tracking and measurements of debris,

database generation, protections and mitigation options (KRAG, 2016). Unfortunately, not all space agencies are committed to the tracking and mitigation of the orbital debris, which are actions as important as the spacecraft launch or the spacecraft operational phase. Recent research in the disaster science, in the area of risk of natural and human catastrophes, shows an increase in the fall of the space objects, due to the dangers to the environment and the risk for the humanity (PIERRO, 2018).

Surveillance of possible reentry objects is a priority for space agencies around the world, and there are different programs, centers, Institutes, Universities and researchers making developments in this area. Actually, Brazilian Space Agency (AEB) is not developing tracking or prediction systems for space debris, which can reentry and impact in its territory. The only country in South America with a program in reentry hazard debris is Argentina. One of the goals of this investigation is to contribute to the analysis and prediction of hazard reentry bodies.

The goal of the present investigation **is the modeling and propagation of the trajectory and attitude of reentry debris including fragmentation to determine their survivability and possible collision areas.** The obtained results implemented an accurate model of the atmospheric activity and the gravitational field of the Earth. The software integrates a 6DOF propagator to estimate the aerodynamic forces in free molecular flow, transition flow, and hypersonic continuum flow. The body rotation generates changes in aerodynamic and aerothermodynamics compared to the fixed body trajectory. For the fragmentation process, it is included a High Architecture Level method (HAL) for computational distribution to reduce the computational cost and simulation time.

The contributions of the present research are to understand the behavior of a space debris reentry in 6DOF, under the hypothesis that the rotational motion generates new loads and forces around the body that changes its trajectory and

fragmentation. It is expected that the rotational motion affects the heat flow around and inside the body, the generation of break-ups, the erosion and possibly the augmentation of the collision area and survival mass, increasing the risk. The computational code allows propagating the reentry trajectories. To validate the model, results of the simulations are compared with previous results from the scientific literature. New study cases are propagated to verify the present hypothesis. Generally, the reentry tools use propagations in 3DOF to save computational cost, time, and to simplify the problem, because it is difficult to obtain the initial conditions of attitude and angular velocity.

The originality of the research is the implementation of voxels in a mesh to determine the fragmentation of rotational reentry debris, including Magnus effect, parallel processing to determine the individual fragment trajectory and reduce the simulation time, and the implementation of more accuracy environmental models. The utility of the research is based in applications like: risk analysis during uncontrolled reentry, orbit propagation to estimate the reentry point, determination of the landing zone and survivability of the debris.

Along the present document, it is shown the mathematical model used to develop the propagator, the differences with other reentries tools and the discussion of the results obtained. In chapter 2 it is presented the uncontrolled reentry debris review. Chapter 3 presents the mathematical model of the translational and rotational dynamics. In chapter 4 it is presented the environmental models. The numerical integrator and the Covariance matrix are shown in chapter 5. In chapter 6 it is presented the aerodynamics and aerothermodynamics models. The break-up and fragmentation conditions are described in chapter 7. The computational methods are described in chapter 8 and continue in chapter 9 with the code structure. Study cases and results analysis are found in chapter 10 and, in chapter 11, is studied the reentry risk analysis of multiple fragments, including the application of the code in the propagation of the orbit of the Tiangong 1 Space Station. Results of the simulations presents a 2 days deviation from the reentry point, simulated 15

days before of the real decay, is an accuracy result, compared with the predictions of the space agencies around the world at the same date. The conclusions and recommendations for future research are presented in chapter 12.

2 REENTRY FRAGMENTATION REVIEW

According to the mission and payload lifetimes, a spaceflight can be divided into three phases, 1) Launch, 2) Orbit and 3) Disposal. In the launch phase, the spacecraft is transported from the surface of the Earth to the select parking orbit by a launcher vehicle, only propelled by chemical rockets to give to the spacecraft the required velocity and altitude. An ascend trajectory has duration around a few minutes. When the spacecraft has the correct altitude and the required velocity it is assumed to be in orbit. Different maneuvers for orbital and attitude maintenance are made along the lifetime of the mission.

When the operational lifetime is finished, the disposal or de-orbit maneuvers began. Naturally, the atmospheric drag generates energy losses (aero-breaking) and orbital decay. Actually, the orbital decay is detected by the measurement of the changes in the orbital elements. Initial conditions for reentry or entry trajectories have altitudes below 120 km and velocity inferior to the orbital velocity at that point, around 7.6 km/s. Due to the atmospheric influence, the spacecraft enters at hypersonic speeds in the free molecular flow. Erosion, ablation, fragmentation, vibration, melting and other associated physical phenomena are present during hypersonic flight conditions. The aerodynamic and gravity forces dominate the ballistic trajectory in the Earth's atmosphere. The entry ends at the higher density zones, around 10 km of altitude (stratosphere, tropopause and troposphere) with the velocity decaying to subsonic flight. In some cases, during the final approach are used decelerator systems (parachutes, retrorockets) to recover the payload (ADLER; WRIGHT, 2010). Without controlled decelerator systems, the debris impacts the Earth's surface freely, in some cases with high energy.

Two types of objects can entry in planetary atmospheres: the natural ones, as meteors; and the artificial ones, as spacecraft or debris. Artificial objects are classified as: controlled (ex: nuclear warheads, spacecraft) or uncontrolled (ex:

Debris) and manned (Space Shuttle, Space Stations, Capsules) or unmanned (probes, satellites).

Since June 30 1908, with the Tunguska meteor incident in the Siberian region, many scientists have studied their possible trajectories and orbits, especially the atmospheric interaction and the planetary entry. Orbital velocities around 25 to 40 km/s was estimated (BRONSHTEN, 1999). In this incident, it was observed the hazardous that can be made by a planetary entry of natural bodies. Before the World War II (WWII), humankind did not have developed vehicles for suborbital or orbital spaceflight. The A4/V2 German missile was the first Ballistic Missile with a suborbital warhead. The A4/V2 begun a new area of research in the trajectory of reentry missiles and warheads, where the objectives were the warhead thermal protection, trajectory prediction, guidance and control (ALLEN; EGGERS, 1958). The first approximation to the linear equations with an analytical solution for the ballistics reentry in 2D was described by the NACA in 1958 (CHAPMAN, 1958). After WWII, many Intercontinental Ballistic Missiles (ICBM) were developed for the Cold War between the United States of America (USA) and the Soviets Socialist Republics (SSRs).

Human spaceflight missions are possible thanks to the materials and spacecraft geometry designed to survive the re-entry. Capsules like: Mercury, Gemini, Apollo, Vostok and Soyuz, returned to Earth from Low Earth Orbits or the Moon (Apollo) without casualties. Only the Space Shuttle Transportation System (SSTS) Columbia was disintegrated due to problems in the heat shield during the reentry in 2002, generating fragmentation and debris in the low atmosphere region. Some of these bodies survived to the heat, structural and aerodynamic loads, and impacted the Earth without control and without casualties (HALLMAN; MOODY, 2005). In other spacecraft, like the Hubble Space Telescope, the MIR Space Station and the International Space Station, were estimated the reentries trajectories applying computational simulations (HALLMAN; MOODY, 2005; SMITH et al., 2005). ESA estimates the number of space launches from 1957 to 2017 January to be around 5250.

The Brazilian space mission SARA and sounding rockets, the SHEFEX II and SHEFEX III with DLR (KOLBE, 2015) and the hypersonic vehicle 14-X were designed to qualify and test unmanned hypersonic vehicles in suborbital flight, where the atmospheric entry is critical for the recovery. Important results were obtained previously with recovered payloads and experiments from sounding rocket missions (AEB, 2012).

2.1. Software reentry tools and applications

The reentry of debris becomes more popular in the latest years due to the increase of space objects around the Earth and the orbital debris clouds. Different studies have been made to estimate the reentry trajectories with the best accuracy possible. Space agencies around the world implemented software simulations of reentry bodies. NASA has the Orbit Survival Analysis Tool (ORSAT) and the Debris Assessment Software (DAS) and ESA have the Spacecraft Atmosphere Reentry and Aerothermal Breakup (SCARAB). In the present section it is presented a review of uncontrolled debris reentry trajectory, tools and comparisons between the ORSAT and SCARAB.

Studies of trajectory reentries were incremented with the access to space and the aerospace development. Desai et al. (1996) show results of a reentry trajectory in 6DOF with dispersion analysis for the METEOR mission. The research implemented a Monte-Carlo method to determine the possible uncertainties to determine the footprint. The results show a 58% probability to recover the module. The development of a software to predict disintegration of uncontrolled spacecraft and to calculate the dispersion of its fragments, the principal body trajectory and attitude to the point where a destruction happens was implemented by Fritche et al. (1997). Sikharulidze et al. (1998) suggest the use of a small ballistic vehicle to survive the reentry. Results show that ballistic coefficient increment generates an increase in downrange in 10:2 ratio. The results also show that the day and the month change the downrange zone.

First uses of the ORSAT and MORSAT software were made to determine the altitude of demise or survivability of simple shape reentry objects. Objects made from aluminum and copper did not survive the reentry heating. Materials like beryllium, steel, titanium, and nickel have more probability to survive. It was studied effects with variable thickness, diameter, ballistic coefficient and materials (ROCHELLE et al., 1999). Studies of controlled reentry with impulsive force and changing the incident angle concluded that the incident angle has a direct relationship with the landing zone dispersion, changes in the flight times, velocity increment or reduction in function of the angle (GUEDES, 2000).

In the year 2000, it was presented the Spacecraft Atmospheric Re-entry and Aerothermal Break-up software (SCARAB). This tool combines flight dynamics, aerodynamics, aerothermal, thermal and structural analysis to determine the motion and destruction of reentry objects and possible fragmentations. Fragments are modeled as primitive solids and trajectories in 3DOF (FRITCHE et al., 2000). The MIR reentry in 2001 was important, so ESA and HTG developed the quasi-deterministic tool SCARAB. Other projects like ATV, ROSAT, Ariane V and Beppo-SAX also used this software. SCARAB's Software was validated with the ORSAT, data from re-entry vehicles, break-up observations, and wind tunnel data (LIPS et al., 2004).

Methods to describe the breakup of a reentering space debris and a probabilistic method to obtain the causality area of the principal fragments were studied by Weaver et al. (2001). The Delft University developed the GESARED, a 6DOF reentry simulator in MATLAB(R)/SIMULINK to design control and guidance systems for reentry vehicles. The software was validated with the ARC capsule trajectory (COSTA et al., 2002).

A study of orbital debris reentry, estimation and prediction was made in 2002. The numerical code takes into account Ballistic Coefficient variations to predict the impact zone. It was implemented a Runge-Kutta 4 numerical integrator including, lift and drag forces, JGM3 gravity model with 70x70 terms,

atmospheric model USATM 1976 from 0 to 127.77 km and Soviet Cosmos model under 600 km. The model did not present fragmentation, attitude and thermal transference (TARDY; KLUEBER, 2002). Other studies of natural body's entries with mass outflow and ballistic considerations are presented in Tirskii and Khanukaeva, (2007). Since 2001, there are estimations of reentry debris impacting zone by ESA (WEAVER et al., 2001).

A trajectory design, guidance and simulation during reentry in 6DOF software was designed in 2004. The methodology and algorithm help in the design process, to increase the effectiveness and efficiency of future entry missions (LU; RAO, 2004). In the same year, Pardini and Anselmo (2004) present the reentry predictions of a Russian Upper stage rocket. The mathematical model uses three atmospheres, solar radiation data, ballistic parameters estimation and TLE orbital propagation. The model has 8th gravitational zonal and tesseral harmonics, atmospheres JR-71, MSIS-86 and TD-88, third body perturbation and drag. The reentry begin at 80 km altitude. Results were compared with the reentry real data and presented an error of 9% with the JR- 71 model. The ESA and Space Italian Agency studied the destructive phase of the BeppoSAX during uncontrolled reentry, implementing the SCARAB. Calculations for casualty risk were higher than 1/10,000, due to the titanium elements (PORTELLI et al., 2004).

The casualty area of Delta II second stage reentry were calculated with the new probabilistic paradigm for calculating the uncertainty in casualty area of randomly reentering debris. It is expected that the results show a stochastic variability and this fact was confirmed with the recovered Space Shuttle Columbia fragments. More than 84,500 debris fragments were recovered from the accident (FRANK et al., 2004).

For reentry, the aerodynamic and aerothermal models are too complex to be modeled, due to the hypersonic flow and the body geometry. Numerical models were validated with experimental data from the SARA's capsule. Scale model

tested in the IEAv Hypersonic Shock Tunnel in freestream from 6 to 8 Mach was necessary to understand the hypersonic flow characteristics (TORO et al, 2004).

Due to the risk of uncontrolled satellite reentry, break up and survival debris, methods and technics to support the reentry predictions were reviewed, where the principal tools are SCARAB and ORSAT (ANSELMO; PARDINI, 2005). The ORSAT was implemented to investigate the reentry survivability, breakup, demise and impact of the 160 components from the UARS satellite. The results showed that 12 types of components with 532 kg total mass will survive. Debris footprint length is around 800 km and causality risk 1:2800 (ROCHELLE et al., 2004). Features of the latest ORSAT version are presented to satisfy the NASA Safety Standard (NSS) 1740.14 and to evaluate the risk of NASA's reentering spacecraft. Features include the GRAM model, 2-D heating model and graphical user interface (DOBARCO-OTERO et al., 2005). A study compares the re-entry tools DAS, ORSAT, SCARAB and SESAM to calculate the ground risk when re-entry objects survive. The results show good agreement among the trajectories between SESAM, SCARAB and ORSAT. The study case was a sphere. Results present differences in body temperatures due to the material properties (LIPS; FRITCHE, 2005). In a complementary study, Lips et al. (2005) compare ORSAT vs SCARAB. Results are in good agreement for objects like spheres and cylinders. They present less than 0.2% mean deviation between the two software for survival mass, but the trajectories are different and the materials properties generate uncertainty. In SCARAB it was simulated the reentry of ARIANE V, ATV, ROSAT, Beppo-SAX and Terrasar. The software has tools to find destruction by melting or fracture. SCARAB architecture and additional information are presented in Koppenwallner et al. (2005a). During the Automated Transfer Vehicle (ATV) reentry it was taken into account possible explosions in the tanks onboard. It was used a modified NASA EVOLVE to simulate the explosion. Results of simulations show an explosion at 75 km altitude generating 6474 fragments and only 5.5% survive and impact the

Earth's surface (KOPPENWALLNER et al., 2005b). In 2006 it was presented an integration between RAMSES, ANGARA and SCARAB software to combine the spacecraft geometry and to propagate the system conditions in a multidisciplinary software. The codes have been developed during 14 years. The integration allowed the reconstruction of the spacecraft configuration based on panelized surfaces and volume panels (KOPPENWALLNER et al., 2006). Fritsche et al. (2007) present analytical and numerical models and the results are compared with the SCARAB simulation to determine the demise of simple-shaped objects. It was found four survival limits by calorimetric, radiative in continuum flow, radiative in free molecular flow and radiative for solid spheres. It was selected aluminum alloys materials. The three methods predict similar situations. Generic satellite geometry was tested in ORSAT and SCARAB to compare the results. In ORSAT it was modeled 33 objects and 2 in SCARAB. Results show differences in quantity survival objects and causality area, but, due to the differences in methodology and geometry, both scenarios are equally plausible (KELLEY et al., 2010.).

Ivanov and Ryzhanskii (2005) present a new methodology to predict the trajectory of small celestial bodies with atmospheric interaction. The model presents an initial fragmentation from the principal body and breakups with scattering for the fragments. The principal factors for the fragmentation are implemented using the aerodynamics and fracture mechanics methodology.

Pardini and Anselmo (2008) describes the uncertainties in the spacecraft ballistic parameter to determine the orbital decay and trajectory reentry. It was analyzed data from previous years from satellites, solar and atmospheric activity to determine the best value for the ballistic parameter used in reentry predictions. The results did not present a good reduction in the prediction errors or better accuracy, because it cannot predict environmental data, the spacecraft attitude, satellite shape and the ballistic parameter.

Simulations of reentry bodies in 6DOF with a thermomechanical breakup, ablation and structural analysis, assuming a fixed Earth, atmospheric model US 1976 from 0 to 2000 km, lift and drag aerodynamic forces, gravitational model J4, a Runge-Kutta 4/5 (RK45) numerical integrator, spherical coordinate system and landing dispersion analysis was developed. Results show disintegrations of debris fragments and it was recommended the verification with real data and test (TEWARI, 2009).

Mooij and Hanninen (2009) presented an optimization trajectory process for the reentry vehicle with moderate lift to drag ratio. The study implemented distributed architecture and minimized heat flux. Analytical solutions for the reentry trajectory equations were searched to be applied to the rocket control. The reentry equations of motion were linearized. The model is valid only for 2-D trajectories, exponential density and constant gravitational acceleration (MITITELU, 2009). The Australian re-entry Risk Hazard Analysis (RHA) developed the Range Safety Template Toolkit (RSTT) for the hypersonic program for air-launched guided weapons. The mathematical model includes 6DOF and fractal fragmentation (WILSON, 2009).

Studies about the impact of cavities in the reentry vehicles surfaces were analyzed, implementing computational fluid dynamics and DSMC (PALHARINI, 2010).

A study for the SARA reentry Brazilian satellite with 0° of AOA and use of DSMC for altitudes between 100 and 85 km. was present by Sampaio and Santos (2010). The results confirmed that the maximum heat value is located in the stagnation point, which is a thermally stressed zone and the pressure coefficient predicted agree with the Newtonian theory prediction.

Different bodies of revolution were studied. Analytic aerodynamics were implemented and the results were compared with the panel methods. It was developed analytical relations for force and moment coefficients for simple

bodies, like cylindrical segments and for general bodies of revolution (GRANT; BRAUN, 2010).

Reentry trajectory analyses for the NASA's Ares I-X rocket, shows the stages separations, tumbling motion and the impact footprints are similar to the computational mathematical model's estimations (TARTABINI, 2011).

From the ORSAT model, a new reradiation heat equation was developed in the software SAPAR, to analyze a tumbling metallic hollow cylinder from the Delta-II second stage. Results from the SAPAR show a decrease in the surface temperature with a similar approach in the trajectories compared to ORSAT (SIM; KIM, 2011).

An object-oriented tool debris reentry and ablation prediction system (DRAPS) was developed by the China Academy of Space Technology. Compared to the ORSAT and SCARAB, the DRAPS has 15 new types of object shapes and 51 predefined motions validated with DSMC. The research compares the two types of methodologies, spacecraft-oriented vs. object-oriented. With the spacecraft-oriented method the spacecraft geometry is more accurate, but it is also more expensive in terms of computational cost. The studies recommend the search of better break up predictions models, because phenomes like shockwaves interaction are not modeled in the software (ZINIU et al., 2011).

The French Space Agency (CNES) developed the DEBRISK tool to estimate the mass, impact energy and risk of collision of the debris after atmospheric reentry. The software uses an object-oriented approach and fragmentation around 78 km with a parent-child approximation to model the new geometries. Simulations are made in 3DOF and using drag coefficients from engineering methods (OMALY; SPEL, 2012). Omaly et al. (2013) show the DEBRISK results compared to the ORSAT. It is presented sensitivity results of the fragmentation process.

Some reentry were predicted with high accuracy because the tracking and monitoring of the debris complement the trajectory propagation and estimation. Trajectory estimation of the Hayabusa spacecraft was investigated in 2013. The mathematical model has inertial acceleration, Lift and Drag components of aerodynamic forces, CIRA72 atmospheric exponential model, ellipsoidal Earth with rotation, ablation model and state estimation with Kalman Filter (SHOEMAKER et al., 2013). During the real reentry of the Hayabusa capsule in 2011, more than 300 fragments were detected (WATANABE et al., 2011). Real fragmentation data and large data of reentries help to test and complement the mathematical models, because the random distribution of reentry makes more difficult the risks prediction in terms of geographical distributions (MATNEY, 2011).

Mazaheri (2013) tested different nose shape configurations to determine the aerothermal analysis during reentry. He finds that variations of $\pm 10^\circ$ of AOA have a negligible effect on the surface heat flux. It uses inflate structures.

The Computational tools for reentry like SCARAB, SESAM, ASTOS and DEBRISK were compared with the Delta-II second stage reentry case. Results show differences due to the tool settings, differences in the aerodynamic and aerothermodynamics models, and recommend future comparisons with simple geometries and a limited number of parameters (LIPS et al., 2013).

A sample return hypersonic capsule was studied to determine the heat flux on the surface. To determine the internal temperatures was implemented an one-dimensional thermal analysis. The engineering correlations present satisfactory agreement (Detra-Hidalgo correlation) with numerical results from DSMC (CARANDENTE et al., 2013).

Simulation of NEO objects with nuclear fragmentation inside the atmosphere of the Earth and hydrodynamics particle simulations in 2D are shown in Kaplinger et al. (2013). The results present feasible solutions in short warning time.

Durin (2013) studied the spacecraft re-entries in 6DOF. It was implemented possible fragmentation by thermal loads, mechanical and explosive causes. The goal was to compare real cases with simulations to increase the model accuracy. It was analyzed a recovered titanium sphere. A small fraction of the mass of titanium is lost during reentry and splashes indicates that the sphere has a constant AOA reentry, without randomly tumbling. The simulations present a good correlation with the element survivability.

Experimental data during atmospheric reentries were collected by Japan's HTV2 and HTV3 vehicles and ESA's ATV-3. To collect the data it was used the reentry breakup recorder. Data recorder from the vehicles indicates fragmentation from 74 to 64 km (FEISTEL et al. 2013).

Classical methods of debris analysis were implemented in the asteroid entry fragmentations, like the Chelyabinsk event. The predictions using the DEBRIS tool are in good agreement with the data of the recovered fragments (PARIGINI et al., 2013).

The SPEAD software was designed to determine the trajectory propagation with thermal analysis and node failure of potential reentry debris. The software was validated with telemetry data from flights and software comparison (LING, 2014).

Pardini and Anselmo (2014) studied the uncontrolled orbital decay and drag satellite attitude controlled during the reentry of GOCE satellite. The results show the possible trajectories over Italy, and it was not possible to predict the real trajectory because the use of the control system did not allow the simulations to take into account possible failures in the systems.

A detailed research shows new approximations to the aeroheating models to simplify the results to determine the ground causality risk. The aeroheating models were tested in the Spacecraft Aerothermal Model Tool (SAM). Panel methods present good results for simple geometries. The Detra-Hidalgo model

reproduces the experimental data for a sphere in hypersonic flows. It is recommended the use of tumble-average shape factors for the models (BECK et al., 2015a). Monte-Carlo methods and Delta stage II trajectories were used to validate the software models (BECK et al., 2015b). The use of the SAM software gives a better aerothermal, fragmentation and demission models. Recommendations require more experimental data from fragmentation during reentries, better material data base and more information about hypersonic heat transfer (MERRIFIELD et al., 2015a; 2015b).

Mehta et al. (2015a) present the development of a computational tool called FOSTRAD. The FOSTRAD aerodynamic and aerothermodynamics models presented good accuracy compared to the numerical results of CFD and direct simulation Monte-Carlo (DSMC). The FOSTRAD is implemented in the estimation of re-entry debris and asteroids. The use of the FOSTRAD with uncertain quantification, is implemented in the sensitivity analysis for the re-entry of cubes, spheres and cylinders, studied by Mehta et al., 2015a. The sensitivity analysis was applied to the drag coefficient, heat flux, free stream and surface temperatures of the selected bodies. Differences between analytical and high-fidelity methods have less than 5% error in drag and around 15% in heat (MEHTA et al., 2015b).

Analytical determination of loads was implemented for the SHEFEX III model to find thermal loads in flight. Analytical solutions minimized the computational time compared to CFD with 10% deviations. These models calculate the heat flux density and the wall temperature in the symmetrical axes (KOLBE et al., 2015).

Debris impact area, break up, survivability, risks and re-contact analysis are estimated with the toolbox DEBRIS. The DEBRIS was selected to be applied in the ESA's ExoMars mission and BIOMASS reentry. Features of this tool are the estimation footprint area of launcher stages, spacecraft reentry and asteroids (PARIGINI et al., 2015).

Bastien et al. (2015) explore the application of Taguchi method to reduce de Monte Carlo simulations and computational time of reentry cases. The analysis was made with the CALIMA tool. The study shows that all reentry tools are deterministic and do not consider the errors in the reentry initial conditions. Trajectory analysis includes simply shaped bodies in 3DOF. For future missions it is presented the Earth's reentry as a disposal strategy. The hypersonic reentry is a low cost option to dispose of satellites (ALESSI, 2015).

Moreschi and Schulz (2016) compare the trajectory propagation in 6DOF of the third stage of Delta-II launcher that impacted in the province of Corrientes, in Argentina. It was compared two atmospheric models, the USATM STD76 and the NRLMSISE-00. Implementing the ARGUS code, the results show a 200 km deviation between the real trajectory and the propagation. The code did not take into account lift, lateral aerodynamic forces and wind models.

Small space debris trajectories were analyzed to determine the survivability of bodies with simple shapes in sizes of 12.5 to 50 cm and materials like graphite epoxy, aluminum and titanium and it includes a catalytic recombination model for the surface heat (PARK; PARK, 2017). The validation process of the computational tool includes the initial conditions of the reentry trajectories analyzed by Lips et al., (2005). Originally, the computational tool was developed in South Korea. It is the Survivability Analysis Program for Atmospheric Reentry (SAPAR) (SIM; KIM, 2011). The results show good agreement with the previous ORSAT simulations.

The determination of the airspace region occupied by reentry debris was studied to support the air traffic controllers to guide aircraft safely. The estimations adopted filtering technics, including the wind fields, and shows good results (FALSONE; PRANDINI, 2017).

Mehta et al. (2017) present the results obtained by the implementation of a new derivation of the high dimensional model representation in a probabilistic analysis for re-entry. The method was compared with a Monte Carlo analysis

during controlled and un-controlled reentries and there are important differences with the Gaussian distribution at the impact time.

The most developed and studied reentry tools are the NASA's ORSAT and ESA's SCARAB. Both software uses the U.S. Standard 1976 atmosphere model and the same material properties. In ORSAT, it is possible to obtain simulations in 3DOF from an object-oriented model with simplified geometric shapes and breakup at 78 km, spherical coordinates system, Runge-Kutta-4 numerical integrator, without lift, heat conduction model in 1D, aerodynamics and aerothermodynamics data from the selected shape in function of the motion and the Knudsen number (KOPPENWALLNER et al., 2006). The SCARAB takes into account dynamic and kinetic equations with propagation in 6DOF, spacecraft-oriented method, local panel methods for structural and aerodynamics, complex geometry, break up based on melting, stress and structural integrity. Three atmospheric models Jacchia 71, MSISE-90 and USATM 1976 are complemented with wind model and RK7/8 numerical integrator (LIPS et al., 2005). The SCARAB tool simulated reentry trajectories of spacecraft like ATV, ROSAT, ARIANE 5 cryogenic main stage, ARIANE 5 upper stage, Bepposax and TERRASAR-X showed excellent results (PASQUALE et al., 2015; KOPPENWALLNER et al., 2006). Comparisons between the two tools were studied and the validation showed a good approximation with the results obtained (ZINIU et al., 2011; LIPS et al., 2005). Other software with reentry estimation are ASTOS, SESAM, DEBRISK and FOSTRAD (MEHTA et al., 2015; LIPS et al., 2013). Table 2.1 shows the principal characteristic tools.

Table 2.1 – Comparison ORSAT vs. SCARAB

	ORSAT	SCARAB
Space Agency	NASA	ESA
Model	Object-oriented	Spacecraft-oriented
Geometries	Spheres, Boxes, Cylinders, Flat Plates	Spacecraft modeled as close to the real geometry
DOF	3	6
Aerodynamic and aerothermodynamics	Shape and Kn, only drag.	Panel methods
Numerical Integrator	RK4	RK7/8
Break Up	Fixed, altitude 78 km	Based on stress and structural integrity
Atmospheric model	US ATM 1976	MSISE-90, HWM, J71
Reference System	Local fixed	Inertial Earth and rotational

Source: Adapted from Lips et al. (2015).

2.2. Reentries in Brazil

In Brazil, researchs about reentry have been developed since 1970. Thesis, patent registers and different experiments have been made in institutions around the country. At the National Institute for Space Research (INPE), it is studied the Orbital Debris fragmentation and Reentry. In 2011, it was presented the research of models and initial conditions for the generation of space debris and their orbital propagation. It was presented a probabilistic model of fragmentation for orbital debris propagation applied to the Chinese weather satellite Fengyun – 1C (BATISTA, 2011). In 2009, a thesis in aerothermodynamically induced fragmentation and prediction of the impact area of a space vehicle with controlled injection of the re-entry was developed, the results including reentry fragmentation of three geometries: a sphere, a cylinder and a parallelepiped, with the model of atmospheric fragmentation of small celestial bodies (OLIVEIRA, 2009; IVANOV; RYZHANSKII, 2005). Another research in numerical investigation of aerothermodynamics of a reentry vehicle with surface discontinuity and molecular simulation using an analytical formulation of the reentry problem with flexibility and vibration effects were developed at INPE (LEITE, 2015; PALHARINI, 2010; FERREIRA, 1989). The

dispersion analysis of a vehicle's reentry into the Earth's atmosphere with respect to the landing point, using a geocentric inertial and lateral maneuvers, was developed by Guedes (1997). More recently, researchers from INPE designed the patent Flight or atmospheric re-entry method using rotation for new reentry trajectories applying rotation and aerodynamics control for surface temperature protection and changes in the flight path (BAMBACE et al., 2014).

The Aeronautical Institute of Technology (ITA), in São José dos Campos, Brazil, have been studying the reentry dynamic equations for artificial satellites since 1983 (SILVIA; MORAES, 1983), as well as the attitude simulation of spacecraft vehicle during reentry (LUNA et al., 1991). Complementing the trajectory analysis, experiments were made in fluids and plasma, like the fluid simulations for flap in wind tunnel and plasma chambers for reentry that was developed in ITA (BARROS et al., 2002; FICO; ORTEGA, 1991).

Some debris recovered in Brazil are shown in Table 2.2. The data was obtained from the reentry statistics of the Center for Orbital and Reentry Debris Studies, in the Aerospace Corporation (2017).

Table 2.2 – Debris impacted and recovered in Brazil

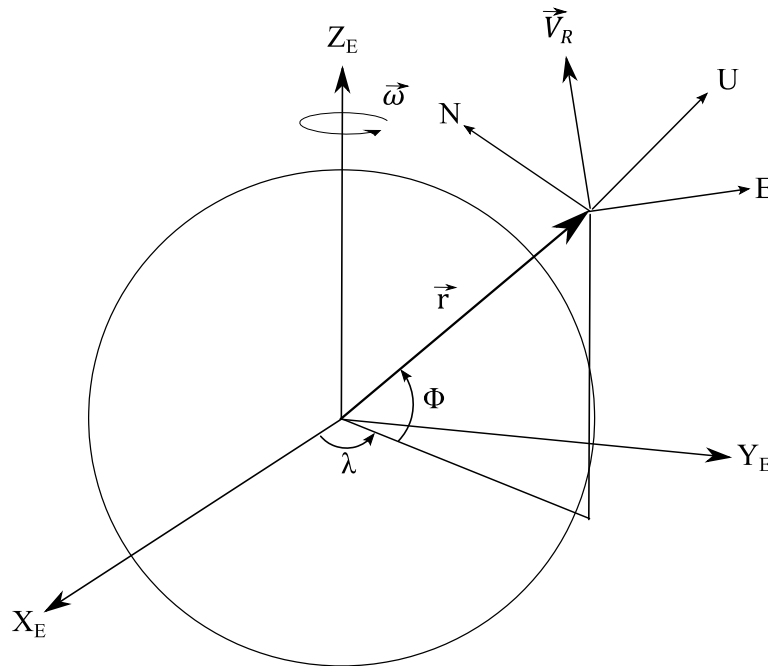
Date	Mission or vehicle	Description
Mach 1962	Atlas booster, Mercury MA-6	11 pieces stainless steel, 2.7 kg average mass
July 1962	U.S. Air force test	0.4 m of diameter spherical vessel in Porto Alegre.
March 1964	Agena rocket stage	11 kg mass, metal spherical pressure vessel. Belem.
April 1966	S-IVB Saturn Booster	Helium pressure sphere, 1m diameter, 113.3 kg. Near coat.
May 1966	S-IVB Saturn S-A5	Piece of metal of 0.5x0.3m, oval-shaped metal piece, black beehive-shaped piece and wire on Rio.
July 2004	Delta II Second stage	Metal sphere 0.5m and 30kg in Cabeça de Vaca and metal fragment 1m length near Batalha.
March 2008	Centaur stage of Atlas V	Composite sphere 0.5m, 10kg near Montividiu
February 2012	Ariane 3 rd stage	Metallic sphere 0.7m diameter and 30kg in Mata Roma.
December 2014	Falcon 9 second stage	3 small cylindrical tanks, Santa Rita do Pardo.

Source: Adapted from Aerospace Corporation (2017).

3 DYNAMICS AND KINEMATICS OF THE REENTRY

A mass-point body (spacecraft) in orbit around the Earth has an inertial velocity vector \vec{V} , a relative velocity vector \vec{V}_R at the position vector \vec{r} from the Earth's mass center that describes the flight path (see Figure 3.1). The Earth's gravity and atmosphere influence on the spacecraft motion generate an orbital decay in long time periods. When the spacecraft describes a trajectory from orbit to the planetary surface, the maneuver is called "reentry". Two types of reentry are known for spacecraft, one controlled by propulsion or shape augmentation, and another one by natural forces due to the solar and atmospheric activities.

Figure 3.1 – Reference Earth's system.

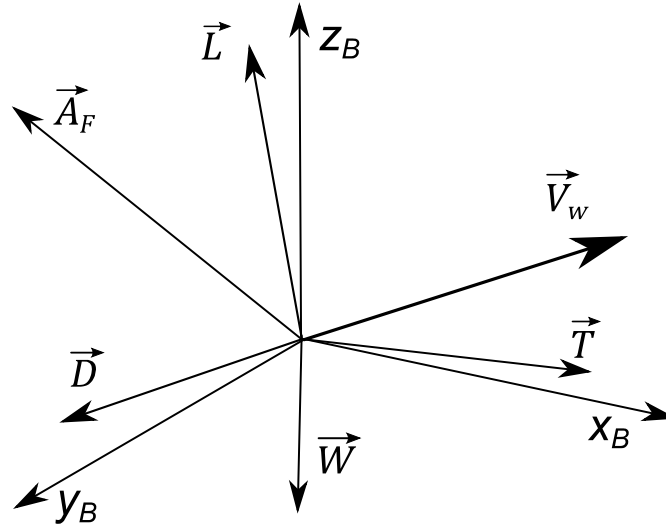


3.1. Dynamics

Generally two forces influence the reentry. The weight (W), that is proportional to the spacecraft mass and Earth's geopotential (U), and the aerodynamic force (A_F), which is proportional to the area and shape of the spacecraft and the atmospheric density. When the reentry is controlled, the thrust force (T) coming from the rocket motors helps to change the trajectory of the spacecraft and then

it is taking into account in the equations of motion. Additional effects like Magnus Force (F), generated by the rotation of the spacecraft in atmospheric fluid, are presented in the mathematical model (see Figure 3.2).

Figure 3.2 – Forces acting in the body.



The general spacecraft equation of motion is:

$$\ddot{\vec{r}} = \nabla \vec{U} + \frac{\vec{T}}{m} + \frac{\vec{A}_F}{m} + \frac{\vec{M}_F}{m}, \quad (3.1)$$

Where m , is the spacecraft mass. In the Inertial Earth Reference System (IERS), the position vector is $\vec{r} = X\hat{X} + Y\hat{Y} + Z\hat{Z}$ and the velocity is $\vec{V} = \dot{X}\hat{V}_X + \dot{Y}\hat{V}_Y + \dot{Z}\hat{V}_Z$, where (^) indicates the unit vector (GALLAIS, 2007; WEILAND, 2010; ZIPFEL, 2007). The aerodynamics force has two components in the Wind Reference System (WRS) $\vec{A}_F = \vec{L} + \vec{D}$, the Lift \vec{L} is perpendicular to the spacecraft-atmospheric relative velocity \vec{V}_W and the Drag \vec{D} is opposite to spacecraft-atmospheric relative velocity. The six differential equations of translational motion are:

$$\dot{X} = V_x, \quad (3.2)$$

$$\dot{Y} = V_y, \quad (3.3)$$

$$\dot{Z} = V_Z, \quad (3.4)$$

$$\ddot{X} = -\nabla U_X \hat{X} - \frac{D}{m} \hat{V}_{WX} + \frac{L}{m} \hat{V}_{WTX}, \quad (3.5)$$

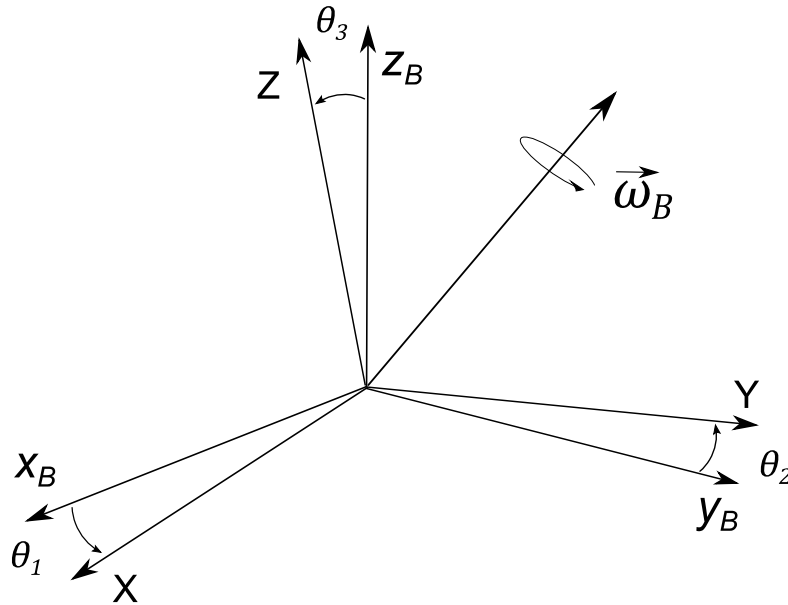
$$\ddot{Y} = -\nabla U_Y \hat{Y} - \frac{D}{m} \hat{V}_{WY} + \frac{L}{m} \hat{V}_{WTY}, \quad (3.6)$$

$$\ddot{Z} = -\nabla U_Z \hat{Z} - \frac{D}{m} \hat{V}_{WZ} + \frac{L}{m} \hat{V}_{WTZ}. \quad (3.7)$$

3.2. Attitude

The Euler angles between the spacecraft axis and the inertial system are θ where the sub-indices 1, 2 and 3 represent the axial, lateral and vertical axis, ω_B is the spacecraft angular velocity; T_r are the resultants torques and moments, I is the inertial tensor (GALLAIS, 2007). In Figure 3.3 it is represented the Euler angles in the Body and Inertial system.

Figure 3.3 – Euler angles in the body system.



The differential equation for the kinematics and spacecraft attitude is:

$$\begin{pmatrix} \dot{\theta}_1 \\ \dot{\theta}_2 \\ \dot{\theta}_3 \end{pmatrix} = \frac{1}{\sin \theta_2} \begin{pmatrix} \sin \theta_3 & \cos \theta_3 & 0 \\ \sin \theta_2 \cos \theta_3 & -\sin \theta_2 \sin \theta_3 & 0 \\ -\cos \theta_2 \sin \theta_3 & -\cos \theta_2 \cos \theta_3 & \sin \theta_2 \end{pmatrix} \begin{pmatrix} \omega_1 \\ \omega_2 \\ \omega_3 \end{pmatrix}, \quad (3.8)$$

The differential equation for the rotational motion due to the inertia tensor (\mathbf{I}), variable mass system with inertia changes ($\dot{\mathbf{I}}$) (Euler's equation) and with the total toques applied to the body (\vec{T}_{or}) is (TEWARI; GALLAIS; ZIPLER 2007):

$$\dot{\vec{\omega}} \mathbf{I} = \vec{T}_{or} - \vec{\omega} \times (\mathbf{I} \vec{\omega}) - \vec{\omega} \dot{\mathbf{I}}, \quad (3.9)$$

For the body voxels, the inertia tensor in the body system is defined by the sum of the mass of the voxels (m_v), and the position in the body Cartesian system (x_v, y_v, z_v), equation (3.10).

$$\mathbf{I} = \begin{pmatrix} \sum_{v=1}^N m_v (y_v^2 + z_v^2) & -\sum_{v=1}^N m_v x_v y_v & -\sum_{v=1}^N m_v x_v z_v \\ -\sum_{v=1}^N m_v x_v y_v & \sum_{v=1}^N m_v (x_v^2 + z_v^2) & -\sum_{v=1}^N m_v y_v z_v \\ -\sum_{v=1}^N m_v x_v z_v & -\sum_{v=1}^N m_v y_v z_v & \sum_{v=1}^N m_v (y_v^2 + x_v^2) \end{pmatrix}, \quad (3.10)$$

3.3. Forces

The forces acting in the fragment are divided in two groups. The aerodynamic forces, where the principal ones are drag that reduces the motion of the fragment, lift and Magnus forces. Induced forces like the thrust are taking into account only for controlled reentries.

3.3.1. Lift and Drag

The force opposite to the motion of the spacecraft, known as drag, is proportional to the projected surface of the body (S), the drag coefficient (C_D), the atmospheric density (ρ) and the relative wind velocity (V_w). The other component of the aerodynamic force, perpendicular to the wind velocity is known as lift, and it depends on the lift coefficient (C_L), area and dynamic pressure (air density and squared wind velocity).

$$D = \frac{1}{2} \rho S C_D V_w^2, \quad (3.11)$$

$$L = \frac{1}{2} \rho S C_L V_w^2, \quad (3.12)$$

The physical relation between air density and the wind velocity is known as dynamic pressure (q_∞), and it is the pressure acting under the spacecraft structure (TEWARI, 2007).

$$q_\infty = \frac{1}{2} \rho V_w^2. \quad (3.13)$$

The aerodynamic coefficients are functions of the Angle Of Attack (α) (AOA), the banking angle (β), wind velocity, flow properties, body shape and others. Generally, the coefficients are calculated and validated from the wind tunnel tests, acceptable approximations can be obtained implementing Computational Fluid Dynamics (CFD).

Other aerodynamic force is generated by the Magnus effect. The Magnus force is only present in the body if it has a rotation, redirectioning the Lift. In spherical bodies at high Reynolds the Magnus force (M_F) was derived from Thorsten et al. (2012), see Equation (3.14). The sphere area is πr_B^2 , and the spin parameter is determined by: $2\pi\omega_B r_B / V_w$. Effects of turbulence and boundary layer are negligible.

$$\vec{M}_F \approx (\pi^2 r_B^3 \rho) \vec{\omega}_B \times \vec{V}_W, \quad (3.14)$$

Where r_B is the radius of the body and ω_B the body angular velocity. The relative atmospheric velocity wind vector is

$$\vec{V}_W = V_{wx} \hat{V}_x + V_{wy} \hat{V}_y + V_{wz} \hat{V}_z. \quad (3.15)$$

In the flow relative velocity system, the aerodynamic drag vector is:

$$\vec{D} = -D \frac{V_{wx}}{V_w} - D \frac{V_{wy}}{V_w} - D \frac{V_{wz}}{V_w}. \quad (3.16)$$

The total aerodynamic force due to Lift, Drag and Magnus is

$$\vec{A}_F = \vec{L} + \vec{D} + \vec{M}_F. \quad (3.17)$$

3.3.2. Thrust

In space vehicles the thrust force is generated by a Rocket Motor System (RMS). The ideal specific impulse (I_{sp}) of the propellant selected and the mass flow (\dot{m}) generates the thrust force. The gravity at the Mean Sea Level (MSL) is g_0 , in this case is used like a performance parameter. The ideal and instantaneous thrust force is represented by:

$$T = I_{sp} g_0 \dot{m}. \quad (3.18)$$

3.4. Angular momentum and auxiliary vector

To determine the thrust and lift direction in the inertial systems, it is necessary to determine a series of auxiliary planes and vector, like the angular momentum. The angular momentum per unit mass h is the vector orthogonal to the motion in the orbital plane. The orthogonality between the vectors position and velocity result in the angular momentum.

$$\vec{h} = \vec{r} \times \vec{V}. \quad (3.19)$$

Replacing the inertial velocity vector from Equation (3.19) by the relative atmospheric velocity wind vector, it is obtained a new angular momentum called relative wind angular momentum (h_w).

$$\vec{h}_w = \vec{r} \times \vec{V}_w. \quad (3.20)$$

To determine the Lift vector direction, an auxiliary vector (A_w) is created. The auxiliary vector is orthogonal to the relative wind angular momentum and the relative atmospheric velocity wind vector (STRACK et al., 1963).

$$\vec{A}_w = \vec{V}_w \times \vec{h}_w. \quad (3.21)$$

3.4.1. Lift vector

The Lift vector is orthogonal to the relative atmospheric velocity wind vector. The relations between Lift, Auxiliary vector and relative angular momentum are:

$$\vec{L} \cdot \vec{V}_w = 0, \quad (3.22)$$

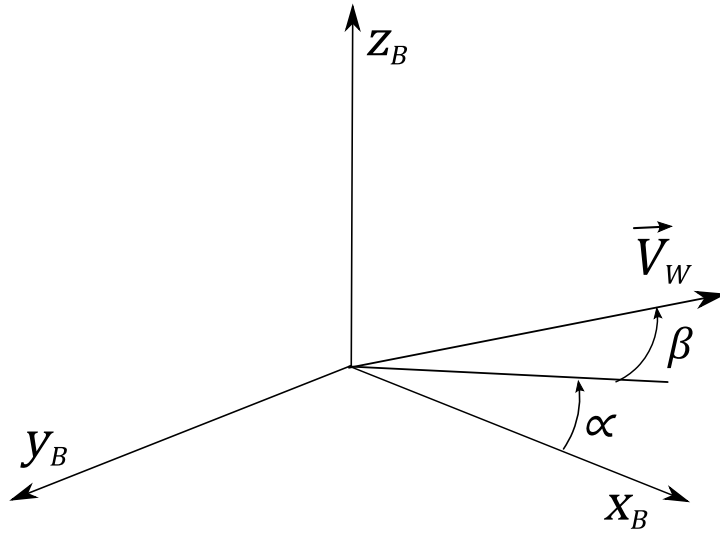
$$\vec{L} \cdot \vec{h}_w = L h_w \sin \beta, \quad (3.23)$$

$$\vec{L} \cdot \vec{A}_w = L A_w \cos \beta. \quad (3.24)$$

In Equations 3.23 and 3.24, β is the banking angle (see figure 3.4) (STRACK et al., 1963). The Lift vector is obtained solving Equations 3.25 to 3.27.

$$\vec{L} = \frac{L}{A_w^2} (h_w \sin \beta \vec{A}_w \times \vec{V}_w + A_w \cos \beta \vec{A}_w). \quad (3.25)$$

Figure 3.4 – Aerodynamics angles.



3.4.2. Thrust vector

In the same way done for the Lift vector, with the relative angular momentum and auxiliary vector, it is possible to determine the direction of the Thrust force in the EIRS. The angle between the relative atmospheric velocity wind vector and the Thrust vector is the Angle Of Attack (α) (see Figure 3.4). The dot products with the Thrust force are (STRACK et al., 1963):

$$\vec{T} \cdot \vec{V}_w = TV_w \cos \alpha, \quad (3.26)$$

$$\vec{T} \cdot \vec{h}_w = Th_w \sin \alpha \sin \beta, \quad (3.27)$$

$$\vec{T} \cdot \vec{A}_w = TA_w \sin \alpha \cos \beta. \quad (3.28)$$

The resulting Thrust vector is

$$\vec{T} = \frac{T}{A_w^2} (V_w \cos \alpha \vec{h}_w \times \vec{A}_w + h_w \sin \alpha \sin \beta \vec{A}_w \times \vec{V}_w + A_w \sin \alpha \cos \beta \vec{A}_w). \quad (3.29)$$

3.5. Coordinate systems

Because the debris trajectory is propagated in the inertial reference system all the forces and variables from the routines modules, they need to be transformed to the inertial system, for example: to calculate the winds in the horizontal systems is needed the position in the spherical system to transform to the inertial system, the gravitational system is calculated in the local rotational. So it is necessary to transform the state vectors to another reference frames. The principal transformations are presented below.

3.5.1. Spherical system

The transformation between Center Earth Inertial Reference System and Earth rotational spherical system is a rotation in the vertical, or Z axis, proportional to the product of the Earth's angular velocity and time, also known like hour angle. See Figure 3.5 (ZIPFEL, 2007).

The Cartesian System was defined in Section 3.1 (Figure 3.1). The relations to transform the position from Cartesian to the spherical system of the World Geodetic System (WGS84) are:

$$X_E = r \cos \Phi \cos \lambda, \quad (3.30)$$

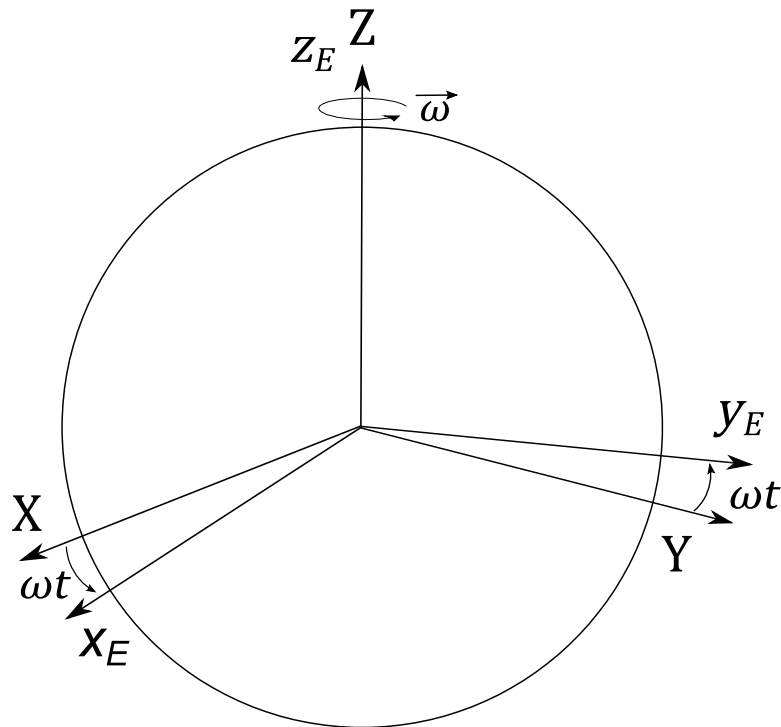
$$Y_E = r \cos \Phi \sin \lambda, \quad (3.31)$$

$$Z_E = r \sin \Phi, \quad (3.32)$$

Where ϕ is the Latitude, λ the Longitude and r it is the magnitude of the position vector. The position is equal to the sum of Earth's radius (R_E) at a given latitude and the altitude (A_{lt}) from the mean sea level.

$$r = A_{lt} + R_E. \quad (3.33)$$

Figure 3.5 – Earth inertial to geographic.



3.5.2. Local horizontal system

The Local Horizontal Reference System (LHRS) is a non-inertial system where the origin is in the center of mass of the spacecraft. The principal vector is the velocity relative to the rotational Earth. The two principal angles are Azimuth, or heading angle (A), and the Relative Flight Path Angle (RFPA) (ϑ_R).

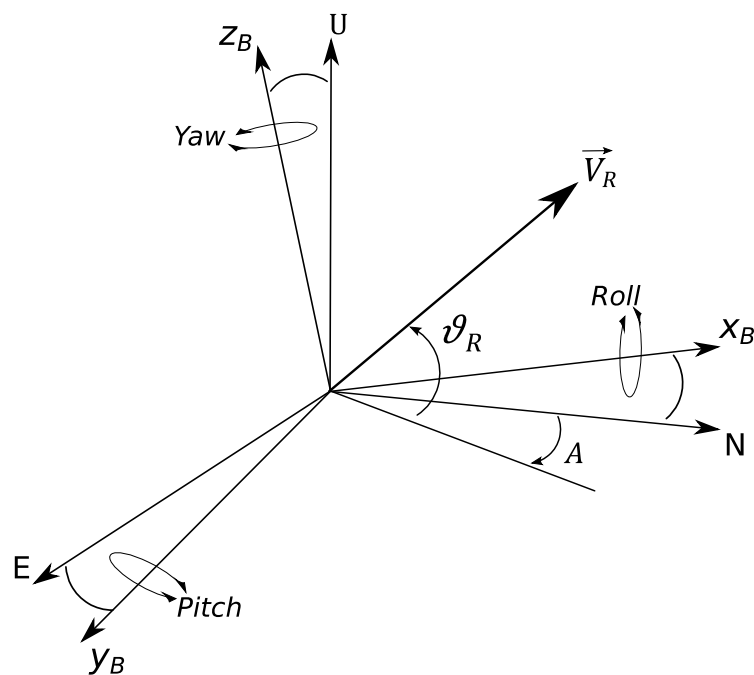
The Azimuth is the angle between the Z-Earth inertial axis and the projection of the relative velocity (\vec{V}_R) in the horizontal plane (See Figure 3.6). These angles are associated to the orbital inclination. The RFPA indicates the inclination of the relative velocity vector with the horizontal plane. The horizontal plane is made for the North axis (N) and East axis (E). Vertical or Up axis (U) is in the radius vector axis.

$$\vec{r} \cdot \vec{V}_R = rV_R \sin \vartheta_R, \quad (3.34)$$

Differences between RFPA and the Flight Path Angle (FPA) (ϑ) are due to the velocity vector. In the last one, the angle is made with the Inertial Velocity Vector (TEWARI, 2007).

$$\vec{r} \cdot \vec{V} = rV \sin \vartheta. \quad (3.35)$$

Figure 3.6 – LHRs and body system.



4 ATMOSPHERE, WINDS AND GEOPOTENTIAL MODELS

During the deorbit maneuver, the spacecraft descent rapidly due to the gravity in the direction of the Earth's center. At the same time, the Earth's atmosphere is more abundant at lower altitudes and this fact increments the action of the aerodynamic force. To determine the impact point and trajectory with better accuracy, it is necessary to know the atmospheric fluid properties and its motion. In the same way, the geopotential model gives a better approximation of the gravitational components as a function of the altitude, latitude and longitude.

Initially, it is possible to consider the Earth's atmosphere velocity relative to the planet (\vec{V}_{Atm}) equal to the product of the spacecraft position and the Earth's rotation ($\vec{\omega}_E$).

$$\vec{V}_{Atm} = \vec{\omega}_E \times \vec{r}. \quad (4.1)$$

The atmospheric wind velocity relative to the spacecraft is:

$$\vec{V}_w = \vec{V}_I - \vec{V}_{Atm}. \quad (4.2)$$

4.1. Atmospheric model

To determine the atmospheric conditions, different mathematical models have been developed, from a simple exponential model to the most recent for aerospace applications, the NASA Earth Global Reference Atmospheric Model 2016 (EGRAM 2016), which is a model with restrictions. Only institutes in the United States of America can apply to get the software.

Regional models like ARDC 1959 and US. ATM1976 were developed with samples from sounding rockets and balloons. It is recommended the use of these models to implement at altitudes below 2000 km and 2500 km, respectively. These models are static. To determine the drag perturbations on satellites it

was created the Jacchia J70 model that has the thermosphere and exosphere models with empirical temperature profiles. The limitation of these models are the operational altitudes, which are from 90 km to 2500 km.

The New Mass Spectrometer and Incoherent Scatter Radar Extended Model NRLMSISE-00, is an atmospheric model that includes data like: the total mass density from satellite observations, solar activity and magnetic activities. The model is in function of the date, hour, altitude, latitude, longitude, local solar time, magnetic index and solar radiation. The model is complemented by the Jacchia models J70, JB2008 and the Mass Spectrometer Models MSIS-86 and MSISE-90. Since it is the most recent model of the global atmosphere, it is dynamical and provides data from 0 km to 3000 km, it is selected to integrate into the present propagator (PICONE et al., 2002).

4.2. Wind model

Since the atmospheric velocity only depends on the rotation of the Earth, it must be included the horizontal wind model to get a better approximation with the reality. Since 1987 the Horizontal Wind Model (HWM) has represented the horizontal wind fields in the Earth's atmosphere. Like the NRLMSISE-00, the HWM is a function of the date, hour, altitude, latitude, longitude, local solar time, magnetic index and solar radiation to generate the planar wind velocities and directions. The model is valid for altitudes from 0 km to 500 km (HEDIN et al., 1996, 1991).

The selected HWM is the 93, because 2007 isn't available for use outside of the United States. Other models like 1987 and 1990 are outdated.

The HWM93 generates information of the meridional wind V_{SN} (South-North) and the zonal wind V_{WE} (West to East). The two wind directions are in the Local Horizontal System and must be rotated to the IERS. The two rotational matrix to transform from the horizontal local to inertial system is:

$$\begin{bmatrix} \hat{X} \\ \hat{Y} \\ \hat{Z} \end{bmatrix} = \begin{bmatrix} \cos \lambda & -\sin \lambda \cos \phi & \sin \phi \sin \lambda \\ \sin \phi & \cos \lambda \cos \phi & -\sin \phi \cos \lambda \\ 0 & \sin \phi & \cos \phi \end{bmatrix} \begin{bmatrix} \hat{x} \\ \hat{y} \\ \hat{z} \end{bmatrix}. \quad (4.3)$$

The HWM calculates the values of the wind velocity in the horizontal system and it is necessary to apply the transformation 4.3 in 2D because the vertical velocity of the wind is null. From equation 4.2, the relative atmospheric velocity wind vector components including the rotational atmosphere and the HWM, are:

$$V_{wx} = V_{Atmx} - \sin \lambda \cos \phi V_{WE} + \sin \phi \sin \lambda V_{SN}, \quad (4.4)$$

$$V_{wy} = V_{Atmy} + \cos \lambda \cos \phi V_{WE} - \sin \phi \cos \lambda V_{SN}, \quad (4.5)$$

$$V_{wz} = \sin \phi V_{WE} + \cos \phi V_{SN}. \quad (4.6)$$

4.3. Geopotential model

The Earth Geopotential Model (EGM) represents mathematically the gravitational field of a non-central body, in this case the Earth. It is represented the disturbances due to the non-spherical and non-symmetrical mass distribution. The EGM is shown in the equation 4.7 (KUGA; CARRARA, 2013).

$$U = \frac{GM}{r} \sum_{n=0}^{\infty} \sum_{m=0}^n \left(\frac{R_E}{r} \right)^n [C_{nm} \cos m\lambda + S_{nm} \sin m\lambda] P_{nm} \sin \phi, \quad (4.7)$$

G is the universal gravitational constant; M the mass of the Earth; P the Legendre's polynomials; C, S the spherical harmonics coefficients of order n and degree m .

The EGM2008 is released by the National Geospatial-Intelligence Agency and is the most accurate and actual model (PAVLIS et al, 2012). The model has spherical harmonics of degree and order 2159 with the possibility to extent for degree 2190 x 2190 (KUGA; CARRARA, 2013). The complete model is incorporated in the propagator.

5 NUMERICAL ANALYSIS

To solve the twelve differential equations of translational and rotational motion (Equations 3.2-3.13), which represent a non-linear and second order system, it is necessary the implementation of a numerical integrator.

The results of the differential equations are analyzed by the covariance matrix method to determine the relation between the different variables and to estimate the standard deviation of the trajectory.

5.1. Runge-Kutta

To solve the differential equations of motion, different numerical methods can be implemented to solve the problem. Some traditional methods are: Gauss, Euler, Taylor series and extrapolation. Since 1968, NASA's implement the Runge-Kutta formulas with step-size control for the orbital numerical propagator to reduce the errors generated by the numerical integrator and to get more accuracy on the results. One of the best numerical integrators is the Runge-Kutta of 7th and 8th order with Fehlberg coefficients (FEHLBERG, 1968). It was recently implemented to develop orbital optimization in the software Copernicus of the NASA (WILLIAMS et al., 2010).

A simple description of the numerical integrator Runge-Kutta-Fehlberg 7/8 (RKF78) is presented in Equations (5.1 to 5.4). The initial function f_0 depends on the initial time t_0 and the initial vector state conditions x_0 . For the step evaluation k , it is generated a new resultant function f_k .

$$f_0 = f(t_0, x_0), \quad (5.1)$$

$$f_k = f(t_0 + \alpha_k h, x_0 + h \sum_{\lambda=0}^{k-1} \beta_{k\lambda} f_\lambda), \quad (5.2)$$

$$x = x_0 + h \sum_{k=0}^{10} c_k f_k, \quad (5.3)$$

$$\hat{x} = x_0 + h \sum_{k=0}^{12} \hat{c}_k f_k, \quad (5.4)$$

In the RKF78 equations h represents the time step, $\alpha_k, \beta_{k\lambda}, c_k, \hat{c}_k$ are the Fehlberg's coefficients, x is the solution for 7th order, and \hat{x} for 8th order. The differences between the two are associated with the truncation error. The tolerance is the evaluation for the step-size control. In RKF78 it is common to use the Richardson's method (FEHLBERG, 1968).

5.2. Covariance matrix

At the end of the propagations, the state vector is included in a covariance matrix to observe the change in the variables in the random vector. The random vector is derived from the simulated data for the position and velocity vectors. The variance-covariance matrix has the variance data related to the standard deviation.

$$[\mathbf{P}] = Cov[\mathbf{X}] = \frac{1}{n-1} \sum_{i=0}^n [\mathbf{X}_i - \bar{\mathbf{X}}][\mathbf{X}_i - \bar{\mathbf{X}}]^T, \quad (5.5)$$

The state vector of i dimension is represented by \mathbf{X} . The mean value matrix is $\bar{\mathbf{X}}$ and n is the data quantity (REAGAN, 1993).

In the present study, the error analysis is determined by the differential equation of the variance and covariance matrix (\mathbf{P}), and the state vector derivate functions or Jacobi matrix (\mathbf{F}), also know like the Ricatti equation (CHEN et al, 2017; GUEDES, 1997).

$$[\dot{\mathbf{P}}] = [\mathbf{F}][\mathbf{P}] + [\mathbf{P}][\mathbf{F}]^T, \quad (5.6)$$

6 AERODYNAMICS AND AEROTHERMODYNAMICS

Aerodynamics and aerothermodynamics are analyzed into three possible flight phases, according to the Knudsen number. The first one is the free molecular flow. The second one is the transition flow between free molecular to continuum flow. The third one is the hypersonic continuous flow.

6.1. Dimensionless numbers

From the atmospheric model (Section 5.1) and the spacecraft dynamics, it is possible to calculate physical values to determine the body-fluid integration.

The Mach number (M) is the dimensionless ratio between the vehicle relative atmospheric velocity and the sound velocity (V_s) at a specific altitude, which is a function of the atmospheric temperature (T_{atm}), gas molecular constant (R) and gas specific heats ratio (γ). According to the Mach number, a vehicle flight is considered subsonic at $M < 0.3$, sonic for $M = 1$, transonic for $0.8 < M < 1.2$, supersonic for $1 < M < 5$ and hypersonic for $M > 5$.

$$M = \frac{V_w}{V_s} = \frac{V_w}{\sqrt{\gamma R T_{atm}}}, \quad (6.1)$$

Other dimensionless numbers are the Reynold's (R_e) and Knudsen's (K_n) numbers, both of them dependent of the body length (l_b) and the air viscosity (μ_f). Low Reynolds numbers are related to subsonic speeds.

$$R_e = \frac{\rho l_b V_w}{\mu_f}, \quad (6.2)$$

Changes in viscosity are a function of the local atmospheric temperature by the Southerland's law (NACA, 1953).

$$\mu_f = 1.716 \times 10^{-5} \text{ kg/ms} \left(\frac{T_{atm}}{273.15K} \right)^{3/2} \frac{273.15K + 110.4K}{(T + 110.4K)}, \quad (6.3)$$

The relation between the Mach and Reynolds numbers is proportional to the Knudsen number.

$$K_n = \frac{M}{Re} \sqrt{\frac{\gamma\pi}{2}}, \quad (6.4)$$

Values of $K_n \geq 1.0$ represent a rarefied or free molecular flow; for $1 > K_n \geq 0.01$ the body is in a transitional flow regimen and, for values of $K_n < 0.01$, the flow is in continuum flow. These classifications of the fluid according to the Knudsen number are important to determine the heat transfer function, the pressure coefficient and the aerodynamic moment functions (TEWARI, 2009; LIPS; FRITSCHKE, 2005).

6.2. Aerodynamics

To determine the aerodynamics characteristics of the body, it is necessary to know the geometry and shape of the body, the position or inclination between the center line and the velocity flow. The interaction between the flow particles and the solid body generates shear stress and normal forces, relative to the surface. Generally, it is used the wind reference system to determine the directions of the aerodynamics forces, Lift and Drag. To calculate aerodynamic force experimentally, it is used wind and shock tunnel testing complementary with numerical methods of Computational Fluid Dynamics (CFD), which have a good approximation with the reality but at high computational cost. The goal of this work is not to implement high precision aerodynamic or aerothermodynamics solutions by CFD, because they are very expensive in computational cost and need more time to solve the trajectory analysis. In the case of basic solids aerodynamics, like: boxes, spheres or plates, the analytical solutions present a good agreement with experimental data from the wind tunnel and with CFD methods (PADILLA; BOYD, 2006; LIPS; FRITSCHKE, 2005; KOPPENWALLNER; LEGGE, 1985). The geometry is simplified to reduce the iteration time and to obtain the aerodynamic forces and moments in each panel to integrate over the total surface of the body.

The method used to solve analytically the aerodynamic forces on the body for the three possible flows is the panel's method and consist in approximating the geometry of the body by small plane surfaces. In each surface, the local flow impact the surface with an incident angle and it generates a normal force orthogonal to the surface, a shear stress and an aerodynamic torque (see figure 6.1). The integration of all normal and shear coefficients over the surface of the body generates the body pressure coefficient, and the position vector multiply by the local aerodynamic force generates the aerodynamic torque. In the hypersonic continuum flow, the method is known as the Newton approximation. To determine the pressure coefficient in the transonic flow, a bridged function between the free molecular coefficient and the continuum coefficient flow are implemented. The bridged function was determined as an interpolation between the free molecular flow data and the continuum hypersonic data of regular solids in wind tunnel. The pressure coefficient indicates a dimensionless ratio between the differences of the static pressures and the dynamic pressure at the evaluated point, and it is integrated to find the aerodynamic coefficients according to the reference system (SCHAAF; CHAMBRE, 1961).

6.2.1. Panels and Voxels

The implementation of aerodynamics and aerothermodynamics analytic solutions requires an approximation of the surface body by finite planes. According to the geometry and dimensions of the body, it is fixed the size of the element and the dimension of the panel. Smaller panel sizes are represented with excellent accuracy, but it increased the computational cost and the quantity of the elements to analyze. Using the fixed element size model (Voxel), with volume $\Delta X_B \Delta Y_B \Delta Z_B$ and the debris material, it is possible to determine the quantity of mass in each volume element Δm , as a function of the material density. The voxel-based meshing is used to construct finite elements models of textiles to find the stress and strain in the composite fibers. The advantages of the voxel meshed is the generation on unit-cell volumes that can be automated and it requires less human interaction than the traditional finite elements

models. In this case it is ideal for automated the mesh generation after the fragmentation (KIM; SWAN, 2003). Another advantage of the voxel technic is the excellent results obtained from the implemented voxel mapped in surfaces, maps, composites and medicine. It allows the voxel to be modelled by complex geometries (GREEN et al, 2014). Voxel discretization was implemented in the analysis of fragmentation of ceramics to find the fracture conditions. The results show a good agreement between the numerical data with the experiments (SAPOZHNIKOV et al, 2015). Another implementations of the voxel-based finite element method are presented by Montero-Chacón (2014). In this research the voxel-based volumetric mesh was validated with a traditional tetra-hedralized mesh, and it was obtained similar results.

In the center of the panel surface and orthogonal to the panel is the vector normal to the surface \hat{n} . The inclination between the panel and the local wind velocity generates the surface incident angle Θ (See Figure 6.1).

$$\sin \Theta = \hat{V}_W \cdot \hat{n}, \quad (6.5)$$

Surfaces with $\Theta = 90^\circ$ indicates a stagnation point where the flow particle impacts opposite to the normal direction and it generates the shockwave. Values of incident angle from $0^\circ < \Theta < 90^\circ$ indicate regions where the fluid impacts the surface, or panels in front of the body. Negative values of the angle indicate regions in the shadow of the fluid-body interaction (SCHAAF; CHAMBRE, 1961).

As a function of the incident angle, the particle collision generates changes in the static and dynamic local pressures. These changes are proportional to the aerodynamic force coefficients and are represented by the pressure coefficient C_p and the shear stress coefficient C_τ . The total aerodynamic force and aerodynamic torque (τ_A) in the body are represented in equations 6.6 and 6.7 (TEWARI, 2009).

$$\vec{A}_F = q_\infty S \sum_{i=1}^N \{C_{P_i}(-\hat{n}_i) + C_\tau[\hat{n}_i \times (\hat{V}_{Wi} \times \hat{n}_i)]\}, \quad (6.6)$$

$$\vec{\tau}_A = q_\infty S \sum_{i=1}^N (\hat{r}_{Pi} \times \{C_{P_i}(-\hat{n}_i) + C_\tau[\hat{n}_i \times (\hat{V}_{Wi} \times \hat{n}_i)]\}), \quad (6.7)$$

The aerodynamic torque is calculated from the body CG to the panel position and it is the vectorial product of the panel position by the aerodynamic force.

6.2.2. Free molecular flow

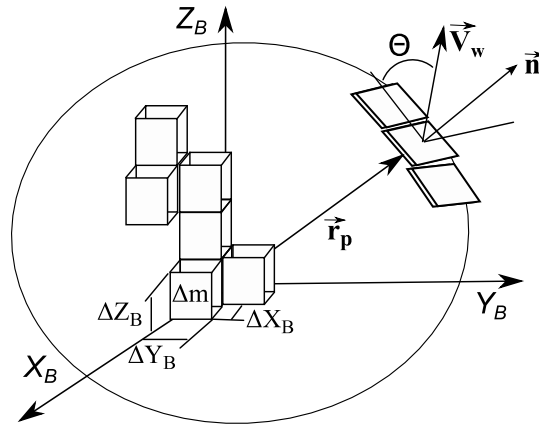
For Knudsen numbers higher than 10, the equations that represent the pressure and shear stress coefficients are:

$$C_{P_{iFM}} = \frac{1}{2S_{MR}^2} \left[\left(\frac{2-\sigma'}{\sqrt{\pi}} S_{MR} \sin \Theta + \frac{\sigma'}{2} \sqrt{\frac{T_w}{T}} \right) e^{-(S_{MR} \sin \Theta)^2} + \left\{ (2 - \sigma') \left[(S_{MR} \sin \Theta)^2 + \frac{1}{2} \right] + \frac{\sigma'}{2} \sqrt{\pi \frac{T_w}{T}} (S_{MR} \sin \Theta) \right\} [1 + \operatorname{erf}(S_{MR} \sin \Theta)] \right] \quad (6.8)$$

$$C_{\tau_i} = -\frac{\sigma' \cos \Theta}{2\sqrt{\pi}} \left\{ e^{-(S_{MR} \sin \Theta)^2} + \sqrt{\pi} (S_{MR} \sin \Theta) \right\} [1 + \operatorname{erf}(S_{MR} \sin \Theta)] \quad (6.9)$$

In this case, σ' represent the reflectivity coefficient of the material, S_{MR} the average molecular speed ratio $\left(\frac{V_w}{\sqrt{2RT}} \right)$, T_w the wall temperature and T the gas temperature. The equations are valid for angles $-90^\circ \leq \Theta \leq 90^\circ$ (TEWARI, 2009; PADILLA; BOYD, 2006; SCHAAF; CHAMBRE, 1961).

Figure 6.1 – Voxel and panel methods.



6.2.3. Continuum Hypersonic flow

The modified Newtonian flow is used to describe the flow acting in the panel during hypersonic flight. When $K_n < 0.01$, the pressure changes over the surface are higher than the shear stress, because $C_{\tau i} = 0$. The particles of compressible flow with rectilinear motion loses their normal momentum in the collision with the panel and the pressure distribution can be modeled by a semi-empirical model as a function of the incident angle.

$$C_{PiCN} = C_{Pmax} \sin^2 \Theta, \quad (6.10)$$

The C_{Pmax} is the pressure coefficient at the stagnation point and the values are a function of the molecular composition, generally values from 1.8-2.0. The modified Newton method is applied to the surface in a collision with the freestream particles, for incident angles range $-90^\circ \leq \Theta < 0^\circ$, the $C_{Pi} = 0$ (VIVIANI; PEZZELLA, 2015; GALLAIS, 2007; PADILLA; BOYD, 2006; HANKEY, 1988).

6.2.4. Transition flow

The value of the coefficients in each panel is calculated by the application of a logarithmic interpolation between the coefficients in the free molecular flow and the coefficients obtained by the Newton method. Computational tools like

SCARAB and ORSAT uses the logarithmic function to calculate the drag coefficient of a simple body without rotation (LIPS; FRITSCHÉ, 2005; KOPPENWALLNER; LEGGE, 1985). It is valid for angles $-90^\circ \leq \theta \leq 90^\circ$.

$$C_{P_{ITR}} = C_{P_{iCN}} + (C_{P_{iCN}} - C_{P_{iFM}})[\sin \pi(0.5 + 0.25 \log K_n)]^3 \quad (6.11)$$

6.3. Aerothermodynamics

The aerothermodynamics models determine the heat flow (\dot{Q}) due to the fluid-body interaction. Like the aerodynamics models, the aerothermodynamics equations are functions of the flow condition and the Knudsen number. The heat transfer flow function is calculated in each panel and the maximum heat point is located at the stagnation point, where the flow shocks with the first edge or surface on the body at 90° of incident angle with the panel surface. In this point, it is calculated the convective heat. The air is assumed to be an ideal gas, not a real gas, due to the uncertainty about the real chemical composition at the evaluation point and the boundary layer conditions. Gas dissociation and solid-fluid chemical interactions are not modelled due to the complexity and the low duration of the physical phenomenon.

One approximation of the heat transfer flow in the stagnation point for a free molecular flow is equivalent to the dynamic pressure by the relative to wind velocity (GOMES et al., 2014; LIPS; FRITSCHÉ, 2005).

$$\dot{Q}_{FM} \approx \frac{1}{2} \alpha_c \rho V_w^3, \quad (6.12)$$

Where α_c is the thermal accommodation coefficient, which value is around 1. In the case of the panel methods, a better approximation is calculated as a function of the incident angle and the gas properties (TEWARI, 2008; SCHAAF; CHAMBRE, 1961).

$$\dot{Q}_{FM} = \alpha_c \rho R T \sqrt{\frac{RT}{2\pi}} \left(S_{MR}^2 + \frac{\gamma}{\gamma-1} - \frac{\gamma+1}{2(\gamma-1)} \frac{T_W}{T} \right) \left\{ e^{-(S_{MR} \sin \Theta)^2} + \sqrt{\pi} (S_{MR} \sin \Theta) [1 + \operatorname{erf}(S_{MR} \sin \Theta)] \right\} - \frac{1}{2} e^{-(S_{MR} \sin \Theta)^2}, \quad (6.13)$$

In the case of the continuum flow, the Detra's formula is used to correlate the heat transfer in the stagnation point.

$$\dot{Q}_{CN} = \frac{11028500 \text{ W/m}^{1.5}}{\sqrt{r_B}} \left(\frac{\rho}{\rho_{sl}} \right) \left(\frac{V_W}{\sqrt{gr}} \right)^{3.15}, \quad (6.14)$$

Where ρ_{sl} is the atmospheric density at Sea Mean level, r_B the stagnation point radius, g the gravity and r the position (VIVIANI; PEZZELLA, 2015, HIRSCHHEL, 2005; LIPS; FRITSCHKE, 2005; DETRA; HIDALGO, 1961). The heat transfer for the stagnation point in transitional flow is simplified by the SESAM model, similar to the one used in the SCARAB, which relates the heat transfer in the transition phase with the values obtained for the free molecular and the continuum flow (LIPS; FRITSCHKE, 2005).

$$\dot{Q}_{TR} = \frac{\dot{Q}_{CN}}{1 + \dot{Q}_{CN}/\dot{Q}_{FM}}, \quad (6.15)$$

In the transitional, like in the continuum flow, the heat transfer is maximum in the stagnation point, where equations (6.14) and (6.15) are solved. The relation applied to calculate the heat transfer function of the inclination angle for the panels of the object is represented by (MERRIFIELD et al., 2015a):

$$\dot{Q}_i = \dot{Q}_{STG} (0.1 + 0.9 \sin \Theta), \quad (6.16)$$

6.4. Total Heat transfer

The convection heat is selected from the flow phase as a function of the Knudsen Number. The total heat transference is estimated to complete the mathematical model. It is composed of one radiative heat in the body surfaces

and conductive heat transference inside the body between the volume elements and the contact faces. The radiation heat flow is proportional to the surface temperature (T_S):

$$\dot{Q}_{rad} \approx K_{rad} K_{boltz} T_S^4, \quad (6.17)$$

Where K_{boltz} is the Boltzmann constant and K_{rad} is the radiation emissivity constant (DUNCAN, 1962). The conductive heat is proportional to

$$\dot{Q}_{con} = -K_{con} A_P \frac{\Delta T}{\Delta x_B}, \quad (6.18)$$

Which is a function of the material conductivity constant K_{con} and the panel area A_P . The net heat transfer in each panel is equal to the sum of all heat flows. The balance is 1D in the time of the integrator step-size implementing the analytic solution. In the case of internal volume, the radiation transfer is zero.

$$\dot{Q}_{cov} = \dot{Q}_{stg} + \dot{Q}_{rad} + \dot{Q}_{con}. \quad (6.19)$$

The storage heat (\dot{Q}_{stg}) by the volume element is a result of the difference between convective heat and the radiative with conductive heats. Solving the differential equation (6.19) makes possible to obtain the storage temperature to determine the melting process. Storage heat is a function of the material density and specific heat (VIVIANI; PEZZELLA, 2015; KOPPENWALLNER et al, 2005).

$$\dot{Q}_{stg} = -\rho_B C_{PB} \frac{\Delta T}{\Delta t}, \quad (6.20)$$

7 FRAGMENTATION AND BREAK-UP

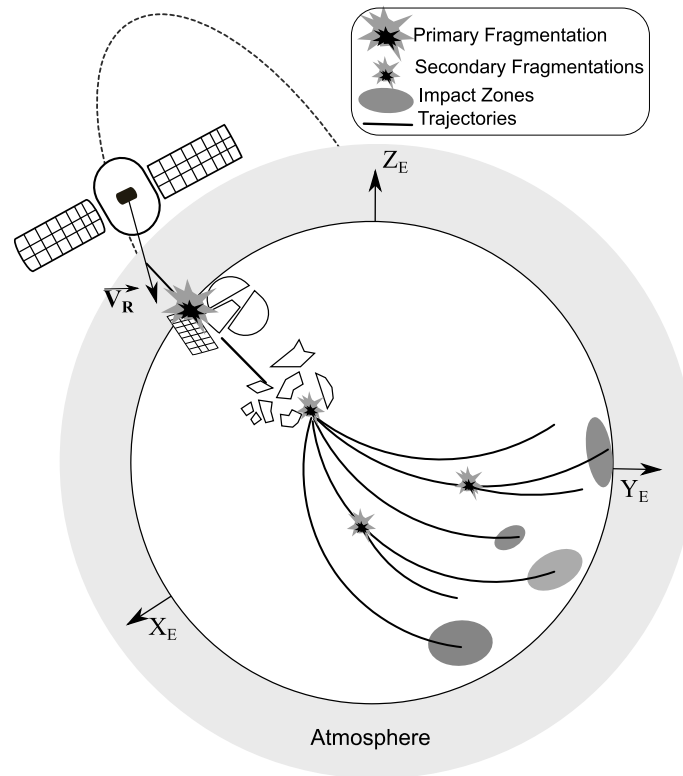
The trajectories are determined by the external forces acting in the center of mass of the body. Altitude, velocity, flow regime and atmospheric conditions determine the aerodynamic and aerothermodynamics effects and all of this generates internal changes in the debris structure that results in possible vibration, erosion, fragmentation, break up or melting, the function of the debris material and structure.

During the reentry, elements like solar panels or structures in materials like aluminum or magnesium alloys, have a primary break up in altitudes between 90 km to 60 km. The primary break up generates the principal and largest fragments from the principal body. Because the atmospheric density increases when the altitude decreases, the fragments generated during the primary break up can generate multiples break-ups, called secondary fragmentations, where new bodies with independent trajectories and masses are generated. Some of these fragments are melting or has erosion and others can survive and impact the Earth. Graphical descriptions of the reentry fragmentation are presented in figure 7.1.

To predict the break-up and fragmentation it is necessary to know the body structural distribution and material properties. Generally, to solve internal structural and heat problems, finite elements methods with nodal analysis are used. Converging solutions of the structural and heat balance problems can delay results and generate higher computational costs, due to the mesh size and body, and the number of boundary conditions. Initially, a mesh is built inside the solid, which generates a given quantity of boxes with fixed dimensions. From the interior of the body to the exterior, meshes or boxes are generated until the external surface boundary condition is reached. In the body reference system centered in the CG, the mesh point or edge position are obtained in the Cartesian system. Two nodes generate a lineal or edge; four

edges connected generates a surface and six surfaces make a volume. The mesh sized control is made manually by the user.

Figure 7.1 – Reentry fragmentation scheme.



For every new volume or box generated by the mesh, it is assumed that the box center of gravity (CG) coincides with the geometrical center and each one is separated by a distance r_P from body CG. The sum of masses of the total boxes is equal to the body mass. To simplify the calculus and the computational cost, the volume control are fixed like boxes. It is only possible to change the minimum boxes dimensions. The surface of the boxes are connected to the surfaces of the panels (see figure 6.1).

The structure and panels are under the action of aerodynamic forces, centrifugal forces (C_F) multiplied by the body angular velocity, aerodynamic and mechanical torques. All of these elements generate the total shear stress (σ_{str}) in the volume element. If the total shear stress is higher than the material ultimate shear stress (σ_{ult}), the volume element generates a fracture and a new

body is separated from the principal body. This process continues until the fragments impact the Earth's surface or are melted.

$$\vec{C}_{Fi} = m_i \vec{\omega}_B \times (\vec{\omega}_B \times \vec{r}_{Pi}), \quad (7.1)$$

$$\sigma_{str} = \frac{\vec{A}_{Fi} + \vec{C}_{Fi}}{5A_{Pi}}, \quad (7.2)$$

$$SF = \frac{\sigma_{str}}{\sigma_{ult}}, \quad (7.3)$$

The total heat transfer is linear in 1D because the real fluid conditions around the body are unknown and have only one approximation by the aerothermodynamics equations in the stagnation point. The total heat flow is calculated from the convective flow, radiative heat and conductive heat in the surface element area, initially from the stagnation point. The convective heat transfer equation inside the body is calculated by finite elements with the physical and mechanical material properties. From the total heat flux, it is estimated the voxels temperatures. The final temperatures of a step are saved in a file to become the new initial temperatures in the next step of propagation.

In the case of the ORSAT, the Thermal Analysis Demise Model calculate the heat conduction in 1D and the solid body is divided into layers. When the stagnation point of the external layer reaches the melting temperature and the heat of ablation, the layer is removed and the heat transference continues in the next layer (ROCHELLE, et al., 1997). For the SCARAB, the surface shell-type elements can be melted and it is calculated the changes in the moments of inertia and the center of mass due to the mass losses, but the melting is only determined at the surface level (LIPS et al., 2005; FRITSCHÉ et al, 2000). In the case of the present computational code, the difference with the ORSAT thermal demises is that, when a VOXEL reaches the heat of ablation and the melting temperature, only these volume elements are demised and it is calculated the new position of the center of mass, inertial tensor, recalculate the

surface and aerodynamic coefficients to determine a better approximation for the new geometry of the fragment and the attitude motion.

8 COMPUTATIONAL DISTRIBUTED METHOD

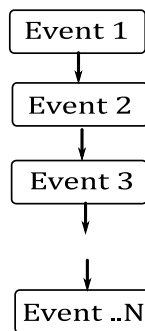
The reentry fragmentation problem considers the possible trajectories of multiple bodies under the same mathematical model and, in this case, with the same computational algorithm. One of the problems with the prediction of the collision point is the computational cost to predict the results with high accuracy. Not just one fragment trajectory, but the trajectories of the multiple bodies. One way to reduce the computational time is simplifying the mathematical models with analytical approximations, to reduce the complexity of the physical models and increment the integration step. There are three computational executions to implement in simulations of discrete-event systems: sequential execution, parallel execution and distributive execution (STENZEL, 2008).

The sequential execution method consists in a linear process that is implemented in one processor to solve the initial trajectory, when the fragmentation is detected, it generates the initial conditions for the n quantity of fragments. In this step the process ends, and began a new propagation with each fragment implementing the same methodology of the main body. If another fragmentation is detected, the process ends and began a new one with the fragment initial conditions. The end of the process is fixed for a fragmentation, melting or impact. The disadvantage of the sequential simulation is the increment of simulation time to obtain the final trajectory, because it is equal to the sum of all the trajectories of all of the fragments (See figure 8.1). Initially, this method can be implemented to simulate the trajectory of a body without fragmentation.

Parallel execution allows the use of all the processors simultaneously, everyone with one specific task or process to solve. In this way, the number of operations at the same time reduces the computational cost and the total time of the simulation. It is ideal for large scale simulations that consume much of the memory and computational power. In the case of the break-up, one initial processor can simulate the first debris until the break-up. In the next time the

fragments began the simulations in parallel and in different logical processor simultaneously. If the number of fragmentations to analyze simultaneously is superior to the number of processors and/or they are busy in others tasks, we must wait to the end of the task to take the new fragment initial conditions to process the trajectory (see figure 8.2).

Figure 8.1 – Sequential execution.

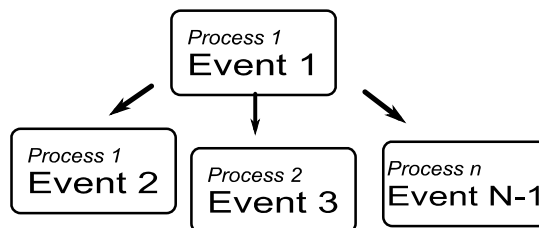


Different methods can be applied to use parallel simulation. One open source method for FORTRAN is OPENMP, which allow the control of threads. Another is CO-ARRAY an ISO Standard for parallel and distributive FORTRAN 2008 (REID; NUMRICH, 2007). CO-ARRAY uses processes like images or mirrors of the original simulation with independent state variables. Basically, the differences between OPENMP and CO-ARRAY is the use of the computational memory. In terms of threads, for OPENMP, the main thread controlled the link with the other threads and the memory is shared between all the threads. On the other hand, in CO-ARRAY, the memory is independent for each processor, and the information is saved for the independent variables (CHIVERS; SLEIGHTHOLME, 2015). Due to the implementation of the high quantity of data, multiple subroutines, the requirements of safety blocks of memory and the distributed simulation, the CO-ARRAYS is selected to implement the simulations.

The final method to apply is the distributed execution. With the parallel execution it is possible to reduce the simulation time in the case of multiple fragments, thanks to the use of all processors. But, in the case of a large

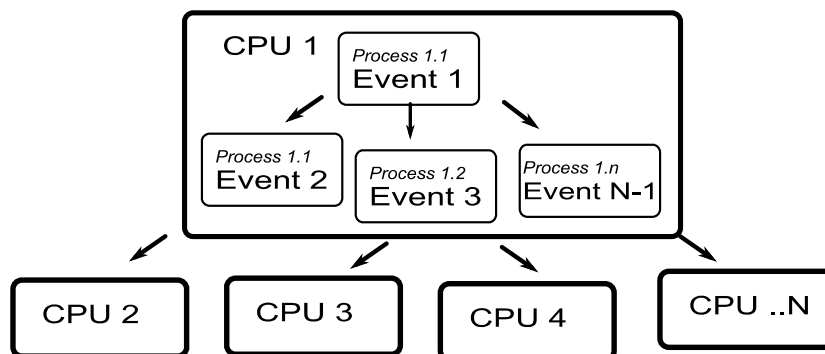
number of fragments, larger than the number of processors, to reduce the simulation time, it is possible to send the task to other computers connected. It requires the interoperability and synchronization (STENZEL, 2008). The local net with multiple computers and multiple processors allows the distribution of process simultaneously, due to the larger quantity of fragments and trajectories required (see figure 8.3).

Figure 8.2 – Parallel execution.



This distributed method is used to analyze multiple fragments and it reduces the computational cost. In the case of an uncontrolled reentry detected by hours or days before the impact, the distributed simulation helps to reduce the prediction time without affecting the final accuracy. Applications of distributed execution with High Architecture Level (HAL) has been presented to simulate collisions between debris clouds in LEO. The implementations of distribution execution allow to reduce the time step simulation, coordinating high quantity of data and to detect collisions quickly (LI et al., 2009).

Figure 8.3– Parallel execution.



9 CODE STRUCTURE

The computational code to propagate the trajectory of a reentry debris without control is developed in nine different sections. Eight of the nine sections were developed in the present research and are independent of another code and/or simulation tools. In these sections, it was included the mathematical model present in the previous chapters. The code sections were written and developed in the present research. Only the libraries with the atmospheric, geopotential and wind models were selected from the scientific literature and were implemented without modifications. The computational code sections developments are described in the present chapter.

Initially, the main program read the initial conditions or state vector in the FLIGHT DATA modulus. From the state vector or the TLE's are calculated the initial variance matrix and the respective coordinates in the inetal system. Next, according to the material data, body geometry, material physical and mechanical properties, the main program calls the MESH subroutine that identify the body geometry and generate the nodes, edges, surfaces and voxels, according to the size dimension selected by the user. The MESH output calculates the center of gravity position in the body reference system, the Inertial Tensor, total mass, number identification and coordinates of the voxels. All the information is saved in independent files for the use in other routines.

The INITIAL subroutine transforms the variables to the inertial frame. From the FLIGHT data, the libraries calculate the gravitational parameters in the inertial system, winds and atmospheric data. The LIBRARIES subroutines are obtained from the scientific literature. In the cases of the wind and atmospheric models the matrices transformation described in chapter 4 are used to transform all the values in the inertial reference system. The FRAGMENTATION module calculates the pressure coefficients of the total body, the total heat transfer and stores them to find the temperatures in the voxels. The attitude is used to determine the air density and calculate the aerodynamics forces and the total

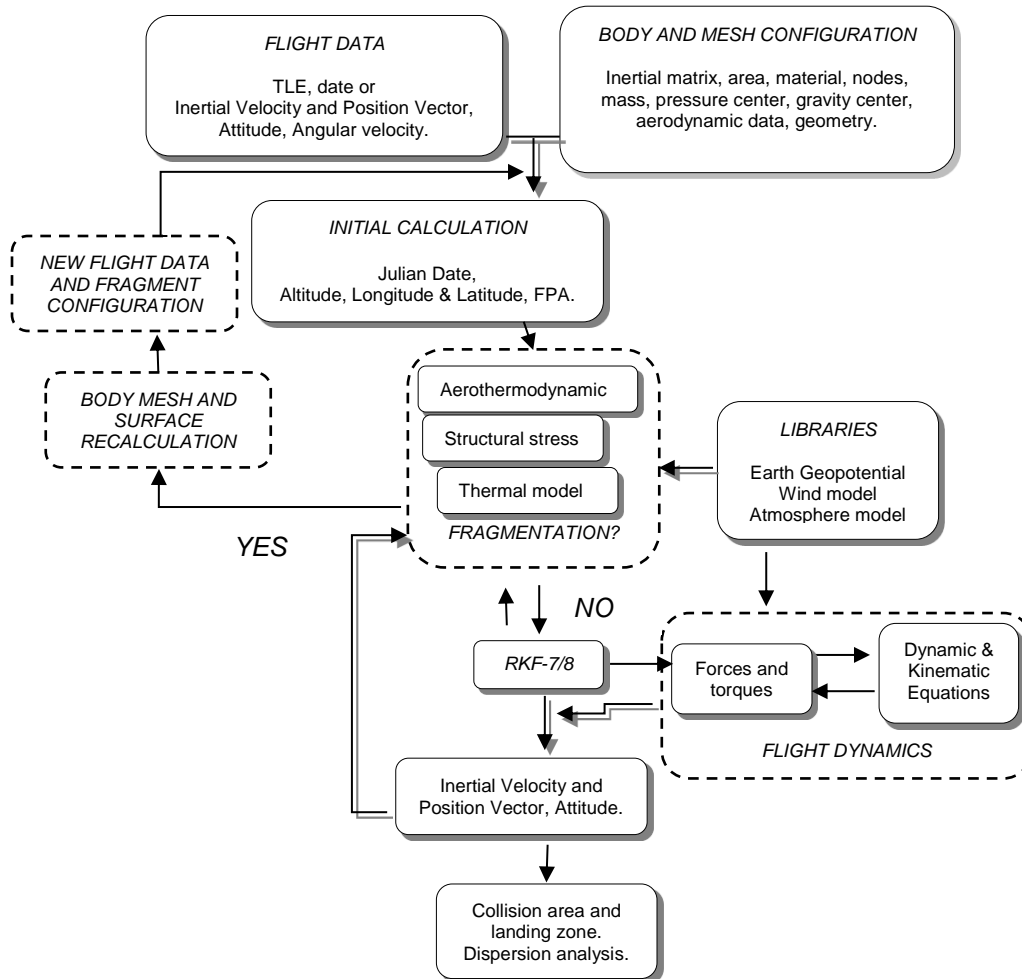
shear stress acting in the voxels, all the data is saved in external files. At this point all data collected is sent to the FLIGHT DYNAMICS that contains the integration module, where the 12 ODEs of motion and 105 ODEs of the covariance matrix are integrated numerically with the numerical integrator RKF7/8. All the torques and forces are calculated to integrate and propagate the trajectory. The resulting data is returned and the fragmentation ablation and structural breakup are evaluated. If the voxel storage heat is equal or superior to the ablation heat and the temperature is superior to the melting temperature, the voxel is ablated and a new body fragment is created and propagated in sequential simulations. This process is like the one used by the ORSAT tool, with the difference that in ORSAT the ablation is calculated at the stagnation point and is removed the skin of the fragment according to one finite thickness. To simplify the calculation is used 3DOF simulation (LIPS; FRITSCHE, 2005). If the body breaks up, new files with the geometry and properties are generated and start the parallel and distributive simulations. After the fragmentation and/or the break up, the final section of FRAGMENT RECALCULATION generate the new files with the new mesh and surface information, calculates the mass losses, variation in the center of gravity and new inertia tensor. The new values are sending to the propagated data for the main program. The data is shared with the other modules in the same process until the debris is dismissed or impact.

Due to the implementation of the transformation matrix of the references frames, it is possible to rotate the state vector in the local, geocentric, rotational and inertial frames. The architecture and modules of the computational code are shown in figure 9.1. It is possible to compare the architecture with the SCARAB presented by Fritsche et al, 2000.

The present computational tool has applications in space technology for the reentry prediction of the debris. Results of the dispersion analysis of the trajectory can be used to evacuate the collision zone, to send warning messages to the populations, propagation of the reentry trajectory of warheads

and satellites, analysis of survivability reentry of future missions, determination of the survival mass, geometry and materials, estimations of the reentry date and other applications of security and defense.

Figure 9.1 – Flow diagram of the computational code.



The computational code was developed in FORTRAN and is made from 25 subroutines. The implementation of a group of subroutines represents a section of the algorithm diagram. The present section describes all the subroutines. For the flight data and the initial calculations, the ENTRY is the main routine in the code, which reads the TLE's or the initial state vector, the body type and dimensions, and the selected material. It is created the main files of the trajectory, attitude, and variance matrix and call the secondary subroutines. This routine also initializes the parallel function in the case of the break up. The

MESH calculates the body boxes, the inertial matrix, center of mass and computational location of the voxels. It is complemented with the MESHARRAYS to vectored the surface voxels and to implement the surface temperature initial conditions. The JULIANDATE calculates the Julian date for the time of the simulations and MONTECARLO is the aleatory numbers generator to modify the initial conditions in a selected variation. JACOBI calculates the Jacobi's matrix.

In the aerothermodynamics section, the AEROATM calculates the atmospheric conditions from the NRLMSIS00 model, the wind velocities vector from the HWM93.FOR and the fluid dimensionless numbers.

The BODYROT is the structural and the thermal model section. In this section are calculates the aerodynamic moments and forces in each voxel, the pressure center locations and the total aerodynamic and moments in the body center of gravity. It also transforms the forces from the body and wind system to the inertial system. In the same subroutine it is calculated the convective heat transference, centrifugal forces, total heat transfer in the voxel and local temperatures. If the code detected centrifugal fragmentation or melted, the DELLVOX and NEWSURF recalculates the surface and erase the voxel fragmented to generate a new body mesh. In RECALMESH is recalculated the body mass, CG location, the inertial tensor and the instantaneous variation of the inertia as a function of time.

The GRAVACC contained the EGM2008 model of the geopotential and calculates the local gravity. The numerical integrator RKF78 contains the subroutine DER, where are the differential twelve equations of rotational and translational dynamics and kinematics with the 105 differential equations of variation of the variance and covariance matrix.

The error analyzes is developed in the subroutine JACOBI, that contains the Jacobian functions in differential equations in a matrix. From JACOBI it is called DERPARR that resolves numerically the differential equations of the Jacobian

matrix in each step of time to propagate the error and to integrate the variance/covariance matrix. The DER routine is coupled with the MATMULT, where it is calculated the matrix product between the Jacobi and Variance/Covariance matrix, to find the Variance/Covariance differential equations. Finally, the TMVARCOV transform the position error in the inertial system to the local system.

In this case, 22 of the 25 subroutines were designed for the present research and contains the mathematical model described in the previous chapters. The complete code is a software product to propagate the trajectory and to estimate the impact of reentry debris. The software is an additional result of this research and a computational tool to contribute to the studies in atmospheric reentry. In terms of the NASA's Technology Readiness Levels (TRL) it is possible to say that the actual software is in a TRL-5, because was validated in a laboratory ambient with the previous results of another software simulated reentries and is waiting to be validated in a relevant environment with data from a real reentry.

The computer implemented to solve the simulations was an Intel Core i5 of 3.0 GHZ, with 8 GB of RAM and $1.110223024 \times 10^{-16}$ of machine error. The processing time of a single trajectory without fragmentation and without error propagations is around 50 s, with the variance matrix is higher than 20 min. According to material, the fragmentation process can increase the processing time.

The computational code is restricted for general public access and is under the domain of the INPE's division ETE/DMC.

10 STUDY CASES, ANALYSIS AND RESULTS

A numerical propagator for reentry cases is written in FORTRAN. The code has the dynamical equations of motion in 6DOF, the Inertial Earth Reference System, the NRLMSISE-00 atmospheric model (ANSI, 2004), the Earth Geopotential model to 100th order (KUGA; CARRARA, 2013), rotational atmosphere with HWM93 wind model and a Runge-Kutta-Fehlberg 7/8 numerical integrator. Compared to other reentry simulation tools, the present propagator is different because it implements a more accuracy integrator, the debris is modeled in 6DOF, includes the atmospheric and local winds, and contains a higher order gravitational model. Also, the total aerodynamic force is modeled with the Magnus force and the solid body is mathematically modeled by voxels to generate the automatic mesh, control of volumes and to determine, with a better approximation, the fragmentation. The voxels allow the studies of different body shapes. Debris resulted from fragmentation and break-ups, are propagated in parallel and/or computation distribution. Due to the implementation of the improvements, it is expected results similar to the ones obtained with other reentries tools in previews simulations.

10.1. Materials

To determine the heat transfer, mechanical loads, break-up and rigid solid properties, it is necessary to know the material physical, mechanical and thermal data. In table 10.1 it is presented the list of the materials included in the computational tool. Graphite Epoxy data is adapted from Lips and Fritsche (2015); Park and Park (2017).

10.2. Mesh

To calculate the pressure coefficient, heat transfer, temperatures, shear stress and centrifugal forces acting on the body, it is necessary to divide the main body in multiple finite bodies, or meshing the body. The mesh is calculated as a function of the volume element (voxel) and the body shape. The mesh divides

the body in a finite number of elements, nodes, edges and faces. To simplify the study case, cubic mesh elements are selected (voxel).

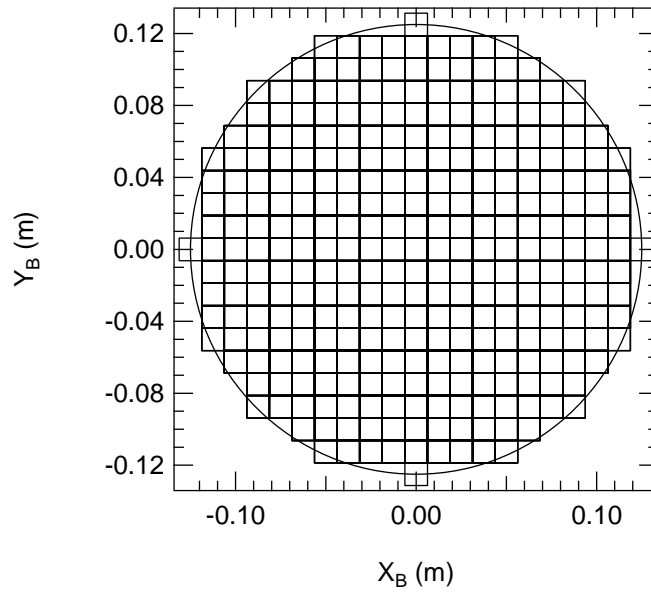
Table 10.1 – Materials data

Material	Density (kg/m ³)	Yield Strength (MPa)	Emissivity (%)	Melting Temperature (K)	Specific Heat (J/kgK)	Thermal conductivity (W/mK)	Heat of Fusion (KJ/kg)
1. Aerospace Aluminum	2700	50	0.90	932	470	237	398
2. Steel 4130 *Iron	7850	460	0.90	1700	477	42.7	272*
3. Titanium	4400	370	0.90	1941	540	19	419
4. Cupper	8960	210	0.90	1410	390	401	205
5. Graphite Epoxy I	1570	829	0.86	850	1100	110	16100 0
6. Graphite Epoxy II	1551	829	0.90	1950	879	0.9	0.237

Source: Adapted from Lips et al. (2005); Park; Park (2017).

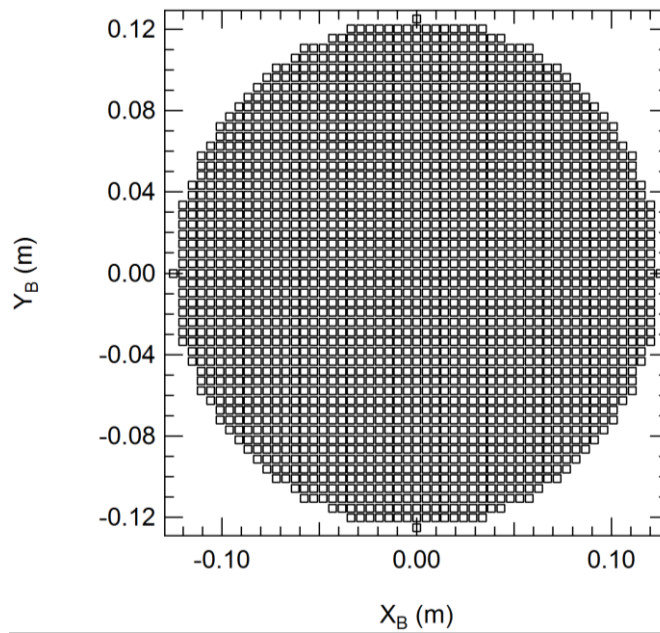
Advantages of the implementation of the voxels in the mesh are the generation of automatic mesh in the moments of break up and fragmentation, the use of the same size for the volume element for all the bodies and simplification of the mesh files. Results for the mesh of the sphere, as a function of the number of elements, are showed in figures 10.1 to 10.4. Figure 10.1 shows a mesh with the largest voxels, which is a poor quality model to represent the spherical surface.

Figure 10.1 – Solid sphere mesh with 4145 nodes.



In figure 10.2 is presented a mesh with medium size voxels. The quantity of voxels is higher than the large size voxel mesh, so it is observed a better match with the selected geometry.

Figure 10.2 – Solid sphere mesh with 73453 nodes.



Inversely proportional to the voxel size is the number of nodes and elements. Small voxel increases the number of nodes and generate a better approximation to the real geometry, figure 10.3. The problem is the computational cost due to the number of voxels to analyze. A low quality mesh reduces the computational cost, but increase the error of the calculations, because it is far from the real geometry. For the present simulations the medium size meshes are selected.

A 3D representation of the medium size voxels in a spherical tank is presented in figure 10.4.

Figure 10.3 – Solid sphere mesh with 523185 nodes.

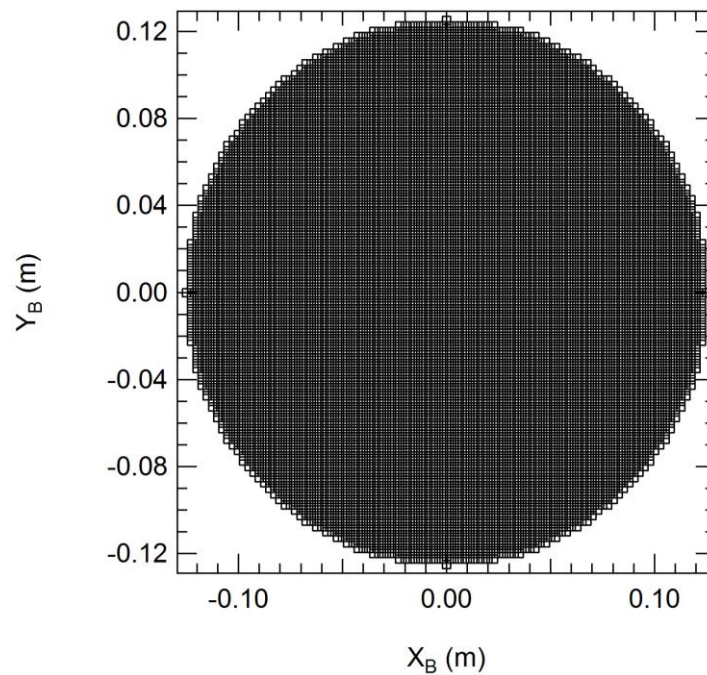
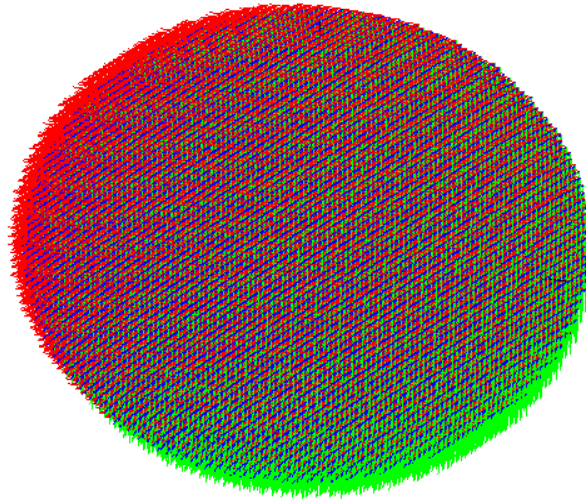


Figure 10.4 – Voxel sphere mesh.



10.3. Validation

For the verification of the propagator, it is selected a study case using data from the ORSAT and SCARAB software to compare the results, like showed in Park and Park, (2017). It is compared the reentry trajectory of a spherical tank of 0.125 m outside radius and 0.075 m of inside radius, with a mass of 10.070 kg. The sphere material is Graphite Epoxy I, because of the resistance to the ablation and/or fragmentation during the reentry (LIPS et al., 2005). The initial conditions are presented in Table 10.2. The values of the aerodynamics and moments coefficients were calculated from the implementation of the panel methods in the three fluid regimens.

The EGM 2008 100 x 100 model was implemented, an integration step time of 0.5 s was used and a medium selected mesh sphere was selected. The computational time is around 1500 s for each trajectory. The computational machine used in the simulations has a Core i5 3 GHz processor, 8 GB in Memory and uses Visual Fortran.

Table 10.2 – Spherical tank Initial Conditions.

Altitude	122000 m
Relative Velocity	7410 m/s
Relative Flight Path Angle	-0.1°
Orbit Inclination	28°
Latitude and Longitude at initial time (0s)	0° and 0°
Euler Angles	0°
Angular Velocity	0°/s

Source: Adapted from Lips et al. (2005); Park and Park (2017).

With the initial conditions, four simulation cases of the study were determined. The first one is a reentry in 3DOF, without rotation and without initial angular velocity force, a ballistic trajectory. The second one has a free rotation (6DOF), which means that the aerodynamic and inertial torques generate rotational velocity and angular moment. In this case, since the torques are smallest, the results are similar to the trajectory with 3DOF. Both trajectories have a good agreement with the data obtained from the ORSAT and SCARAB. These results allow validating the reentry in 3DOF (see Figures 10.5 and 10.6).

The altitude as a function of time and the altitude as a function of the velocity are related and they are accord with the results reported by the other computational tools (LIPS et al., 2005; PARK; PARK, 2017). Only these variables are compared because these are the only available data reported in the scientific publications.

Two special cases were selected to observe the influence of the angular velocity during the debris reentry. Initially, the inertial axis and the body axis are aligned and is applied an initial angular velocity in the Z-axis, orthogonal to the trajectory plane. The angular velocity selected is 1200 RPM and was applied in the prograde and retrograde direction.

In figure 10.5 it is observed the altitude of the trajectories as a function of time. Initially, all the trajectories have the same behavior. They decay linearly, until around 90 km of altitude, where the atmospheric density increases and then begin an exponential decay. Differences between ORSAT, SCARAB and the propagator are associated with the differences between the mathematical models, but all the results presented a good agreement. The four trajectories propagated are similar to the 60 km of altitude, where the trajectories that influence the initial rotational motion move away from the trajectories with 3DOF and 6DOF. The difference is more significant at altitudes below 20 km, in the highest density zone. Due to the influence of the Magnus force and attitude changes, the final trajectories have a higher flight time than the trajectories in 3DOF and 6DOF, also change the impact zones (see Figure 10.6). It is possible to observe that there are difference between the trajectories with 3DOF and 6DOF. Trajectories with rotation, generate Magnus force in a radial direction, reducing the vertical velocity and increasing the time of flight. In the case of positive rotation (blue line), the direction of the rotation reduces the relative air velocity, reducing the effect of the Magnus force and having a time of flight lower than the negative rotation trajectory (red line), where the direction of rotation increases the effects of the Magnus force. This type of phenomena are not observed in the ORSAT and SCARAB trajectories, because they do not take into account the rotation and Magnus force. The differences between the propagated trajectories in 3DOF with the ORSAT and SCARAB results are generated due to the differences in the dynamical, atmospheric and integration models.

Figure 10.5 – Spherical tank altitude vs time.

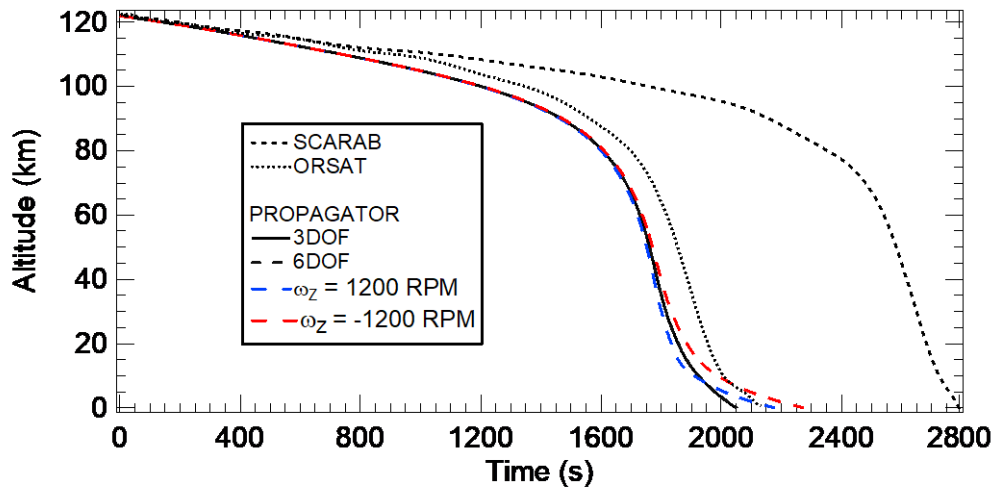
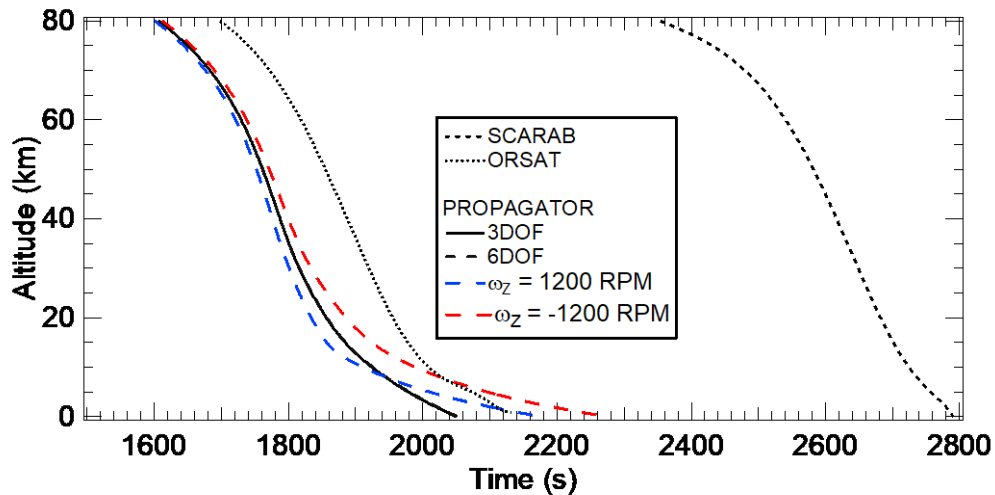
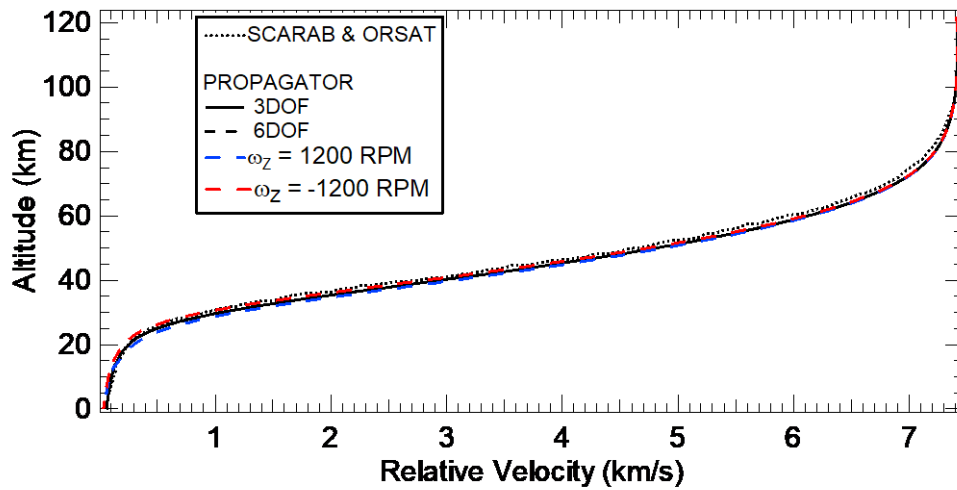


Figure 10.6 – Spherical tank altitude vs time, zoom.



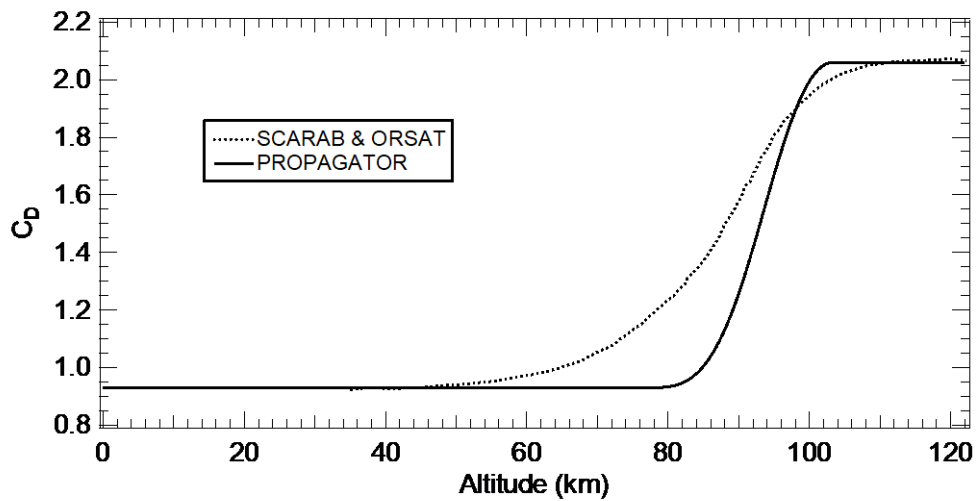
The variation of the relative velocity with the altitude shows the same behavior and correlation for all the reentry cases. See figure 10.7. The velocity presents a small variation in altitudes between 90 km to 120 km, due to the low density of the air. The increment of density with the reduction of the altitude, generates a breaking of around 7 km/s in altitudes between 80 km to 20 km. The debris velocity is subsonic in the troposphere. The impact velocity is inferior to 100 m/s due to the influence of the highest density zone. In subsonic flow the drag coefficient is the minimum (see figure 10.8) and it reduces the velocity losses.

Figure 10.7 – Spherical tank altitude vs relative velocity.



Differences between the trajectories are related to differences in the aerodynamics coefficients and the aerothermal functions in the transitional flow. In the case of ORSAT, it implements a bridge function in the transitional flow from fixed data from the geometry and wind tunnel validation, since ORSAT implements simulations in 3DOF, the lift and rotational aerodynamic effect don't show variations in the drag coefficient. In the case of the SCARAB, the function implemented isn't present in the literature. It only shows that it is calibrated with wind tunnel and real reentries data. The difference with the actual propagator is the method used to calculate the aerodynamic coefficients. The implementation of winds and better atmospheric model, generate changes in the Mach, Reynolds and Knudsen Numbers, which affect the solutions of the aerodynamic coefficients. A similar difference in the drag coefficients between the SCARAB and the ORSAT-J is reported by Lips and Fristche in 2005. Figure 10.8 shows the drag coefficients as a function of the altitude. In the highest altitudes the rarefied flow presents the largest drag coefficient, but the low density generates a slow breaking. The transition regime is present in altitudes between 90 km to 80 km, where the aerodynamic coefficient decay rapidly until the continuum flow, below 80 km and where the increase of the density generate the highest velocity losses.

Figure 10.8 – Spherical tank drag coefficient vs altitude.



10.4. Results of spherical tank in 6DOF

Additional results of the reentry tank are shown in figures 10.9 to 10.24. Since there is no specific data reported and geographic coordinates of the reentry spherical tanks, the next results are generated with the actual computational tool to analyze the behavior of a rotational spin, reentry in 6DOF and the 3DOF propagation. The results are not reported in scientific publications. The four cases to compare are the sphere reentry in 3DOF, the sphere reentry in 6DOF without initial angular velocity and the spherical tank rotational initially at 1200 RPM in the plane of the trajectory in clockwise and counter clockwise directions. The geographical coordinates of the trajectories are presented in figure 10.9. Initially, the four trajectories have the same behavior but, in figure 10.10, it can be observed that the trajectory with the sphere at 1200 RPM's hits back of the trajectories with 3DOF. The trajectory with -1200 RPM's shows a larger displacement. The Magnus force is orthogonal to the angular and translational velocities. This direction makes trajectories with positive rotation to generate a component in the opposite direction to the trajectories with negative rotation and without rotation. This behavior is only visible at low altitudes because of the air density increases. With the results of the figures, it is possible to observe that the unknown of the attitude and rotation of the reentry debris can increase the

impact zone in a ratio of 80 km around of the 3DOF trajectory. With the increase of the landing zone, the hazard probability is increased, making the debris more dangerous.

Figure 10.9 – Reentries spherical coordinates.

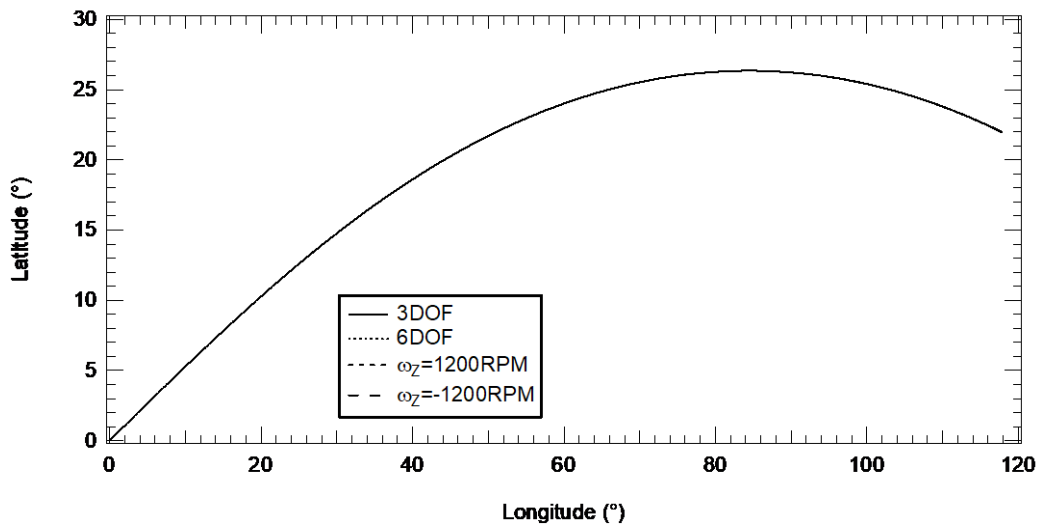
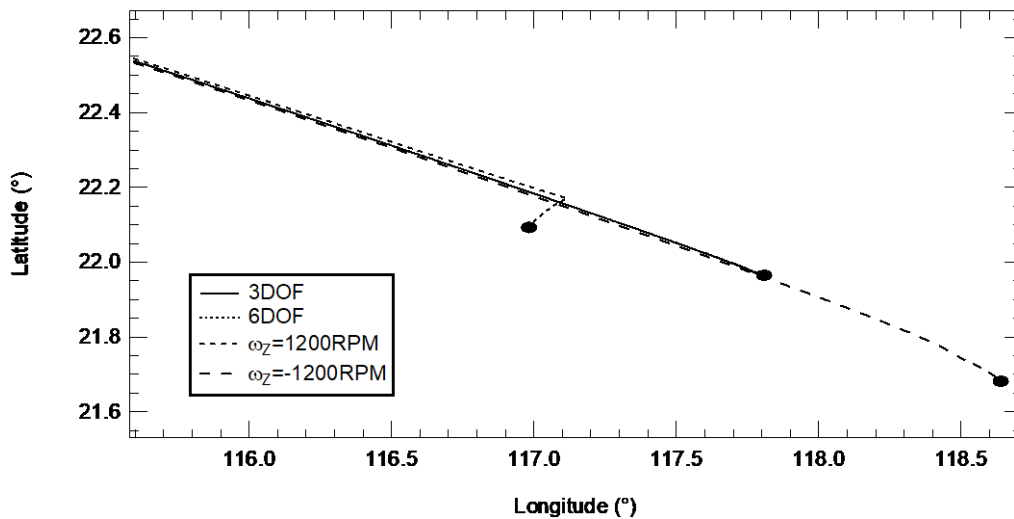


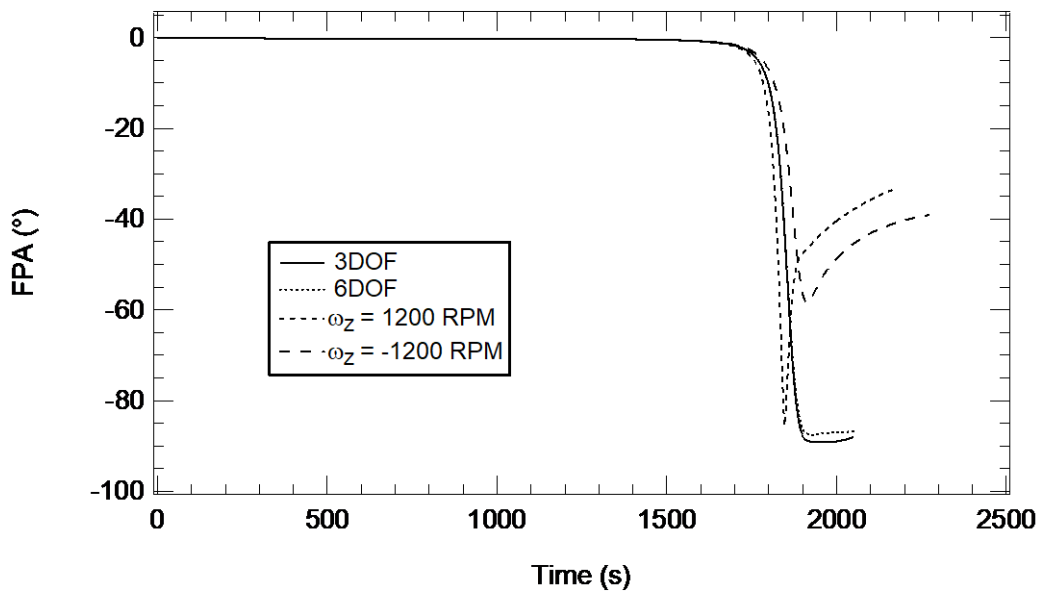
Figure 10.10 – Reentries impact zone estimations.



Because the lift and the Magnus force are generated during the rotational reentry, the fragment reduces the vertical speed and increase the lateral speed in the wind system, generating a higher time of flight and increasing the flight path angle. From figure 10.11 it is possible to observe the differences between the flight path angles for a reentry in 3DOF or without rotation and other

trajectories with rotations speed around 12000 RPM's. Trajectories without rotation generate a flight path angle around -90° , indicating the direction of the relative speed in the horizontal plane. In other words, vertical to the Earth's surface. For trajectories with higher rotations, the flight path angle increased in the final seconds due to the aerodynamic forces.

Figure 10.11 – Debris flight path angle vs time.



The total energy of the debris is equal to the sum of the Kinect energy plus the potential and rotational energy. In the local system, it is possible to observe an initial energy equivalent to the orbit energy. The energy began to dissipate due to the atmospheric drag and decay rapidly during the reentry, having losses in the kinetic and potential energy (see Figure 10.12). The general behavior of the rotational spheres energy dissipation is similar to the sphere in 3DOF. The differences are significant in the rotational energy diagram (Figure 10.13), where the rotational spheres can have losses or energy gains due to the interaction with the winds directions. The rotational energy increments the impact energy and generates an increase in the risk of the fragment.

External conditions coming from the relation between the fluid and the body in the stagnation point are analyzed along the trajectory with the values of the heat

flux and the dynamic pressure, as shown in figures 10.14 and 10.16, respectively.

Figure 10.12 – Spherical tank relative energy vs time.

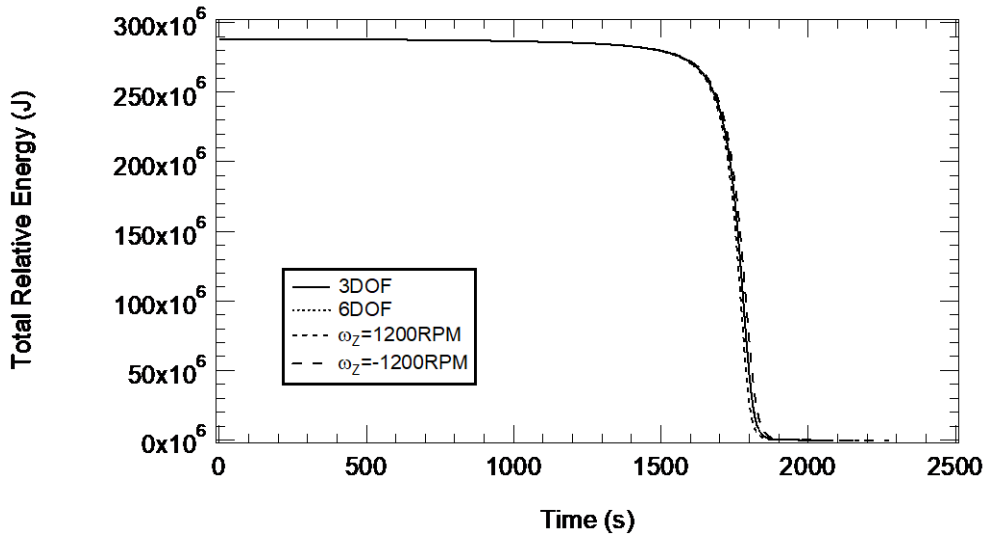
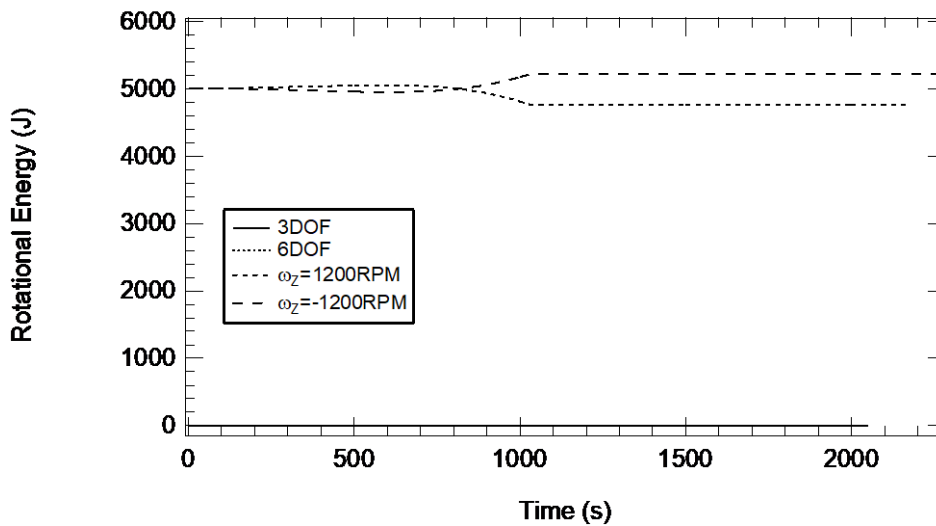


Figure 10.13 – Spherical tank rotational energy vs time.



During the reentry, the heat flux increased as a function of the altitude decay and the fluid conditions. At altitudes around 100 km the change between the rarefied flow and the transitional generates a rapidly decay in the heat flux. The maximum values for heat flux and dynamic pressure are reached in the continuum flow zone, due to the air density increment. The heat flux is

maximum around 60 km of altitude, when the debris velocity is around 6 km/s. The maximum value for the dynamic pressure is around 40 km of altitude, due to the increment in the air density. With the drag increment, the fragment obtains a higher deceleration (figure 10.15). The combination of the increase in density and the highest deceleration at altitudes between 60 km to 20 km, generate the maximum flight conditions, where, generally the objects are fragmented. Similar results of heat transfer for spheres during reentry are presented by Park and Park in 2017, with maximum heat around 250 kWatts at 1800 s. Trajectories with positive rotation increased the values of the acceleration, heat transfer and dynamic pressure due to the increase in the velocity of the relative wind at the stagnation point, and trajectories with negative rotation have the lowest heat flux and structural factors, due to the reduction of the relative velocity with the flow, which allows the survivability of the fragment.

Figure 10.14 – Spherical tanks altitude vs heat flux.

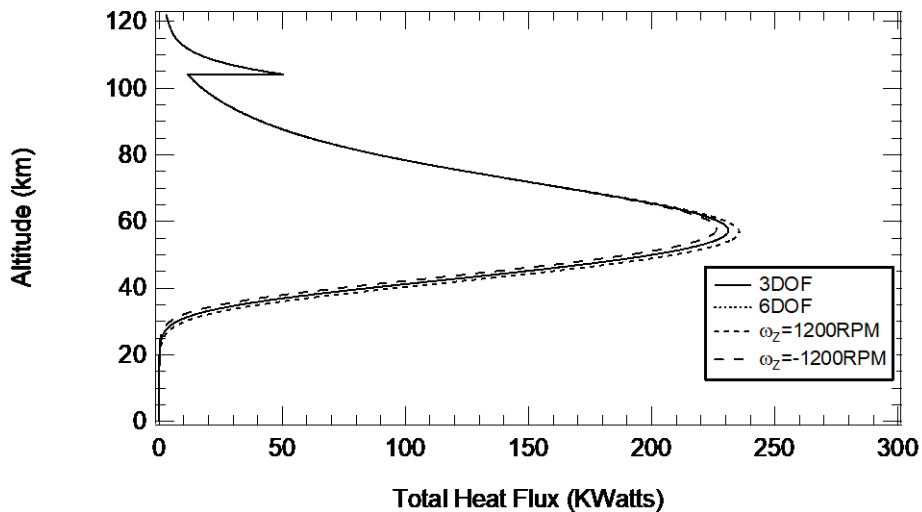


Figure 10.15 – Spherical tanks altitude vs load factor.

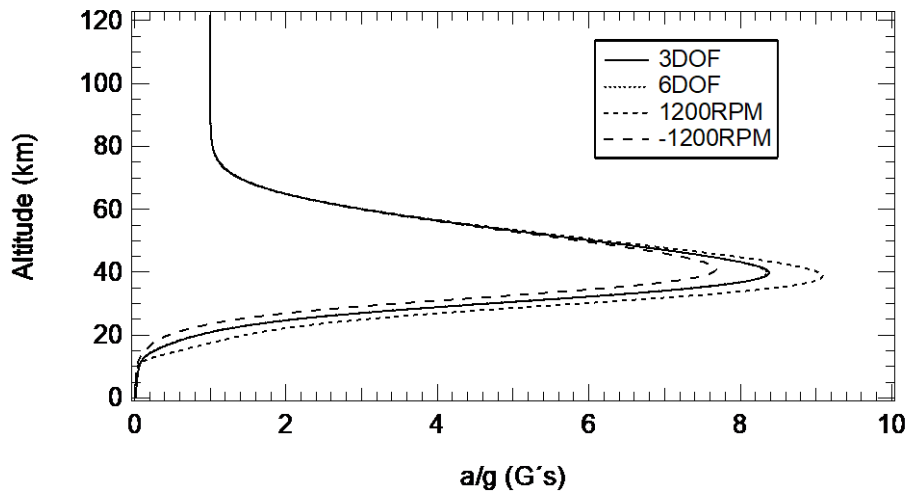
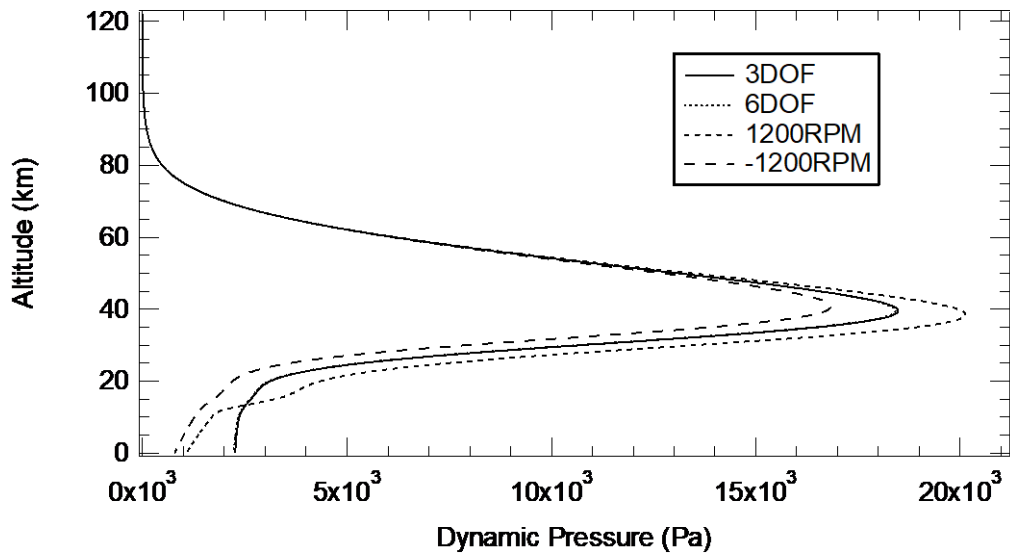


Figure 10.16 – Spherical tanks altitude vs dynamic pressure.



For the four trajectories simulated, we selected altitudes of 120 km, 90 km, 60 km and 30 km to observe the temperatures and the pressure coefficient distribution in the surface of the body. The altitudes were selected according to figure 10.14, where 120 km is the initial condition. Around 90 km the fluid model changes from rarefied to transitory, and near 60 km occurs the maximum heat

flow. Finally, around 30 km, the body begin to cool down. Figures 10.17 to 10.24 show the surface of the tank in the four cases of study.

The Pressure Coefficient (C_P) distribution shows the localization of the stagnation point around the body (maximum C_P). Tanks simulated with 3DOF generate higher temperatures, superior to 3000 K at 60 km of altitude, and the rotational tanks present temperatures inferior to 2000 K at the same altitude. This behavior indicates that rotational tanks experiment a refrigeration process due to the rotational motion and the changes in the position of the stagnation point in each instant of time. In the same way that the rotational motion generates changes in the trajectory, in this case it generates changes in the heating process, decreasing the surface temperatures and reducing the melting fragmentation and increasing the survival probability. These are examples of the possibilities given by the code to make detailed observations of the phenomena along the trajectory.

Figure 10.17 – Surface temperature distribution tank in 3DOF.

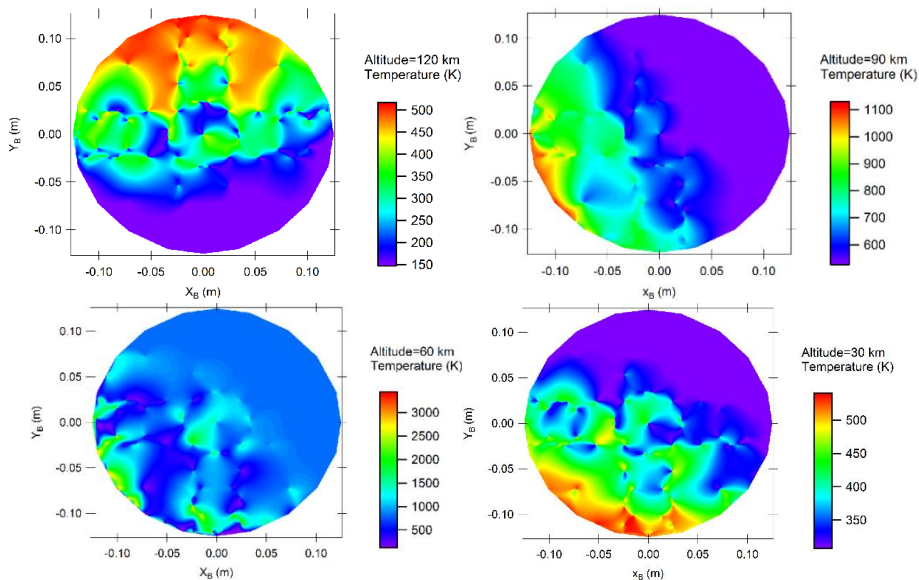


Figure 10.18 – Surface CP distribution tank in 3DOF.

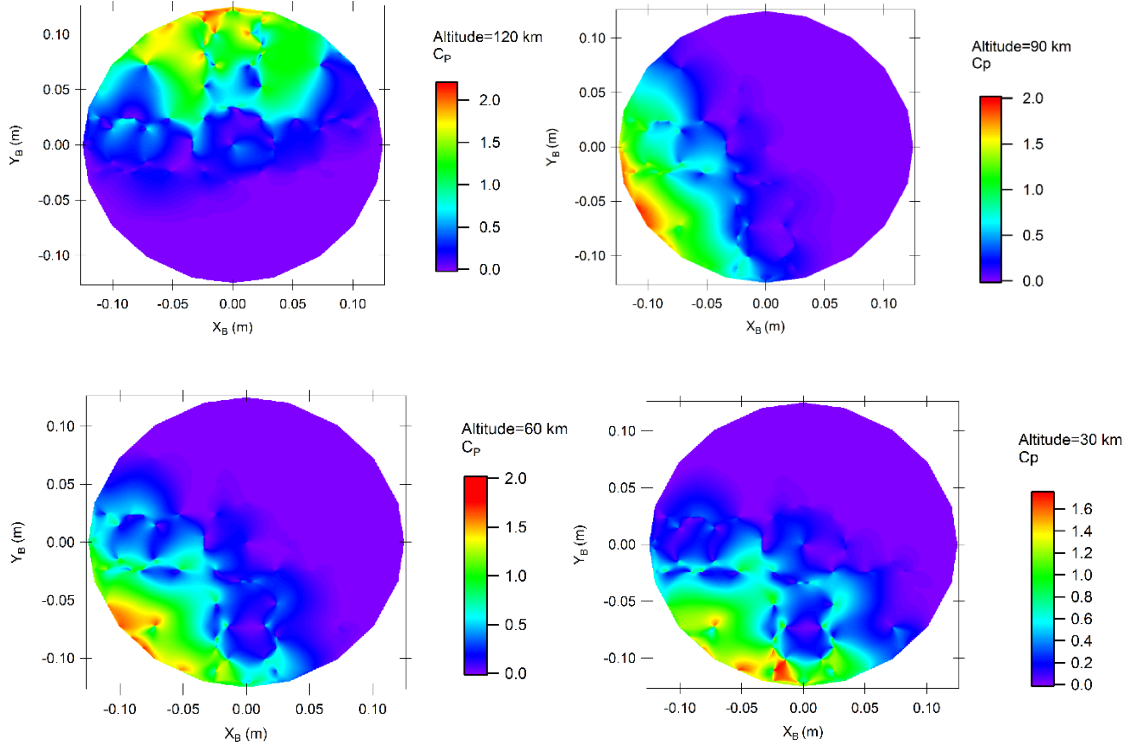


Figure 10.19 – Surface temperature distribution tank in 6DOF.

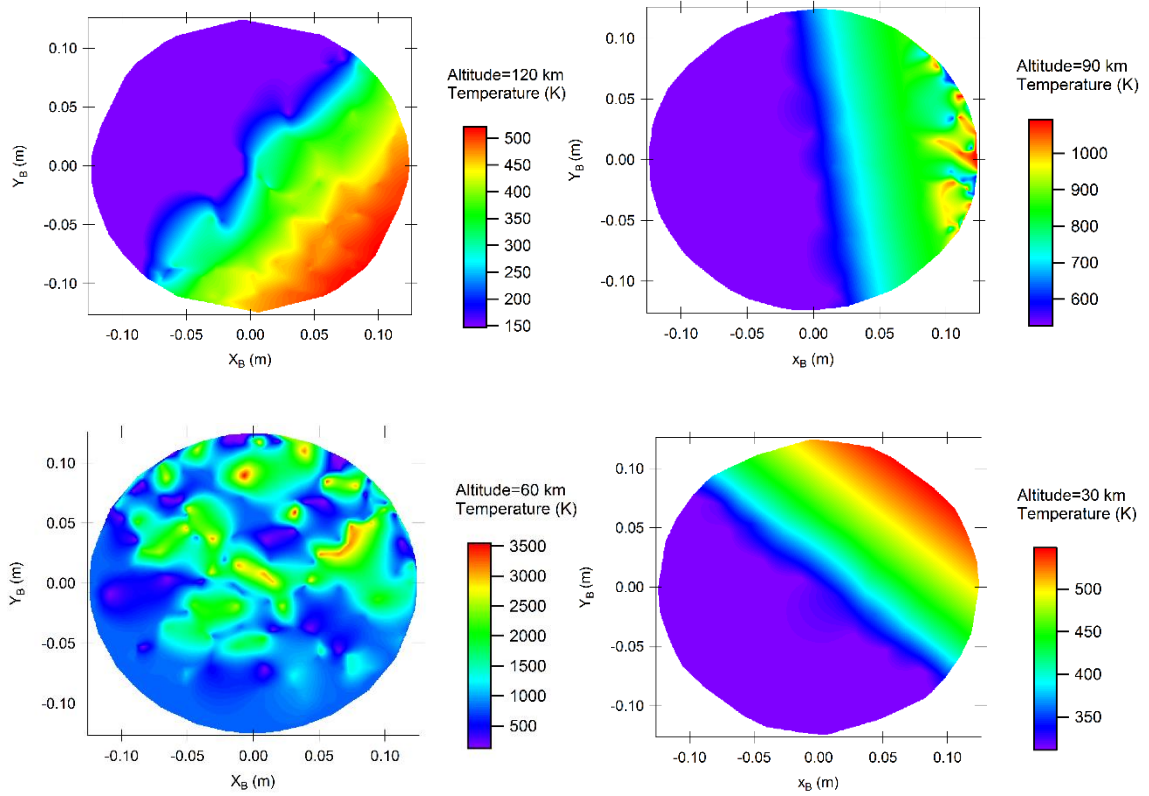


Figure 10.20 – Surface CP distribution tank in 6DOF.

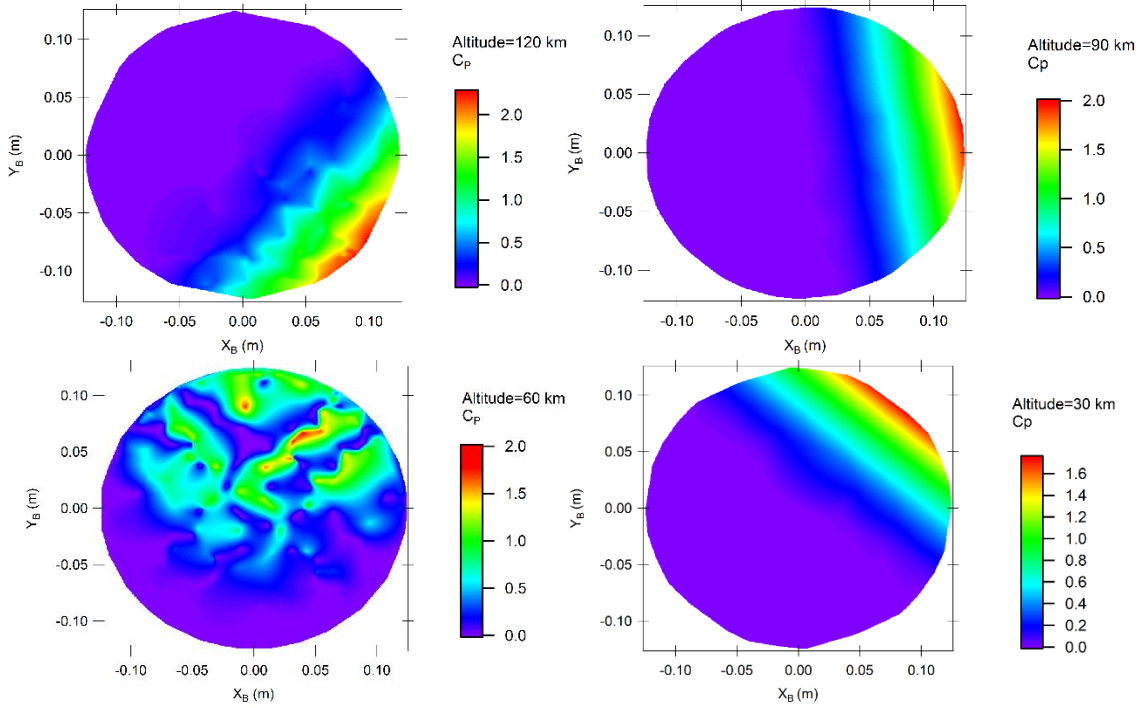


Figure 10.21 – Surface temperature distribution tank at 1200RPM.

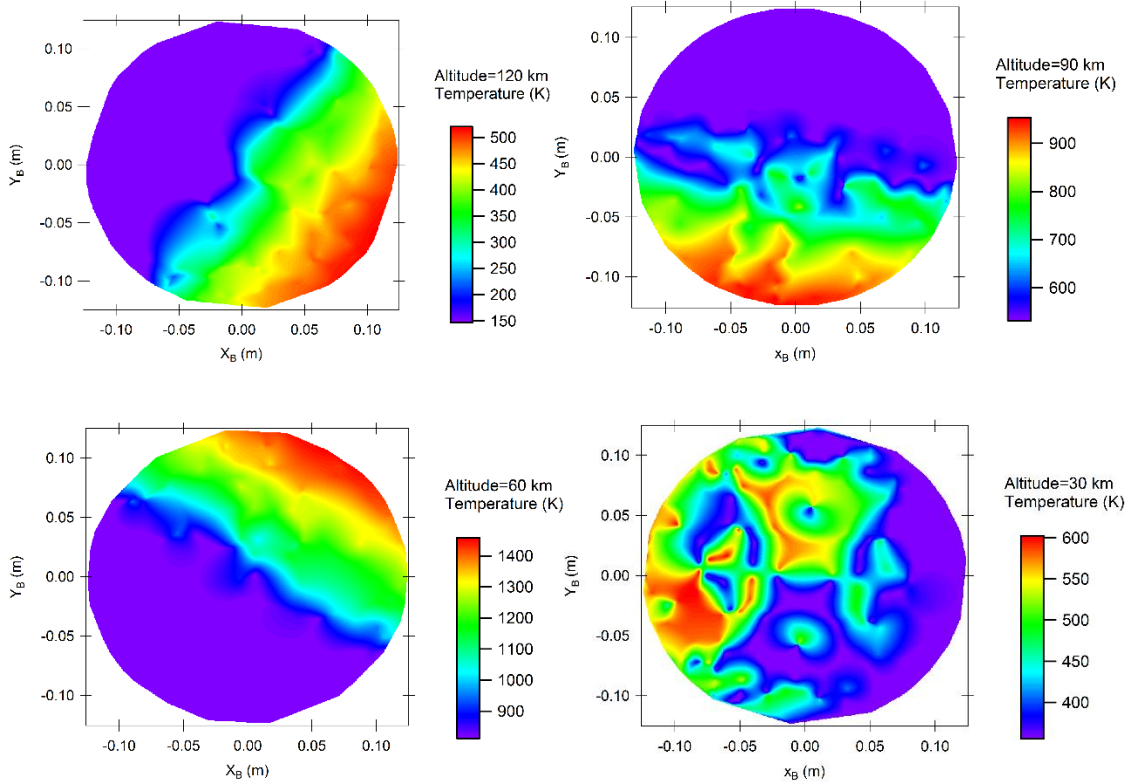


Figure 10.22 – Surface CP distribution tank at 1200RPM.

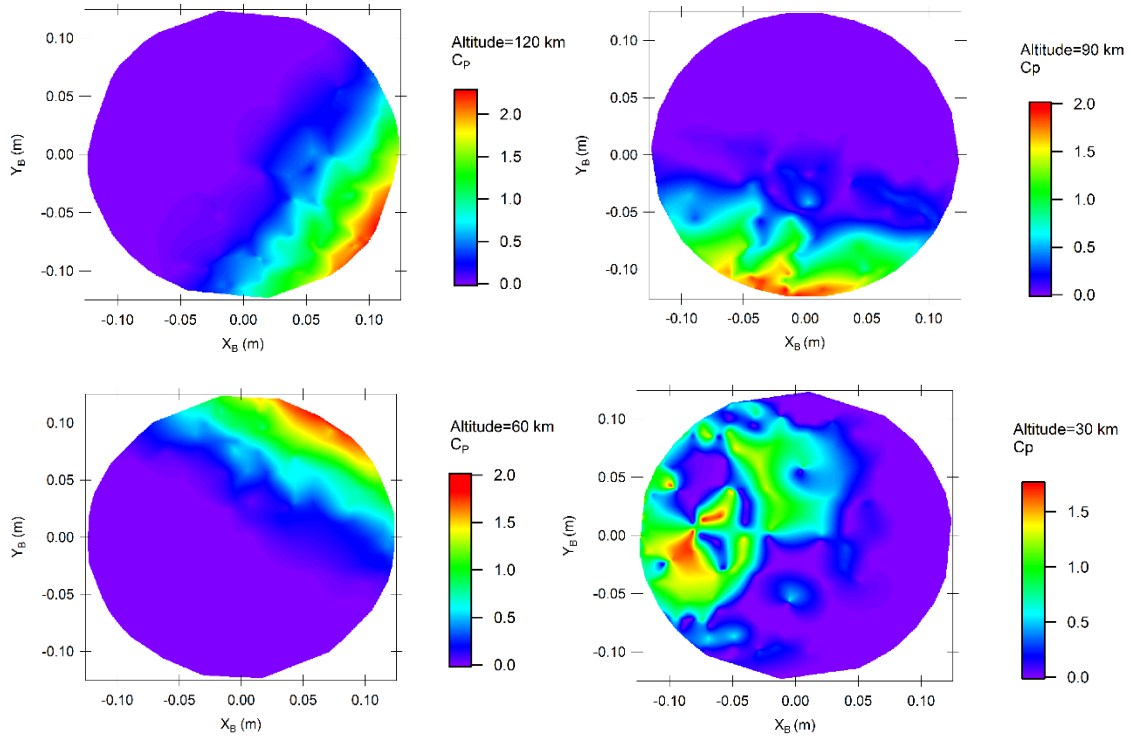


Figure 10.23 – Surface temperature distribution tank at -1200RPM.

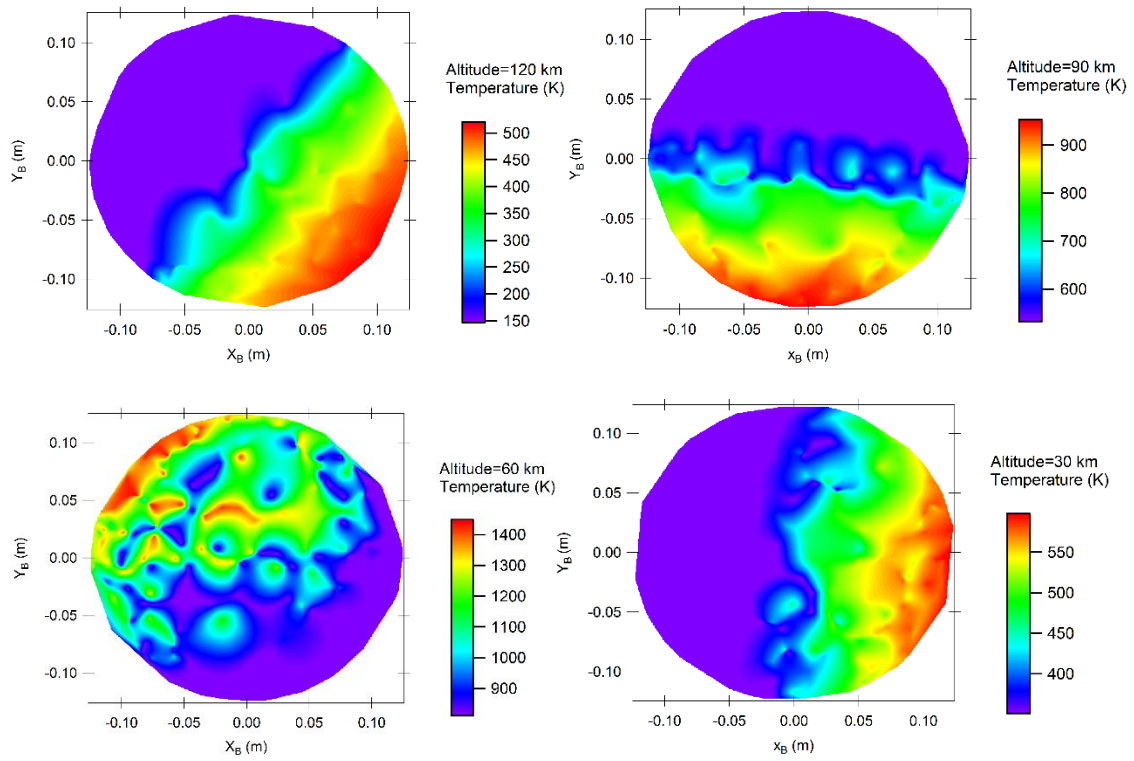
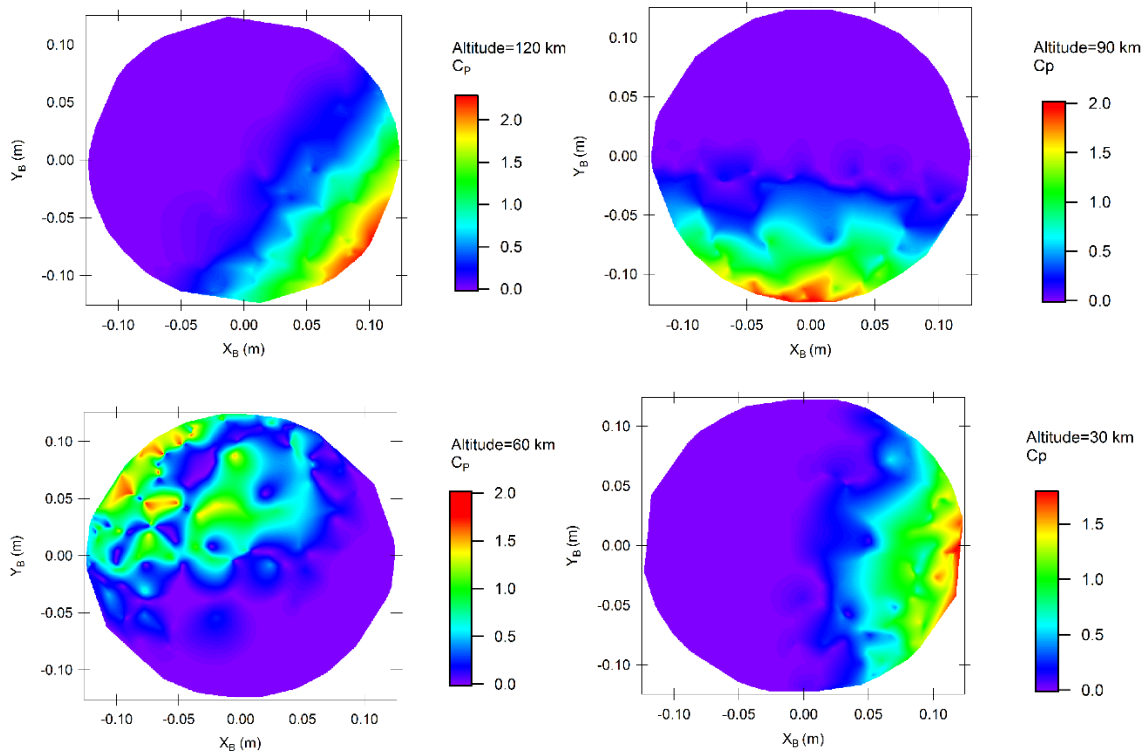


Figure 10.24 – Surface CP distribution tank at -1200RPM.



10.5. Results of reentry tank with different materials

To determine the fragmentation conditions and survivability of the tank with different materials, the spherical tank is simulated in a 3DOF reentry with the same initial conditions shown in Table 10.2, implementing the materials from Table 10.1. Because the density changes, the mass of the sphere is increased as a function of the density and it reduces the effect of the aerodynamic forces, generating a higher reentry time. The four materials that can survive are the Graphite Epoxy, Aluminum, Titanium and steel. The copper tank is dismissed around 65 km (see figure 10.25). The other materials are affected by the fragmentation, but don't reach the total ablation point. The material density affects the mass in the equations of motion and generates variations in the trajectory. One of these variations is the velocity as a function of altitude, with the mass increase, decreasing the fragment velocity at lower altitudes (figure 10.26). Due to the material properties, the ablation and fragmentation process is

characterized for each fragment. At the same time, the changes in the surface area, moment of inertia and aerodynamic coefficient are functions of the mass and geometry of the fragment and it generates a characteristic trajectory for each material.

Figure 10.25 – Tank altitude vs time reentry with different materials.

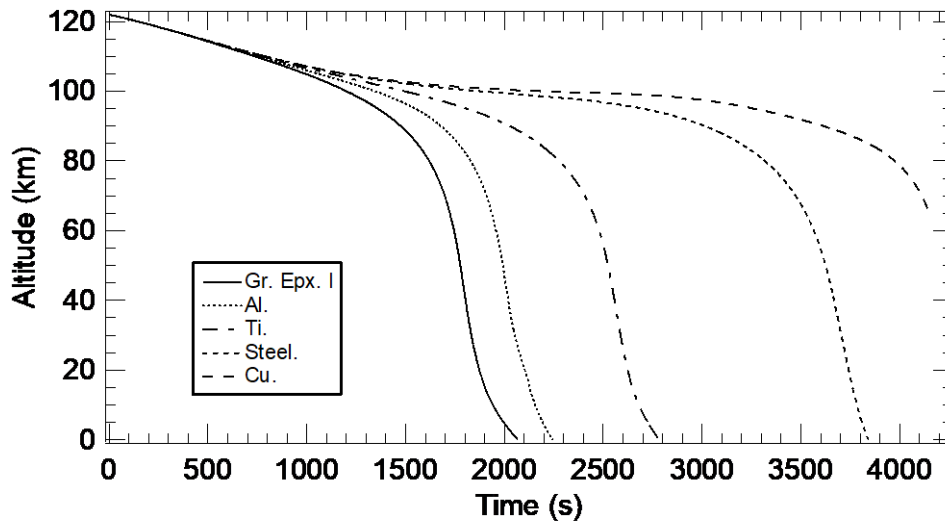
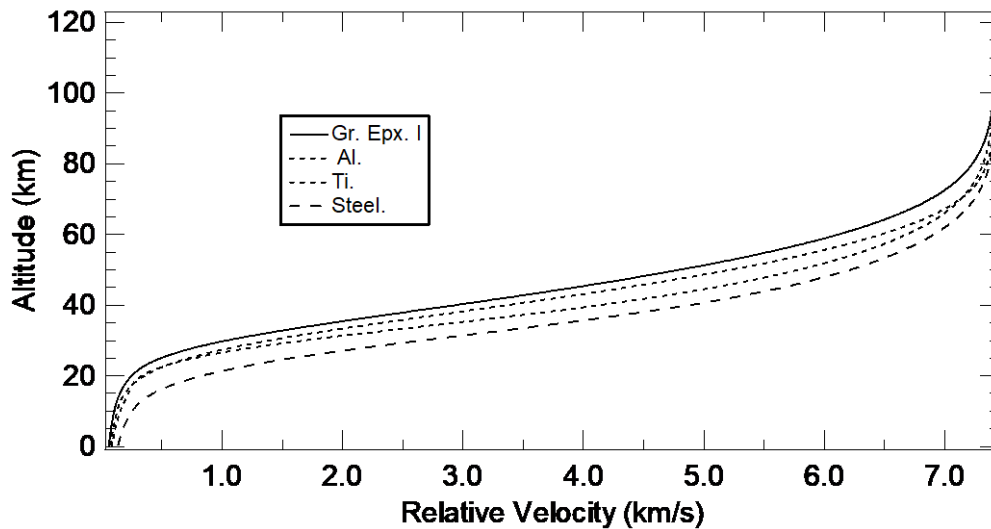


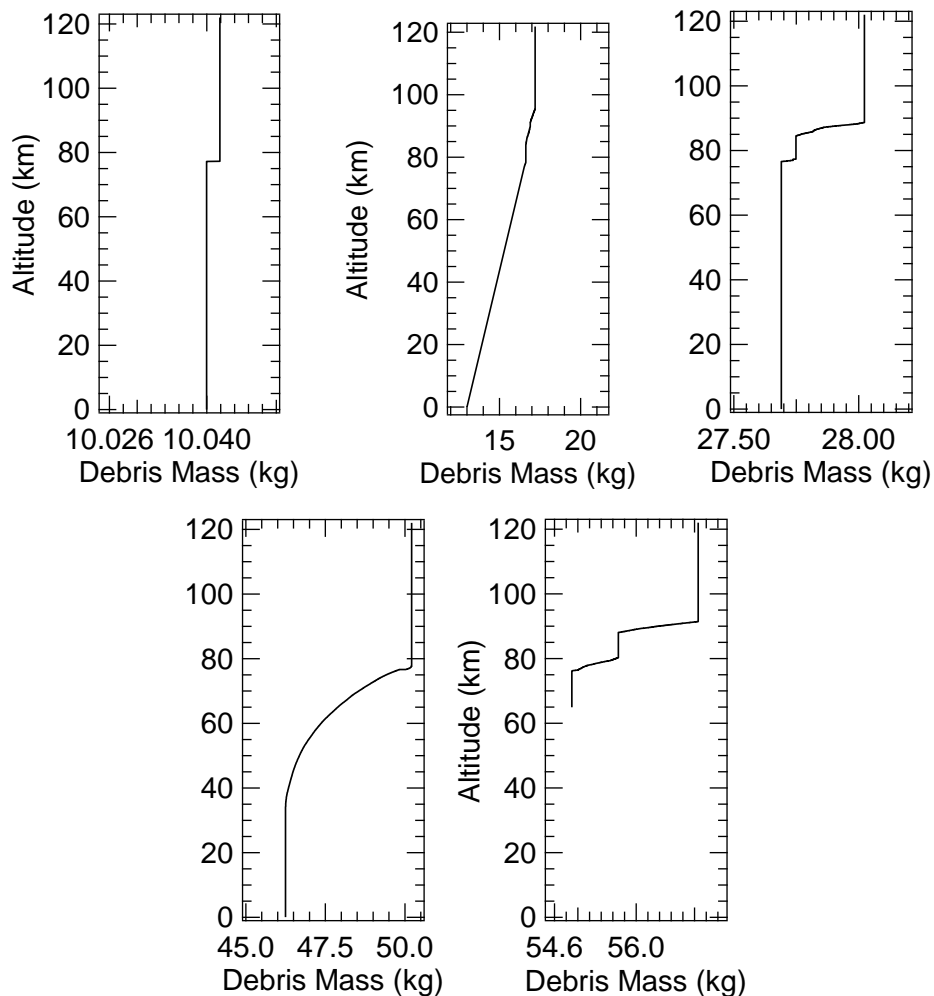
Figure 10.26 – Tank altitude vs velocity reentry with survival materials.



The loss of mass is related to the surface heat storage and the material thermo-mechanical properties. For the Graphite Epoxy only, one fragmentation by

ablation is presented along with the trajectory. Materials like aluminum and copper present fragmentation before 90 km of altitude. The copper is demised due to the heat transfer in the material and the lowest point of melted. The steel presents a mass loss from the 80 km to 30 km of altitude and loss of 4 kg of mass. Titanium presents multiple fragmentations but don't pass 1 kg of mass losses. Augmentation in the final mass is proportional to the increment in the energy at the impact, increasing the risk. In figure 10.27 it is possible to see the fragmentation and mass losses of the tanks during the reentry. Results of survival in the Graphite Epoxy I, Aluminum and Titanium tanks were reported in Park and Park (2017).

Figure 10.27 – Tank altitude vs mass, from left to right: Graphite, Aluminum, Titanium, Steel and Copper.



11 LEO (LOW EARTH ORBIT) DEBRIS REENTRY ANALYSIS

In the previous chapter, the code was validated with results of the trajectory propagation of a spherical tank using different materials and angular velocities. Results show good agreement with the data reported from Lips et al. (2005); Park and Park (2017). Now, the main goal is to observe the effects of the Magnus force in the trajectory, changes in the landing zone, survival probability, kinetic energy and survival mass. In other words, the requirements for the Re-entry Casualty Risk Analysis (RCRA) according to the Space Debris Mitigation Compliance Verification (SDMCV) (ESA; 2015).

11.1. Re-entry rotational spherical tanks analysis

The LEO is selected for propagating the debris tanks trajectories, because the objects in de-orbit have 100% of probability of reentry. LEO, is also the orbit with the highest population of bodies in the disposal phase (WEN et al, 2018; KLINKRAD, 2010). In LEO the smallest debris with high energy are located, resulting from collisions and explosions. The smaller debris dimension varies from 1mm to 100mm (WEN et al, 2018). According to Klinkrad (2010), more than 194 breakups are detected in this region, where 42% are from propellant malfunctions and explosions; 35% are controlled explosions; 0.1% resulted from collisions; 4.9% came from battery explosions and 17.9% are unknown. The LEO region with the highest density of debris is located in inclinations from 60° to 100° (WEN et al, 2018; ESA, 2015; KLINKRAD, 2010). The principal bodies without break-ups are aluminum cylinders and metallic spheres made of sodium potassium alloys (KLINKRAD, 2010). According to ESA, to simulate the orbit of the debris and reentry propagation, it is recommended the implementation of the atmospheric model NRLMSISE-00, due to the 15% of uncertainty in the density value in mean range time, a gravitational model including J2, J3, J4, J15 and J22, uncertainty in drag around 10%, minimum simulations in 3DOF and initial altitudes between 120 km and 130 km (ESA, 2015). It is important to remember that the legal principles that govern the space activities are

registered in the: “Treaty on Principles Governing the Activities of States in the Exploration and Use of the Outer Space, including the Moon and other Celestial Bodies” (UN, 2017).

To determine and observe the influence of the Magnus force in the reentry bodies, three materials are selected; aluminum alloy, due to its application in many aerospace structures; titanium and graphite epoxy I, due to their highest melting point and specific heat. Generally, these materials are used in tanks and rocket motors. It is also interesting to compare the results of the propagations with the ones presented by Park and Park (2017). Three rotational velocities are selected to observe the influence of the angular motion in the dynamics, trajectory and survivability of the debris. The initial Euler angles are 0° , 28° and 91° , respectively, to align the X_B -axis with the velocity vector at the initial time. Table 11.1 shows the six geometries of spherical tanks to analyze.

Table 11.1 – Spherical tank dimensions.

Outside radius (m)	Internal radius (m)
0.5	0.462
0.25	0.209
0.125	0.075
0.1	0.05
0.05	0.025
0.025	0.0125

Source: Adapted from Park and Park (2017).

According to the SDMCV for the RCRA, the results of the simulations represent graphically the evolution of the altitude as a function of time; the velocity and mass as a function of the altitude; the latitude and longitude of the trajectory, the possible impact point and the final kinetic energy. The first propagations were made in 6DOF, without initial angular velocity. In the other propagations it is changed the direction of the angular velocity between the three mean axes of the body. Objects like spherical balls generally rotate below 1800 RPM’s (BRIGGS, 1959).

11.1.1. Reentry of spherical tanks of Graphite Epoxy – I

In this subsection it is presented the results of the reentry propagation for six spherical tanks with variations in radius, under four different reentry initial conditions. Initially, it is analyzed the decay as a function of time. In figures 11.1 to 11.4 it is showed the altitude as a function of time for each tank. In the case of the reentry without angular velocity (Figure 11.1), it is observed that the smaller debris reentry in shorter times, compared to the debris with higher mass. The results are in agreement with the data reported by Park and Park (2017). It is observed that the highest mass generates lower decelerations, decreasing the influence of the aerodynamic forces and delaying the reentry.

When the initial angular velocity is applied, it is observed an increase in the time of flight (Figures 11.2, 11.3 and 11.4), because the Magnus force reduces the vertical velocity, increasing the aerodynamic force in the vertical and lateral directions. Spheres with radius lower than 10 cm presented a significant increase in the time of flight, due to the lower mass, because it increments the influence of drag and the aerodynamic forces, reducing the velocity, it is possible to see this behavior in altitudes lower than 20 km, when the trajectory as a function of time presents a lateral displacement, reducing the decay. Comparing figures 11.1 to 11.4, it is observed significant changes in altitudes lower than 20 km, due to the increment in the air density, proportional to the influence of the winds, aerodynamic forces and the Magnus effect in the trajectory. In the case of trajectories with angular velocities in Y_B , there is an increase in the time of flight due to the reduction in the vertical velocity. In the case of angular velocities in the Z_B axis, the trajectories for the debris with the highest mass show the largest times of flights due to the direction of the Magnus force, generating lateral displacement of the impact point.

Figure 11.1 – Graphite epoxy I spherical tanks reentry without initial angular velocity, altitude vs time.

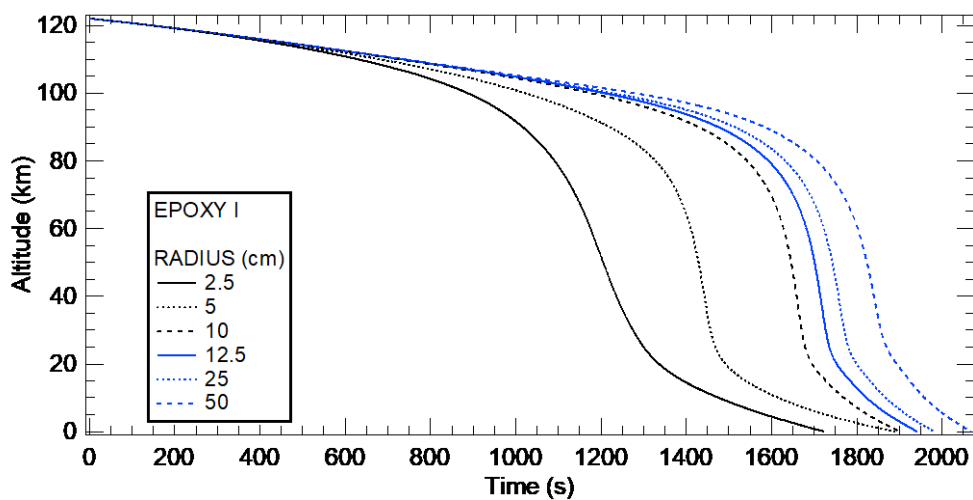


Figure 11.2 – Graphite epoxy I spherical tanks reentry $w_x=1200$ RPM, altitude vs time.

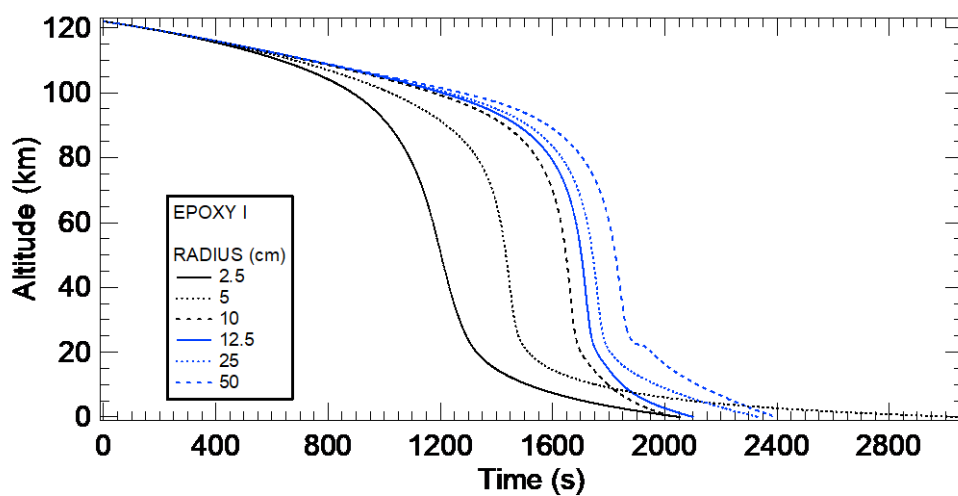


Figure 11.3 – Graphite epoxy I spherical tanks reentry $w_y=1200$ RPM, altitude vs time.

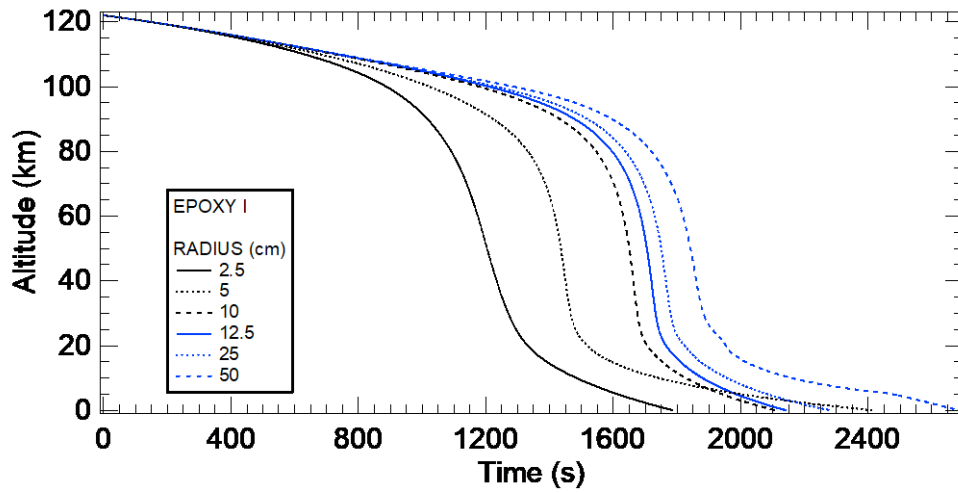
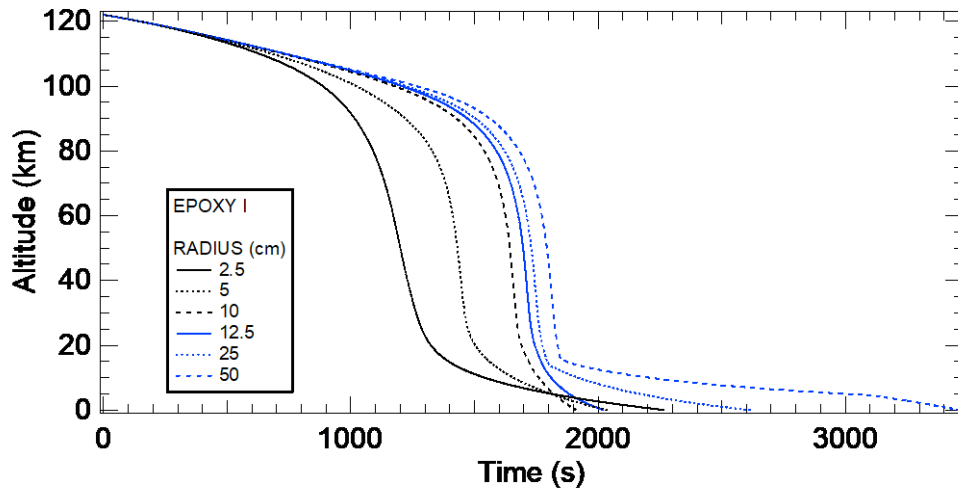


Figure 11.4– Graphite epoxy I spherical tanks reentry $w_z=1200$ RPM, altitude vs time.



The velocities as a function of altitudes are showed in figures 11.5 to 11.9. For spheres with a radius of 2.5 cm and 5 cm it is observed that the velocity decays faster than the other tanks, or have the largest deceleration due to the low mass that increases the aerodynamic forces. When they have a mean altitude of 40 km the increment of the air density generates the aero-breaking. In the case of tanks with 10 cm or larger, the breaking is observed at altitudes around 20 km and they don't show significant changes in the velocity profiles. Tanks with

higher masses show an increase in the relative velocity as a function of the altitude. In the final approach all the tanks present velocities inferior to 100 m/s. The influence of rotation and Magnus effect show significant changes in the relative velocity of the spherical tank of 50 cm at 6 km of altitude, incrementing the velocity at the impact.

Figure 11.5 – Graphite epoxy I spherical tanks reentry without initial angular velocity, altitude vs relative velocity.

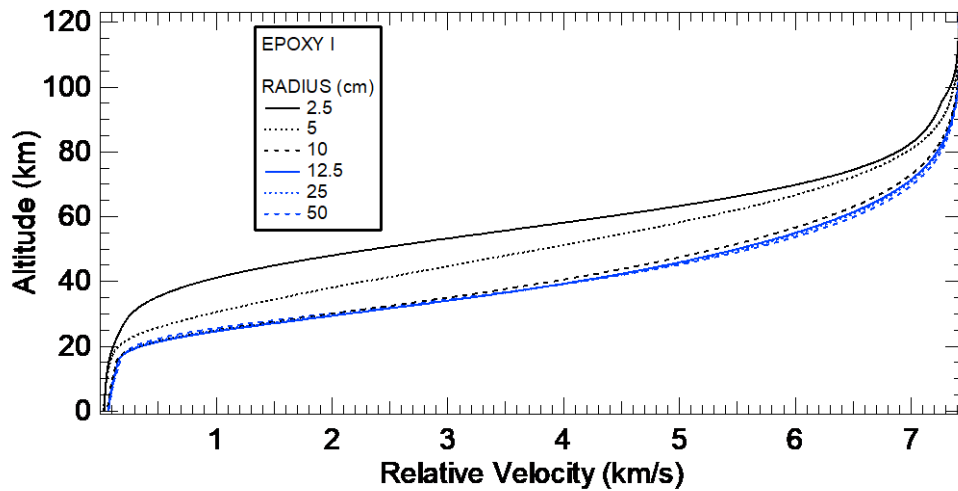


Figure 11.6 – Graphite epoxy I spherical tanks reentry $w_x=1200$ RPM, altitude vs relative velocity.

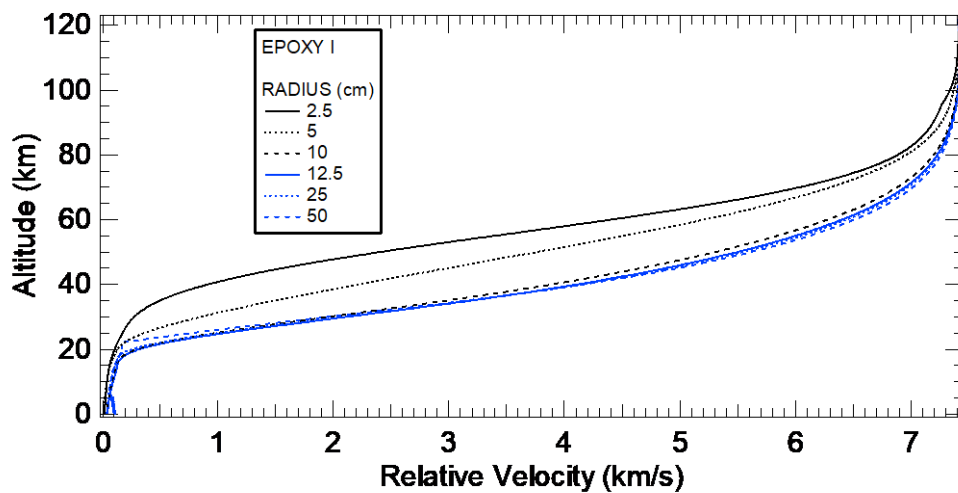


Figure 11.7 – Graphite epoxy I spherical tanks reentry $w_y=1200$ RPM, altitude vs relative velocity.

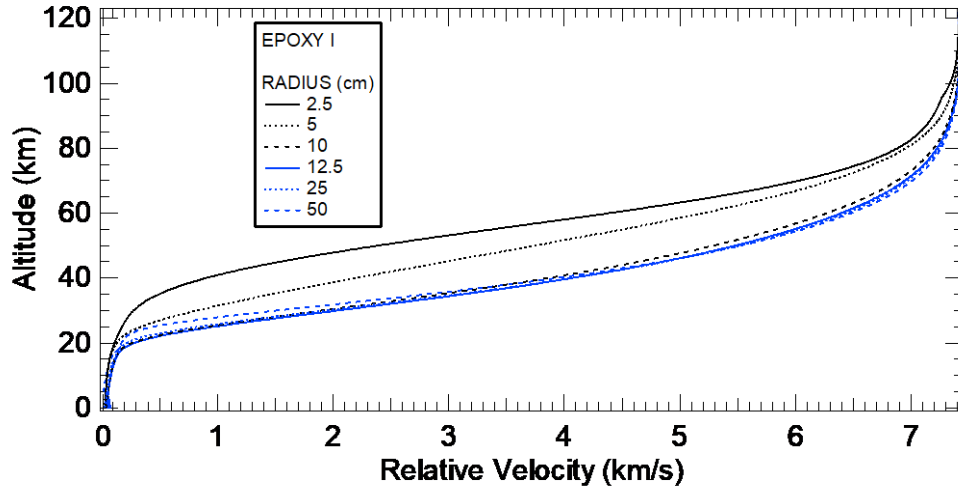
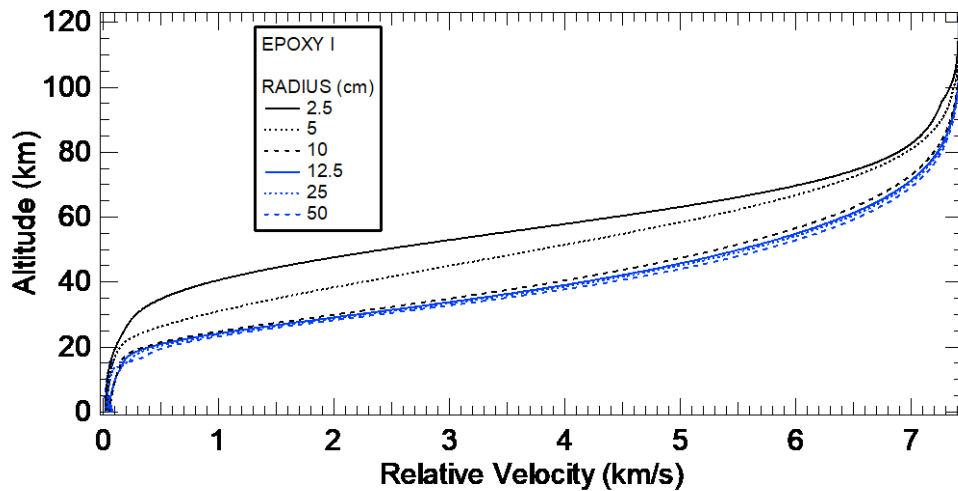


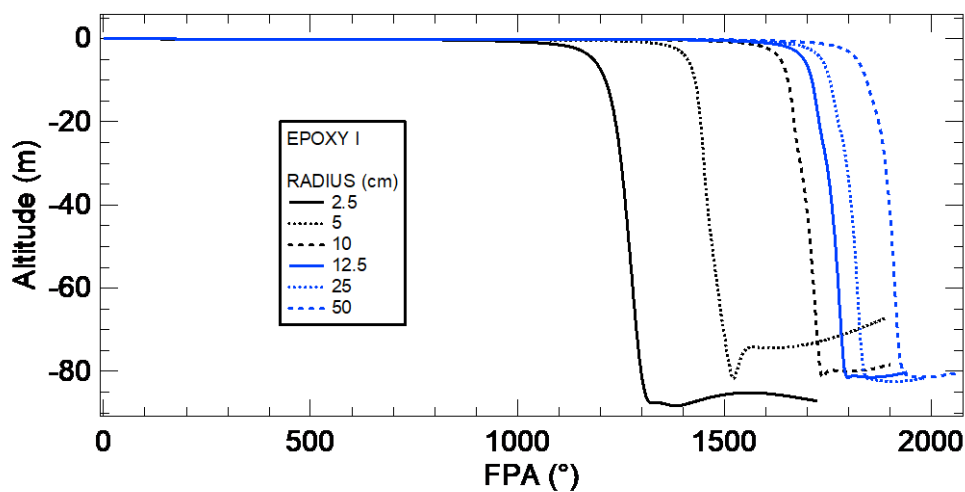
Figure 11.8 – Graphite epoxy I spherical tanks reentry $w_z=1200$ RPM, altitude vs relative velocity.



Due to the highest deceleration of the lower mass spheres, they presented an increase in the vertical flight, with FPA inferior to -80° . In the final approach, the FPA are around -90° indicating a vertical flight in the lower atmosphere, the condition is represented by a linear function (Figure 11.9). When angular velocities are applied, the FPA decays, but rapidly increases when the debris is below 20 km of altitude, due to the Magnus effect. This effect reduces the vertical component of the velocity and the lateral component dominates the

trajectory, which increases the FPA value. In other words, the Magnus effect generates a lateral reentry and increases the time (Figures 11.10 to 11.12). This behavior is present in all trajectories with angular velocities. Increases of the FPA are more significant in trajectories for spheres of 2.5 and 5 cm, due to the initial fast decay and the influence of the aerodynamic forces in the dynamic equations.

Figure 11.9 - Graphite epoxy I spherical tanks reentry without initial angular velocity, FPA vs Time.



The reentry tanks with the largest dimensions present a higher velocity during the final approach, between 20 km to 0 km of altitude. At the same time, they have a larger surface area, which implies in an increase in the influence of the aerodynamic forces. The Magnus force vector is orthogonal and proportional to the rotational body velocity and to the relative wind velocity. The increment of the body radius, the angular and translational velocities and atmospheric density at low altitudes, generates an increase in the Magnus force. This behavior is observed in the FPA at the end of the trajectories, for spherical tanks of 25 cm and 50 cm. The Magnus forces change its direction as a function of the angular and translational velocity of the body, generating variations in the direction of the acceleration and velocity. This is observed in the oscillations of

the FPA at the final approach, for the tanks with rotations, as shown in figures 11.10, 11.11 and 11.12.

Figure 11.10 - Graphite epoxy I spherical tanks reentry $w_x=1200$ RPM, FPA vs Time.

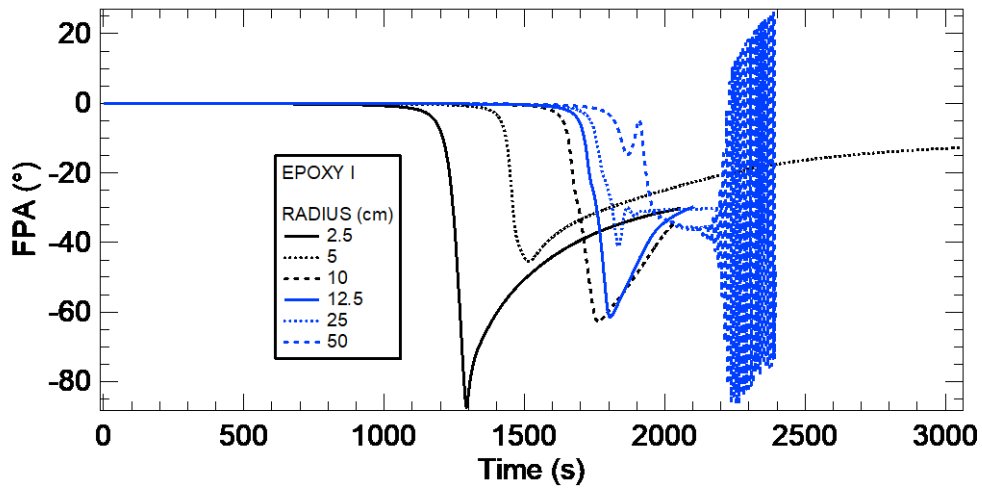


Figure 11.11 - Graphite epoxy I spherical tanks reentry $w_y=1200$ RPM, FPA vs Time.

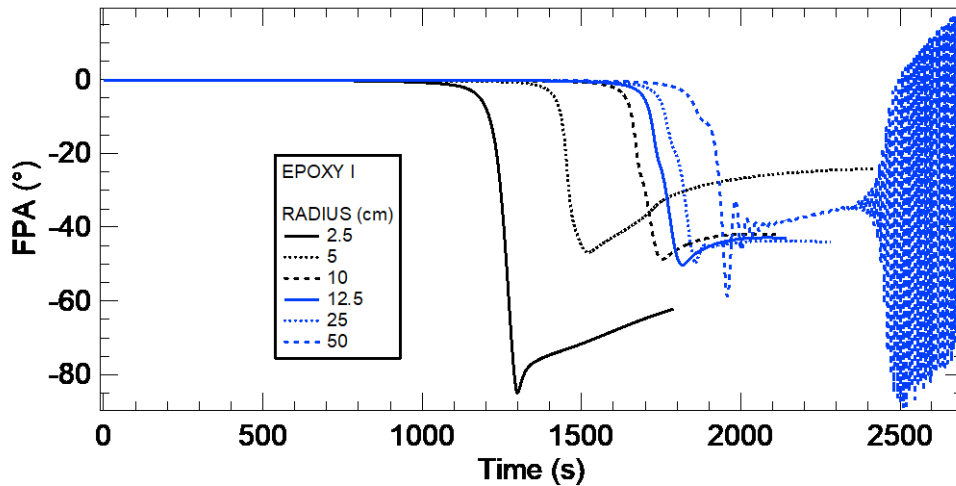
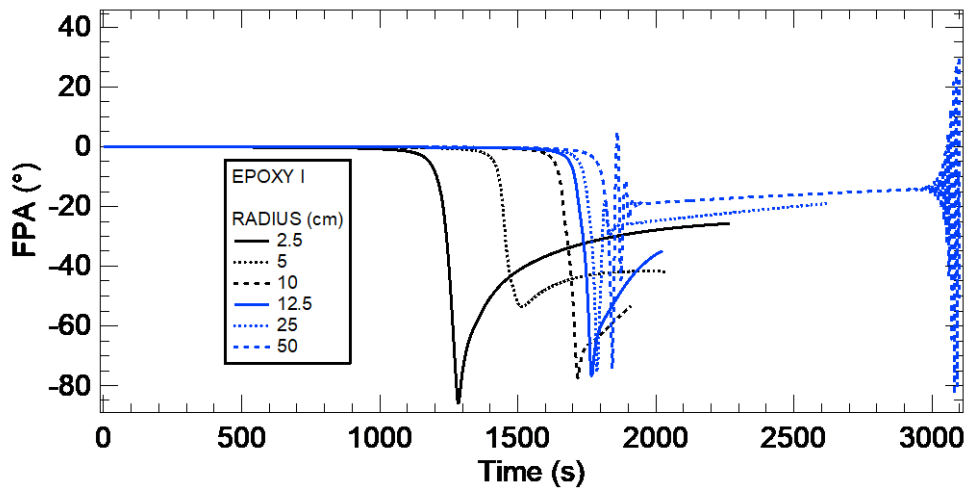


Figure 11.12 - Graphite epoxy I spherical tanks reentry $w_z=1200$ RPM, FPA vs Time.



The kinetic energy decays during the reentry maneuver due to the altitude and velocity losses from the aerodynamic forces made by the density increment, as shown in figure 11.13. However, due to the order of magnitude, it's not possible to observe the final energy in the figure, which is the most important value to analyze the risk during the reentry. At the end of the section, in table 11.2, it is presented the final energy for the reentry of each trajectory.

Figure 11.13 - Graphite epoxy I spherical tanks reentry, Energy vs Time.

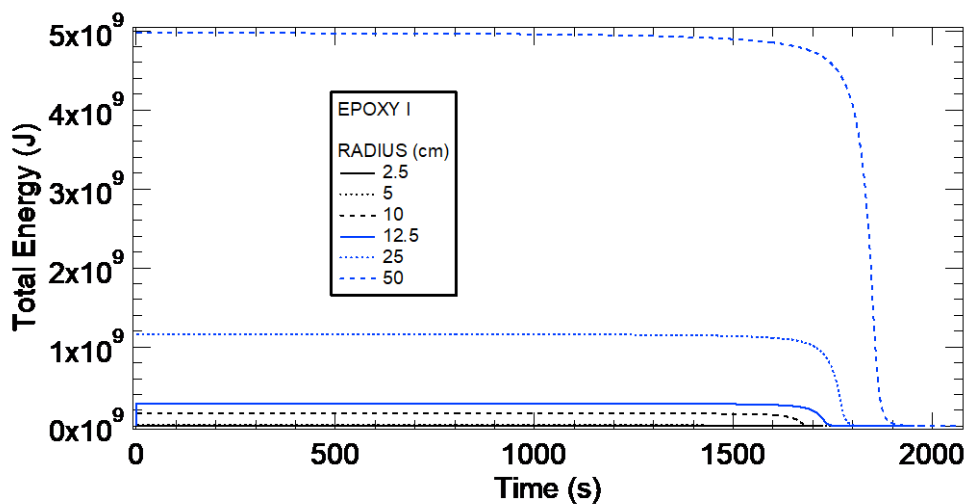
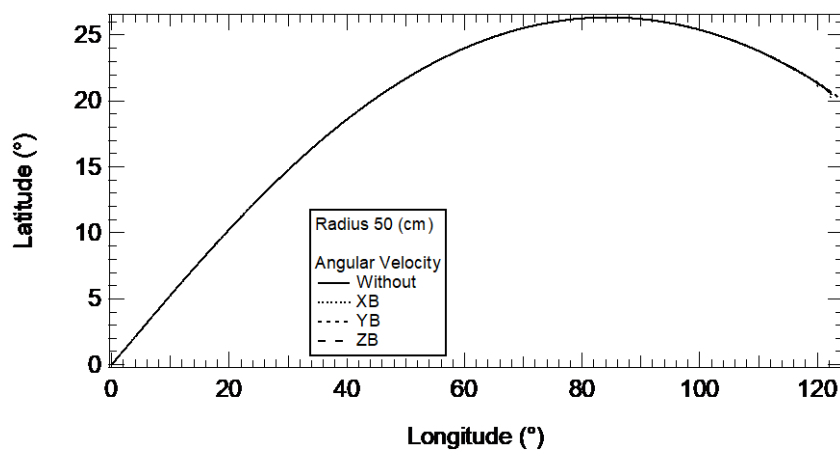


Figure 11.14 describes a general trajectory for the debris. To observe the possible landing zones, the trajectories are compared for each tank. Initially the

trajectories in the four reentry cases have the same behavior, but, at 20 km of altitude, with the increment in the air density, the Magnus effect and winds dominate the trajectory and generate the difference of position in the final time of flight. Trajectories without angular velocity don't show the significant deviation from the mean trajectory, but debris with rotation present important changes in the position at the landing zone, due to the influence of the aerodynamic force. See figures 11.15 to 11.20.

Figure 11.14 - Graphite epoxy I spherical tanks reentry trajectory.



In the cases where the angular velocity was assumed to be in the X_B direction, trajectories were closer to the mean trajectory without angular velocity. In these cases, the angular velocity was applied in the same axis of the initial velocity direction, and the Magnus force doesn't present significant deviation in the trajectories. When the angular velocity was applied in the Y_B and Z_B directions, the changes in longitude and latitude were more visible than the X_B rotation, because the resulting Magnus force is applied lateral and vertical to the body. During the final approach, the wind direction influences the trajectory, especially for small bodies. Trajectories with spheres higher than 2.5 cm present reduction in the latitude and deviation to the south-west direction for angular velocities in X_B , an increase in the longitude in south-east direction for angular velocities in Y_B , as well as a reduction in the longitude with a deviation in west-north when the angular velocity was applied in the Z_B direction (see figures 11.15 to 11.20).

In the case of 2.5 cm, the trajectories with rotation in YB and ZB are deviated to the south-west direction due to the Magnus and the wind influence.

According to the Earth radius, 1° in Latitude and/or Longitude is equivalent to 111.3195 km. It is important to determine the possible landing zones for the risk analysis. In this case, due to the Magnus influence, it were selected the maximum and minimums in latitude and longitude to determine the landing area for each spherical tank. In the case of the sphere of 2.5 cm, the possible landing zone is an area around 15.6 km in the north – south (N-S) direction and around 33.4 km in the west – east (W-E) direction (see figure 11.15). In the case of the sphere of 5 cm the differences were 44.5 km in N-S and 77.9 km in W-E direction (Figure 11.16). The 10 cm spheres present an area around 89 km in the W-E and 18 in N-S (Figure 11.17). For the 12.5 cm tank the values are 110 km in W-E and 22 km in the N-S, see Figure 11.18. The tank of 25 cm present an impact area of 200 km in W-E and 27 in N-S, and the tank of 50 cm have a possible landing area of around 440 km in the W-E and 88 km in N-S (figures 11.19 and 11.20), which means that the increase of the debris mass generates an increase in the displacement and in the impact area.

Figure 11.15 – Survival Graphite epoxy I 2.5 cm tank, impact zone.

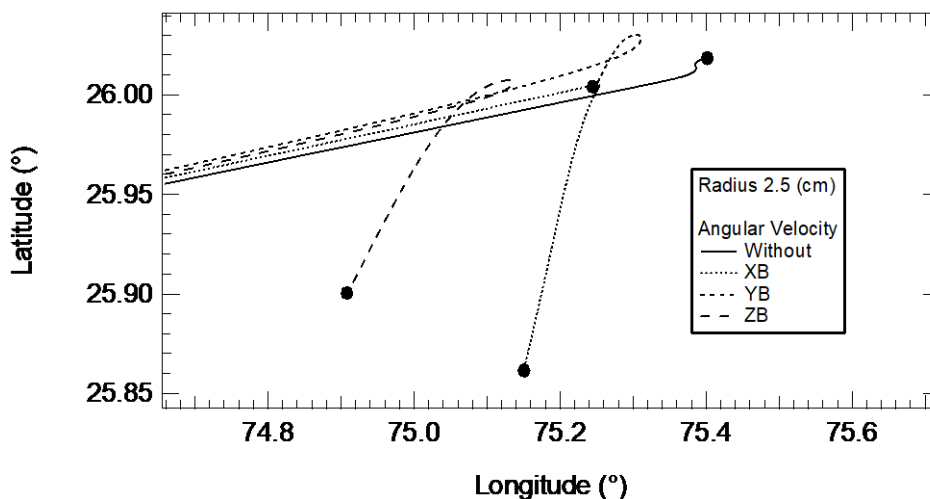


Figure 11.16 – Survival Graphite epoxy I 5 cm tank, impact zone.

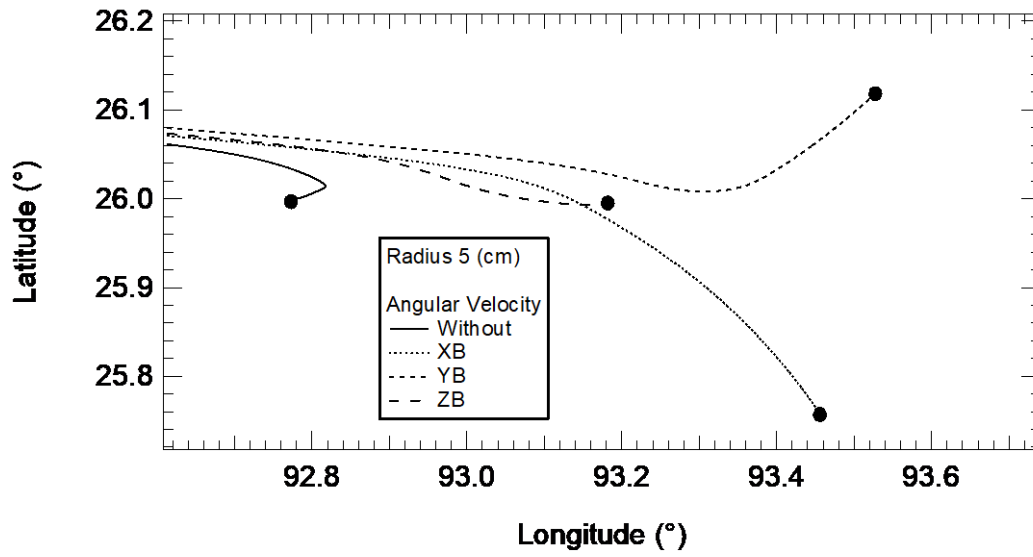


Figure 11.17 – Survival Graphite epoxy I 10 cm tank, impact zone.

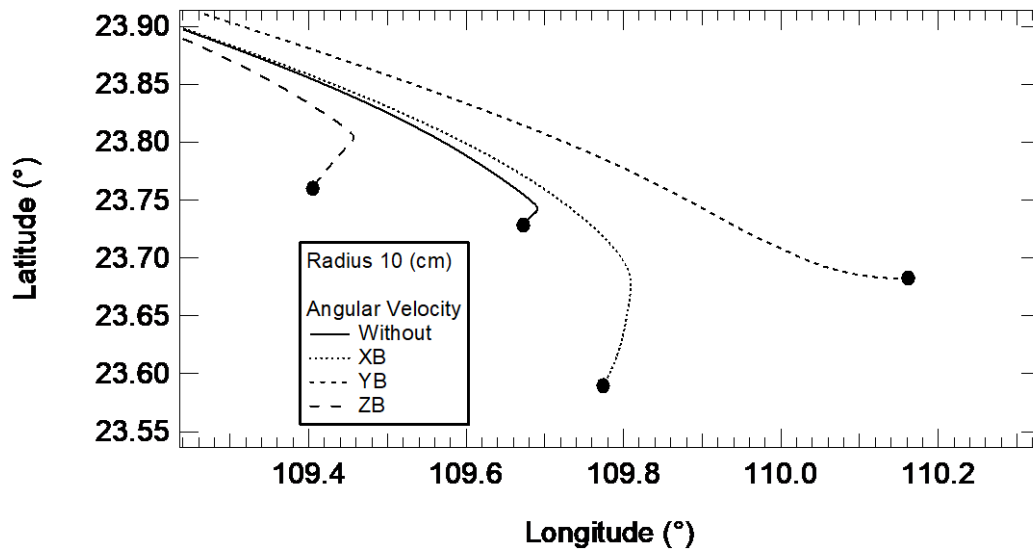


Figure 11.18 – Survival Graphite epoxy I 12.5 cm tank, impact zone.

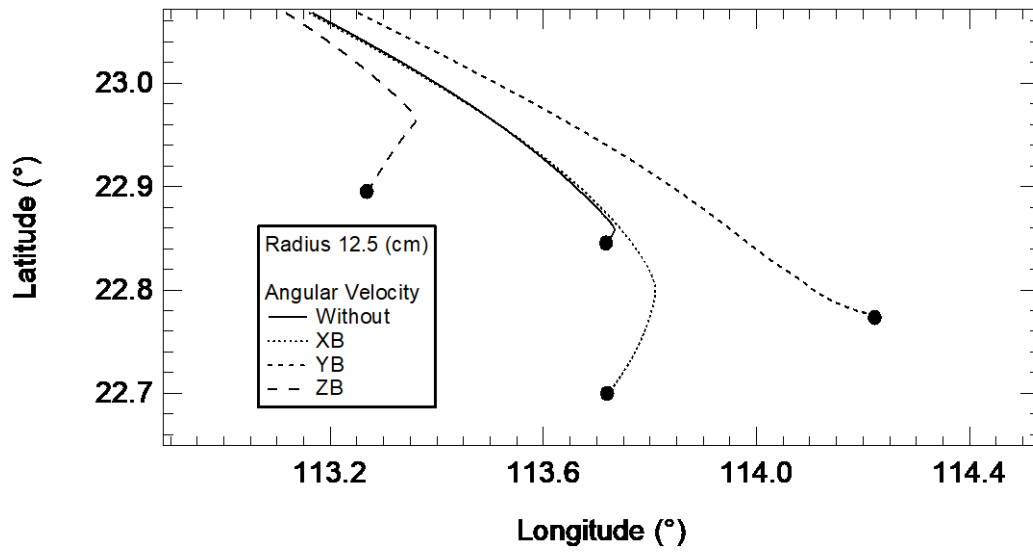


Figure 11.19 – Survival Graphite epoxy I 25 cm tank, impact zone.

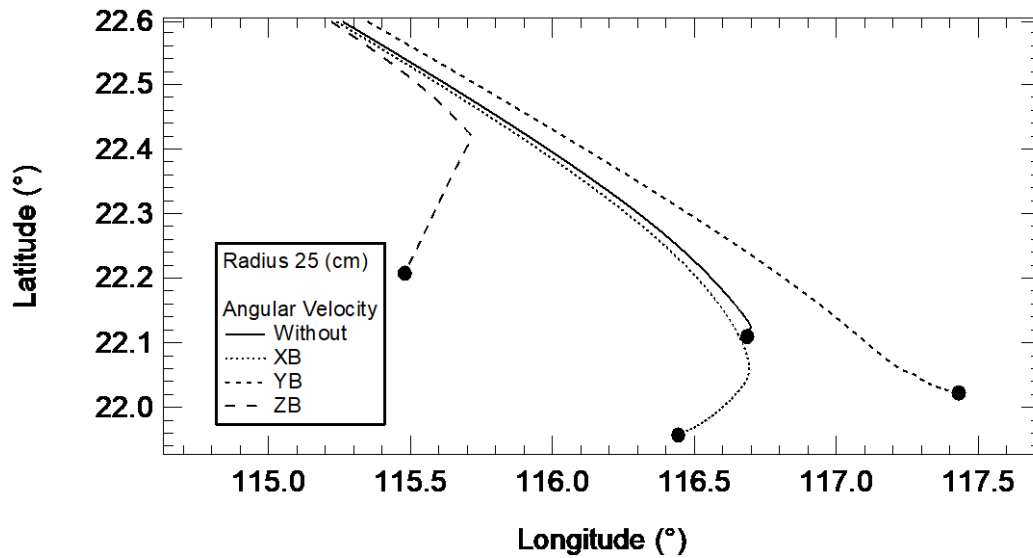
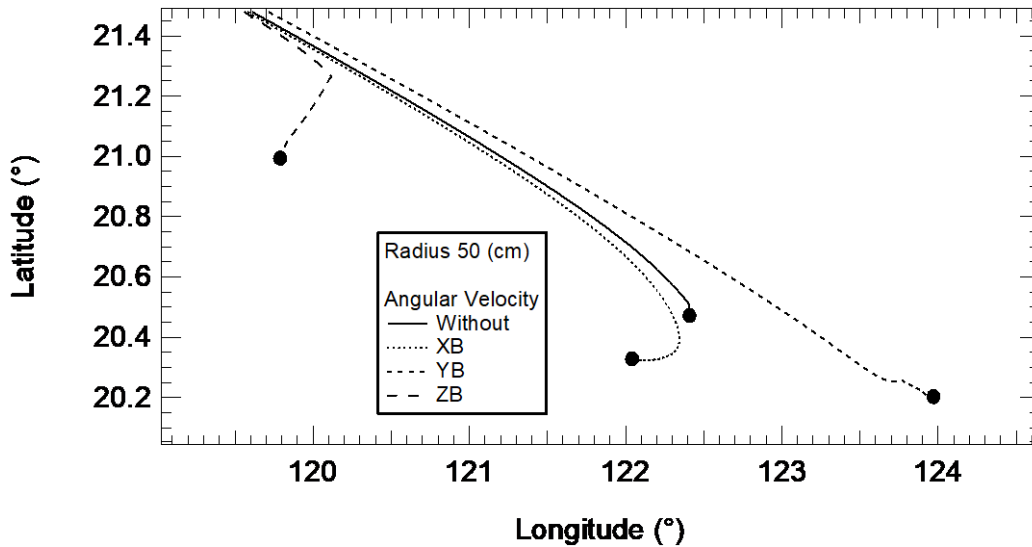


Figure 11.20 – Survival Graphite epoxy I 50 cm tank, impact zone.



The final energy of the trajectories at the impact time is presented in table 11.2. All the simulated debris with Graphite –Epoxy I survived the reentry trajectory and the impact energies are superior to 15 J, so they are a risk for the population. The final kinetic energy is proportional to the survival mass and relative velocity. Trajectories with angular velocity, with the exception of the 50 cm tank, present a lower energy, compared to survival debris without rotation. This is due to the influence of the Magnus effect, which reduces the vertical velocity and increases the deceleration, because the direction of the force is opposite to the movement. In the specific case of the 50 cm tank, the higher Magnus influence, generates variations in the acceleration, which increases the impact velocity, and the energy.

With the results obtained for the reentry cases of the spherical tanks, it is possible to say that all the reentry survival fragments are a hazard and a risk to the population. None of them presented mechanical fragmentation and the mass losses in the best cases were lower than 2%. All of this debris can survive the reentry and represents a risk.

Table 11.2 – Final Energy in Jules for spherical tanks of Epoxy I.

Radius (cm)	Without	Wx	Wy	Wz
2.5	48.3	21.6	35.7	18.5
5	278.5	70.64	198.2	253.93
10	9,997.4	5,061.9	3,827.8	8,736.6
12.5	21,628	11,084.2	7,481.7	10,384
25	96,748	36,966.7	15,726	12,129
50	447,934.5	2'311.139.5	650,629.8	886,072

11.1.2. Reentry of spherical tanks of Titanium

In the same way that it was selected and analyzed the reentries for the Graphite Epoxy - I tanks, simulations were made for the Titanium tanks, to observe the behavior of the trajectories with this material. Basically, the trajectories have the same profile of the Epoxy-I tanks trajectories, with the difference that the reentries with Titanium generate total fragmentation of the smallest bodies (tank of 2.5 cm of radius). Compared to the trajectories with Epoxy, the Titanium reentry have longer times of reentry, due to the increment of material density. See Figures 11.21 to 11.24. The Magnus influence is observed in the final approach, below 20 km of altitude, and in trajectories with initial angular velocity. In 50% of the cases, the sphere of radius 2.5 cm is fragmented by melting around 78 km of altitude, which is the same behavior reported by Park and Park (2017) in a non-rotational reentry. In this case the difference is due to the implementation of a model in 6DOF with rotation and the voxel mesh that allows a better approximation of the attitude of the debris and the fragmented material. In 3DOF, like in Park and Park (2017), only the stagnation point is taking into account to determine the fragmentation.

Figure 11.21 – Titanium spherical tanks reentry without initial angular velocity, altitude vs time.

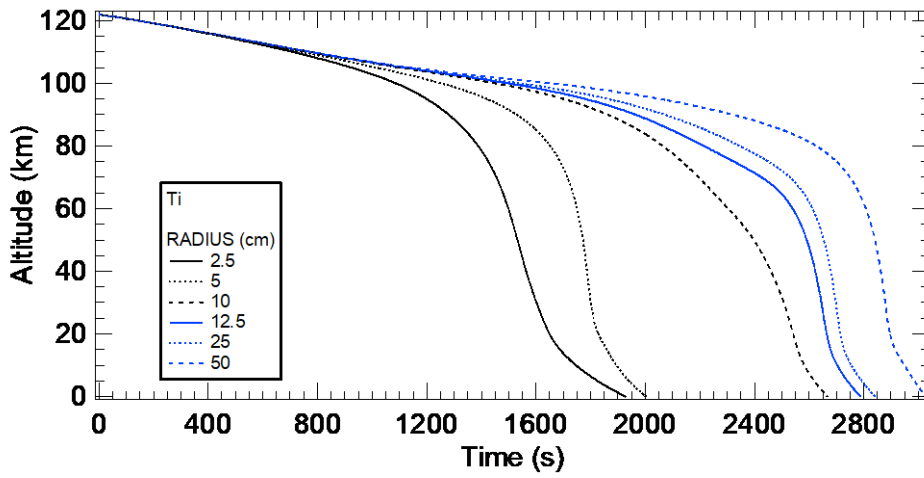


Figure 11.22 – Titanium spherical tanks reentry $w_x=1200$ RPM, altitude vs time.

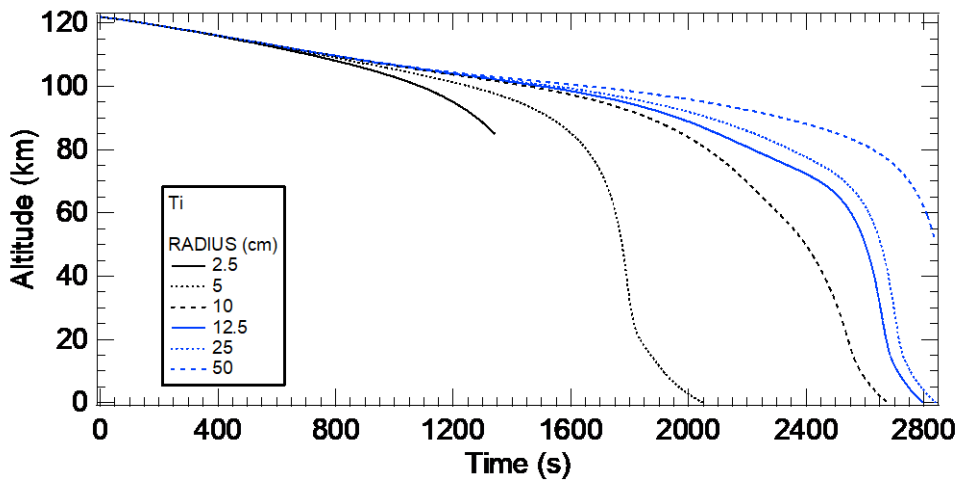


Figure 11.23 – Titanium spherical tanks reentry $w_y=1200$ RPM, altitude vs time.

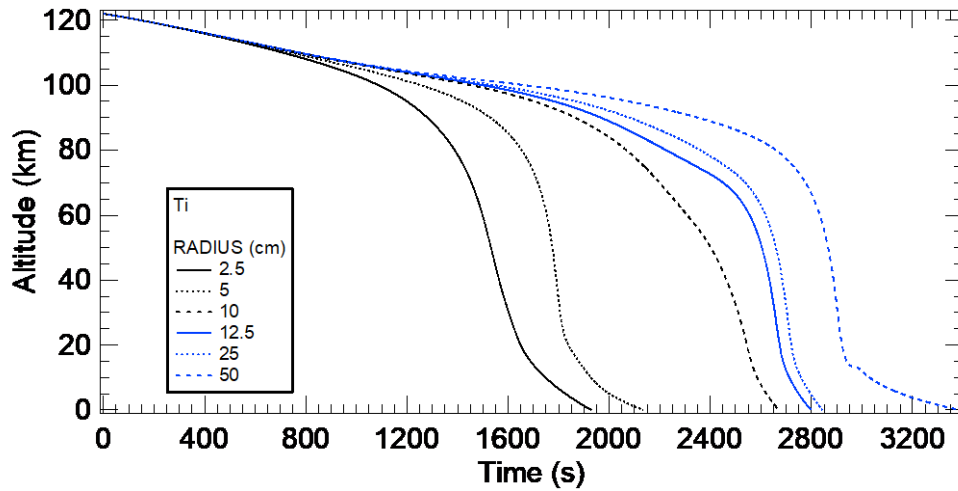
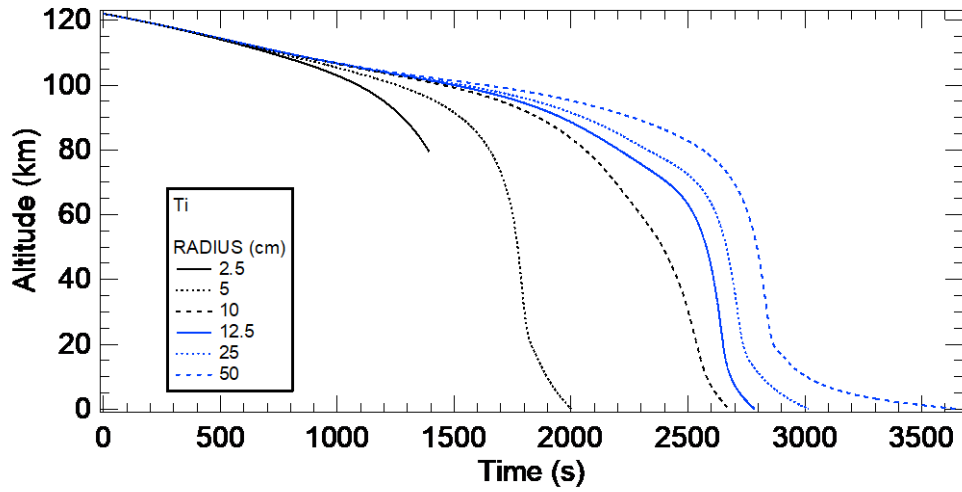


Figure 11.24 – Titanium spherical tanks reentry $w_z=1200$ RPM, altitude vs time.



In the reentry velocity as a function of the altitude (figures 11.25 to 11.28), it is observed that the melted bodies suffered a higher deceleration compared to the other bodies. This fact and the lower mass of the debris of 2.5 cm, generates a larger influence of the drag and an increase in the temperatures and heat flux to melt the particles. Higher decelerations increment the convective heat flow, and the smallest bodies do not have enough mass to survive the reentry. The entry without initial rotation is in 6DOF and the body changes the attitude along the trajectory due to the winds and torques, so influencing the angular motion. In the case of reentry without initial rotation, fragments of the tank with 2.5 cm survived the reentry due to the free rotations, in the same way that the fragment of the tank with rotation in Y_B . In the cases of rotations in X_B and Z_B the fragment of the tank cannot survive due to the velocities and heat concentration in a specific zone of the surface which generates a melting equal to the tank wall thickness.

Figure 11.25 – Titanium spherical tanks reentry without initial angular velocity, altitude vs relative velocity.

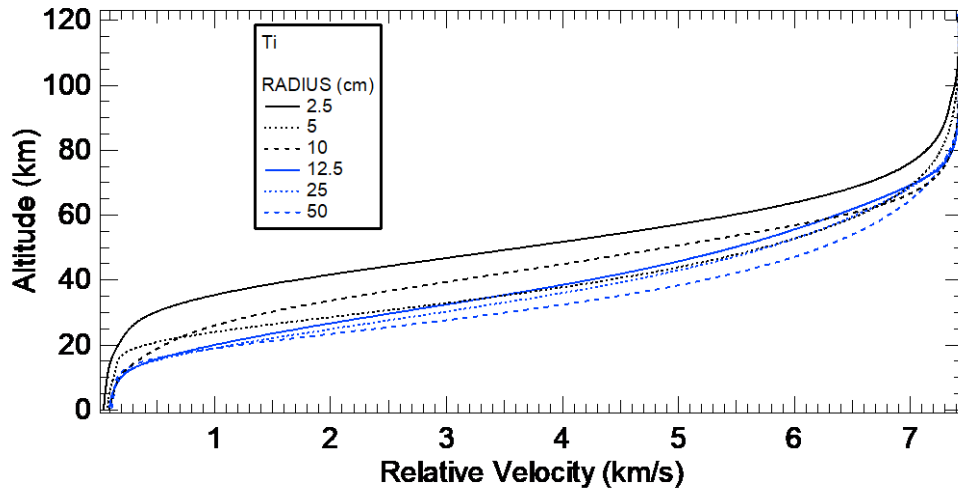


Figure 11.26 – Titanium spherical tanks reentry $\omega_x=1200$ RPM, altitude vs relative velocity.

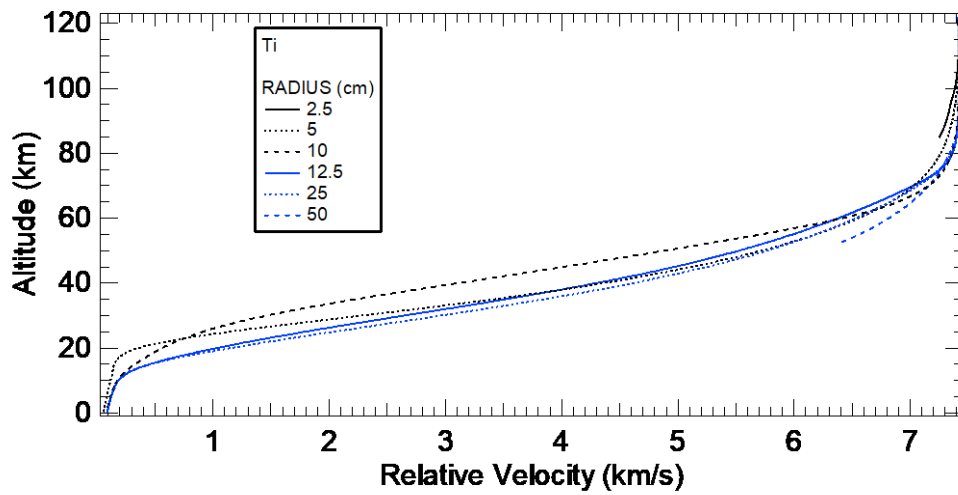


Figure 11.27 – Titanium spherical tanks reentry $w_y=1200$ RPM, altitude vs relative velocity.

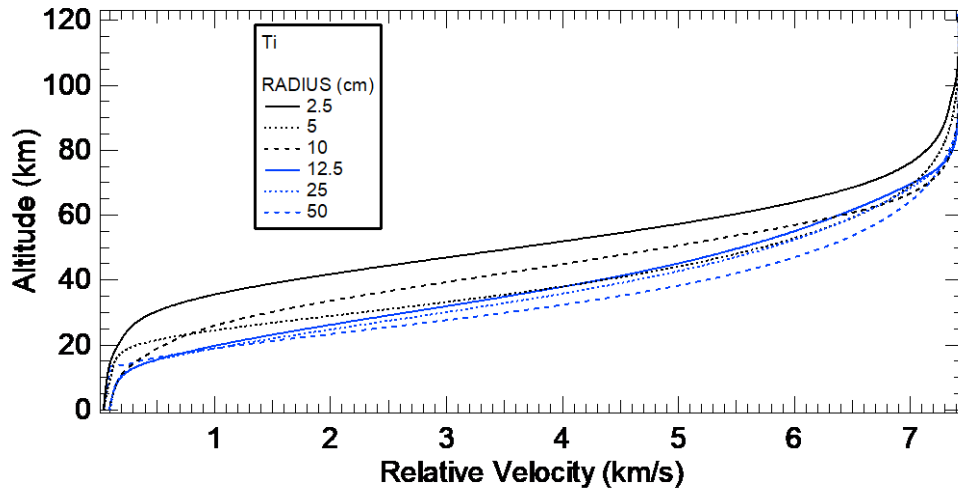
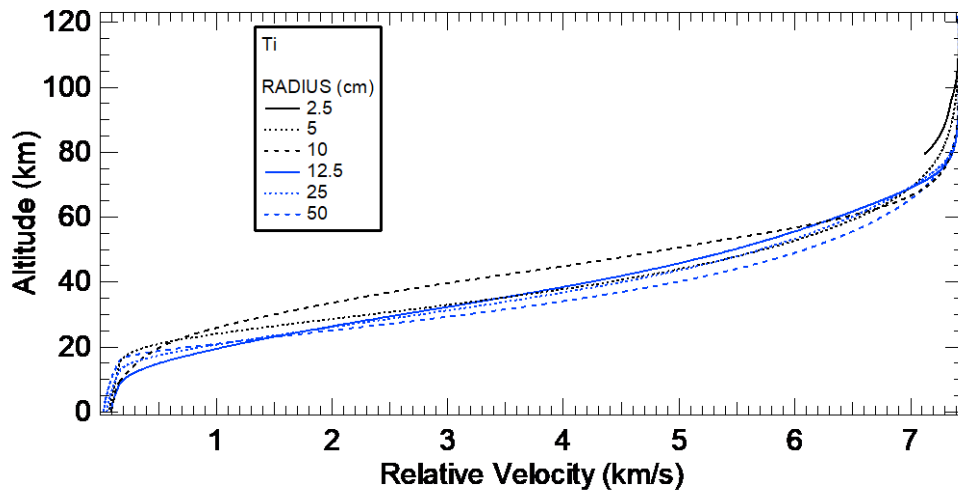


Figure 11.28 – Titanium spherical tanks reentry $w_z=1200$ RPM, altitude vs relative velocity.



For the FPA, trajectories without angular velocity presented lower angles, comparing to the same trajectories with Epoxy. The reason is the material density and the mass increment, which reduces the influence of the winds and other accelerations due to the aerodynamic forces. In the cases where the initial angular velocity is applied, the FPA increases in the zones of highest density and generates oscillations around the mean value, due to the changes in the direction of the Magnus force. See figures 11.29 to 11.32. It is possible to

observe that the melted bodies have the highest FPA at the moment of the disintegration. They started the decay phase with the highest velocity in the horizontal direction.

Figure 11.29 - Titanium spherical tanks reentry without initial angular velocity, FPA vs Time.

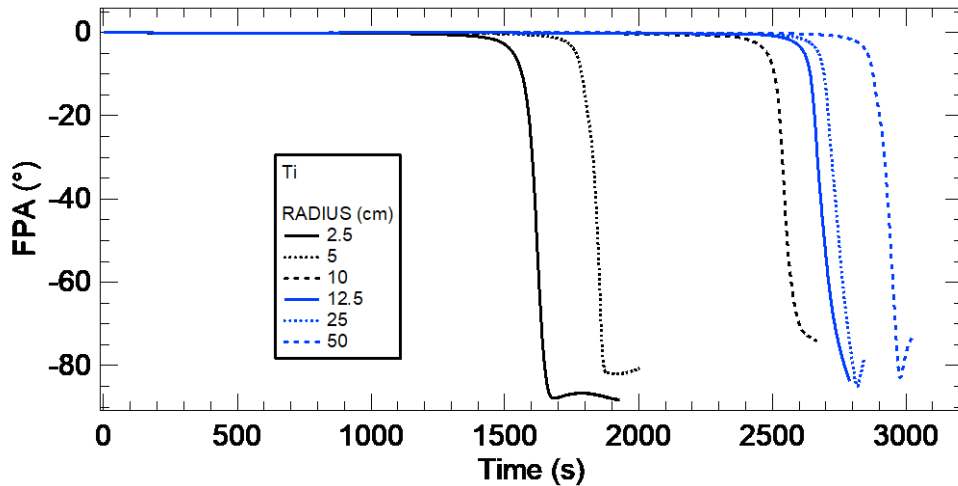
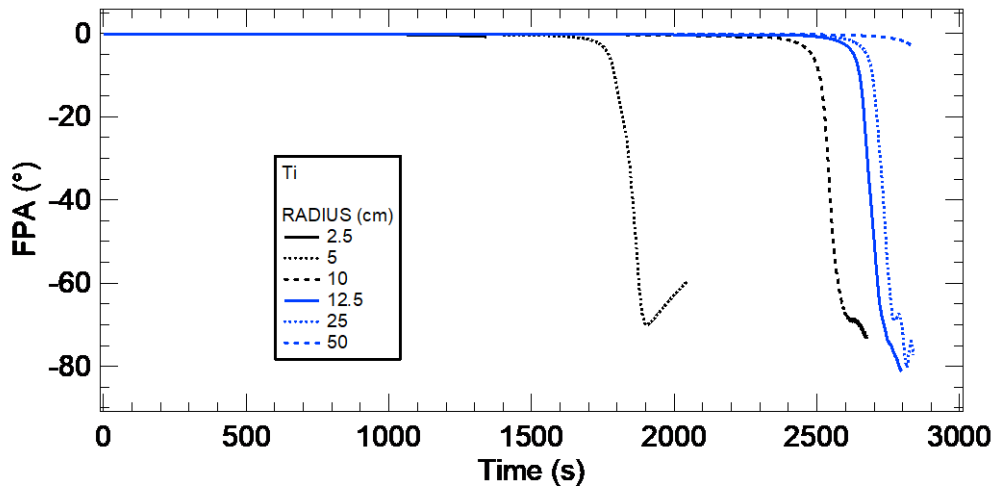


Figure 11.30 - Titanium spherical tanks reentry $w_x=1200$ RPM, FPA vs Time.



In figures 11.32 and 11.32 it is observed the FPA evolution for the reentries with angular velocities in Y_B and Z_B , respectively. It is observed that trajectories for Titanium fragments present more influence of the Magnus force, compared with the epoxy tanks. During the high density fly, at altitudes lower than 20 km, it is presented an oscillation in the final FPA, indicating the changes in the direction of the Magnus forces and accelerations for each instant of time. The behavior is

observed in these tanks because the selected material increases the mass of the fragment, which increases the velocity and the Magnus effect. The fragmentation also generates changes in the rotation that increase the Magnus influence, and, the directions of the forces when the angular velocities are applied in the Y_B and Z_B directions. The resulting forces directions of forces lie in the vertical and lateral directions of the local body, affecting the vertical descent. The increment of mass reduces the FPA because of the high velocities of the fragment in the lateral direction and the body area which increases the Magnus effects.

Figure 11.31 - Titanium spherical tanks reentry $w_y=1200$ RPM, FPA vs Time.

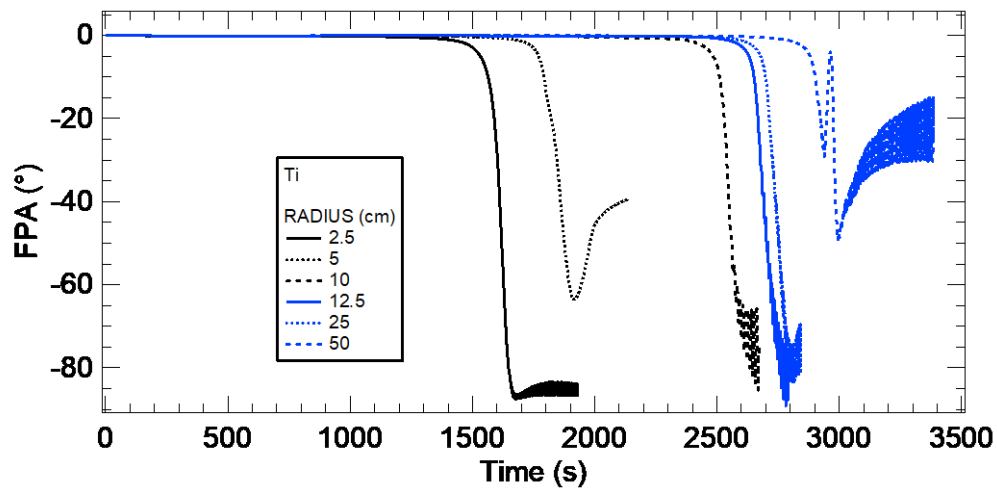
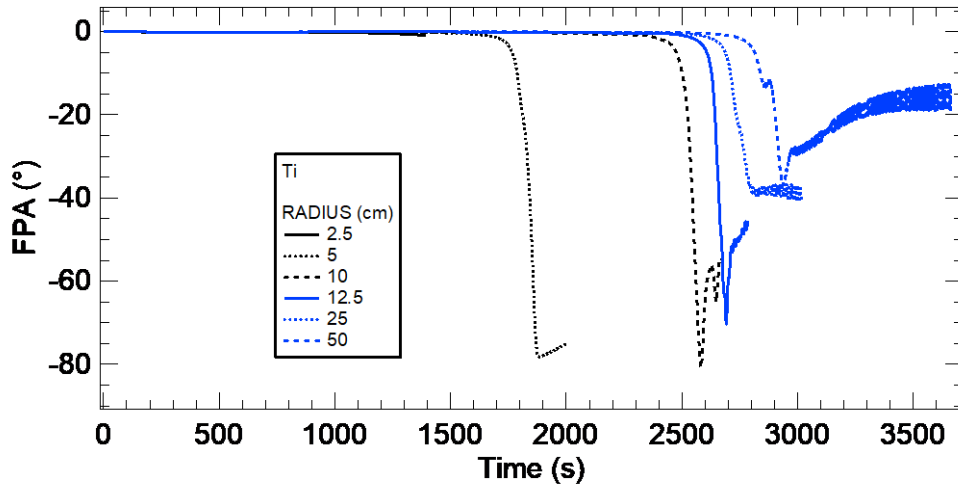


Figure 11.32- Titanium spherical tanks reentry $w_z=1200$ RPM, FPA vs Time.



The possible impact zones are determined for the survival fragments. In the cases of spheres with radius superior to 10 cm, the landing points are located in the south hemisphere and in the west direction, due to the increase of the flying time (see figures 11.36 to 11.38). The possible landing zone area are expanded with the mass increment, as observed in the Epoxy – I reentries.

Figure 11.33 – Survival Titanium 2.5 cm tank, impact zone.

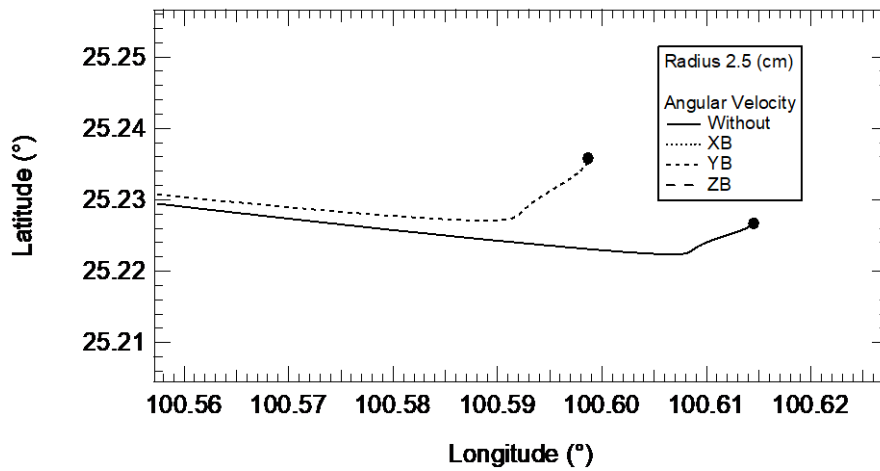


Figure 11.34 – Survival Titanium 5 cm tank, impact zone.

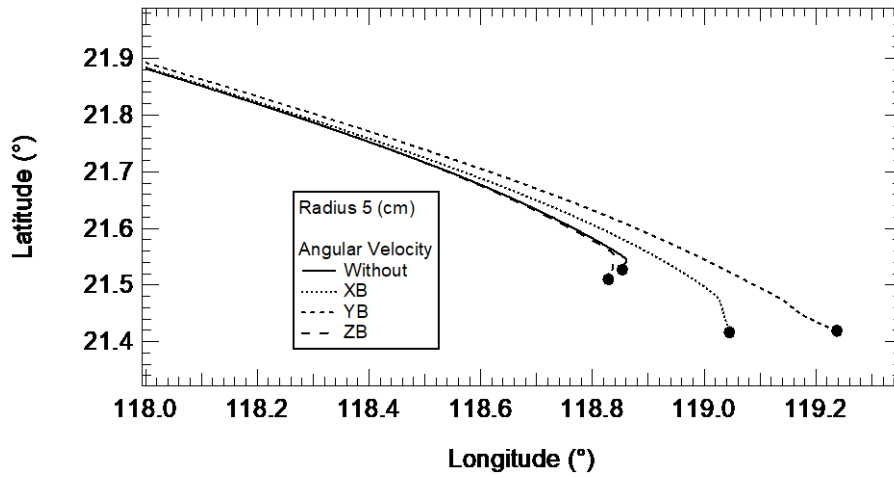


Figure 11.35 – Survival Titanium 10 cm tank, impact zone.

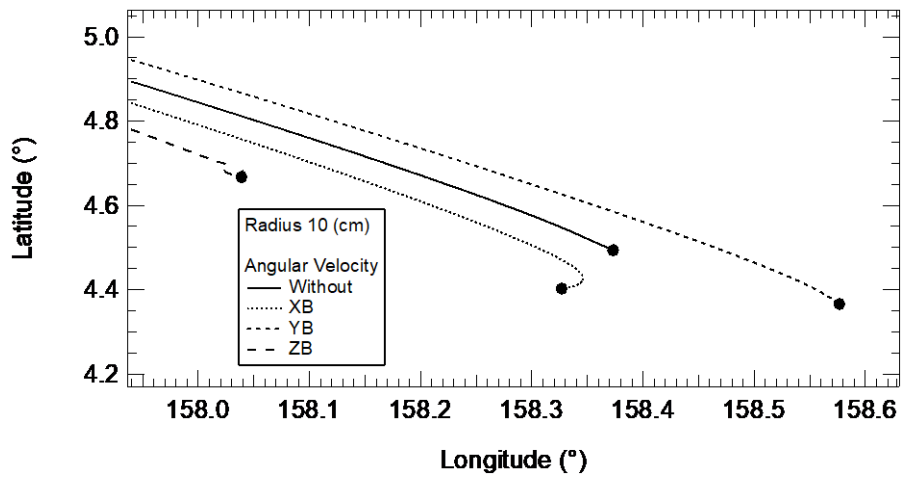


Figure 11.36 – Survival Titanium 12.5 cm tank, impact zone.

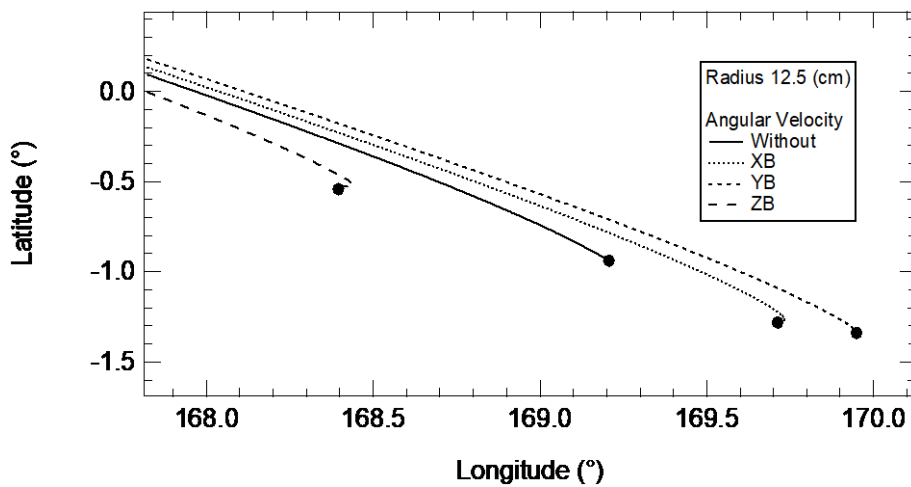


Figure 11.37 – Survival Titanium 25 cm tank, impact zone.

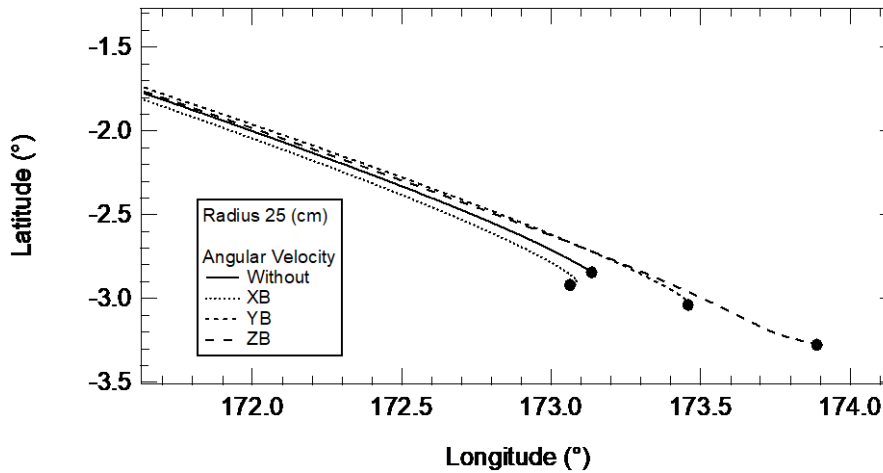


Figure 11.38 – Survival Titanium 50 cm tank, impact zone.

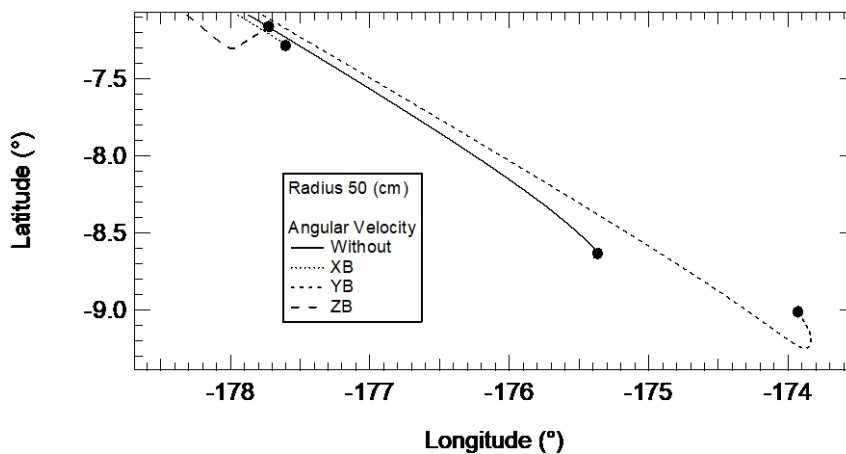


Table 11.3 shows the impact energy of the titanium tanks. It is observed the increase of the final energy compared to the epoxy tanks, due to the increase of the final mass caused by the material density, and the increase of the final velocities. Two reentries melted the debris without survival fragments. Trajectories with angular velocities presented variations in energy compared to the trajectories without angular velocity, but, in these cases, the material fragmentation generated changes in the mass, inertia and rotational velocity, which also modified the geometry of the debris, so affecting, the heat transfer and the aerodynamic forces. For each reentry case, the conditions are unique and generate independent variations in the trajectory. All the survival fragments

are risky and the changes in the direction of the angular velocity can increase the survival probability of the elements.

Table 11.3 – Final Energy in Jules for spherical tanks of Titanium.

Radius (cm)	Without	Wx	Wy	Wz
2.5	183.6	N/A	204.5	N/A
5	5,050	446.4	2,212.86	5,510
10	70,221	60,162	73,339.15	64,790.8
12.5	113,125	117,900	141,281.2	114,437.2
25	477,891	481,397.8	711,800	157,709
50	2'822,802	N/A	504,311.5	159,937.5

The spherical tanks don't show fragmentation before 80 km of altitude, because the air density is too low to increase the dynamic pressure and heat transfer, the two principal factors that generate the ablation, fragmentation and break-up. Between 80 and 50 km of altitude, the debris experiment losses of mass or fragmentation in the surface exposed to the atmospheric flow, due to the high velocities that increase the heat flux and the material storage temperatures. According to the references from the section 2.1, most of the software found the fragmentation at 78 km of altitude. The results presented here confirm that at this point is where the fragmentations begins. Figures 11.39 to 11.42 show the mass percentage as a function of the altitude. The initial mass of each tank is showed in the boxes of the figures. It is important to say that, in each fragmentation, the computational code recalculates the internal mesh, surface, inertial matrix, location of center of mass and heat transfer by conduction. In figures 11.39 to 11.42, it is possible to observe that the two cases with highest losses of mass are the 2.5 cm tank and the 50 cm tank. In the case of the 2.5 cm tank, there is a 50% probability to survive and depend on the initial conditions in terms of angular velocity. The fragmentation of these tanks are related to the low mass of the tanks, the highest reentry velocities and small radius that propagates rapidly the heat into the body and generates more heat in the smallest area of the surface. The next tank of 5 cm of radius is not melted during the reentry. In the case of the 50 cm tank, the largest surface exposed to

the flow increases the drag, friction and the heat transfer, allowing the fragmentation in the surface. The same behavior is present for the tanks with 25 cm and 12.5 cm of radius. It is important to remind that the losses of mass generate changes in the inertial matrix, increasing the angular velocity and producing mechanical fragmentation. Tanks of 5 cm and 10 cm present the lowest percentage of mass losses due to a medium area at slow velocities during the descent. The two tanks survived the four possible reentries. It shows that a medium mass and smaller surface area reduce the heat transfer and increase the survival probabilities.

The computational code detects break-ups by shear stress on the material or mechanical fragmentation. In this case the propagation continues in parallel or in distributive simulation until the element reach the heat point or the impact. In the case of the fragmentation by aerothermodynamics, it is presented by heat load and each fragment is removed from the principal debris body when the heat is superior to the fusion heat and the temperature of fusion. In this case, when a hole is created in the surface of the body and goes to the interior faces of the structure, the code assimilate the total destruction of the body by aerodynamic interference, because in this scenario the aerodynamic fluid is around and inside de body, generating aerothermodynamics uncertainties.

Figure 11.39 – Survival percent of mass, tanks of Titanium without initial angular velocity.

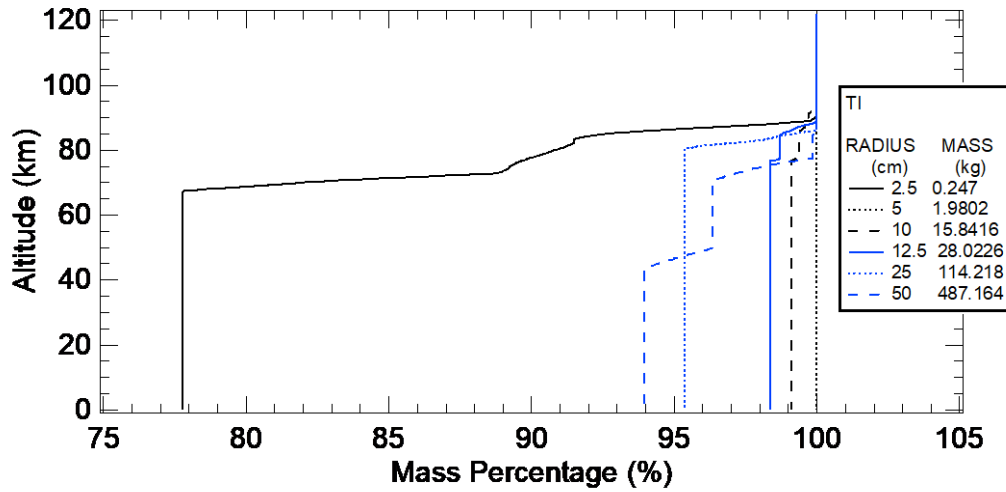


Figure 11.40 – Survival percent of mass, tanks of Titanium $w_x=1200$ RPM.

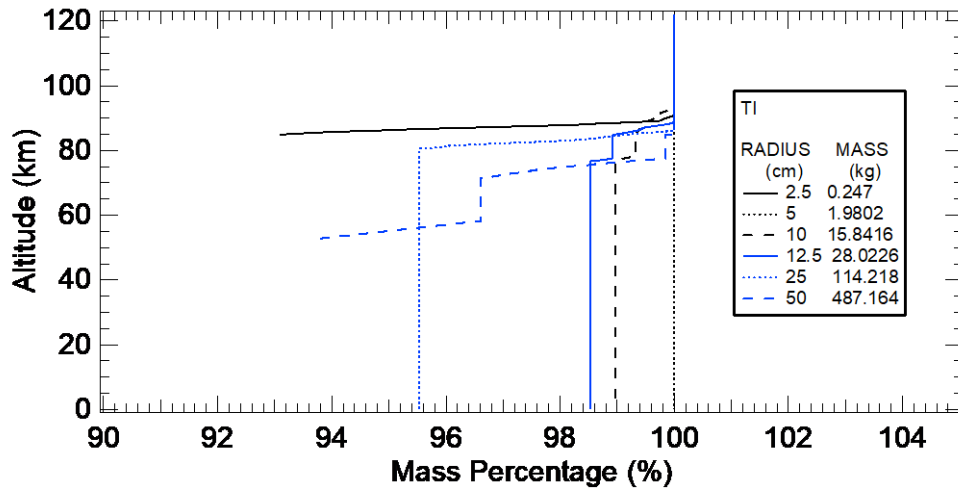


Figure 11.41 – Survival percent of mass, tanks of Titanium $w_y=1200$ RPM.

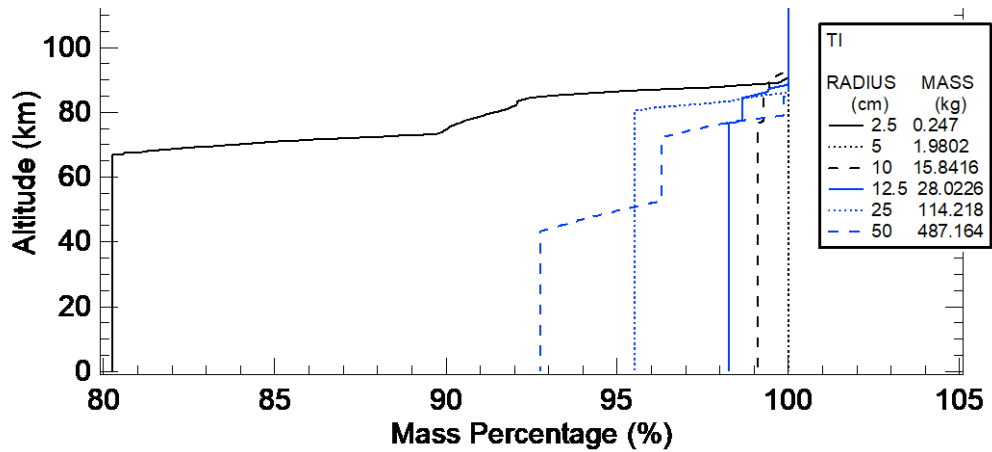
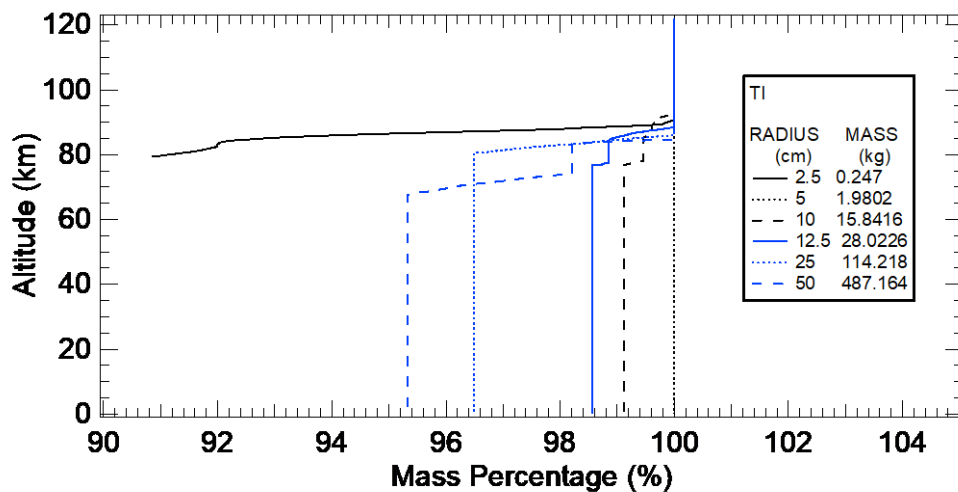


Figure 11.42 – Survival percent of mass, tanks of Titanium $w_z=1200$ RPM.



11.1.3. Reentry of spherical tanks of Aluminum

During the reentry of aluminum tanks, spheres of 50, 25 and 12.5 cm of radius survived in all of the four study cases. The smaller debris with 2.5, 5 and 10 cm of radius were the objects with the highest probabilities to melt during the reentry. Trajectories without initial angular velocity influence show similar results in terms of times of flight. Compared to trajectories with angular velocity in X_B

and Y_B , the only difference is the survival probability and the fragmentation altitudes of the three smaller debris tanks.

In figures 11.43 to 11.46 it is observed an increment in the altitude for tanks with 10 cm and 12.5 cm of radius. The phenomena are present around 70 km of altitude in all the trajectories and when the primary fragmentation is ended. The new body geometry after the fragmentation, with the velocity and appropriated flight path angle, plus the increment of density in this region, generate the ideal conditions to the lift force to influence a ricochet trajectory, only available in these two cases. Later, the tanks continue to lose velocity due to the atmospheric drag and then they decay.

When it is assumed an angular velocity in the Z_B -axis, the influence of the Magnus effect is greater than in the other three maneuvers, because it is acting in the vertical axis of the body. This rotations increases the flight time. The altitude as a function of time for the aluminum reentry cases is presented in figures 11.43 to 11.46.

Figure 11.43 – Aluminum spherical tanks reentry without initial angular velocity, altitude vs time.

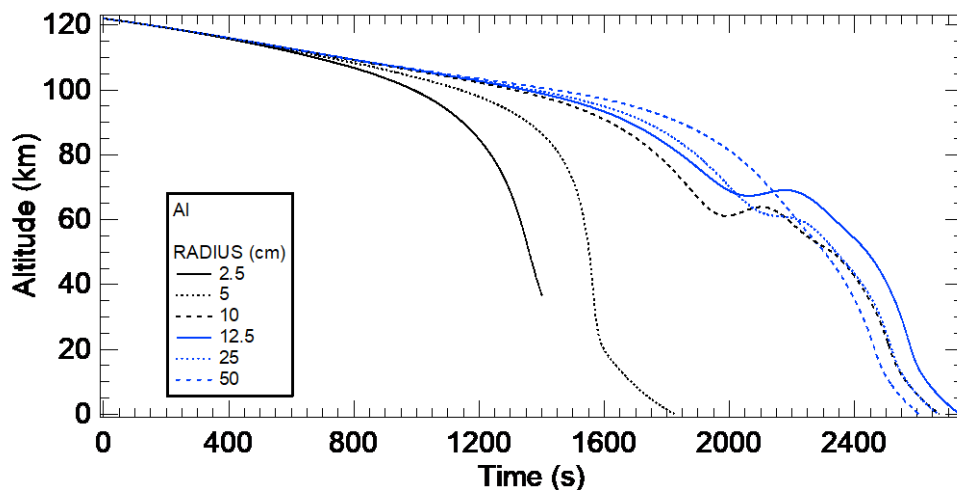


Figure 11.44 – Aluminum spherical tanks reentry $w_x=1200$ RPM, altitude vs time.

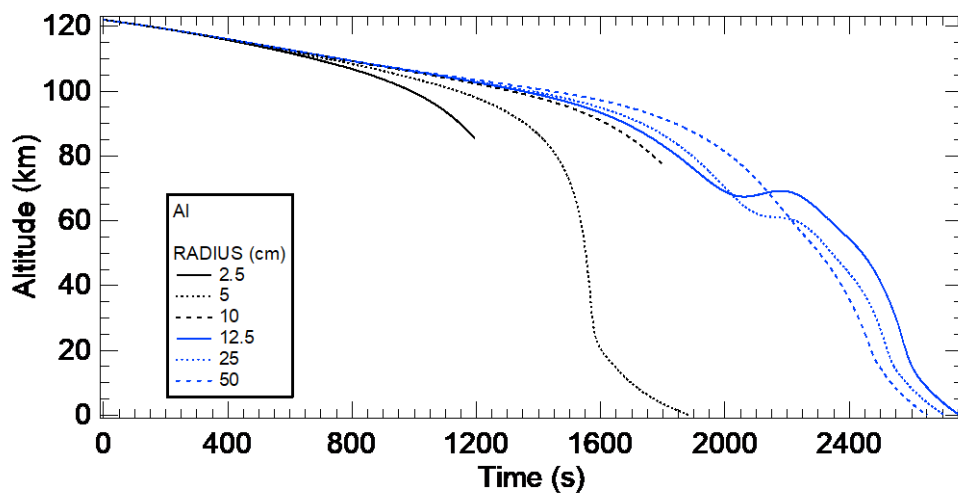


Figure 11.45 – Aluminum spherical tanks reentry $w_y=1200$ RPM, altitude vs time.

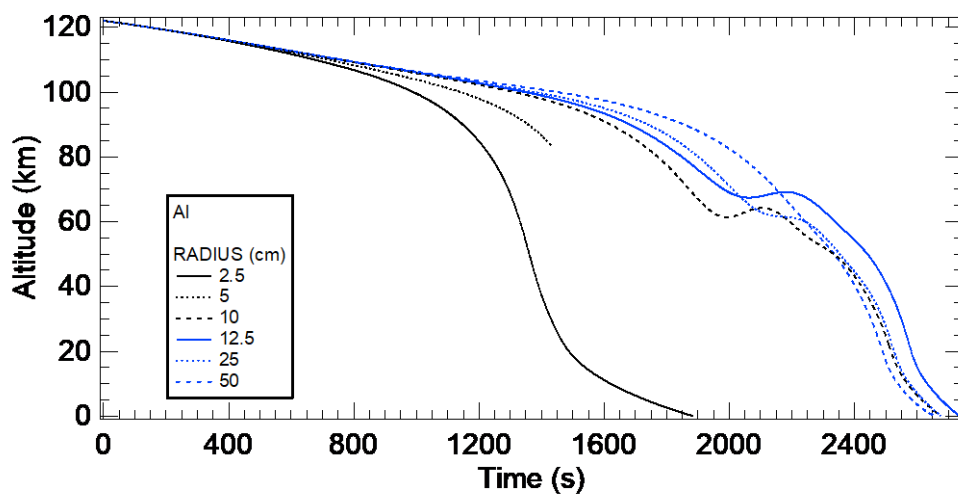
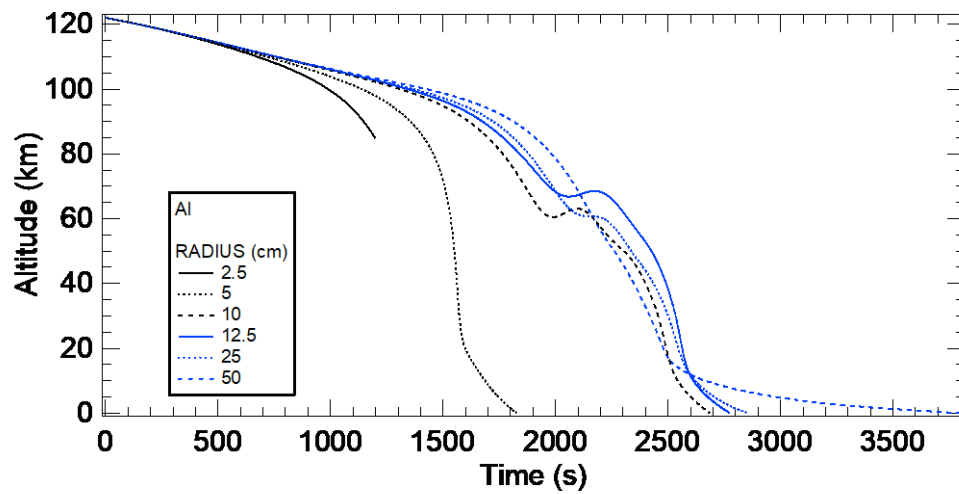


Figure 11.46 – Aluminum spherical tanks reentry $w_z=1200$ RPM, altitude vs time.



The 5 cm spherical tank of aluminum presents an interesting profile of velocity during the reentry. In the first part, between 120 and 80 km, it presents lower velocity compared to the other tanks, when it is in a transitional flow section. Around 60 to 20 km the debris increase the velocity, compared to the other survival debris, due to the smallest area, the mass losses and the reduction of the aero-breaking forces. But in the final approach, between 20 km to 0 km, the debris fragments present the lowest velocities and the highest deceleration, because the fragments come with the maximum velocity in the transition zone and they are rapidly braked by the increment of density in the low atmosphere, (see figures 11.47 to 11.50).

Figure 11.47 – Aluminum spherical tanks reentry without initial angular velocity, altitude vs relative velocity.

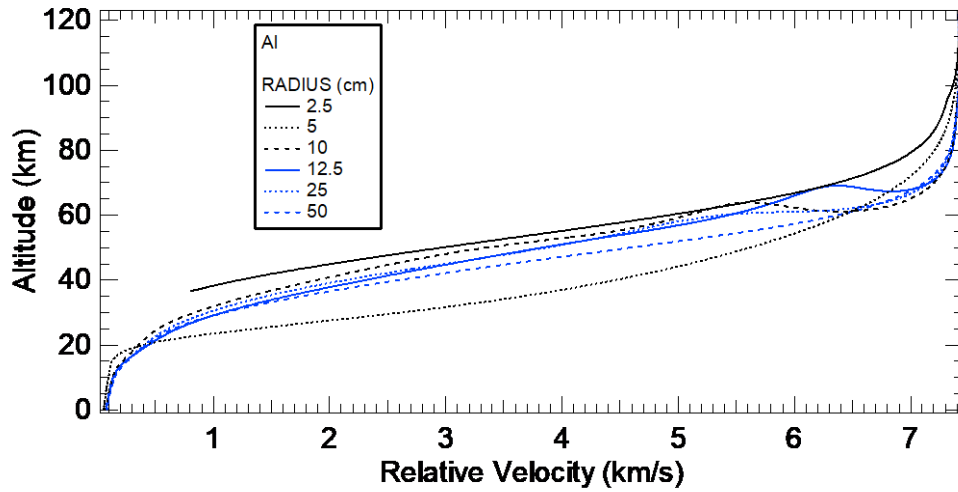


Figure 11.48 – Aluminum spherical tanks reentry $w_x=1200$ RPM, altitude vs relative velocity.

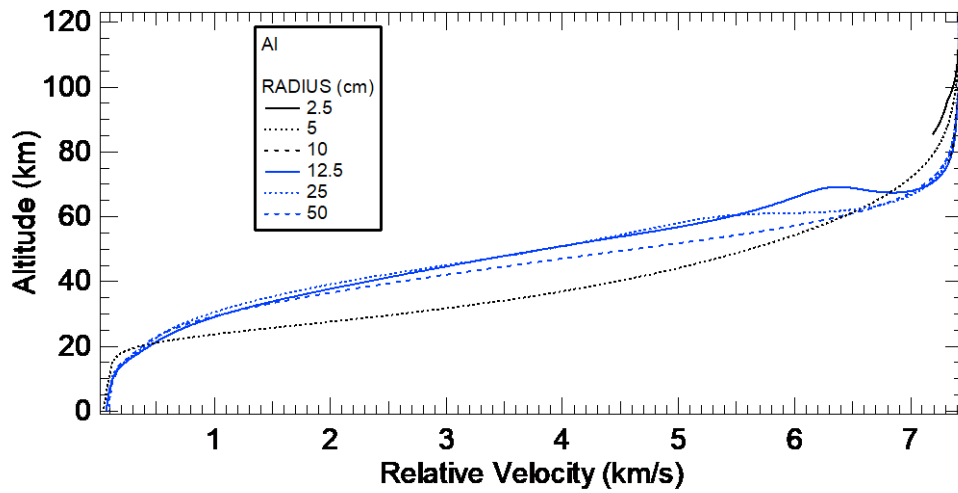


Figure 11.49 – Aluminum spherical tanks reentry $w_y=1200$ RPM, altitude vs relative velocity.

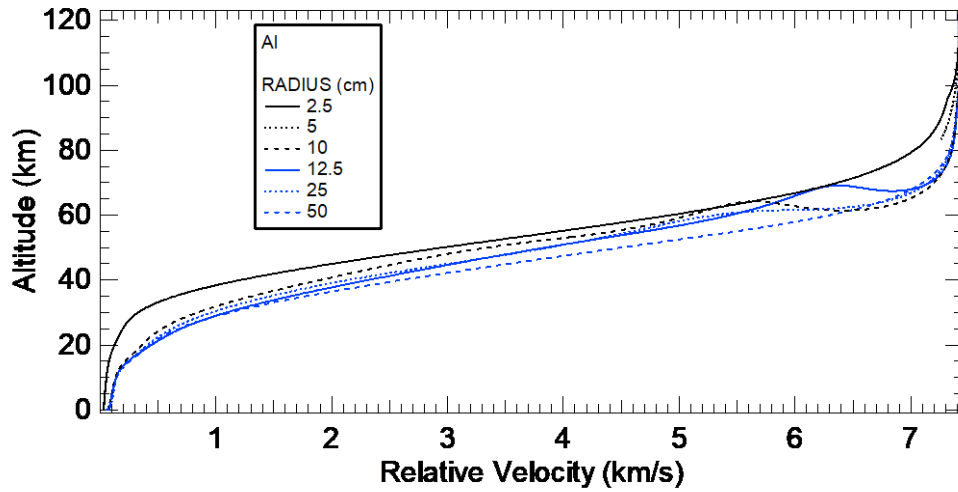
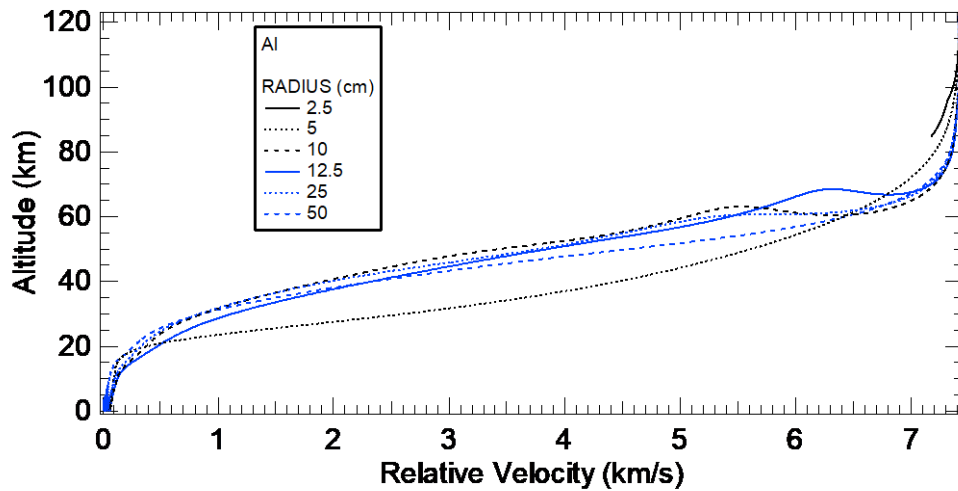


Figure 11.50 – Aluminum spherical tanks reentry $w_z=1200$ RPM, altitude vs relative velocity.



The FPA evolution decay rapidly to values around -80° , indicating a vertical descent in the final stage of the flight without the initial angular velocity (figure 11.50). When the Magnus influence is higher, the angle increases to values above -60° , indicating a lateral component of the velocity in a gliding mean trajectory. The angle influenced by the Magnus force is visible in the case of 50 cm, oscillating around the mean value of the angle due to the highest velocities of the reentry tank and the larger area, which increases the Magnus influence.

See figure 11.54. The FPA as a function of time for aluminum fragments presents the same behavior of the described for the titanium debris.

Figure 11.51 - Aluminum spherical tanks reentry without initial angular velocity, FPA vs Time.

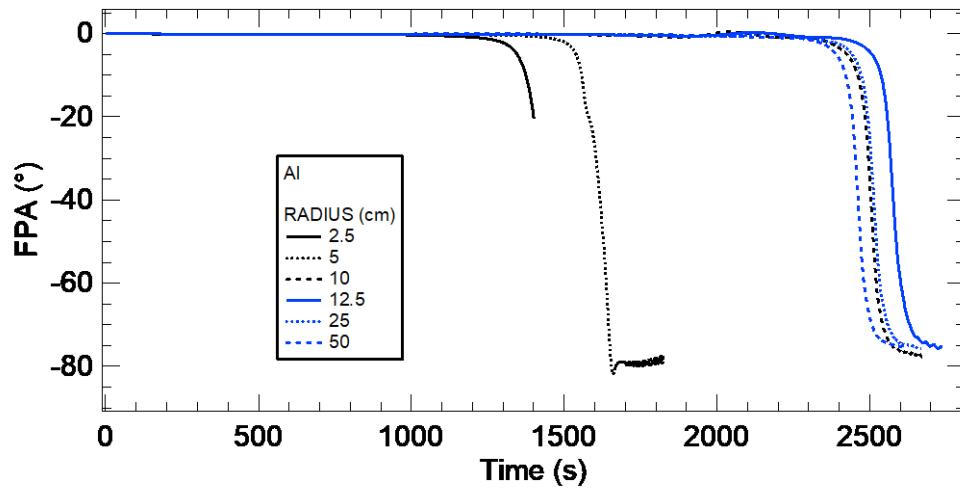


Figure 11.52 - Aluminum spherical tanks reentry $w_x=1200$ RPM, FPA vs Time.

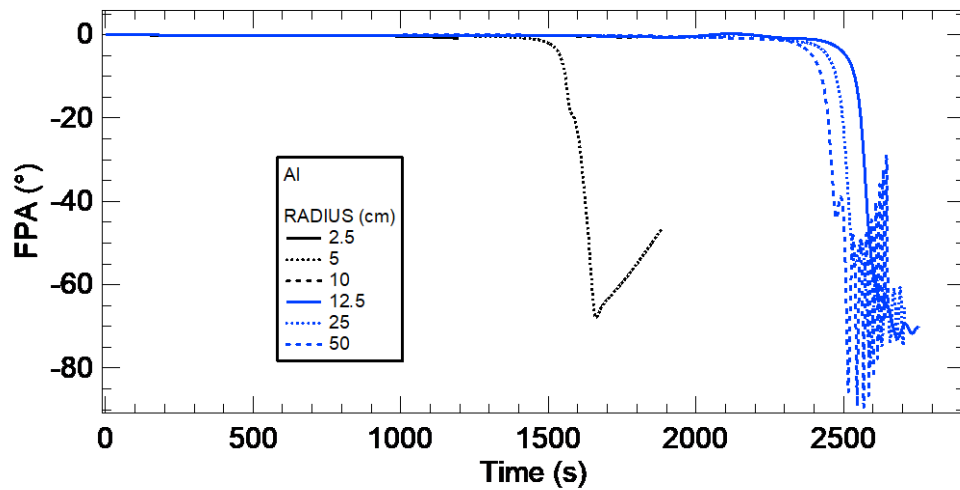


Figure 11.53 - Aluminum spherical tanks reentry $w_y=1200$ RPM, FPA vs Time.

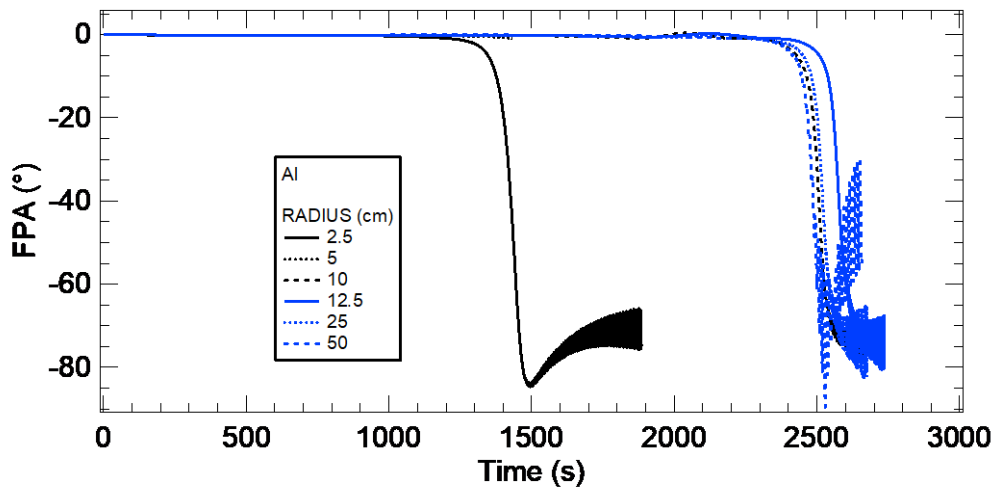
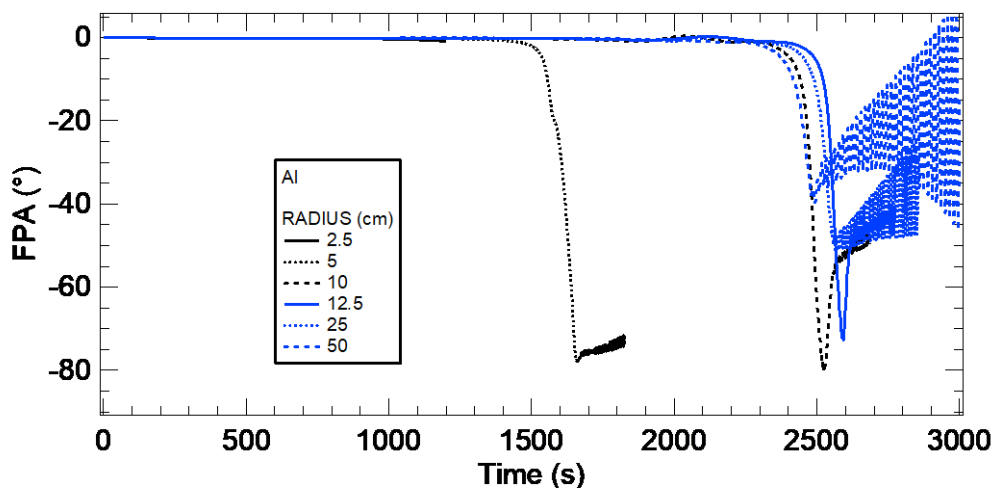


Figure 11.54 - Aluminum spherical tanks reentry $w_z=1200$ RPM, FPA vs Time.



The dispersion area of the landing zone has the same distribution of the previous study cases. The increase of mass of the fragment increases the time of flight and presents the largest differences between the impact coordinates of latitude and longitude. The higher mass objects increase the impact area and the final energy, becoming a higher risk, because it has larger probabilities to survive. Landing zone conditions are showed in figures 11.55 to 11.60 and the energies are registered in table 11.4, where, again all the survived trajectories are risk.

Figure 11.55 – Survival Aluminum 2.5 cm tank, impact zone.

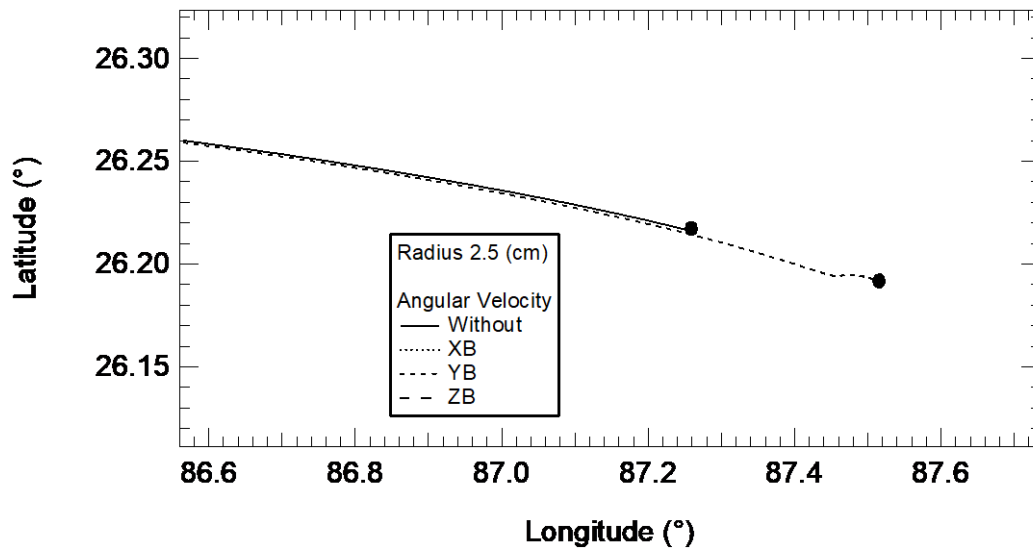


Figure 11.56 – Survival Aluminum 5 cm tank, impact zone.

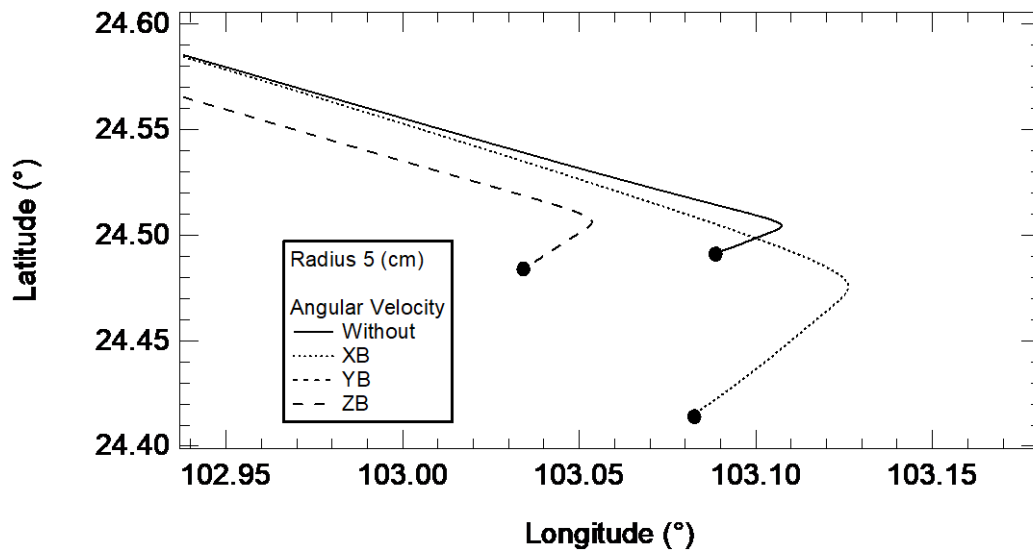


Figure 11.57 – Survival Aluminum 10 cm tank, impact zone.

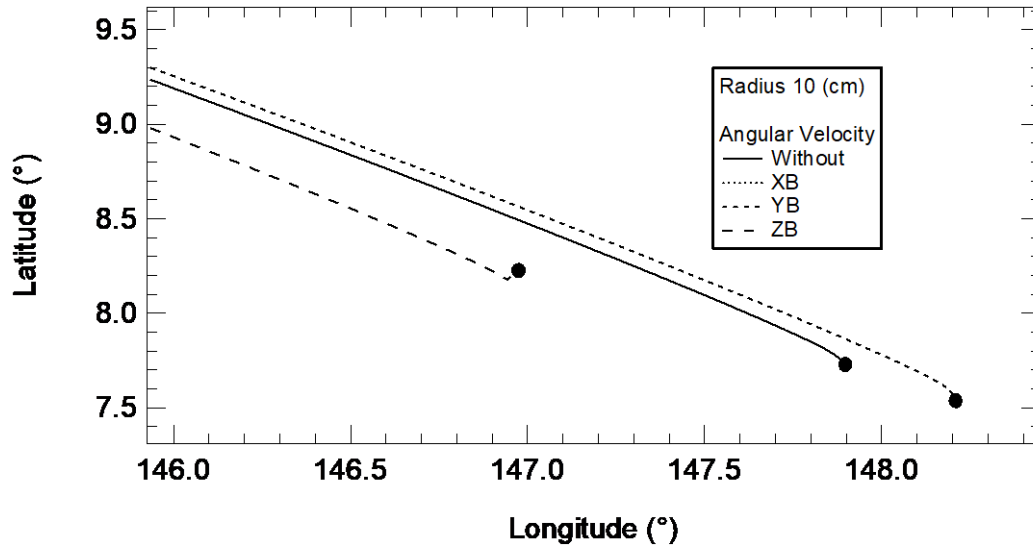


Figure 11.58 – Survival Aluminum 12.5 cm tank, impact zone.

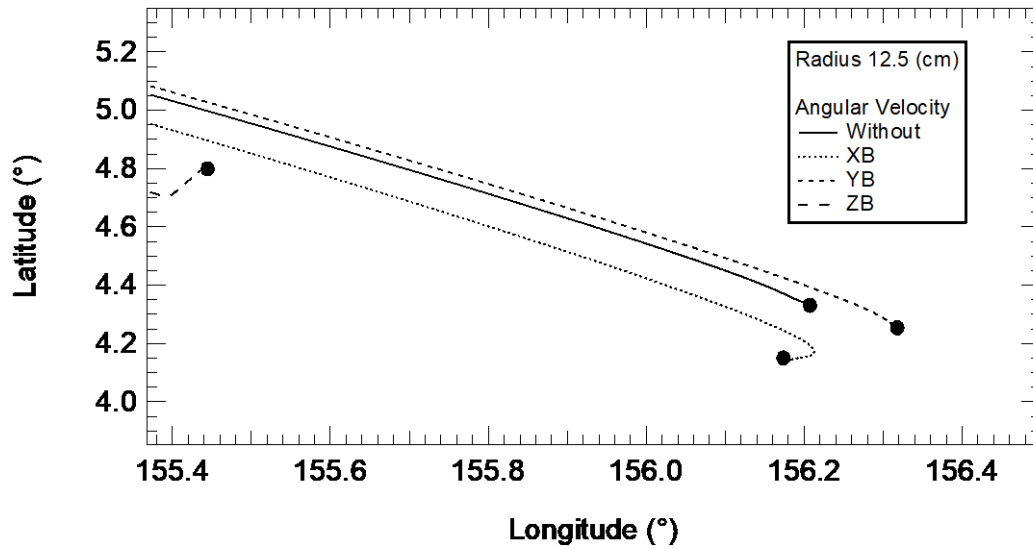


Figure 11.59– Survival Aluminum 25 cm tank, impact zone.

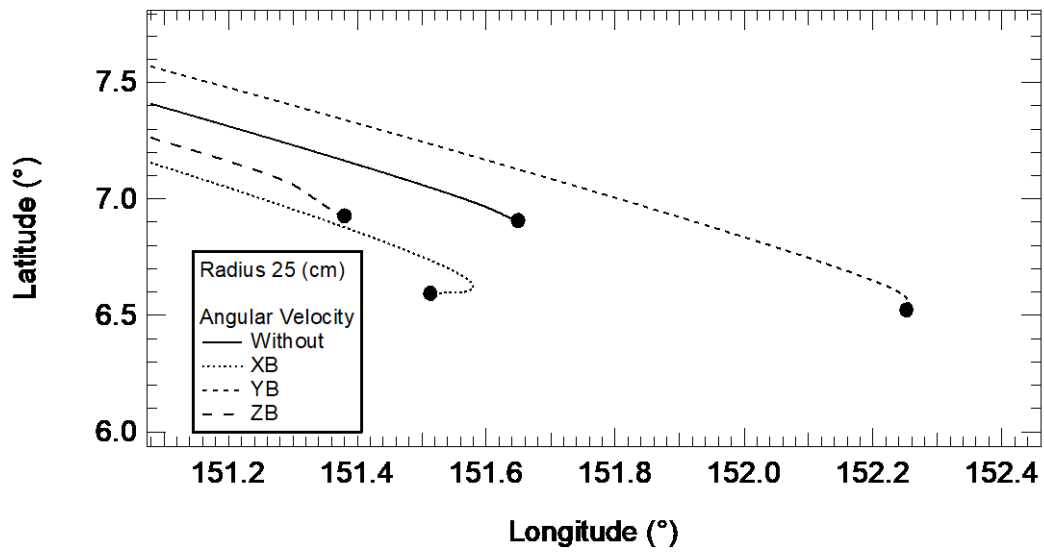


Figure 11.60 – Survival Aluminum 50 cm tank, impact zone.

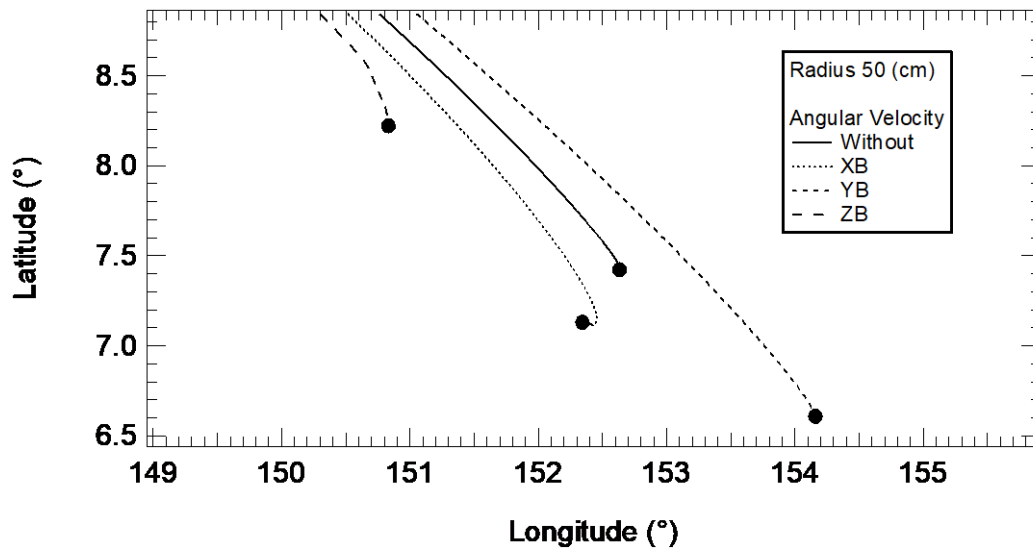


Table 11.4 – Final Energy in Jules for spherical tanks of Aluminum.

Radius (cm)	Without	Wx	Wy	Wz
2.5	N/A	N/A	63.08	N/A
5	1,978	1,270.2	N/A	2,191.9
10	25,661	N/A	30,651.7	20,914.8
12.5	48,145	39,455	66,906.3	30,698.8
25	214,940	173,615	333,553.9	61,072.2
50	1'030,004	2'032,831.8	841,774	75,824.1

In this case, all debris present fragmentation around 80 km of altitude. For each of the four cases, using the aluminum alloy, one of the reentry tanks is disintegrated, reducing the probability of survival for bodies made from aluminum alloy. Tanks of 2.5 cm and 10 cm presented the larger losses of mass. The lower is in the reentry of the tank of 50 cm. Figures 11.61 to 11.65 show the variations of masses as a function of the altitude. Compared to the Titanium tanks, the aluminum tanks present more fragmentation and a lower percentage of mass survive.

Figure 11.61 – Survival percent of mass, tanks of Aluminum without initial angular velocity.

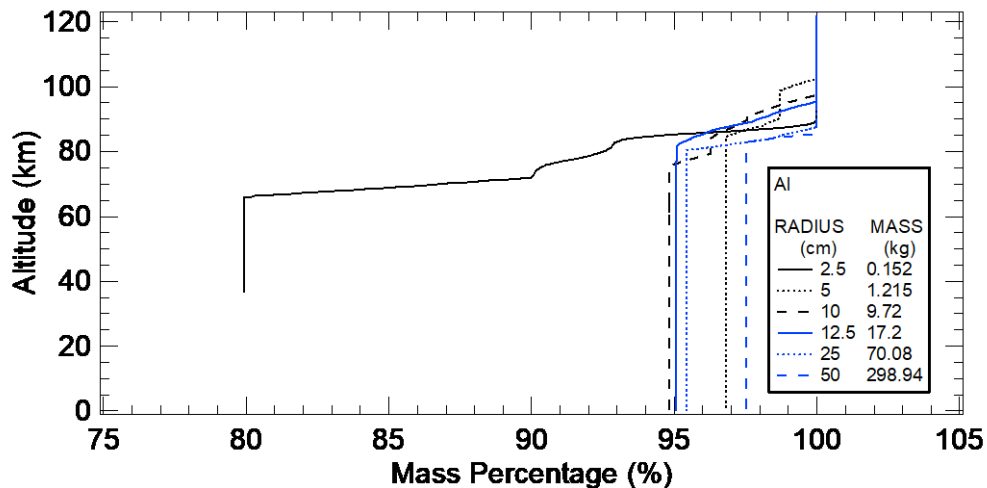


Figure 11.62 – Survival percent of mass, tanks of Aluminum $w_x=1200$ RPM.

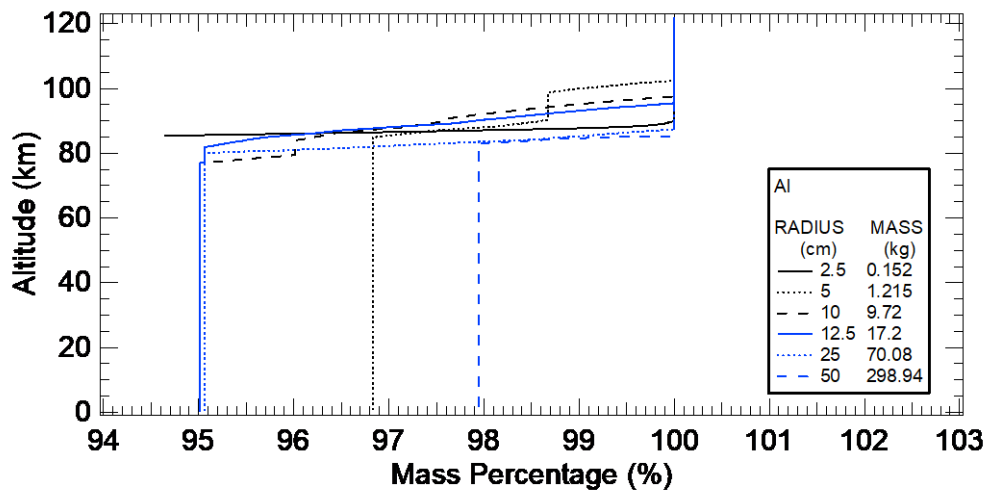


Figure 11.63 – Survival percent of mass, tanks of Aluminum $w_y=1200$ RPM.

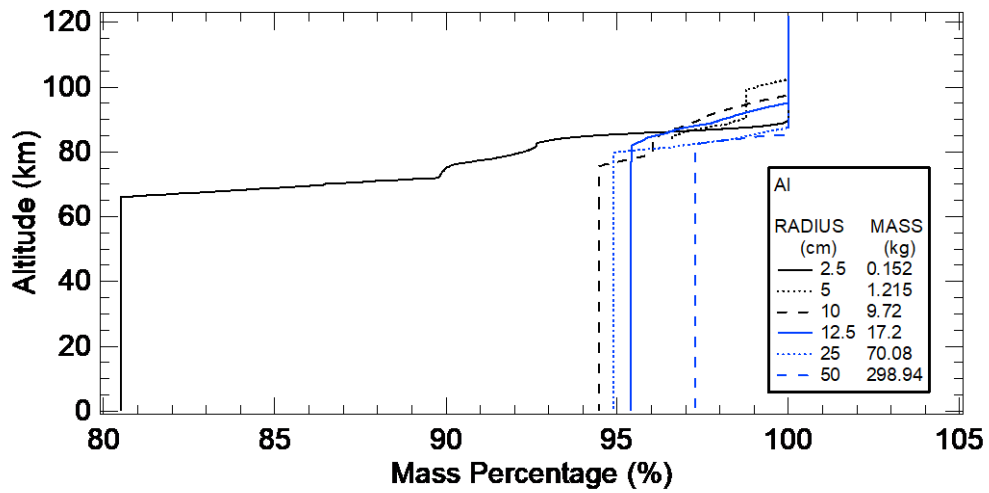
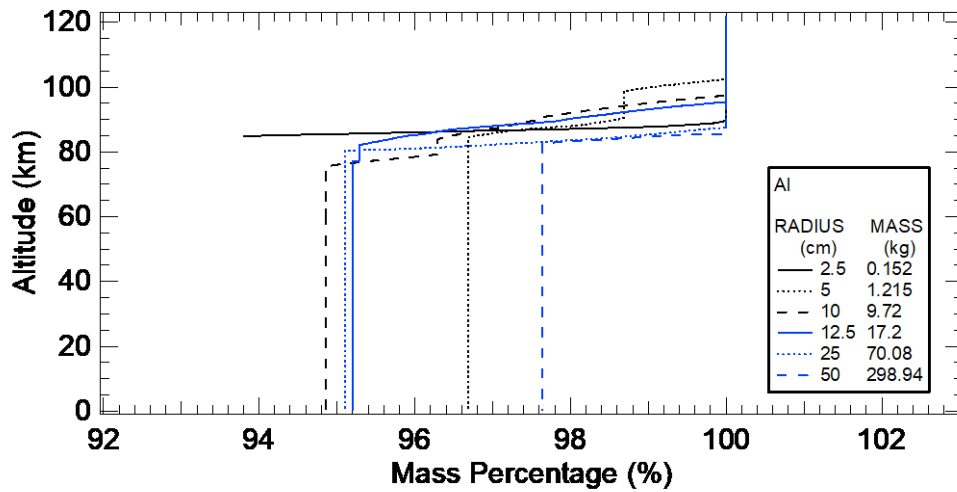


Figure 11.64 – Survival percent of mass, tanks of Aluminum $w_z=1200$ RPM.



11.2. Error analysis

Trajectories of the reentry tanks were propagated to determine the possible impact zones, the survival mass and the final energy according to the RCRA. Due to the uncertainty of the mean trajectory propagation, it is necessary to determine the error and the standard deviation of the state vector as a function of time, to know the final error in the impact zone. In these cases, it is implemented the variation of the variance/covariance matrix from the Riccati equation, to observe the evolution of the variation and the influence of the initial errors in the propagation of the mean trajectory. The variance/covariance matrix includes the twelve terms of the state vector (3 positions, 3 velocities, 3 angles, 3 angular velocities), one aerodynamic influence due to the changes of the pressure coefficient and one atmospheric error corresponding to the uncertainty in the mean density value of the atmospheric model. The Jacobi matrix, which relates the state vector derivate with the variables is presented in equation 12.1. Differential equations of the matrix are solved numerically by the definition of the derivate, implementing the finite differences method used by Guedes (1997).

$$[\mathbf{F}] = \begin{bmatrix}
\frac{\partial \dot{x}}{\partial x} & \frac{\partial \dot{x}}{\partial y} & \frac{\partial \dot{x}}{\partial z} & \frac{\partial \dot{x}}{\partial V_X} & \frac{\partial \dot{x}}{\partial V_Y} & \frac{\partial \dot{x}}{\partial V_Z} & \frac{\partial \dot{x}}{\partial \theta_1} & \frac{\partial \dot{x}}{\partial \theta_2} & \frac{\partial \dot{x}}{\partial \theta_3} & \frac{\partial \dot{x}}{\partial \omega_1} & \frac{\partial \dot{x}}{\partial \omega_2} & \frac{\partial \dot{x}}{\partial \omega_3} & \frac{\partial \dot{x}}{\partial C_p} & \frac{\partial \dot{x}}{\partial \rho} \\
\frac{\partial \dot{y}}{\partial x} & \frac{\partial \dot{y}}{\partial y} & \frac{\partial \dot{y}}{\partial z} & \frac{\partial \dot{y}}{\partial V_X} & \frac{\partial \dot{y}}{\partial V_Y} & \frac{\partial \dot{y}}{\partial V_Z} & \frac{\partial \dot{y}}{\partial \theta_1} & \frac{\partial \dot{y}}{\partial \theta_2} & \frac{\partial \dot{y}}{\partial \theta_3} & \frac{\partial \dot{y}}{\partial \omega_1} & \frac{\partial \dot{y}}{\partial \omega_2} & \frac{\partial \dot{y}}{\partial \omega_3} & \frac{\partial \dot{y}}{\partial C_p} & \frac{\partial \dot{y}}{\partial \rho} \\
\frac{\partial \dot{z}}{\partial x} & \frac{\partial \dot{z}}{\partial y} & \frac{\partial \dot{z}}{\partial z} & \frac{\partial \dot{z}}{\partial V_X} & \frac{\partial \dot{z}}{\partial V_Y} & \frac{\partial \dot{z}}{\partial V_Z} & \frac{\partial \dot{z}}{\partial \theta_1} & \frac{\partial \dot{z}}{\partial \theta_2} & \frac{\partial \dot{z}}{\partial \theta_3} & \frac{\partial \dot{z}}{\partial \omega_1} & \frac{\partial \dot{z}}{\partial \omega_2} & \frac{\partial \dot{z}}{\partial \omega_3} & \frac{\partial \dot{z}}{\partial C_p} & \frac{\partial \dot{z}}{\partial \rho} \\
\frac{\partial \dot{V}_X}{\partial x} & \frac{\partial \dot{V}_X}{\partial y} & \frac{\partial \dot{V}_X}{\partial z} & \frac{\partial \dot{V}_X}{\partial V_X} & \frac{\partial \dot{V}_X}{\partial V_Y} & \frac{\partial \dot{V}_X}{\partial V_Z} & \frac{\partial \dot{V}_X}{\partial \theta_1} & \frac{\partial \dot{V}_X}{\partial \theta_2} & \frac{\partial \dot{V}_X}{\partial \theta_3} & \frac{\partial \dot{V}_X}{\partial \omega_1} & \frac{\partial \dot{V}_X}{\partial \omega_2} & \frac{\partial \dot{V}_X}{\partial \omega_3} & \frac{\partial \dot{V}_X}{\partial C_p} & \frac{\partial \dot{V}_X}{\partial \rho} \\
\frac{\partial \dot{V}_Y}{\partial x} & \frac{\partial \dot{V}_Y}{\partial y} & \frac{\partial \dot{V}_Y}{\partial z} & \frac{\partial \dot{V}_Y}{\partial V_X} & \frac{\partial \dot{V}_Y}{\partial V_Y} & \frac{\partial \dot{V}_Y}{\partial V_Z} & \frac{\partial \dot{V}_Y}{\partial \theta_1} & \frac{\partial \dot{V}_Y}{\partial \theta_2} & \frac{\partial \dot{V}_Y}{\partial \theta_3} & \frac{\partial \dot{V}_Y}{\partial \omega_1} & \frac{\partial \dot{V}_Y}{\partial \omega_2} & \frac{\partial \dot{V}_Y}{\partial \omega_3} & \frac{\partial \dot{V}_Y}{\partial C_p} & \frac{\partial \dot{V}_Y}{\partial \rho} \\
\frac{\partial \dot{V}_Z}{\partial x} & \frac{\partial \dot{V}_Z}{\partial y} & \frac{\partial \dot{V}_Z}{\partial z} & \frac{\partial \dot{V}_Z}{\partial V_X} & \frac{\partial \dot{V}_Z}{\partial V_Y} & \frac{\partial \dot{V}_Z}{\partial V_Z} & \frac{\partial \dot{V}_Z}{\partial \theta_1} & \frac{\partial \dot{V}_Z}{\partial \theta_2} & \frac{\partial \dot{V}_Z}{\partial \theta_3} & \frac{\partial \dot{V}_Z}{\partial \omega_1} & \frac{\partial \dot{V}_Z}{\partial \omega_2} & \frac{\partial \dot{V}_Z}{\partial \omega_3} & \frac{\partial \dot{V}_Z}{\partial C_p} & \frac{\partial \dot{V}_Z}{\partial \rho} \\
\frac{\partial \dot{\theta}_1}{\partial x} & \frac{\partial \dot{\theta}_1}{\partial y} & \frac{\partial \dot{\theta}_1}{\partial z} & \frac{\partial \dot{\theta}_1}{\partial V_X} & \frac{\partial \dot{\theta}_1}{\partial V_Y} & \frac{\partial \dot{\theta}_1}{\partial V_Z} & \frac{\partial \dot{\theta}_1}{\partial \theta_1} & \frac{\partial \dot{\theta}_1}{\partial \theta_2} & \frac{\partial \dot{\theta}_1}{\partial \theta_3} & \frac{\partial \dot{\theta}_1}{\partial \omega_1} & \frac{\partial \dot{\theta}_1}{\partial \omega_2} & \frac{\partial \dot{\theta}_1}{\partial \omega_3} & \frac{\partial \dot{\theta}_1}{\partial C_p} & \frac{\partial \dot{\theta}_1}{\partial \rho} \\
\frac{\partial \dot{\theta}_2}{\partial x} & \frac{\partial \dot{\theta}_2}{\partial y} & \frac{\partial \dot{\theta}_2}{\partial z} & \frac{\partial \dot{\theta}_2}{\partial V_X} & \frac{\partial \dot{\theta}_2}{\partial V_Y} & \frac{\partial \dot{\theta}_2}{\partial V_Z} & \frac{\partial \dot{\theta}_2}{\partial \theta_1} & \frac{\partial \dot{\theta}_2}{\partial \theta_2} & \frac{\partial \dot{\theta}_2}{\partial \theta_3} & \frac{\partial \dot{\theta}_2}{\partial \omega_1} & \frac{\partial \dot{\theta}_2}{\partial \omega_2} & \frac{\partial \dot{\theta}_2}{\partial \omega_3} & \frac{\partial \dot{\theta}_2}{\partial C_p} & \frac{\partial \dot{\theta}_2}{\partial \rho} \\
\frac{\partial \dot{\theta}_3}{\partial x} & \frac{\partial \dot{\theta}_3}{\partial y} & \frac{\partial \dot{\theta}_3}{\partial z} & \frac{\partial \dot{\theta}_3}{\partial V_X} & \frac{\partial \dot{\theta}_3}{\partial V_Y} & \frac{\partial \dot{\theta}_3}{\partial V_Z} & \frac{\partial \dot{\theta}_3}{\partial \theta_1} & \frac{\partial \dot{\theta}_3}{\partial \theta_2} & \frac{\partial \dot{\theta}_3}{\partial \theta_3} & \frac{\partial \dot{\theta}_3}{\partial \omega_1} & \frac{\partial \dot{\theta}_3}{\partial \omega_2} & \frac{\partial \dot{\theta}_3}{\partial \omega_3} & \frac{\partial \dot{\theta}_3}{\partial C_p} & \frac{\partial \dot{\theta}_3}{\partial \rho} \\
\frac{\partial \dot{\omega}_1}{\partial x} & \frac{\partial \dot{\omega}_1}{\partial y} & \frac{\partial \dot{\omega}_1}{\partial z} & \frac{\partial \dot{\omega}_1}{\partial V_X} & \frac{\partial \dot{\omega}_1}{\partial V_Y} & \frac{\partial \dot{\omega}_1}{\partial V_Z} & \frac{\partial \dot{\omega}_1}{\partial \theta_1} & \frac{\partial \dot{\omega}_1}{\partial \theta_2} & \frac{\partial \dot{\omega}_1}{\partial \theta_3} & \frac{\partial \dot{\omega}_1}{\partial \omega_1} & \frac{\partial \dot{\omega}_1}{\partial \omega_2} & \frac{\partial \dot{\omega}_1}{\partial \omega_3} & \frac{\partial \dot{\omega}_1}{\partial C_p} & \frac{\partial \dot{\omega}_1}{\partial \rho} \\
\frac{\partial \dot{\omega}_2}{\partial x} & \frac{\partial \dot{\omega}_2}{\partial y} & \frac{\partial \dot{\omega}_2}{\partial z} & \frac{\partial \dot{\omega}_2}{\partial V_X} & \frac{\partial \dot{\omega}_2}{\partial V_Y} & \frac{\partial \dot{\omega}_2}{\partial V_Z} & \frac{\partial \dot{\omega}_2}{\partial \theta_1} & \frac{\partial \dot{\omega}_2}{\partial \theta_2} & \frac{\partial \dot{\omega}_2}{\partial \theta_3} & \frac{\partial \dot{\omega}_2}{\partial \omega_1} & \frac{\partial \dot{\omega}_2}{\partial \omega_2} & \frac{\partial \dot{\omega}_2}{\partial \omega_3} & \frac{\partial \dot{\omega}_2}{\partial C_p} & \frac{\partial \dot{\omega}_2}{\partial \rho} \\
\frac{\partial \dot{\omega}_3}{\partial x} & \frac{\partial \dot{\omega}_3}{\partial y} & \frac{\partial \dot{\omega}_3}{\partial z} & \frac{\partial \dot{\omega}_3}{\partial V_X} & \frac{\partial \dot{\omega}_3}{\partial V_Y} & \frac{\partial \dot{\omega}_3}{\partial V_Z} & \frac{\partial \dot{\omega}_3}{\partial \theta_1} & \frac{\partial \dot{\omega}_3}{\partial \theta_2} & \frac{\partial \dot{\omega}_3}{\partial \theta_3} & \frac{\partial \dot{\omega}_3}{\partial \omega_1} & \frac{\partial \dot{\omega}_3}{\partial \omega_2} & \frac{\partial \dot{\omega}_3}{\partial \omega_3} & \frac{\partial \dot{\omega}_3}{\partial C_p} & \frac{\partial \dot{\omega}_3}{\partial \rho} \\
\frac{\partial \dot{C}_p}{\partial x} & \frac{\partial \dot{C}_p}{\partial y} & \frac{\partial \dot{C}_p}{\partial z} & \frac{\partial \dot{C}_p}{\partial V_X} & \frac{\partial \dot{C}_p}{\partial V_Y} & \frac{\partial \dot{C}_p}{\partial V_Z} & \frac{\partial \dot{C}_p}{\partial \theta_1} & \frac{\partial \dot{C}_p}{\partial \theta_2} & \frac{\partial \dot{C}_p}{\partial \theta_3} & \frac{\partial \dot{C}_p}{\partial \omega_1} & \frac{\partial \dot{C}_p}{\partial \omega_2} & \frac{\partial \dot{C}_p}{\partial \omega_3} & \frac{\partial \dot{C}_p}{\partial C_p} & \frac{\partial \dot{C}_p}{\partial \rho} \\
\frac{\partial \dot{\rho}}{\partial x} & \frac{\partial \dot{\rho}}{\partial y} & \frac{\partial \dot{\rho}}{\partial z} & \frac{\partial \dot{\rho}}{\partial V_X} & \frac{\partial \dot{\rho}}{\partial V_Y} & \frac{\partial \dot{\rho}}{\partial V_Z} & \frac{\partial \dot{\rho}}{\partial \theta_1} & \frac{\partial \dot{\rho}}{\partial \theta_2} & \frac{\partial \dot{\rho}}{\partial \theta_3} & \frac{\partial \dot{\rho}}{\partial \omega_1} & \frac{\partial \dot{\rho}}{\partial \omega_2} & \frac{\partial \dot{\rho}}{\partial \omega_3} & \frac{\partial \dot{\rho}}{\partial C_p} & \frac{\partial \dot{\rho}}{\partial \rho}
\end{bmatrix}, \quad (12.1)$$

The present analysis allows the determination of the variance in the state vector (position, velocity, Euler angles and angular velocity) at the impact point in the local coordinate system, and the influence of the variance by the pressure coefficient in aerodynamic and atmospheric density, generating significant changes in the trajectory. The derivation of the variance/covariance matrix is useful for aerospace applications, like: to calculate the error in velocity and position of satellites around the Earth (VALLADO, 2004; VALLADO et al, 2009; CHEN et al, 2017) and to determine the impact areas in the reentry cases (GUEDES, 1997; REAGAN; ANANDAKRISHNAN, 1993). With the implementation of the present methodology, it is possible to estimate the position and velocity errors in the same propagation. Generally, to determine

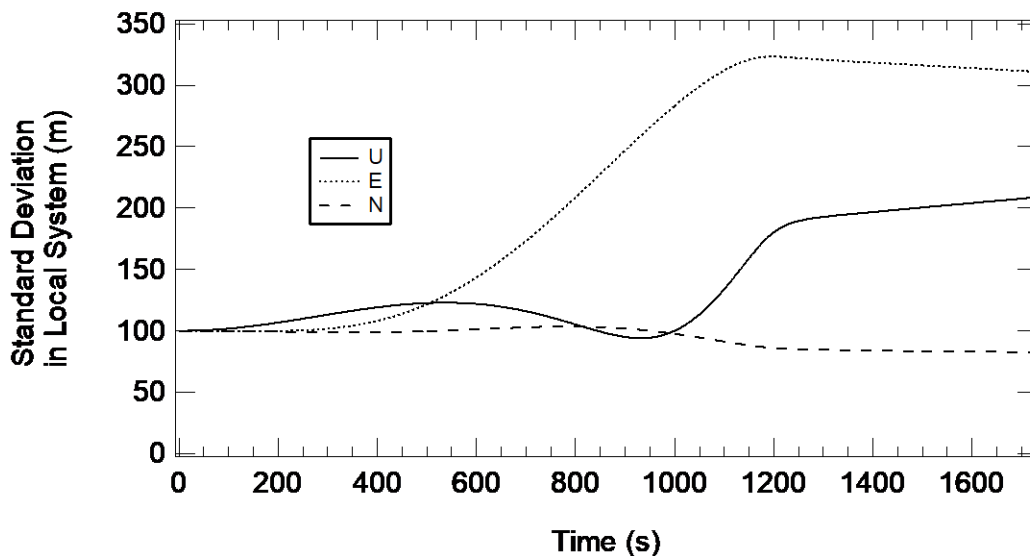
the variance, it is applied methods like Monte Carlo, but it requires multiple propagations (hundreds), becoming more expensive in terms of computational cost and time.

With the propagation of the reentry tanks it is possible to observe that all of the tanks made of Graphite-Epoxy survive and impact the surface with energies superior to 15 J. This is the reason why the Graphite-Epoxy tanks were selected to implement the propagation of the variance/covariance matrix and to analyze the dispersion of the state vector at the impact point. The tanks to be analyzed are the 2.5 cm and 50 cm of radius in the four initial conditions. According to Chen et al. (2017), the uncertainty in the satellite position is around ± 100 m for each component, and around ± 0.1 m/s in velocity, in other words, the standard deviation. Because the covariance matrix uses the variance like initial conditions, the variance in position are $\sigma^2_{x,y,z} = 1 \times 10^4$ m² and in velocity components it is $\sigma^2_{vel} = 1 \times 10^{-2}$ m²/s². These are the initial conditions for the main diagonal of the variance/covariance matrix.

The propagation matrix is derived in the inertial system, but, for practical uses, the variance is transformed to the local horizontal frame. Figures 11.65 to 11.72 shows the evolution of the standard deviation in position for each trajectory. In the inertial system, all of the propagated elements have an increase but, due to the transformation in the coordinate system and the implementation of a variable drag coefficient as a function of the fluid state, the results show reductions in the region of the transitional flow. Initially, the variables present a linear increase during the phase of rarefied flow. Next they present an exponential increment in the East and Upper positions and a small reduction in the north positions, during the phase of transfer flow, to finally present a quasi-linear tendency during the final approach in the supersonic continuum flow. The reentry duration is shorter compared to the periods in LEO. Some seconds instead of hours, which reduces the error propagation.

During the reentry of the 2.5 cm tank it is observed an exponential increment in the east coordinate and a decrement in the North position, because the inclination of the orbit and its proximity with the equator influence (getting more effects of the gravity) present more variations in the East than in the North direction. In terms of the landing zone area the mean trajectory presents a deviation of $\pm 311\text{ m}$ in the East-West direction, $\pm 83\text{ m}$ in the North – South direction and $\pm 208\text{ m}$ in the Upper – Lower direction. It represents a spheroid of the impact zones and increases the dispersion area of the fragment. Similar results are presented in the landing zone area when it is compared the four coordinates of latitude and longitude. Deviation of the total relative velocity vector is around $\pm 0.0326\text{ m/s}$, due to the significant reduction of the velocity vector in the atmospheric flight.

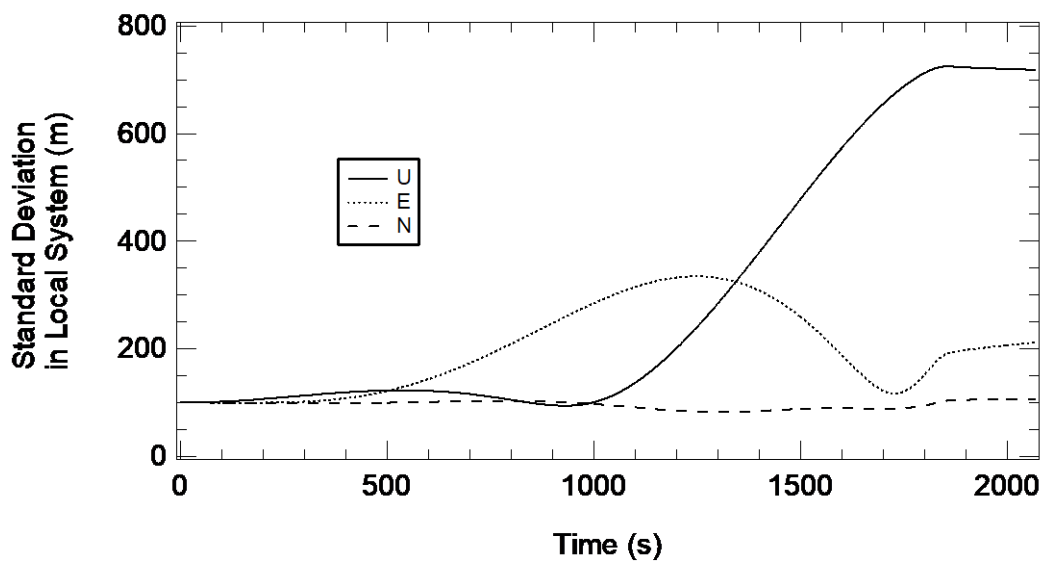
Figure 11.65 – Standard Deviation in Position for a sphere of 2.5 cm.



Similar to the behavior of the standard deviation in position for the spherical tank of 2.5 cm, it is propagated of the error in position for the spherical tank of 50 cm. In this case, the main deviation is in the vertical coordinate due to the vertical descent and highest vertical velocity. The east coordinate is smaller than the one for the 2.5 cm tank due to the lower influence of the winds, and the north-south is the smallest deviation, due to the orbit inclination. The impact

point presents a standard deviation in the vertical axis of $\pm 718.4\text{ m}$, in the east-west direction of $\pm 212.1\text{ m}$ and in the north – south direction $\pm 106.58\text{ m}$. In the case of the relative velocity the standard deviation has a reduction to $\pm 0.093\text{ m/s}$, as shown in figure 11.66. Compared with the standard deviation of the 2.5 cm tank, the 50 cm tanks presents an increase in the time of flight and an increment in the position and velocities deviations.

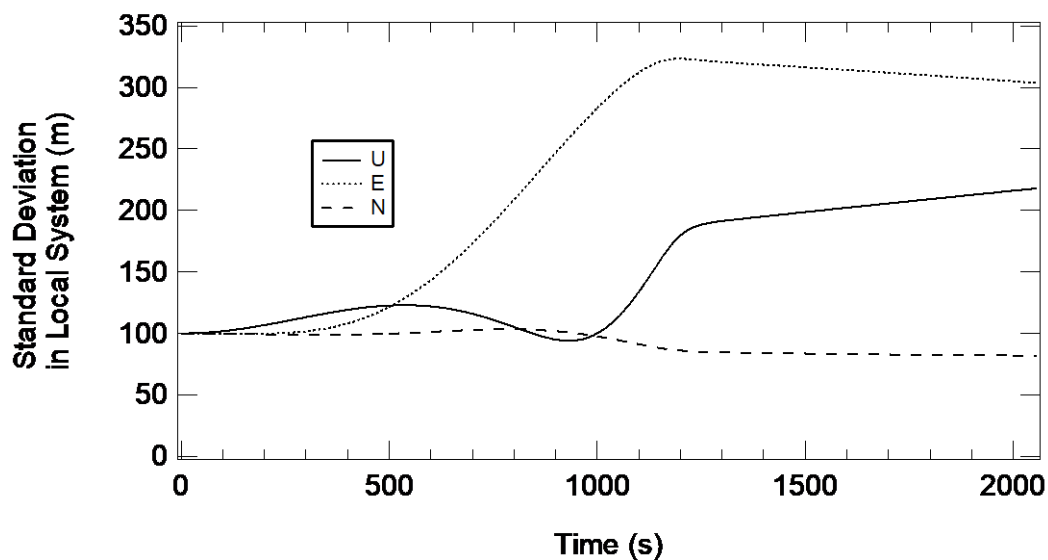
Figure 11.66 – Standard Deviation in Position for a sphere of 50 cm.



Next, the evolution of the propagation matrix is applied to the reentries of the tanks with rotation. In this case, the most important thing is the evolution of the standard deviation in the angular position and angular velocity. Due to the highest angular velocities and the smallest parameters of evaluation (360° is the maximum possible error in angular position) the Euler angles and angular velocity standard deviation presents undetermined values around 90 km of altitude, when the aerodynamic torques begin. This uncertainty is propagated along the trajectory generating numerical errors in the position and velocity deviations. For this reason the deviation of the Euler angles and angular velocity cannot be determinate for the reentries with high angular velocities. To avoid the numerical error propagation and to determine the deviations in position and velocity, the elements of the Jacobi matrix as a function of the

Euler angles and the angular velocity are null. Results show similar behavior to the ones observed in cases without angular velocity. The only significant change is the time of flight. For the tank with 2.5 cm, the deviation in the East-West direction is $\pm 303.6\text{ m}$, it is $\pm 81.9\text{ m}$ in the North – South direction and $\pm 217.95\text{ m}$ in the Upper – Lower direction. In the velocity it is $\pm 0.033\text{ m/s}$ (see figure 11.67). For the 50 cm spherical tank with initial angular velocity in the X_B the final deviation in the East-West direction is $\pm 236.9\text{ m}$, $\pm 110.8\text{ m}$ in the North – South direction and $\pm 708.9\text{ m}$ in the Upper – Lower direction, velocity is $\pm 0.094\text{ m/s}$. Graphical results are presented in figure 11.68.

Figure 11.67 – Standard Deviation in Position for a sphere of 2.5 cm with angular velocity in X_B .



Propagations of the standard deviation for reentry trajectories with angular velocities in the Y_B and Z_B axis don't show significant differences compared to the previous results. The differences are only in the times of flight and in the durations of the continuum flow flight, where there is an increase. These results are showed in figures 11.69 to 11.72.

Figure 11.68 – Standard Deviation in Position for a sphere of 50 cm with angular velocity in X_B .

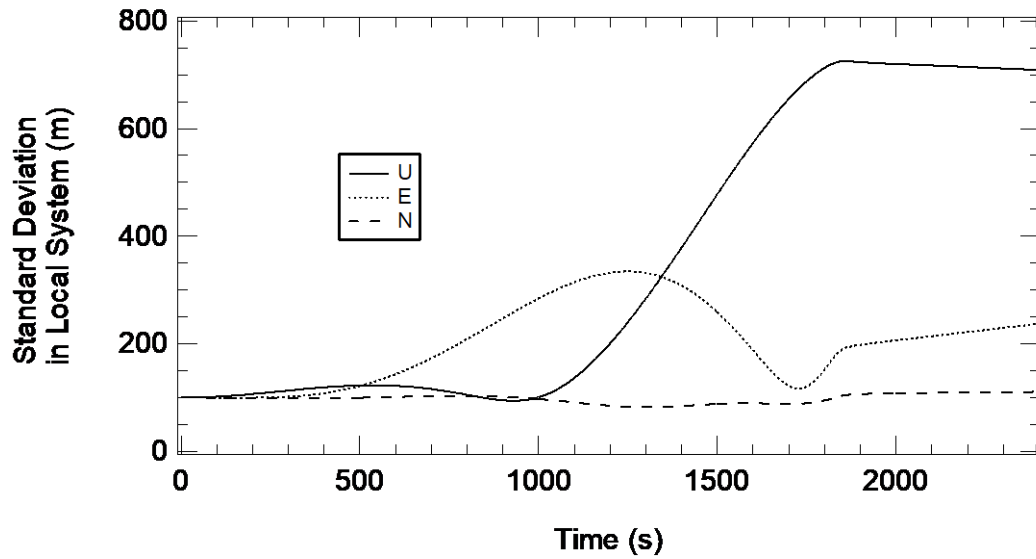


Figure 11.69 – Standard Deviation in Position for a sphere of 2.5 cm with angular velocity in Y_B .

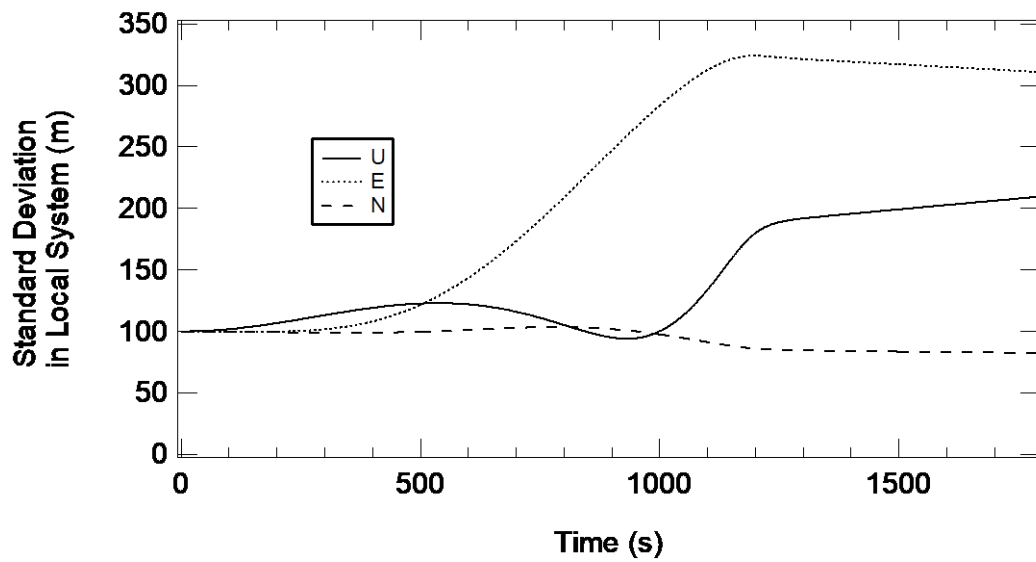


Figure 11.70 – Standard Deviation in Position for a sphere of 50 cm with angular velocity in Y_B .

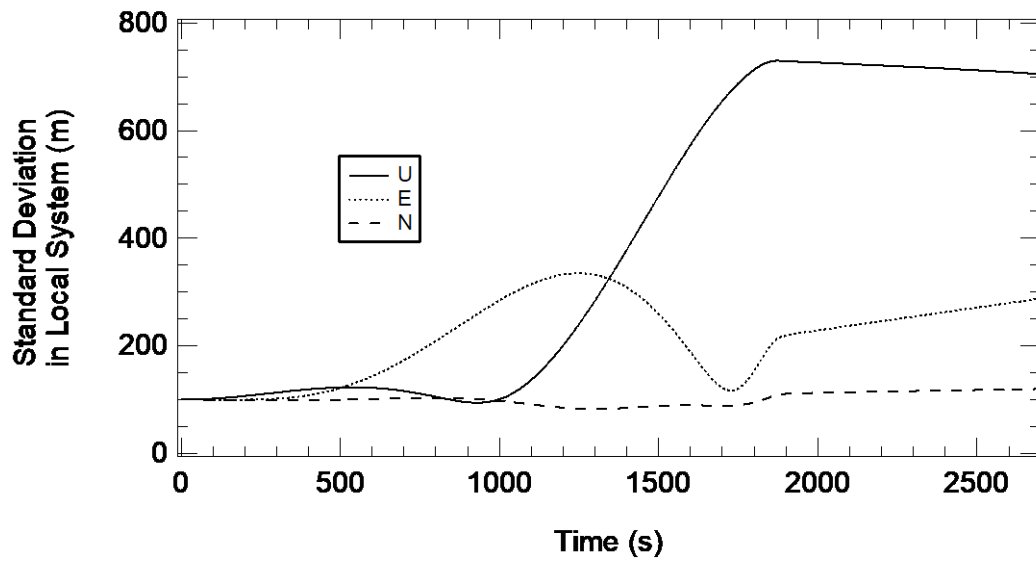


Figure 11.71 – Standard Deviation in Position for a sphere of 2.5 cm with angular velocity in Z_B .

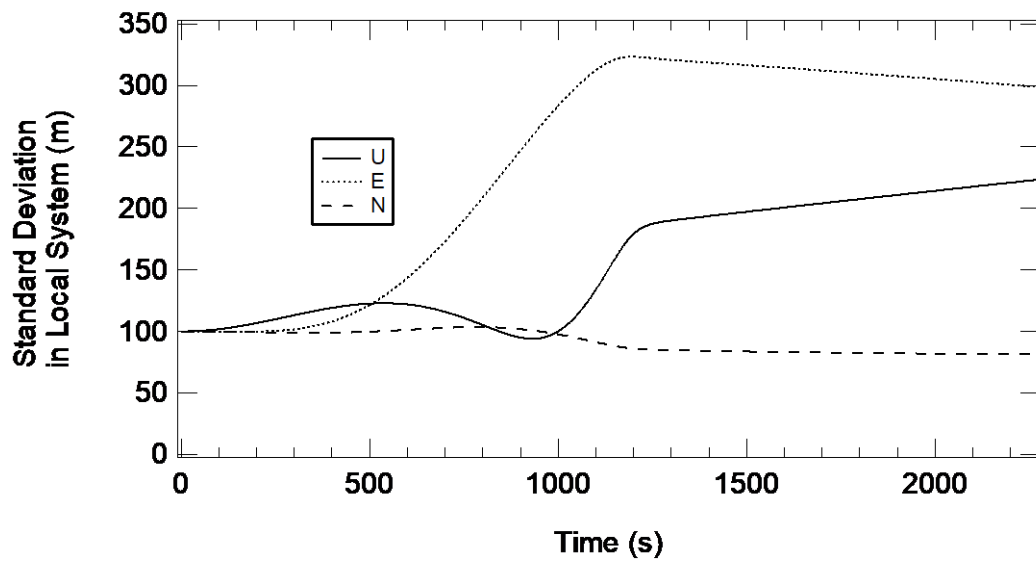
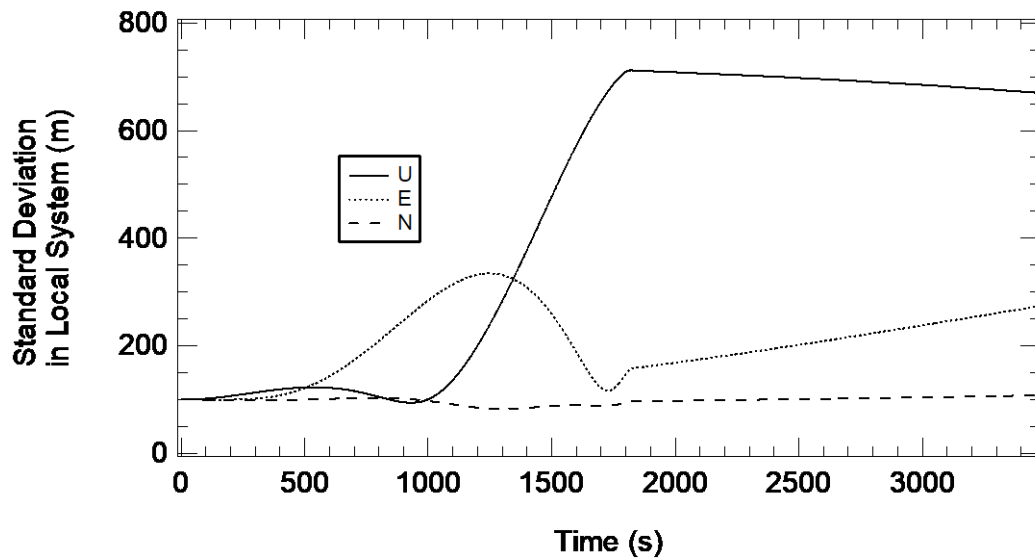


Figure 11.72 – Standard Deviation in Position for a sphere of 50 cm with angular velocity in Z_B .



The propagation of the variance/covariance matrix for satellite applications only requires the initial variation of the position and velocity, described previously. In the case of the reentry and applying the RCRA, it is important to analyze the variation of the variance under atmospheric and aerodynamic changes. Due to the atmospheric model, the uncertain error is around 15% of the density value, and according to the RCAR the total pressure coefficient uncertainty is around 10% (in the total C_p are included the values of lift, drag and Magnus coefficients) due to the uncertainty in the geometry and attitude of the debris. The new propagations take into account the same variations in the position and velocity vector and, in these cases, with initial standard deviations of 10% in the initial value of C_p value and 15% in the local density.

At 122 km of altitude, the mean value of the atmospheric density is 1.5×10^{-8} kg/m³. For a 15% of deviation, the variance is 5.0625×10^{-18} . In the case of the pressure coefficient, with the initial conditions in a rarefied flow, it is 2.06, and the estimated standard deviation is 10% with a variance of 0.043. The two new terms are included in the initial diagonal of the variance/covariance matrix.

With the implementation of the variance in density and pressure coefficient, the standard deviation in position increases significantly, to the order of kilometers. Figures 11.73 and 11.74 show the standard deviation of the position in the local frame. In the case of the tank of 2.5 cm, it is observed a linear increment of the deviations until 800 s, when the debris is around 100 km of altitude. At this point the increment of the density and the transition of the atmospheric flow generate an exponential increase in the standard deviation, around 800 s to 1300 s of flight, as shown in figure 11.73. During the final approach, in the supersonic continuum flow phase the deviation increment is linear. The error in altitude is the maximum for the two cases due to the influence of the density variation during the reentry. The final impact point of the mean trajectory presents a dispersion area in the horizontal plane with $\pm 66 \text{ km}$ in the East – West direction and $\pm 40 \text{ km}$ in the North – South direction. These standard deviations represent an elliptical region of 8293.8 km^2 for the landing zone error. The relative velocity presents a deviation of $\pm 8 \text{ m/s}$. The $\pm 100 \text{ km}$ deviation in the upper direction, indicates that small variations in density and in the pressure coefficient can delay the reentry, and in some cases, indicate that using that value for the initial density variation, the debris do not reenter.

Figure 11.73 – Standard deviation in position for a sphere of 2.5 cm with atmospheric and aerodynamic errors.

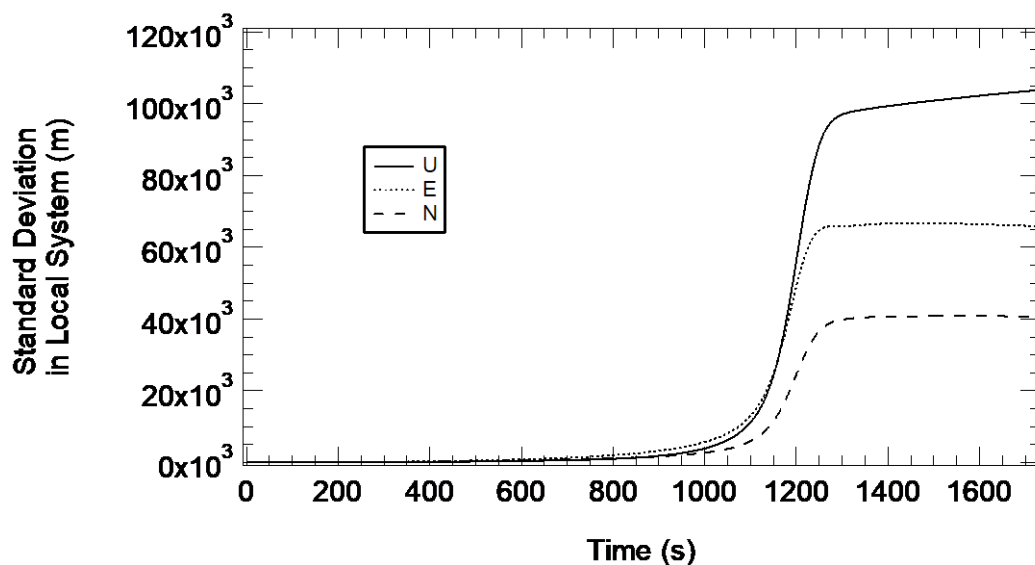
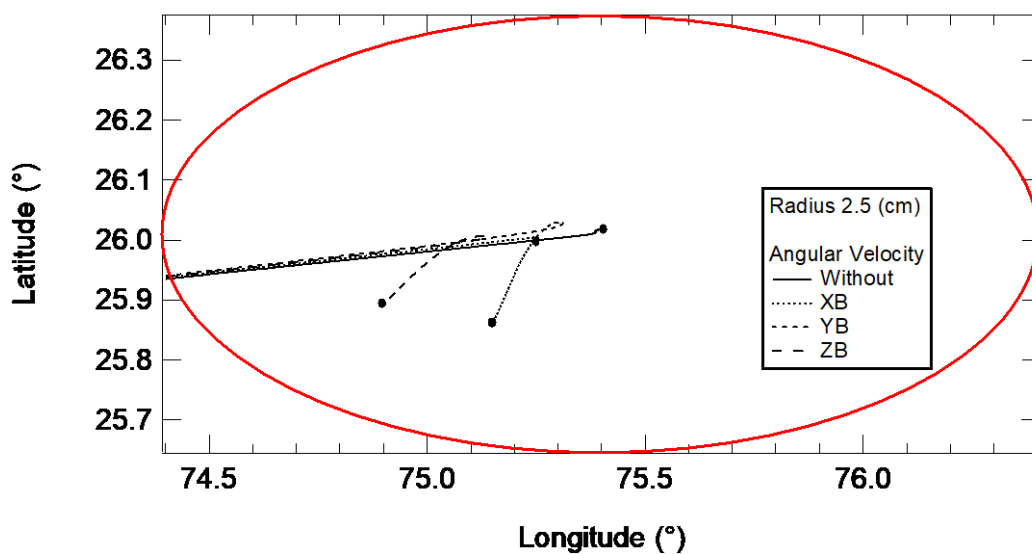


Figure 11.74 presents the dispersion area of the debris impact for the 2.5 cm entry tank. The red ellipse is proportional to the standard deviation in the horizontal plane for the nominal trajectory without induced angular velocity. It is possible to observe that the other trajectories, with the influence of the Magnus effect, are inside the red ellipse. In this case the propagation matrix and the final standard deviation of the mean trajectory, take into account the other possible landing points obtained due to the angular velocity and Magnus effect.

Figure 11.74 – Dispersion area for 2.5 cm tank.



The behavior of the standard deviation in the simulation of the 50 cm tank is similar to one presented by the 2.5 cm tank. See figure 11.75. At the beginning, the propagation of the deviation is linear with an exponential increment during the transition flow. The possible impact area is located below 82 km of altitude with ± 2.2 km in the East – West direction and ± 28 km in the North – South direction, equivalent to an elliptical region of 193.5 km^2 . The variation in velocity is $\pm 18.7 \text{ m/s}$.

Figure 11.76 shows the dispersion area of the impact zone. In this case, the red ellipse doesn't have the other trajectories propagated with the initial angular velocity, because the influence of the winds is reduced in the debris of 50 cm and it has the smallest deceleration due to the largest mass.

Figure 11.75 – Standard deviation in position for a sphere of 50 cm with atmospheric and aerodynamic errors.

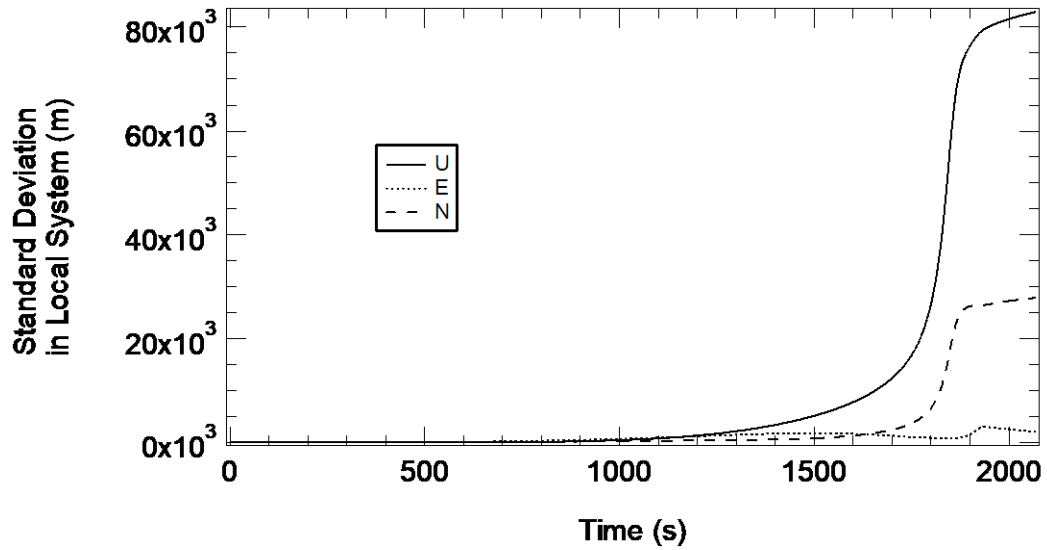
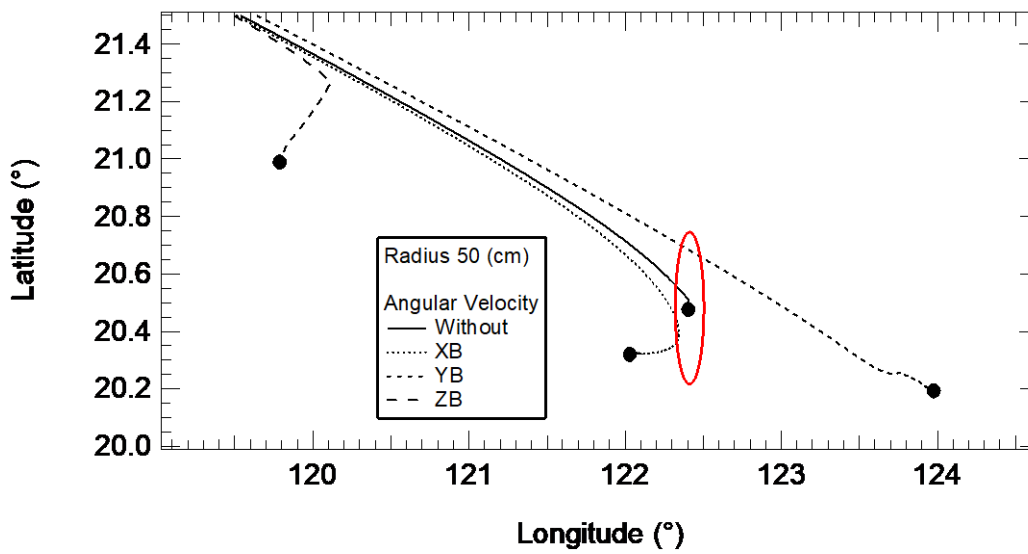


Figure 11.76 - Dispersion area for 50 cm tank.



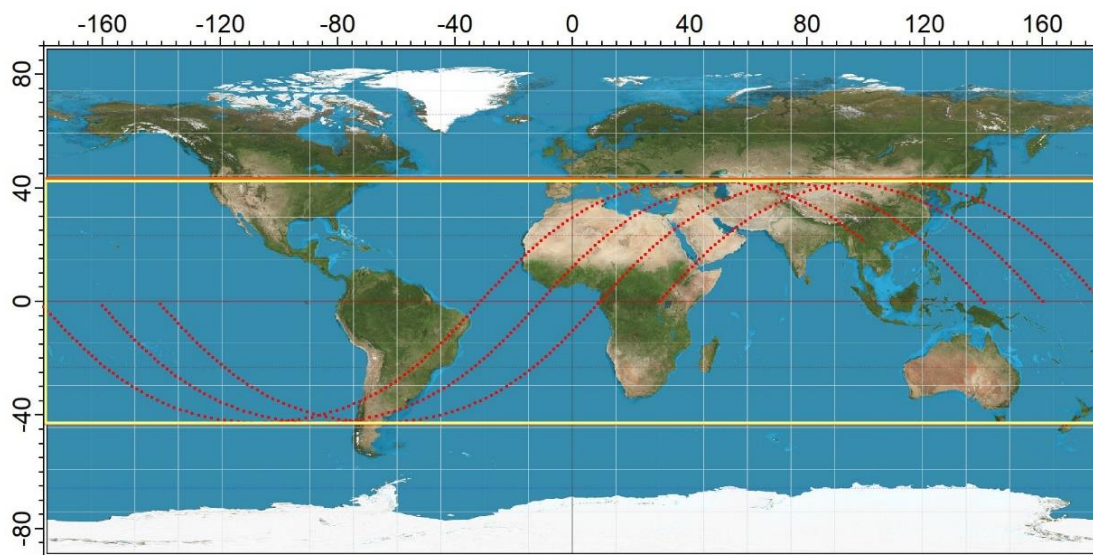
11.3. Study case: Tiangong – I China Space Station, reentry estimation.

Since March 2016, the first China's Space Station Tiangong-I is decaying rapidly. According to ESA, the reentry estimations are around 29 March to 6 April 2018, with an error in the estimation of one week (ESA, 2018).

The Tiangong – I orbited the Earth for the first time on 29 September 2011. On March 2016 it ended its service and China's Space Agency lost control. According to the Aerospace Corporation, (2018), the Space station has 8,500 kg of total mass, length of 10.5 m and diameter of 3.4 m.

The mean inclination of the orbit on 15 March 2018, is around 42.7° , with a mean semi-major axis of 6615.2 km. Figure 11.77 shows the orbit of the station (red dots) and the possible reentry region (yellow box). The horizontal axis indicates the longitude and the vertical axis the latitude. Due to the orbit inclination, the reentry region is located in latitudes between -42.7° S and 42.7° N, where, around 70% of the area are oceans and 30% is continental surface.

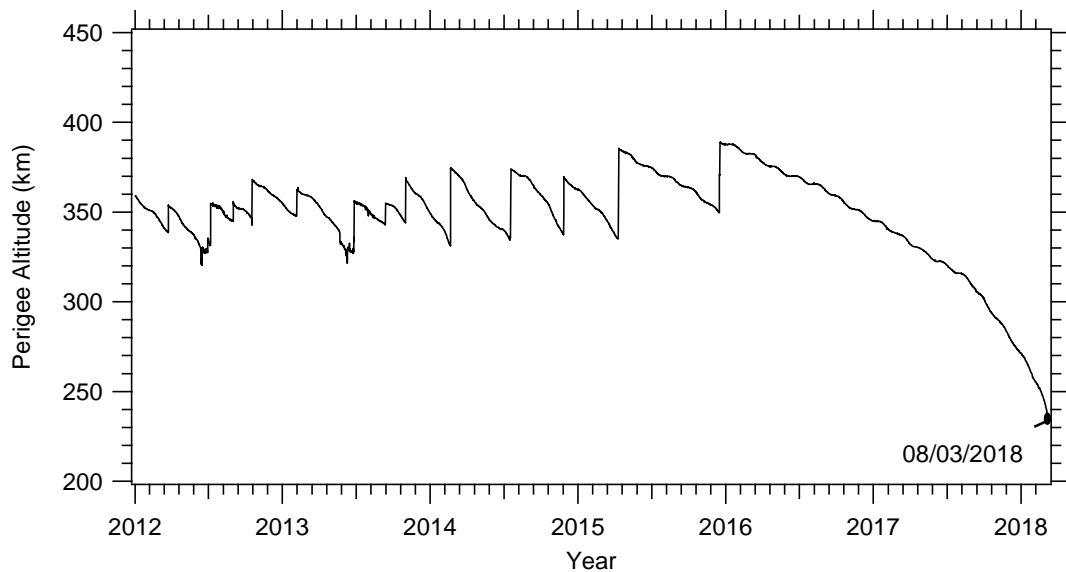
Figure 11.77 – Tiangong I orbit representation.



Since 2011 China's Space Agency effectuated multiple maneuvers to keep the orbit altitude, due to the orbital decay influenced by atmospheric and solar activity. The evolution of the perigee as a function of time is presented in figure

11.78, where the maintenance maneuvers are represented by vertical lines. Since the beginning of 2016 it is observed an altitude decay without maneuvers, due to the lost control. The Station present a decay larger than 110 km in the last two years.

Figure 11.78 – Tiangong I historical perigee altitude.



A computational propagator is implemented to determine the orbit decay and to estimate the possible reentry point. In this case, many variables can affect the results of the propagation, like: the unknowns of the space station attitude, material information, distribution of mass, geometry, space weather, aerodynamics coefficients, atmospheric variable conditions, etc. The station is a large complex flexible structure at hypersonic flight, with multiple objects inside, made of different materials and multiple shapes. The specific internal and structural distributions are only known by the manufacturers. All of these considerations generate a large uncertainty. Since the real dimensions of the space station are unknown, it is necessary to approximate of the geometry by an uniform cylinder with dimensions of 10 m of length and 3.4 m in diameter. The center of mass located in the geometric center, the cylinder is simulated without rotation and without solar panels. The selected material is aluminum

with 2.5 cm of wall thickness, because the total mass of the cylinder has about the space station reported mass, due to the material density.

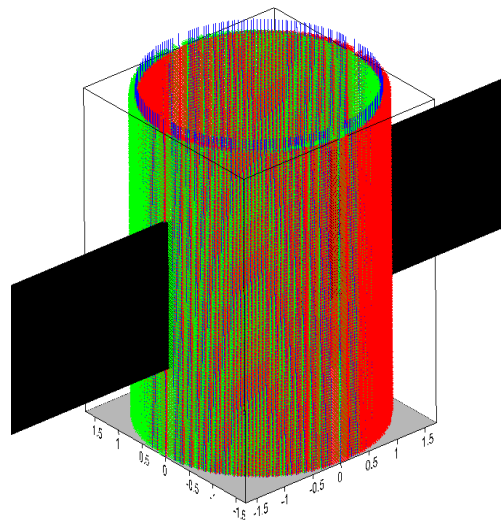
In figure 11.79 it is observed the diagram of the Tiangong-I space station and in figure 11.80 it is presented the computational model made with the reentry propagator (routine MESH) to simulate the reentry of the space station. Only in its surface, the model has more than 47,000 voxels.

Figure 11.79 - Tiangong-I diagram.



Source: Adapted from Aerospace Corporation (2018).

Figure 11.80 - Tiangong-I computational model approximation.

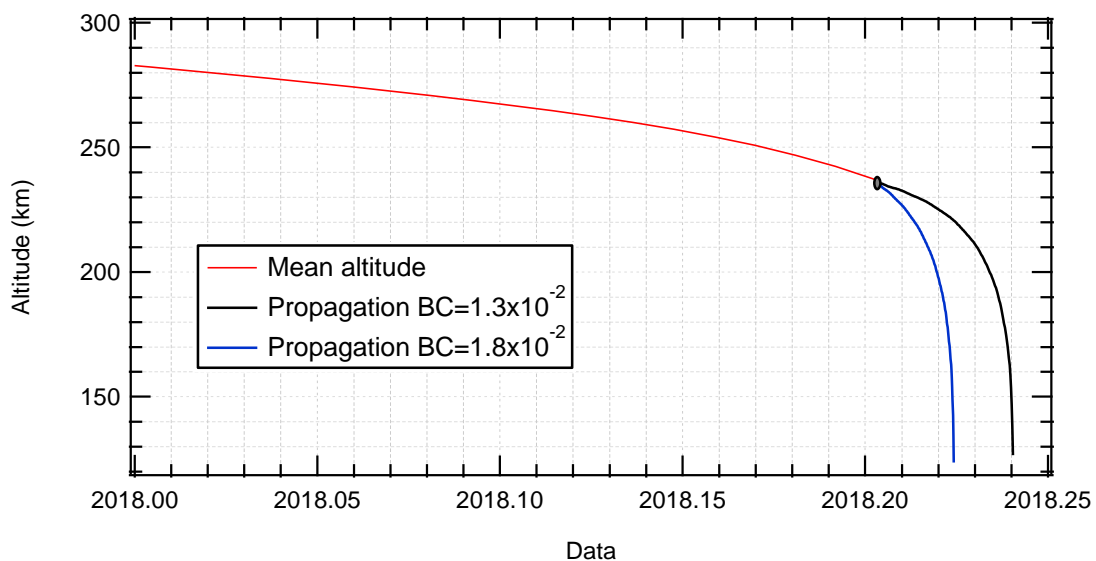


Many agencies are tracking and monitoring daily the evolution of the Tiangong-I orbit, to adjust the propagation models and reentry estimations. In this case, the computational code developed is used to propagate the mean orbit from the

TLE's. The goal is to analyze the reentry of a cylinder with similar conditions of the space station. The orbit is propagated in the inertial frame with adjustments in the hour angle from the epoch, actualizing the wind and atmospheric information for the selected data. The step-size of the orbit propagation is 0.005 s.

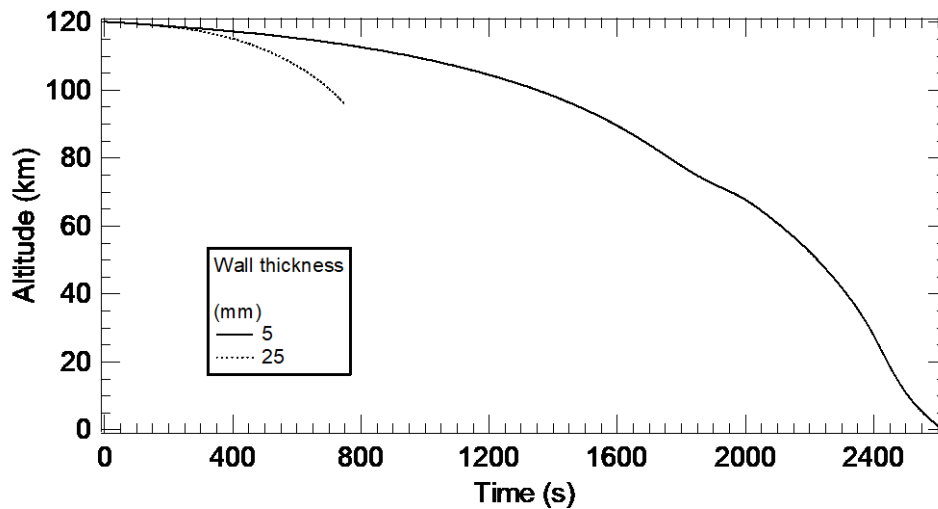
Figure 11.81 shows the mean altitude to the epoch 20180.74 from the TLE historical data. From the mean orbital elements at this point and the epoch, two orbits are propagated with changes in the ballistic coefficient (BC). Due to the unknown in the attitude of the space station and its rotation, it is analyzed the B^* from the TLE's. From 2016 to the propagated Epoch the maximum mean value of BC is $1.8 \times 10^{-2} \text{ m}^2/\text{kg}$ and the minimum is $1.3 \times 10^{-2} \text{ m}^2/\text{kg}$. Using the propagations of the orbit it is possible to estimate the reentry data. The orbit propagation ends at an altitude of 120 km, at this point begin the reentry phase and specific settlements are selected for better propagations. The reentry estimation, with the propagation from 15/03/2018, is expected to happen between the 23 to 31 March. The results are according to the ESA and Aerospace predictions. To get better accuracy, it is necessary to recalculate the propagated orbit with the TLE's daily evolution.

Figure 11.81 - Tiangong-I decay propagations.



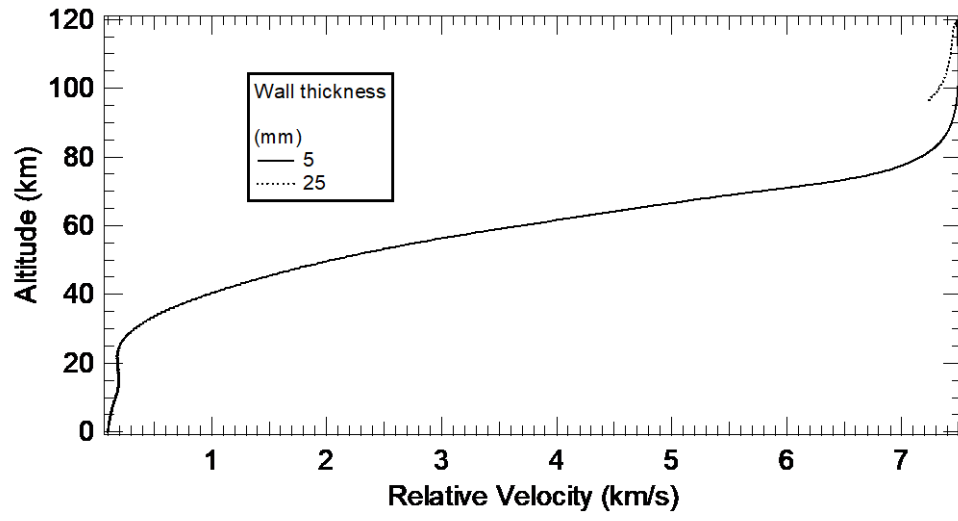
Using the meshed cylinder of the aluminum wall of 25 mm and also using the propagated conditions for the reentry, the trajectory is simulated. For a more realistic scenario, another aluminum cylinder with 5 mm of wall thickness (representing the structural station skin) is propagated with the same conditions of the 25 mm cylinder. The results are shown in figures 11.82 and 11.83. The cylinder of 5 mm is melted at altitudes around 90 km, where generally the panels, antennas and small structures are fragmented. The other case, the 25 mm fragment survived the reentry with more than 7,000 kg of mass, of course this is a hypothetical scenario. The survival of the 25 mm is due to the wall thickness. The high temperature voxels of the surface are fragmented along the trajectory, but the heat and velocity are not enough to melt or disintegrate the debris. The estimate impact velocity is superior to 20 m/s, becoming a risk.

Figure 11.82 – Tiangong-I cylinders approximation reentry.



The propagation of the Tiangong-I space station serves as an example of the potential and possible applications of the computational code developed. Nevertheless, the unknowns of many factors of the space station state, materials, geometry, etc., reduces the precision and increases the difficulty to estimate the real behavior of the reentry trajectory. Additionally, reentry estimations must be adjusted daily with real data for better accuracy.

Figure 11.83 - Tiangong-I cylinders velocity during reentry.



12. CONCLUSIONS

It is a fact that the increment in the population of space objects due to the space industry increases. A consequence of this increment is the accelerated increase of reentry debris, in particular of uncontrolled objects. Possible collisions and fragmentation of orbital debris will generate more objects to reentry, which is a complex problem and a risk to the population and Earth's activities, like air traffic control. Actually, many space agencies around the world are working in the reduction of the environmental impact of space activities.

The reentry object propagation and estimation is a multidisciplinary problem, which involves research areas like orbital mechanics, aerodynamics, aerothermodynamics, heat transfer, computational sciences, solid mechanics and others. Initially, unknown variables make the system determination, propagation and prediction more difficult. Lack of information in the debris area, mass, attitude, material data, internal distribution, aerodynamics and the lack of control, makes more difficult the task of generating a good agreement between the mathematical models, the simulations and the reality. External factors, like atmospheric models, winds, solar and geomagnetic activity, increase the errors and reduce the prediction effectivity. Due to all those reasons, the reentry problem is a chaotic system that implements deterministic models to solve the problem.

Similar to the air traffic control systems, some countries like The United States of America and others of the North Hemisphere implement radar and satellite systems to monitor debris. Due to the use of real data, some reentries are predicted with good accuracy and can be observed. Recording data from observational debris help to validate and improve the computational tools. From the moment that the debris is detected in a reentry maneuver to the impact point, only a few seconds are elapsed. To make predictions of the possible trajectory in real time, high fidelity models can't be used, because it increments the computational cost and time. It is necessary to simplify the

mathematical models to obtain data before the impact. The distributed simulation reduce the computational cost (time) and it allows better mathematical models to be used. The reentry uncertainty is similar to an aircraft crash. You have the initial conditions to find the impact zone, but you don't know the system state and the external variables with good accuracy.

For the modeling and propagation of trajectories and attitude of reentry debris without control, including fragmentation, to determine the survival and possible collision areas, it was developed a computational code in FORTRAN to determine the mean trajectory, attitude, temperatures and related phenomenon during the reentry. At the end of the research, one computational code was developed and more than 100 reentry cases were simulated and studied.

The modeling of the attitude, allows to observe the behavior of the debris surface due to the fluid/body interaction, to determine the points of maximum temperature and heat transference, the fragmentation process and the changes in the inertia moments due to the mass losses. The influence of the rotational motion of the body in the atmospheric flight generates the Magnus Effect. The results of propagations in 6DOF allows observing significant changes from the trajectories propagated in 3DOF, like: an increase in the collision area and, in the case of Titanium and Aluminum tanks, the reduction in the survivability of the object.

The implementation of the Voxels simplifies the meshing process, reduce the computational cost and allows to model any type of geometric shape with good agreement. Each voxel stores information of the temperature, heat, structural stress and fluid interaction, simplifying the structural analyzes and the reconfiguration of the new meshes. In this case, the voxels were used to model solid spheres, spherical tanks and cylinders. The results of voxel implementation present good agreement with the object-oriented model from ORSAT and can generate the spacecraft-oriented model like the SCARAB. Those computational tools were developed for the engineering teams of NASA

and ESA respectively, for more than 20 years, and are currently receiving updates. The present computational code generates equivalent results and was developed in less time with fewer resources.

The mass quantity is an important value that influences the trajectory, the rotational motion and the survivability of the debris. It is observed that the mass increment reduces the influence of the aero-breaking acceleration. It is possible to see, in the trajectories of the 50 cm tanks, which have the lowest orbit decay and the highest velocities, which the winds don't increment significantly the time of flight and the lateral velocity, like observed in the cases of the 2.5 cm tank trajectories. Results show that the landing zone estimated area for tanks of 50 cm is higher than the landing zone for the tanks of 2.5 cm, due to the increase of the decay velocity and surface area, which increase the Magnus effect. The increment in the debris mass generates increases in the landing zone.

The mass losses occurring during the fragmentation generate changes in the moments of inertia, incrementing the angular velocity and increasing the Magnus effect which changes the trajectory. The increase of the angular velocity increases the Magnus force, but its influence is only perceived at the low atmosphere, below 20 km of altitude, due to the atmospheric density. In highest altitudes the rotational motion doesn't show significant variations with the trajectories without the Magnus influence. In altitudes larger than 20 km, the increment in the angular velocities changes the fragmentation of the material due to the distribution of the heat flow in different points of the surface, reducing the possibility of melting and increasing the survivability. In the final approach, the increment of the angular velocity increased the Magnus effect, reducing the vertical velocity and increasing the flight path angle.

With the objective of using the computational code for the reentry analysis risk, it was implemented the ESA's methodology. 62 trajectories of possible reentry tanks were simulated with three possible materials and four rotational initial conditions. The results show that all the survival fragments are dangerous

because the final energy is superior to 15 J. In the case of the 2.5 cm titanium and aluminum tanks, the results also show that the rotational velocity and direction reduce the survival probabilities. To complement the analysis, trajectories were propagated with the variation/covariation matrix to observe the dispersion and the variations of the errors from the mean trajectory. The propagation of the position and velocity deviation is in agreement with the results reported by the scientific literature in the case of the satellites, but, in this case, it is necessary to propagate the trajectories with the atmospheric and aerodynamic uncertainties. Results of the variance/covariance propagation with uncertainties show variations in the 2.5 cm tank, which are higher than the results reported for the 50 cm tank, due to the influence of the winds that increased the lateral flight in the 2.5 cm tank. In the case of the 50 cm tank, due to the largest mass, winds influence and the lateral flight are reduced, but the Magnus effect is increased. For all the reentry analyses, the variance/covariance matrix with atmospheric and aerodynamics uncertainties must be propagated to get a better determination of the possible impact zones.

The main objective of this research was achieved. The results showed that the attitude of the debris generated significant changes along the flight trajectory and inside the structure of the body. To reach this conclusion, it was necessary to develop a computational code and a multidisciplinary research in areas, like: orbital debris, space engineering, computational sciences, Earth sciences, materials and structures, aerodynamics and aerothermodynamics, statistics, space regulations, disaster risk and others. The final product contributes to increasing the knowledge of the rotational reentry debris in hypersonic flight.

For future works, it is recommended specific analyzes to determine the aerodynamics, aerothermodynamics and structural properties for each tank along the trajectory. It is recommended the implementation of the code in the orbit decay estimation, orbit propagation, prevision of satellites collision and controlled reentry. It is also recommended the use of real data from tracking objects to validate the propagator, and to continue researches in areas like

hypersonic and aerothermodynamics to get better results. It is recommended the implementation of explosions models and/or two materials in the structure to produce the break-up and implemented the parallel function, also the study of better models in 3-D heat transference.

It is also recommended the implementation of a standard to generate a controller disposal, to reduce the debris orbiting time and to generate a controlled reentry and destruction.

REFERENCES

ADLER, M.; WRIGHT, M. **Draft entry, descent, and landing roadmap**. Washington: National Aeronautics and Space Administration NASA, 2010. 32p.

AGENCIA ESPACIAL BRASILEIRA - AEB, **Programa Nacional de Atividades Espaciais**: PNAE 2012-2021. Brasília: Ministério da Ciência, Tecnologia e Inovação, 2012. 35p.

AEROSPACE CORPORATION. **Reentry data**: Center for orbital and reentry debris studies. 2017. Available from: <
<http://www.aerospace.org/cords/research/reentry-data/>> Access in: 24 Aug. 2017.

AEROSPACE CORPORATION. **Tiangong-1 reentry**. Center for orbital and reentry debris studies. 2018. Available from: <
<http://www.aerospace.org/cords/reentry-predictions/tiangong-1-reentry/>> Access in: 18 Mar. 2018.

AILOR, W. **Space debris and other threats from outer space**. New York: Springer, 2013.

AILOR, W.; WILDE, P. Requirements for warning aircraft of reentering debris. In: IAASS CONFERENCE: BUILDING A SAFER SPACE TOGETHER, 3., 2008, Rome. **Proceedings...** 2008.

ALESSI, E. The reentry to Earth as a valuable option at the end-of-life of libration point orbit missions. **Advances in Space Research**, v. 55, n. 12, p. 2914-2930, 2015.

ALLEN, J.; EGGERS, J. R. **A study of the motion and aerodynamic heating of ballistic missiles entering the Earth's atmosphere at high supersonic speeds**. Washington: NACA, 1958. (NACA Report, 1381).

ANDERSON, J. **Hypersonic and high temperature gas dynamics**. New York: McGraw Hill, 1989. 53 p.

ANSELMO, L.; PARDINI, C. Computational methods for reentry trajectories and risk assessment. **Advances in Space Research**, v. 35, n. 1, p. 1343-1352, 2005.

ANSI. **Guide to reference and standard atmospheric models**. Reston: AIAA, 2004. 100p.

BAMBACE, L.; MILANI, P.; GUEDES, U. **Método de voo ou reentrada na atmosfera utilizando rotação**. São José dos Campos: INPE, 2014. (BR n. WO2014063210).

BARROS, E.A.; MACIEL, H.S.; PETRACONI FILHO, G. **Câmara de plasma reativo para ensaio de materiais de sistema de proteção térmica em ambiente de reentrada**. 2002. (CTA/ITA-IEF/TM-003/2002). Dissertação (Mestrado em Física de Plasma) - Instituto Tecnológico de Aeronáutica (ITA), São José dos Campos, 2002.

BASTIEN, P.; MARTIN, S.; VINCENT, R.; DIDIER, E. Monte-Carlo analysis of object reentry in Earth's atmosphere based on Taguchi method. In: EUROPEAN SYMPOSIUM ON AEROTHERMODYNAMICS OF SPACE VEHICLES, 8., 2015, Lisbon, Portugal. **Proceedings...** 2015.

BATISTA, A. **Estudo de modelos de condições iniciais da geração a priori de detritos espaciais e sua propagação orbital**. 2011. 354p. (INPE 02.28.17.49-TDI). Dissertação (Mestrado em Engenharia e Tecnologia Espaciais/ Mecânica Espacial e Controle) - Instituto Nacional de Pesquisas Espaciais (INPE), São José dos Campos, 2011.

BECK, J.; MERRIFIELD, J.; HOLBROUGH, I.; MARKELOV, G.; MOLINA, R. Application of the SAM destructive re-entry code to the spacecraft demise integration test cases. In: EUROPEAN SYMPOSIUM ON

AEROTHERMODYNAMICS OF SPACE VEHICLES, 8., 2015, Lisbon, Portugal.

Proceedings... 2015a.

BECK, J.; MERRIFIELD, J.; MARKELOV, G.; HOLBROUGH, I.; MOLINA, R. Verification and application of the sam re-entry model. In: SGOBBA, T.; RONGIER, I. (Eds.). **Space safety is no accident**. Switzerland: Springer, 2015b. p. 437-443.

BOWMAN, B.; TOBISKA, W.; MARCOS, F.; VALLADARES, C. The JB 2006 empirical thermospheric density model. **Journal of Atmospheric and Solar-Terrestrial Physics**, v. 70, n. 5, p. 774-793, 2008.

BRIGGS, L. J. Effect of spin and speed on the lateral deflection (curve) of a baseball; and the Magnus effect for smooth spheres. **American Journal of Physics**, v. 27, n. 8, p. 589-596, 1959.

BRONSHTEN, V. Trajectory and orbit of the Tunguska meteorite revisited. **Meteoritics & Planetary Science**, v. 34, n. 4, p. 137-143, 1999.

CARANDENTE, V.; SAVINO, R.; IACOVAZZO, M.; BOFFA, C. Aerothermal analysis of a sample-return reentry capsule. **Fluid Dynamics & Materials Processing Tech Science Press**, v. 9, n. 4, p. 461-484, 2013.

CHAPMAN, D. **An approximate analytical method for studying entry into planetary atmospheres**. Washington: NACA, 1958. 103p. (NACA Technical Note, 4276).

CHEN, L.; BAI, X.; LIANG, Y.; LI, K. Orbital prediction error propagation of space objects. In: CHEN, L.; BAI, X.; LIANG, Y.; LI, K. (Eds.). **Orbital data applications for space objects**. Singapore: Springer, 2017. p. 23-75.

CHIVERS, I.; SLEIGHTHOLME, J. **Introduction to programming with FORTRAN**. 3. ed. London, UK: Springer-Verlag, 2015. 452p.

CHOBOTOV, V. **Orbital mechanics**. 3. ed. Virginia: American Institute of Aeronautics and Astronautics AIAA, 2002. 455p.

COSPAR. **Models of the Earth's upper atmosphere**: COSPAR International reference atmosphere. 2012. Available from:

<<http://sol.spacenvironment.net/CIRA-2012>> Access in: 10 May 2016.

COSTA, R.; SILVA, J.; WU, S.; CHU, Q.; MULDER, A. Atmospheric reentry modeling and simulation. **Journal of Spacecraft and Rockets**. v. 39, n. 4, p. 636-639, 2002.

DESAI, P.; BRAUN, R.; POWELL, R.; ENGELUND, W.; TARTABINI, P. Six degree-of-freedom entry dispersion analysis for the meteor recovery module. In: AEROSPACE SCIENCES MEETING & EXHIBIT, 34., 1996, Reno.

Proceedings... 1996.

DETRA, R.; HIDALGO, H. Generalized heat transfer formulas and graphs for nose cone re-entry into the atmosphere. **ARS Journal**, v. 31, n. 3, p. 318-321, 1961.

DOBARCO-OTERO, J.; SMITH, R.; BLEDSOE, K.; DELAUNE, R.; ROCHELLE, W.; JOHNSON, N. The object reentry survival analysis tool (ORSAT): version 6.0 and its application to spacecraft entry. In: INTERNATIONAL ASTRONAUTICAL CONGRESS OF THE INTERNATIONAL ASTRONAUTICAL FEDERATION, 56., 2005, Fukuoka, Japan. **Proceedings...** 2005.

DROB, D. et al. An empirical model of the Earth's horizontal wind fields: HWM07. **Journal of Geophysical Research**, v. 113, n. a12, p. 1-18, 2008.

DUNCAN, R. **Dynamics of atmospheric entry**. New York: McGraw Hill, 1962.

DURIN, C. Study of spacecraft elements surviving an atmospheric re-entry. In: IAASS CONFERENCE, 6., 2013, Montreal, Canada. **Proceedings...** 2013.

EUROPEAN SPACE AGENCY ESA. **ESA space debris mitigation compliance verification guidelines**. Noordwijk: ESA, 2015.

EUROPEAN SPACE AGENCY ESA. **Space debris by numbers: operations, space debris**. 2017. Available from:
<http://www.esa.int/Our_Activities/Operations/Space_Debris/Space_debris_by_the_numbers> Access in: 24 Aug. 2017.

EUROPEAN SPACE AGENCY ESA. **Tiangong-1 reentry updates: rocket science blog**. 2018. Available from:
<<http://blogs.esa.int/rocketscience/2018/01/12/tiangong-1-reentry-updates/>>
Access in: 15 Mar. 2018.

FALSONE, A.; PRANDINI, M. A randomized approach to probabilistic footprint estimation of a space debris uncontrolled reentry. **IEEE Transactions on Intelligent Transportation Systems**, v. 18, n. 10, p. 2657-2666, 2017.

FEISTEL, A.; WEAVER, M.; AILOR, W. Comparison of reentry breakup measurements for three atmospheric reentries. In: IAASS CONFERENCE, 6., 2013, Montreal, Canada. **Proceedings...** 2013.

FEHLBERG, E. **Classical fifth-, sixth-, seventh-, and eighth-order Runge-Kutta formulas with step size**. Washington: NASA, 1968. (NASA Report, TRS-287).

FERREIRA, L. O. **Formulação analítica para o problema da interação da dinâmica de reentrada com efeitos de flexibilidade e vibração em veículos aeroespaciais**. 1989. 235 p. (INPE-4963-TDL/392). Dissertação (Mestrado em Engenharia e Tecnologia Espaciais / Mecânica Espacial e Controle) - Instituto Nacional de Pesquisas Espaciais (INPE), São José dos Campos, 1989.

FICO JÚNIOR, N. R.; ORTEGA, MA. **Simulação do escoamento na região do flape de reentrada de um túnel de vento transônico**. 1991. (TA_8513596411dd1e33d25727534f9ef1b9). Tese (Doutorado em

Aerodinâmica, Propulsão e Energia) - Instituto Tecnológico de Aeronáutica (ITA), São José dos Campos, 1991.

FRANK, M.; WEAVER, M.; BAKER, R. A probabilistic paradigm for spacecraft random reentry disassembly. **Reliability Engineering and System Safety**, v. 90, n. 1, p. 148-161, 2004.

FRITSCHÉ, B.; KLINKRAD, H.; KASHKOVSKY, A.; GRINBERG, E. Spacecraft disintegration during uncontrolled atmospheric re-entry. **Acta Astronautica**, v. 47, n. 2, p. 513-522, 2000.

FRITSCHÉ, B.; LIPS, T.; KOPPENWALLNER, G. Analytical and numerical re-entry analysis of simple-shaped objects. **Acta Astronautica**, v. 60, n. 1, p. 737-751, 2007.

FRITSCHÉ, B.; ROBERTS, T.; ROMAY, M.; IVANOV, M.; GRINBERG, E.; KLINKRAD, H. Spacecraft disintegration during uncontrolled atmospheric re-entry. In: EUROPEAN CONFERENCE ON SPACE DEBRIS ESOC, 2., 1997, Berlin, Germany. **Proceedings...** 1997.

GALLAIS, P. **Atmospheric re-entry vehicle dynamics**. Berlin: Springer, 2007. 43p.

GOMES, W.; MARCONI, E.; CARRARA, V. Trajectory control during an aeroassisted maneuver between coplanar circular orbits. **Journal Aerospace Technology Management**, v. 6, n. 2, p. 159-168, 2014.

GRANT, M.; BRAUN R. Analytic hypersonic aerodynamics for conceptual design of entry vehicles. In: AIAA AEROSPACE SCIENCES MEETING INCLUDING THE NEW HORIZONS FORUM AND AEROSPACE EXPOSITION, 48., 2010, Florida. **Proceedings...** 2010.

GREEN, S. D.; MATVEEV, M. Y.; LONG, A. C.; IVANOV, D.; HALLETT, S. R. Mechanical modelling of 3D woven composites considering realistic unit cell geometry. **Composite Structures**, v. 118, n. 1, p. 284-293, 2014.

GUEDES, U. Análise da manobra de injeção de reentrada comandada com aumento e redução da velocidade de injeção da velocidade de injeção. In: COLÓQUIO BRASILEIRO DE DINÂMICA ORBITAL CBDO, 10., 2000, Nazaré Paulista. **Anais...** 2000.

GUEDES, U. **Relação ao ponto de pouso, utilizando Sistema geocêntrico inercial e manobras laterais**. 1997. 116p. Tese (Doutorado em Engenharia e Tecnologia Espaciais / Mecânica Espacial e Controle) - Instituto Nacional de Pesquisas Espaciais (INPE), São José dos Campos, 1997.

HANKEY, W. L. **Re-entry aerodynamics**. Virginia: AIAA, 1988. 68p.

HALLMAN, W.; MOODY, D. **Trajectory reconstruction and heating analysis of Columbia composite debris pieces**. Washington: FAA, 2005. (ATR-2005, FAA/AST-300).

HEDIN, A.; FLEMING, E.; MANSON, A.; SCHMIDLIN, F.; AVERY, S.; CLARK, R.; VINCENT, R. Empirical wind model for the upper, middle and lower atmosphere. **Journal of Atmospheric and Terrestrial Physics**, v. 58, n. 13, p. 1421-1447, 1996.

HEDIN, A.; BIONDI, M.; BURNSIDE, R.; HERNANDEZ, G.; JOHNSON, R.; KILLEEN, T.; SPENCER, N. Revised global model of thermosphere winds using satellite and ground-based observations. **Journal of Geophysical Research**, v. 96, n. A5, p. 7657-7688, 1991.

HIRSCHEL, E, et al. **Basics of aerothermodynamics**. Berlin: Springer, 2005. 42p.

INTERNATIONAL ACADEMY OF ASTRONAUTICS - IAA. **Space debris mitigation, implementing zero debris creation zones**. Paris: IAA, 2005. 61p.

INTERNATIONAL ORGANIZATION FOR STANDARDIZATION (ISO). **Space environment (natural and artificial): Earth upper atmosphere**. Switzerland: ISO/FDIS, 2013. 46 p.

IVANOV, A.; RYZHANSKII, V. Model for the atmospheric fragmentation and scattering of a small celestial body. **Journal of Combustion, Explosion, and Shock Waves**. v. 41, n. 3, p. 346-356, 2005.

JACCHIA, L. **Thermospheric temperature, density, and composition: new models**. Washington: SAO, 1977. (Special Report, 375).

KAPLINGER, B.; WIE, B.; DEARBORN, D. Nuclear fragmentation/dispersion modeling a simulation of Hazardous Near-Earth Objects. **Acta Astronautica**, v. 90, n. 1, p. 156-164, 2013.

KELLEY, R.; HILL, N.; ROCHELLE, W.; JOHNSON, N.; LIPS, T. Comparison of ORSAT and SCARAB reentry analysis tools for a generic satellite test case. In: COSPAR SCIENTIFIC ASSEMBLY, 38., 2010, Bremen, Germany. **Proceedings...** 2010.

KIM, H. J.; SWAN, C. C. Voxel-based meshing and unit-cell analysis of textile composites. **International Journal for Numerical Methods in Engineering**, v. 56, n. 7, p. 977-1006, 2003.

KLINKRAD, H. **Space debris**. New York: John Wiley & Sons, 2010.

KOLBE, A.; DITTER, C.; REIMER, T.; WEIHS, H.; WARTEMANN, V. Analytical determination of the thermal loads on the re-entry vehicle SHEFEX III. In: EUROPEAN SYMPOSIUM ON AEROTHERMODYNAMICS FOR SPACE VEHICLES, 8., 2015, Lisbon. **Proceedings...**2015.

KOPPENWALLNER, G.; FRITSCHKE, B.; LIPS, T.; MARTIN, T.,
FRANCILLOUT, L.; PASQUALE, E. Analysis of ATV destructive re-entry
including explosion events. In: EUROPEAN CONFERENCE ON SPACE
DEBRIS, 4., 2005, Darmstadt, Germany. **Proceedings...** 2005.

KOPPENWALLNER, G.; FRITSCHKE, B.; LIPS, T. Multidisciplinary analysis
tools for orbit and re-entry. INTERNATIONAL WORKSHOP ON
ASTRODYNAMICS TOOLS AND TECHNIQUES ESTEC, 3., 2006, Germany.
Proceedings... 2006.

KOPPENWALLNER, G.; FRITSCHKE, B.; LIPS, T.; KLINKRAD, H. SCARAB - A
multidisciplinary code for destruction analysis of space-craft during re-entry. In:
EUROPEAN SYMPOSIUM ON AEROTHERMODYNAMICS FOR SPACE
VEHICLES ESA, 5., 2005, Germany. **Proceedings...** 2005.

KOPPENWALLNER, G.; LEGGE, H. Drag of bodies in rarefied hypersonic flow.
Thermophysical Aspects of Re-Entry Flows proceedings series, v. 103, n.
1, p. 44-59, 1985.

KRAG, H. The Inter-Agency Space Debris Coordination Committee (IADC). In:
UNITED NATIONS WORKSHOP ON SPACE LAW, 10., 2016, Vienna.
Proceedings... 2016.

KUGA, H.; CARRARA, V. FORTRAN and C-codes for higher order and degree
geopotential and derivatives computation. In: SIMPÓSIO BRASILEIRO DE
SENSORIAMENTO REMOTO, 16., 2013, Foz de Iguazu, Brazil. Proceedings...
2013.

LEITE, P. H. M. **Computational analysis of the aerothermodynamics effects
in a reentry vehicle with surface discontinuity like a combined GAP/STEP.**
2015. 189 p. Tese (Doutorado em Combustão e Propulsão) - Instituto Nacional
de Pesquisas Espaciais (INPE), São José dos Campos, 2015.

LI, Y.; LI, Y.; YANG, Y.; GE, X. An HLA based design of collision simulation system for large-scale LEO objects. **IEEE Intelligent Computation Technology and Automation**, v. 2, n. 1, p. 3-6, 2009.

LING., L. Simulation for Prediction of Entry Article Demise (SPEAD): an analysis tool for spacecraft safety analysis and ascent/reentry risk assessment. In: INTERNATIONAL SPACE SAFETY CONFERENCE, 7., 2014, Germany. **Proceedings...** 2014.

LIOU, J. C.; JOHNSON, N. L. Risks in space from orbiting debris. **Science-New York**, v. 311, n. 5759, p. 340-341, 2006.

LIPS, T.; FRITSCH, B. A comparison of commonly used re-entry analysis tools. **Acta Astronautica**. v. 57, n. 1, p. 312-323, 2005.

LIPS, T.; FRITSCH, B.; KOPPENWALLNER, G.; KLINKRAD, H. Spacecraft destruction during re-entry - latest results and development of the SCARAB software system. **Advances in Space Research**. v. 34, n. 1, p. 1055-1060, 2004.

LIPS, T.; HUERTAS, I.; VENTURA, S.; OMALY, P. Results of the IAASS re-entry analysis test campaign 2012. In: IAASS CONFERENCE, 6., 2013, Montreal, Canada. **Proceedings...** 2013.

LIPS, T.; WARTEMANN, V.; KOPPENWALLNER, G.; KLINKRAD, H.; ALWES, D.; DOBARCO-OTERO, J.; SMITH, R.; DELAUNE, R.; ROCHELLE, W.; JOHNSON, N. Comparison of ORSAT and SCARAB reentry survival results. In: EUROPEAN CONFERENCE ON SPACE DEBRIS, 4., 2005, Darmstadt, Germany. **Proceedings...** 2005.

LU, P.; RAO, P. An integrated approach for entry mission design and flight simulations. In: AIAA AEROSPACE SCIENCES MEETING AND EXHIBIT, 42., 2004, Reno. **Proceedings...** 2004.

LUNA, L.; SIELAWA, J.; SILVA, W. **Simulação da atitude de um veículo durante sua reentrada na atmosfera terrestre**. São José dos Campos: ITA, 1991.

MATNEY, M. Empirical tests of the predicted footprint for uncontrolled satellite reentry hazards. In: IAASS CONFERENCE, 5., 2011, Versailles, France. **Proceedings...** 2011.

MAZAHERI, A. High-energy atmospheric reentry test aerothermodynamic analysis. **Journal of Spacecraft and Rockets**. v. 50, n. 2, p. 270-281, 2013.

MEHTA, P.; KUBICEK, M.; MINISCI, E.; VASILE, M. Sensitivity analysis and probabilistic re-entry modeling for debris using high dimensional model representation based uncertainty treatment. **Advances in Space Research**. v. 59, n. 1, p. 193-211, 2017.

MEHTA, P.; MINISCI, E.; VASILE, M. Sensitivity analysis towards probabilistic Re-entry modeling of spacecraft and space debris. In: AIAA MODELING AND SIMULATION TECHNOLOGIES CONFERENCE, 2015, Dallas. **Proceedings...** 2015a.

MEHTA, P.; MINISCI, E.; VASILE, M.; WALKER, A.; BROWN, M. An open source hypersonic aerodynamic and aerothermodynamics modeling tool. In: EUROPEAN SYMPOSIUM ON AEROTHERMODYNAMICS FOR SPACE VEHICLES, 8., 2015b, Lisbon, Portugal. **Proceedings...** 2015.

MERRIFIELD, J.; BECK, J.; MARKELOV, G.; LEYLAND, P.; MOLINA, R. Aerothermal heating methodology in the spacecraft aerothermal model (SAM). In: SGOBBA, T.; RONGIER, I. (Eds). **Space safety is no accident**. Switzerland: Springer, 2015a. p. 463-468.

MERRIFIELD, J.; BECK, J.; MARKELOV, G.; MOLINA, R. Simplified aerothermal models for destructive entry analysis. In: EUROPEAN

SYMPOSIUM ON AEROTHERMODYNAMICS FOR SPACE VEHICLES, 8., 2015b, Lisbon, Portugal. **Proceedings...** 2015.

MITITELU, G. Analytical solutions for the equations of motion of a space vehicle during the atmospheric re-entry phase on a 2-D trajectory. **Celestial Mechanics and Dynamical Astronomy**, v. 103, n. 1, p. 327-342, 2009.

MONTERO-CHACÓN, F.; MARÍN-MONTÍN, J.; MEDINA, F. Mesomechanical characterization of porosity in cementitious composites by means of a voxel-based finite element model. **Computational Materials Science**, v. 90, n. 1, p. 157-170, 2014.

MOOIJ, E.; HANNINEM, P. Distributed global trajectory optimization of a moderate lift-to-drag re-entry vehicle. AIAA GUIDANCE, NAVIGATION AND CONTROL CONFERENCE, 2009, Chicago. **Proceedings...** 2009.

MORESCHI, L.; SCHULZ, W. Aerodynamic resistance in upper atmosphere: case of the last stage Delta rocket fall in Argentina. **Journal of Computational and Applied Mathematics**, v. 35, n. 1, p. 727-737, 2016.

MROZINSKI, R.; MENDECK, G.; CUTRI-KOHART, R. Overview of entry risk predictions. **Advances in Space Research**. v. 34, n. 1, p. 1044-1048, 2004.

NATIONAL ADVISORY COMMITTEE FOR AERONAUTICS (NACA). **Equations tables and chart for compressible flow**. Washington: NACA, 1953. (NACA Report, 1135).

NATIONAL AERONAUTICS AND SPACE ADMINISTRATION (NASA). A review of space environment implications of CubeSat traffic, 2003-2014. **Orbital Debris Quarterly News**, v. 18, n. 1, p. 4-6, 2014.

NATIONAL AERONAUTICS AND SPACE ADMINISTRATION (NASA). Monthly effective mass of objects in Earth orbit by region. **Orbital Debris Quarterly News**, v. 19, n. 1, p. 9, 2015.

NATIONAL AERONAUTICS AND SPACE ADMINISTRATION (NASA). Monthly number of objects in Earth orbit by object type. **Orbital Debris Quarterly News**, v. 19, n. 3, p. 10, 2015.

NATIONAL AERONAUTICS AND SPACE ADMINISTRATION (NASA). Monthly number of objects in Earth orbit by object type. **Orbital Debris Quarterly News**, v. 21, n. 1, p. 12, 2017.

NATIONAL AERONAUTICS AND SPACE ADMINISTRATION (NASA). **Technical standard**. Washington: NASA, 1998. (STD, 8729.1).

NATIONAL OCEANIC AND ATMOSPHERIC ADMINISTRATION (NOAA). **U.S. standard atmosphere 1976**. Washington, D.C.: NOAA, 1976. 241 p.

OLIVEIRA, S. **Fragmentação por ação aerotermodinâmica e predição da área de impacto de um veículo especial com injeção controlada da re-entrada**. 2009. 409p. (INPE-16586-TDI/1575. 2009). Tese (Doutorado em Engenharia e Tecnologia Espaciais / Mecânica Espacial e Controle) - Instituto Nacional de Pesquisas Espaciais (INPE), São José dos Campos, 2009.

OMALY, P.; MAGNIN, C.; GALERA, S. DEBRISK, CNES tool for re-entry survivability prediction: validation and sensitivity analysis. In: IAASS CONFERENCE, 6., 2013, Montreal, Canada. **Proceedings...** 2013.

OMALY, P.; SPEL, M. DEBRISK, a tool for re-entry risk analysis. In: IAASS CONFERENCE A SAFER SPACE FOR SAFER WORLD, 5., 2012, Noordwijk, Netherlands. **Proceedings...** 2012.

PADILLA, J.; BOYD, I. Assessment of rarefied hypersonic aerodynamics modeling and wind tunnel data. In: AIAA/ASME JOINT THERMOPHYSICS AND HEAT TRANSFER CONFERENCE, 9., 2006, San Francisco. **Proceedings...** 2006.

PALHARINI, R. **Numerical investigation of aerothermodynamics in a reentry vehicle with surface discontinuity-like cavity**. 2010. 153p. (INPE-16789-TDI/1706). Dissertação (Mestrado em Combustão e Propulsão) - Instituto Nacional de Pesquisas Espaciais (INPE), São José dos Campos, 2010.

PARDINI, C.; ANSELMO, L. GOCE Reentry predictions for the Italian civil protection authorities. In: INTERNATIONAL GOCE USER WORKSHOP, 5., 2014, Paris. **Proceedings...** 2014.

PARDINI, C.; ANSELMO, L. Impact of the time span selected to calibrate the ballistic parameter on spacecraft Re-entry predictions. **Advances in Space Research**, v. 41, n. 7, p. 1100-1114, 2008.

PARDINI, C.; ANSELMO, L. On the accuracy of satellite reentry predictions. **Advances in Space Research**. v. 34, n. 1, p. 1038-1043, 2004.

PARIGINI, C.; CANO, J.; RAMOS, R. **Preliminary estimation of the footprint and survivability of the Chelyabinsk Meteor fragments**. 2013. Available from: < <https://arxiv.org/abs/1304.2410> > Access in: 30 May. 2016.

PARIGINI, C.; FUENTES, I.; RAMOS, R.; BONETTI, D.; CORNARA, S. Debris tool and its use in mission analysis activities. In: EUROPEAN SYMPOSIUM ON AEROTHERMODYNAMICS FOR SPACE VEHICLES, 8., 2015, Lisbon, Portugal. **Proceedings...** 2015.

PARK, S.; PARK, G. Reentry trajectory and survivability estimation of small space debris with catalytic recombination. **Advances in Space Research**, v. 60, n. 1, p. 893-906, 2017.

PASQUALE, E.; STEINKOPF, M.; FRANCILLOUT, L.; ESCANE, I.; BENARROCHE, P.; DELATTRE, S.; ARZEL, L. ATV5 shallow reentry mission: challenge and achievements. In: EUROPEAN SYMPOSIUM ON

- AEROTHERMODYNAMICS FOR SPACE VEHICLES, 8., 2015, Lisbon, Portugal. **Proceedings...** 2015.
- PAVLIS, N.; HOLMES, S.; KENYON, S.; FACTOR, J. The development and evaluation of the Earth Gravitational Model 2008 (EGM2008). **Journal of Geophysical Research: Solid Earth**, v. 117, n. B4, p. 1-38, 2012.
- PATERA, R.; AILOR, W. The realities of reentry disposal. In: AAS/AIAA SPACE FLIGHT MECHANICS MEETING, 8., 1998, Monterey. **Proceedings...** 1998.
- PICONE, J.; HEDIN, A.; DROB, D.; AIKIN, A. NRLMSISE-00 empirical model of the atmosphere: Statistical comparisons and scientific issues. **Journal of Geophysical Research: Space Physics**, v. 107, n. A12, p. 1-16, 2002.
- PIERRO, B. Ciência do desastre. **Revista Pesquisa FAPESP**, n. 264, p. 36-39, 2018.
- PORTELLI, C.; SALOTTI, L.; ANSELMO, L.; LIPS, T.; TRAMUTOLA, A. BeppoSAX equatorial uncontrolled re-entry. **Advances in Space Research**, v. 34, n. 1, p. 1029-1037, 2004.
- REAGAN, F.; ANANDAKRISHNAN, S. **Dynamics of atmospheric re-entry**. Washington: AIAA, 1993.
- REID, J.; NUMRICH, R. Co-arrays in the next Fortran Standard. **Scientific Programming**, v. 15, n. 1, p. 9-26, 2007.
- ROCHELLE, W.; MARICHALAR, J.; JOHNSON, N. Analysis of reentry survivability of UARS spacecraft. **Advances in Space Research**, v. 34, n. 1, p. 1049-1054, 2004.
- ROCHELLE, W.; KINSEY, R.; REID, E.; REYNOLDS, R. Spacecraft orbital debris reentry aerothermal analysis. In: INTERNATIONAL ASTRONAUTICAL CONGRESS, 50., 1999, Amsterdam, The Netherlands. **Proceedings...** 1999.

ROCHELLE, W.; KINSEY, R.; REID, E.; REYNOLDS, R.; JOHNSON, N. Spacecraft Orbital Debris Reentry: Aerothermal Analysis. In: ANNUAL THERMAL AND FLUIDS ANALYSIS WORKSHOP: SPACECRAFT ANALYSIS AND DESIGN, 8., 1997, Houston. **Proceedings...** 1997.

SAMPAIO, P.; SANTOS, W. Computational analysis of the aerodynamic heating and drag of a reentry Brazilian satellite. In: CONGRESSO NACIONAL DE ENGENHARIA MECÂNICA CONEM, 6., 2010, Campina Grande, Brazil. **Proceedings...** 2010.

SAPOZHNIKOV, S.; KUDRYAVTSEV, O.; DOLGANINA, N.; Experimental and numerical estimation of strength and fragmentation of different porosity alumina ceramics. **Materials & Design**, v. 88, n. 1, p. 1042-1048, 2015.

SCHAAF, S.; CHAMBRE, P. **Flow of rarefied gases no. 8**. New Jersey: Princeton University, 1961. 55 p.

SHOEMAKER, M.; VAN DER HA, J.; ABE, S.; FUJITA, K. Trajectory estimation of the Hayabusa spacecraft during atmospheric disintegration. **Journal of Spacecraft and Rockets AIAA**, v. 50, n. 2, p. 326-336, 2013.

SIKHARULIDZE, Y.; MORAES, P.; KORCHAGIN, A. **Analysis of accuracy at ballistic re-entry in the Earth atmosphere**. 1998. Available from: < http://issfd.org/ISSFD_1999/pdf/ODR_2.pdf > Access in: 28 Aug. 2016.

SILVA, J.; MORAES, R. **Dinâmica da reentrada de veículos na atmosfera**. 1983. Dissertação (Mestrado em Engenharia Aeronáutica e Mecânica) - Instituto Tecnológico de Aeronáutica (ITA), São José dos Campos, 1983.

SIM, H.; KIM, K. Reentry survival analysis of tumbling metallic hollow cylinder. **Advances in Space Research**, v. 48, n. 1, p. 914-922, 2011.

SMITH, R.; BLEDSOE, K.; DOBARCO-OTERO, J.; ROCHELLE, W.; JOHNSON, N.; PERGOSKY, A.; WELSS, M. Reentry survivability analysis of

the Hubble space telescope (HST). In: EUROPEAN CONFERENCE ON SPACE DEBRIS, 4., 2005, Darmstadt, Germany. **Proceedings...** 2005.

STENZEL, C. Distributed simulation in technical applications. In: INTERNATIONAL PHD WORKSHOP OWD, 10., 2008, Wisla, Poland. **Proceedings...** 2008.

STRACK, W.; DOBSON, W.; HUFF, V. **The N-Body code a general FORTRAN code for solution of problems in space mechanics**. Washington: NASA, 1963. (Technical Note, D-1455).

TARDY, J.; KLUEBER, C. Estimation and prediction of orbital debris reentry trajectories. **Journal of Spacecraft and Rockets AIAA**, v. 39, n.6, p. 845-851, 2002.

TARTABINI, P.; BRETT, S. Ares I-X separation and reentry trajectory analyses. In: AIAA ATMOSPHERIC FLIGHT MECHANICS CONFERENCE, 2011, Oregon, **Proceedings...** 2011.

TEWARI, A. **Atmospheric and space flight dynamics**. Boston: Birkhauser, 2007.

TEWARI, A. Entry trajectory model with thermomechanical breakup. **Journal of Spacecraft and Rockets AIAA**, v. 46, n. 2, p. 299-306, 2009.

THORSTEN, K.; JORG, F.; WOLFRAM, F. Magnus effect on a rotating sphere at high Reynolds numbers. **Journal of Wind Energy and Industrial Aerodynamics**. v. 110, n. 1, p. 1-9, 2012.

TIRSKII, G.; KHANUKAEVA, Y. Ballistics of a non-fragmenting meteor body with allowance made for mass outflow in the Non-isothermal Atmosphere I. **Cosmic Research**, v. 45, n. 6, p. 476-485, 2007.

TORO, P.; MINUCCI, M.; CHANES, J.; RAMOS, A. Experimental hypersonic investigation over the Micro-Satellite SARA. In: BRAZILIAN CONGRESS OF

THERMAL SCIENCES AND ENGINEERING ENCIT, 10., 2004, Rio de Janeiro. **Proceedings...** 2004.

UNITED NATIONS (UN). **International space law**: United Nations instruments. Vienna: United Nations, Office for Outer Space Affairs, 2017.

VALLADO, D. A. Covariance transformations for satellite flight dynamics operations. In: AAS/AIAA ASTRODYNAMICS SPECIALIST CONFERENCE, 2004, Big Sky, Montana. **Proceedings...** 2004.

VALLADO, D.; SEAGO, J. Covariance realism. **Advances in the Astronautical Sciences**, v. 135, n. 1, p. 49-67, 2009.

VIVIANI, A.; PEZZELLA, G. **Aerodynamic and aerothermodynamics analysis of space mission vehicles**. New York: Springer, 2015. 70p.

VINH, N.; BASEMANN, A.; CULP, R. **Hypersonic and planetary entry flight mechanics**. Toronto: The University of Michigan Press, 1980.

WALBERG, G. A survey of aero-assisted orbit transfer. **Journal of Spacecraft and Rockets AIAA**, v. 22, n. 1, p. 3-18, 1985.

WATANABE, J.; OHKAWA, T.; SATO, M.; OHNISHI, I.; IJIMA, Y. Fragmentation of the Hayabusa spacecraft on re-entry. **Journal of Astronomical Society of Japan**. v. 63, n. 11, p. 955-960, 2011.

WEAVER, M.; BAKER, R.; FRANK, M. **Probabilistic estimation of reentry debris area**. Paris: ESA, 2001. (SP, 473-515W).

WEILAND, C. **Computational spaceflight mechanics**. Berlin: Springer, 2010.

WEN, Q.; YANG, L.; ZHAO, S.; FANG, Y.; WANG, Y.; HOU, R. Impacts of orbital elements of space-based laser station on small scale space debris removal. **Optik-International Journal for Light and Electron Optics**, v. 154, n. 1, p. 83-92, 2018.

WILSON, S.; VULETICH, I.; BRYCE, I.; BRETT, M.; WILLIAMS, W.;
FLETCHER, D.; COOPER, N. Space Launch & Re-entry Risk Hazard Analysis–
A New Capability. In: INTERNATIONAL ASTRONAUTICAL CONGRESS (IAC),
60., 2009, Daejeon, Korea. **Proceedings...** 2009.

WILLIAMS, J.; SENENT, J.; OCAMPO, C.; MATHUR, R.; DAVIS, E. C.
Overview and software architecture of the Copernicus trajectory design and
optimization system. In: INTERNATIONAL CONFERENCE ON
ASTRODYNAMICS TOOLS AND TECHNIQUES, 4., 2010, Madrid, Spain.
Proceedings... 2010.

ZINIU, W.; RUIFENG, H.; XI, Q.; XIANG, W.; ZHE, W. Space debris reentry
analysis methods and tools. **Chinese Journal of Aeronautics**. v. 24, n. 1, p.
387-395, 2011.

ZIPFEL, P. **Modeling and Simulation of Aerospace Vehicle Dynamics**. 2 ed.
Reston: AIAA, 2007.

PUBLICAÇÕES TÉCNICO-CIENTÍFICAS EDITADAS PELO INPE

Teses e Dissertações (TDI)

Teses e Dissertações apresentadas nos Cursos de Pós-Graduação do INPE.

Manuais Técnicos (MAN)

São publicações de caráter técnico que incluem normas, procedimentos, instruções e orientações.

Notas Técnico-Científicas (NTC)

Incluem resultados preliminares de pesquisa, descrição de equipamentos, descrição e ou documentação de programa de computador, descrição de sistemas e experimentos, apresentação de testes, dados, atlas, e documentação de projetos de engenharia.

Relatórios de Pesquisa (RPQ)

Reportam resultados ou progressos de pesquisas tanto de natureza técnica quanto científica, cujo nível seja compatível com o de uma publicação em periódico nacional ou internacional.

Propostas e Relatórios de Projetos (PRP)

São propostas de projetos técnico-científicos e relatórios de acompanhamento de projetos, atividades e convênios.

Publicações Didáticas (PUD)

Incluem apostilas, notas de aula e manuais didáticos.

Publicações Seriadas

São os seriados técnico-científicos: boletins, periódicos, anuários e anais de eventos (simpósios e congressos). Constam destas publicações o Internacional Standard Serial Number (ISSN), que é um código único e definitivo para identificação de títulos de seriados.

Programas de Computador (PDC)

São as sequências de instruções ou códigos, expressos em uma linguagem de programação compilada ou interpretada, a ser executada por um computador para alcançar um determinado objetivo. São aceitos tanto programas fonte quanto executáveis.

Pré-publicações (PRE)

Todos os artigos publicados em periódicos, anais e como capítulos de livros.